THE MECHANICS OF ABRASION RELATING TO HOUSEHOLD CLEANING

By ANTHONY CLIFFORD KENT

A thesis submitted to the
University of Birmingham
for the degree of
ENGINEERING DOCTORATE

Centre for Formulation Engineering
School of Chemical Engineering
College of Engineering and Physical Sciences
University of Birmingham
October 2015

Abstract

Abrasion of polymer surface films or coatings is an everyday occurrence, whether in the home, work or industry. As a result a wide variety of polymer films can be found on surfaces. Despite the numerous applications, three body thin film abrasion appears a niche area of study and as a result under-researched.

This investigation focuses on identifying, characterising and quantifying the abrasive wear of a baked dehydrated castor oil deposit formed on stainless steel. The primarily aim of this project is to understand how the fundamental properties of the liquid abrasive cleaning system contribute to the material removal. Investigations have primarily been carried out using a reciprocating linear tribometer for the cleaning and a profilometer to measure the wear.

The wear of the baked oil film was found to largely follow the established Archard wear equation in terms of sliding distance and load, despite the fact it was derived to describe two body and not three body wear. However the wear rate was not inversely proportional to hardness and there were significant effects when parameters not in the Archard equation are considered. In particular changing the speed, viscosity, particle size and distribution all had an impact on the wear.

Acknowledgements

Firstly I would like to recognise all the staff and students at the University of Birmingham I have worked with. There are many people I would like to thank for their knowledge, support and friendship. For now I would in particular I offer my heartfelt thanks to Simon Johnson, Mike Adams, Neil Rowson, Alex Ashcroft, Steve Singleton and Richard Greenwood for their encouragement and support in producing this thesis.

I also thank the EPSRC, the University of Birmingham and Unilever Research and Development Port Sunlight for funding this work.

Finally I would like to thank my wife Emma for the invaluable love and support provided throughout this project.

Contents

Symbols and abbreviations

δ	phase angle
ζ	damping coefficient
ϕ	phase change
χ	volume fraction of the particles
η_s	dynamic viscosity of a suspension
η_c	continuous phase dynamic viscosity
η_0	zero shear viscosity
η_∞	infinite shear viscosity
$[\eta]$	intrinsic viscosity
ω	angular frequency of oscillation

ω_0	angular resonant frequency
A	area of indentation (standard indentation)
A_c	area of the contact in nanoindentation
α	a power law fit parameter used in nanoindentation
β	a power law fit parameter used in nanoindentation
BSE	Back scattered electron
c	particle concentration
C_i	indenter setup damping coefficient
C_s	oil surface damping coefficient
c_1 to c_5	constants used to calculated the area of contact in nanoindentation
μ	friction coefficient
DCO	dehydrated castor oil
DMA	dynamic mechanical analysis
d	mean particle diameter
E*	Complex modulus
E’	Storage modulus
E’’	Loss modulus
E_i	Indenter modulus
E_r	Reduced modulus
E_s	Surface modulus
mE_s	measured storage modulus
F_0	force amplitude for harmonic motion
FGNC	fine ground natural chalk
h	indentation depth

h^f	film thickness
h_{min}^{EHL}	minimum elastohydrodynamic film thickness
h_{min}^{HL}	minimum hydrodynamic film thickness
h_{max}	maximum displacement of the indenter
h_c	depth of the contact based on the initial unloading
h_r	residual displacement after removing the indenter
HV	Vickers indentation hardness
mH	measured hardness from nanoindenation
I	indentation depth
k	wear coefficient
K	overall system stiffness
K_i	indenter setup stiffness
K_s	oil surface stiffness
l	length of a single pass
L	total sliding distance
LAC	liquid abrasive cleaning
LAS	linear alkyl benzene sulphonate (sulphuric acid)
m	mass of the probe
R	radius of the probe
P	indentation load
PCC	precipitated calcium carbonate
PMMA	poly(methyl methacrylate)
SEM	scanning electron microscope
SE	Secondary electron

u	sliding speed
URDPS	Unilever Research and Development Port Sunlight
V	wear volume
W	load
x	displacement of the sample subject to harmonic motion

Table of figures

Table of tables

1. INTRODUCTION

The formation of stains/soils/fouling deposits on surfaces is a problem that affects most people on a daily basis. Often the removal of fouling deposits from equipment either before or after it has been used takes considerable time and energy. Hence the formation of stains/soils/fouling deposits and their removal through "cleaning science" is often a critical underlying topic that affects quality in the food, personal care, medical, hospitality and electronics industries, amongst others, as well as being a key part of life in the work place and home [1-3].

To remove the different types of soils that can form on a surface many cleaning processes have been developed. They are all based on either physical or chemical actions or a combination of actions including, but not limited to, chemical reaction, plasticisation, emulsification, erosion and abrasion. The key aim of all cleaning processes is to maximise the removal of the fouling deposit(s) whilst minimising negative factors such as the damage to the underlying surface, the time to carry out the cleaning, the energy required, cost and safety concerns [1, 3, 4]. This project is focused on one particular type of cleaning process, that of liquid abrasive cleaning (LAC), and understanding the fundamental science underpinning the LAC process.

LAC fluids in forms similar to that of modern toothpastes have been used for over a hundred years and basic abrasive systems were used as far back as the ancient Egypt [5]. In the late 19^{th} and early 20^{th} century LAC pastes were developed to include surfactants, soaps and

other cleaning agents giving us the basis of modern day toothpastes. However, it was not until 1969 that the first recognisable mass produced gentle, household cream cleanser, Vim, was launched by Lever Brothers [6]. Today LAC fluids are mainly used for cleaning teeth and tough household soils: situations in which chemical cleaning is difficult either because the soil is too inert or using the chemicals required for an appropriate amount of removal are too hazardous or produce other undesired side affects [7]. The reason for avoiding the use of abrasives in all cleaners is due to inherent potential to cause damage to the underlying surface [8].

Despite this long history, there is a lack of understanding of the fundamental science of abrasion being carried out by the LAC fluids (see literature review). Although the reason appears not through lack of effort but rather because the process of abrasive cleaning involves many interlinked factors, which are hard to separate, and, like other cleaning processes, because much research is carried out in industry and not reported in the open literature [1]. A range of techniques could be used to investigate the influence the abrasive and liquid base has on the effectiveness of an abrasive cleaning product. Measurements in this investigation have focussed on indentifying and quantifying the cleaning properties of model household fluid systems acting on baked dehydrated castor oil (DCO) stains on stainless steel (SS). The aim is to be able to understand how the fundamental properties of the cleaning system contribute to the material removal. Investigations have been carried out primarily under tribological wearing conditions of an oil stain. However, some measurements have been done on the potential polishing nature of some abrasive fluids on a polymer surface.

1.1 Abrasives market

For many people the image for LAC cleaners is that of a tool of last resort. Most people would not use abrasives in the first instance to clean a surface due to the risk of damage to the substrate. However, that is not to say that the products do not have value as many people keep a bottle of the product for occasional use. The global market for scouring agents was valued at approximately one billion Euros in 2013 [9]. The Unilever Cif /Jif brand is currently brand leader with about a 25% market share. However there is a perception that quality in an abrasive is desirable and so one may expect good brand loyalty compared to other fast moving consumer goods [10] and indeed the brand share of Cif has been reasonably constant since 2008.

As has already been mentioned, abrasive products have a long history and innovation is often slow with occasional breakthroughs. Therefore in order to grow the business or expand market share to new users it would be beneficial to be able to show a significant shift in the technology used in the product. The primary aim in abrasive cleaning is the material removal. Hence the development of a product that can rapidly remove a soil is desirable. Alternatively it may be possible to expand the market for a product into a new sector. In particular the polishing market may provide a suitable expansion market as polishing may often involve an abrasion like process. Although the polishing market is made up of many products for different applications, making the estimated potential of a product expansion difficult, the Brasso brand of metal polish alone had an estimated value in 2013 similar to the entire household abrasive market i.e. one billion Euros. Hence from a business

point of view the purpose of this thesis is not just to understand how the material removal can be improved but also whether new benefits can be found.

1.2 Areas of study

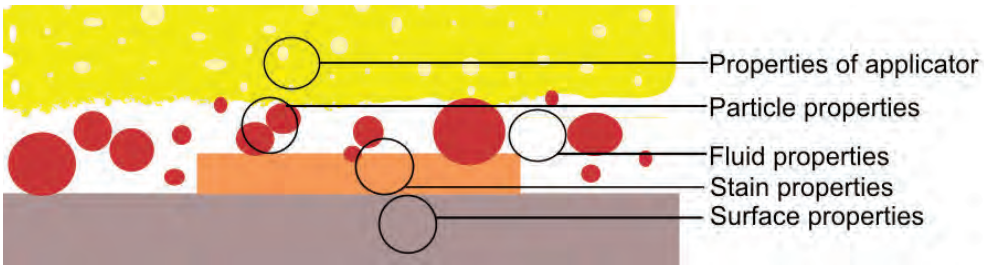

Figure 1.1: Simplified view of an abrasive cleaning system highlighting the key system variables /possible investigative areas

As can be imagined from even the most simplified view of an abrasive cleaning system (see figure 1.1) there are many interlinked factors which combine to form an abrasive cleaning problem. Each one of these variables provides an area for investigation. This work will study the fluid, particle, and stain properties (see later chapters of this report). Alongside this the driving conditions of sliding distance, load and speed will be studied. The investigation measures the impact of these properties on stain removal and wear of the surface can be observed and quantified. The substrate properties and applicator parameters are considered outside the main scope of this investigation.

During the course of the abrasive investigation it was found that the shape of the particles used can enhance the surface via polishing effect. As this is an additional benefit this effect

was investigated as an additional area of study adjoined to the main research. The surface and particles properties were the key areas for study in this subsequent investigation.

1.2.1 Surface and soil

Prior to discussing the details of the experiments performed as part of this study, it is prudent to give a context and justification for the particular choice of substrate and soil used. It is believed that through careful consideration of how a surface interacts with a fouling deposit that it may be possible to reduce cleaning time, energy and cost. A study has already been conducted in the literature on the current understanding of chemistry behind the oxidisation of DCO onto stainless steel and its relation to other materials but does not include reference to the physical properties relevant to abrasive cleaning [11].

Stainless steel (SS) is a common choice of a material for applications across a wide range of industries from household equipment such as cookers and cutlery, to industrial equipment such as reactor vessels and pipes. The chemistry of oxidation of fats and oils to SS has been studied previously [11] and has relevance not only in the food industry but also to a range of other applications including lubricants, paints, biofuels and coatings[12-14].

Castor oil by comparison is not the most widely used or an obvious choice oil or fatty material. However, like the majority of oils and fats, castor oil is primarily comprised of triglycerides, which contains both saturated and unsaturated bonds in the straight aliphatic chains. The presence of the double bonds in vegetable oils, which are the source of unsaturated fatty acids, is a major cause of their poor oxidative stability and the extent of

their oxidisability increases as the number of the double bonds increase in the chains[15]. The oxidative instability of oils presents a major problem in many applications, and undesirable polymerisation and toughening of oil on a steel surface might lead to a hard to remove tough cooker top or pan soil in the kitchen but may also lead to the deterioration of the quality of lubricating oils and potentially biofuels, contributing to the deterioration of efficiency of an engine or motor. DCO provides a model solution to the properties of oils as its chemistry is dominated by the influence of a high ricinoleic acid concentration; most other vegetable oils contain a wider variation of acid compositions, leading to a wider variation in properties [16]. However, despite this model behaviour it is worth noting that the use of castor oil instead of other vegetable oils in the real world is limited due to potentially undesirable proprieties of the oil. Specific problems include: its relatively high viscosity, making it difficult to transport within machinery; the fact that it reacts easily and forms lacquer or varnish layers inhibits its use in engines (though this property has led to an established use of castor oil as an additive in various surface coatings); and in food applications some regard it as inedible as there are undesired side effects to its use, such as its laxative properties, though this has not always prevented its use in foods and forms a major part of its use in medicine[12-14, 17].

Finally poly (methyl methacrylate) (PMMA) is used as the surface for the surface polishing investigation. This polymer surface was chosen as it is widely available and used in applications such as baths, skylights, light fitting covers, aquariums and protective barriers amongst others [18]. Often it is used as a replacement for glass where its strong and ductile nature is more important than the hardness that glass would give. As a polymer, the

material is not as hard as other everyday items made of metals and ceramics, and so it can easily be pitted and scratched. The damage of the surface can slowly lead to matt opaquing of the surface, which is a particular problem when its transparency is of primary interest. Therefore the ability to polish and smooth the surface of PMMA is of interest.

The primary method used in this investigation to measure the physical surface topography was laser profilometry. By measuring the surface before and after wear using a relocation technique the material removal could be quantified. This work was supported using microscopy to inspect the surface damage. Later in the project some additional work was conducted using a microscope-based interferometer.

Surfaces were also characterised outside of the wear experiment. This involved the direct measurement of the physical properties of castor oil soils bonded to the steel surfaces. Direct measurement was carried out using an atomic force microscope (AFM) and nanoindentation. In some instances scanning electron microscopy (SEM), with an energy-dispersive X-ray spectroscopy (EDS) module was used to further investigate the properties of the steel surface. However the use of the SEM in this part of the investigation was limited. Primarily the SEM was used to acquire detailed particle images.

Studying the influence that the mechanical properties of DCO have on wear rate is novel. The application of tribology to baked oil is not something that appears to have been systematically studied in the scientific literature before. However, industry testing uses the steel DCO systems as a reference test for cleaning [19, 20]. These systems can vary

depending on the baking conditions for the oil. As a result most patents compare work conducted in one set of tests and not multiple series. Hence the first area for investigation was to establish a method of producing consistent oil surfaces and then understanding how this surface's properties can be varied. Then the series of baked oil films can be worn in order to study the effect of the film's mechanical properties on wear rate and wear mechanism. As oil soils and similar films are unlikely to be mechanically similar across industries, the application of oil soil wear with a range of properties is likely to be of greater relevance and interest in applications away from household care.

Before testing on a DCO system it is important to understand the wear process in terms of its basic variables. In the literature the most widely used were equation, the Archard equation, identifies these as sliding distance and load [21]. The effect of these variables on the wear is covered in chapter 4.

1.2.2 Fluid properties

In order to keep the fluid properties simple the primary fluid systems were a model and inert Newtonian continuous phase. This is far from the structured, surfactant and solvent containing systems used commercially. However, the more complex commercial liquids introduce many variables due to the complex rheology and chemistry.

Non-Newtonian rheology would impact the lubrication of the system in a complex way that would be difficult to predict or calculate. Additionally, the rheologies of commercial cleaners vary between different manufacturers and individual batches of a product [3, 4]. Hence a

non-Newtonian formulation would be limited in its applicability. However a Newtonian fluid provides simple fundamental model systems for the study.

The chemistry of commercial cleaning products will involve surfactants, solvents and other ingredients. The surfactants are likely to alter the lubrication of any probe or particle and hinder interpretation of the effect of bulk properties, such as viscosity, on wear. Solvents can soften, corrode or otherwise alter the surface. In both cases, complicating the chemistry will make the details of the wear observed harder to distinguish. Hence keeping the chemistry simple should improve the relevance of the observations.

The bulk flow properties of the continuous phase and full formulation of the liquid are characterised using standard rheological equipment and methods. This was done because knowing the structure of the liquid, and having reliable rheological information, is important in understanding the fluid and assists in interpreting and evaluating tribological data. Ideally it is hoped that friction and material removal/movement can be interrelated back to fundamental mechanisms, lubrication and particle motion. The investigation of the fluid lubrication will be assessed in chapter 5. As lubrication and viscosity is often linked to speed, this will also be investigated in chapter 5. It is also arguable that speed is a fundamental tribological system variable that could be investigated prior to this in the first results section. However, this was not done as speed is not part of the well-established Archard wear equation and speed's effect on wear is linked to the lubrication of the system. Similarly viscosity is a factor in the Archard equation and is linked to lubrication.

1.2.3 Particle properties

Perhaps the most readily variable parameter from a manufacturer's point of view is the properties of the particles in the fluid. Particles can be varied in terms of their size, distribution, shape and material. However, it is difficult to generate samples with the necessary predefined properties. Instead the variation is limited to the selection of particles that can be readily mass produced. Materials are commonly ground minerals but synthetic materials are also used. Modern LAC systems use a wide variety of abrasive materials including hydrated silica, calcite, perlite and sodium bicarbonate. For this investigation, calcite (also known as calcium carbonate) particles are of primary interest due to their long history of use in LACs.

The calcite in many abrasive solutions is fine ground natural chalk (FGNC). FGNC is readily available worldwide as calcite. Calcite is a common, globally distributed mineral [22], which has the appropriate mechanical properties for an abrasive cleaner (see section 2.5.1). Mass produced, repeatable samples can be made by a simple, easy to set up and operate milling process. The particles produced by grinding are far from ideal as there is not only the risk of other mineral contaminants, such as silica and asbestos [22], but the size of particles is far from monodisperse (see later notes). In fact the raw FGNC distributions are so wide that for this investigation the particles were sieved into narrower distributions. These narrow particle distributions are as uniform as possible in terms of size whilst being a relevant model for the particles in commercial LAC systems.

Particle size was measured using a laser diffraction particle sizer. Further investigation of the particles was done using an SEM. The SEM gives an impression not only of the size but also the shape of the particles. The particles used were primarily “blocky” in nature. In the first part of the final results section the particles are measured and the differences the particle sizes from different the sieve fractions have on wear. Then the particles concentration is varied in order to study the effect of particle number on the wear rate. In this section the fractions are also mixed in order to investigate the effect particle size distribution.

In the final part of the thesis particle shape is studied; focussed on rod-shaped precipitated calcium carbonate (PCC) rods. Results are included that are in terms of polishing and cleaning experiments separate from the bulk of the thesis. The results presented are different from the standard calcite particle data in order to highlight the mechanisms and benefits of using the higher aspect ratio particles.

1.3 Project aims and objectives

The objective of any scientific study into cleaning system(s) is to discover the optimal liquid abrasive system(s) in terms of maximising cleaning and minimising negative side-effects and /or costs. This was the primary aim of this investigation. However the nature of the task proved too large for this study and so this thesis focuses on the work to:

- Find the relationship(s) between cleaning of a stained surface and the system parameters.

Form research it is possible to define a maximum cleaning system but not an optimum system as the associated impact of cost and side effects such as damage have not be considered.

As already outlined above there were three key areas of interest in order to understand the nature of the cleaning, which form three aims:

1. Understand how the wear of a model baked DCO soil depends on Archard wear parameters of sliding distance, load and surface hardness.
2. Characterise the behaviour of the soil wear in response to changes in the flow properties of the suspending fluid (this includes not only the viscosity of the continuous phase but also the speed of the applicator's motion.)
3. Study the impact of the particle in terms of the concentration, size and distribution of size of particles on the wear.

Below, table 1-1, summarises the system properties and how they were varied in this investigation. The table also highlights how the properties relate to the aims and outlines the justification for the parameters chosen. The table also gives some of the many system properties that can be investigated in future.

Table 1-1: Summary of system properties in the abrasion of household soils and the nature of their variation (or how they were fixed) in this study

Properties	Variables investigated or approximation used	Justification	Relevant aim	Thesis Chapter
Applicator	Fixed as a Viton, 12.7 mm diameter, half sphere	Real world users may use a variety of applicators such as nylon bristle brushes, porous cloths or sponges, gloved or ungloved hand amongst others. This range gives counterface properties too wide for inclusion in this investigation.	N/A	N/A
Particles	Size (limited work on shape)	Most commercial LACs are made from ground calcite. Their size varies depending on the grinding parameters. The aim is to investigate the optimum size through a series of sizes.	3	6
Fluid (continuous phase)	Viscosity (of Newtonian fluids)	Newtonian fluids simplify the continuous phase to makes interpretation of the results easier. Non-Newtonian fluids, surfactants, solvents and structurants are all included in commercial products but have not been covered as the potential number of physical and chemical compositions is too wide for inclusion in this investigation.	2	5
Stain	Mechanical properties	The mechanical properties are varied through a systematic study of baking temperature and time for DCO films. These variations lead to a wide range of properties, but all were based on an oil-polymer stain. The study of other materials with potential quite different mechanical properties and	1	4

		therefore wear behaviour was not studied.		
Surface	Fixed as a 304 stainless steel	Many different surfaces exist in the home. 304 steel is a common material, that is significantly harder than the particles (so it will not be easily worn by the particles) and known to catalyse the oil cross-linking reaction.	N/A	N/A
Load	Weight on the balance arm	Load was both varied on its own and alongside surface hardness and viscosity.	1	4 (& 5)
Speed	Speed setting	Speed was both varied on its own and alongside particle size.	2	5 (& 6)
Sliding distance	Number of reciprocating passes	This is varied throughout the thesis, but discussed in detail in chapter 4. The results in subsequent chapters are all based on a linear fit to wear volume as a function of sliding distance in order to ensure wear rate is in a linear regime.	1	4 (and through out)

1.4 Thesis summary

As with any thesis there are a number of supporting chapters at the beginning and end. The bulk of the thesis consists of this introduction followed by a literature review. The literature review firstly considers the related properties of the system: rheology and particle properties. The measurement and understanding of the relevant materials is explored, particular focus will be given to the process of mechanical properties measurement and topographical techniques. Friction and lubrication is discussed next as it is connected to the surface properties as well as fluid properties. This tribology subject leads in to the wear review. As there are few directly applicable papers an overview of abrasive wear is also given. Finally there is a review of relevant polishing science.

The next three thesis chapters contain the results and their discussion and cover the subject areas outlined previously: surface properties, viscosity, and particle properties. This is followed by the conclusion. Figure 1.2 shows an overview of the thesis structure. This overview will be included at the start of each section as a reminder of the thesis structure and to indicate a sections relation to the overall thesis.

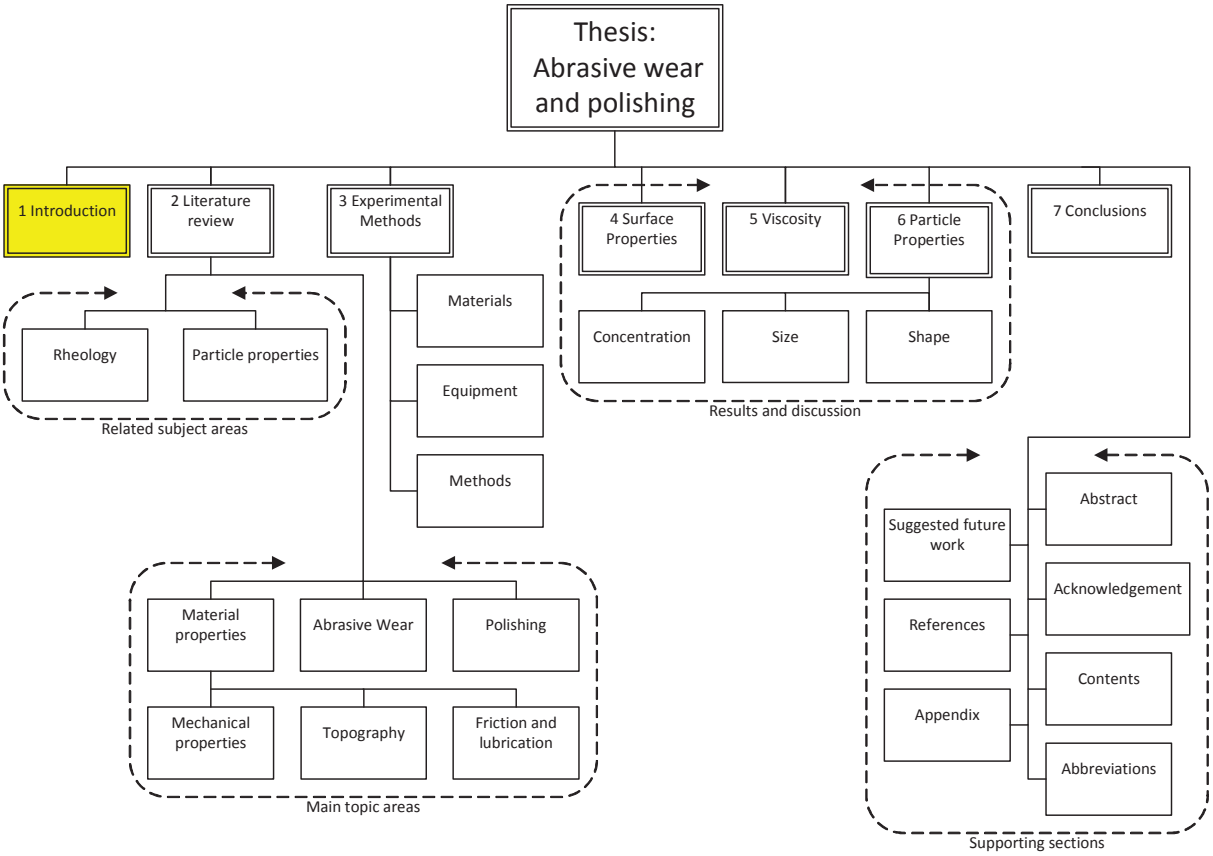

Figure 1.2: Thesis structure overview with the introduction, chapter 1, highlighted

2. LITERATURE REVIEW

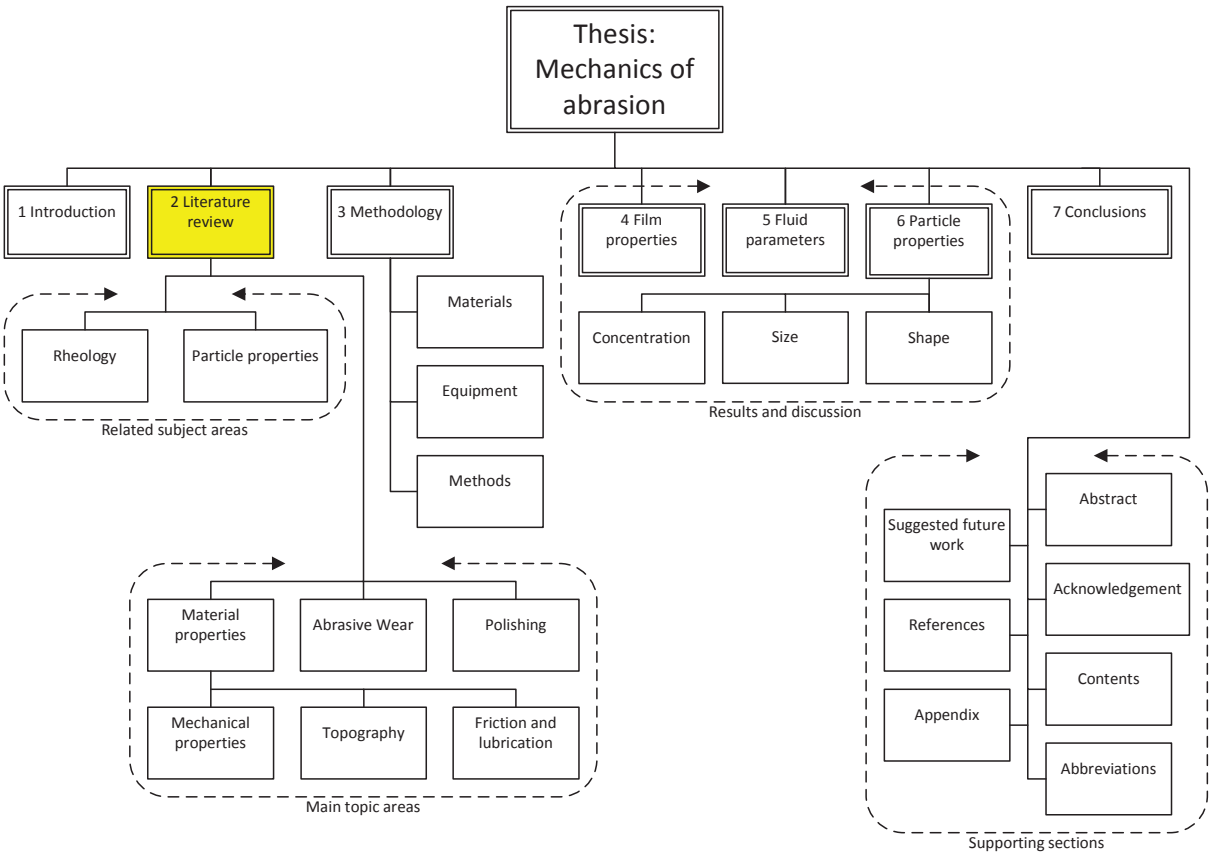

Figure 2.1: Thesis structure overview with the literature review chapter highlighted

It has been outlined in the introduction that LACs have a long history and are widely used. However searching for abrasive cleaning in the academic literature yields few direct results for applications that are not related to oral care. As such a survey of the state of the art in household abrasive cleaning would be short and relatively uninformative. This literature review surveys the related knowledge required to understand of the fluid system, the surface properties and wear and polishing with respect to three body abrasion.

2.1 Rheology

The flow properties of both aspects of the commercial samples (base formulation or full formulation) are discussed here. It was thought that these solutions introduce a large degree of uncertainty in the contact zone fluid properties and so justify moving to a similar, Newtonian system. The study of rheology was done as knowing the structure of the liquid and having reliable rheological information is of importance in interpreting and evaluating tribological data: in terms of interrelating friction and material removal/movement back to fundamental mechanisms and particle motion.

2.1.1 Commercial products

The typical LAC products, sold and used in the home contain calcite suspended in a surfactant solution. The main ingredients for the suspending structure are a surfactant system (such as sodium linear alkyl-benzene sulphonate (NaLAS)). Other ingredients are added for building the structure and for psychophysical reasons. The structure of the NaLAS base system formed here is often referred to as being lamellar in structure [23]. Work has been conducted on similar, simpler systems [24-27] however no specific evidence is available for this exact system. By extrapolation from the work done on similar systems, the chemical composition and the fact that the fluid flows, the range of liquid structures that a commercial LAC may be present in the liquid, it can be deduced that hexagonal and cubic phases can be ruled out. In addition the fact that calcite particles can be suspended in the base fluid infers that the structure must consist of small, closely packed droplet structures

either in the form of micelles, agglomerates of micelles or lamellar droplets and onion-like lamellar.

It is well established that systems of interacting surfactant particles, such as in this base formulation, are often affected by shear history (in terms of both time and rate) [28]. If the effect of shearing causes a gradual decrease of viscosity with time and the change in viscosity is reversible (i.e. viscosity will gradually increase once the shear is removed or reduced) the change is called thixotropy [29]. However, this effect is not well understood and there is growing interest in the subject with many model systems have recently been proposed [30-33], even ones specifically targeted to understand the rheological properties of micelle and liquid crystal solutions [34, 35], though useful mechanistic and fully developed models have yet to be established. These investigations employed an array of techniques including rheometry and identify the continuous phase of a typical LAC to be thixotropic.

When, in addition to the structured fluid phase, the presence of calcite particles that are irregular in shape and have a distribution of sizes is considered in the full formulation it is understandable that such complexity precludes any models for this of bulk rheology in the literature. Even simpler systems, such as studies of dilute suspensions, suspensions of distributions of irregular particles in Newtonian fluids and dispersions in viscoelastic media, are relatively poorly understood topics. However, the mathematical models are getting better at predicting the experimental results [28, 36-39]. Overall the bulk rheology of the system present in the full formulation is much more complex than model systems that are currently understood.

2.1.2 Newtonian continuous phase suspensions

In order to simplify the problem the decision was made to use a Newtonian continuous phase. If the structure of the full formulation could be modelled as a distribution of stable spherical structures in a Newtonian fluid, previous modelling of such rheology has been done [28, 40, 41]. This is due to the fact that much theoretical effort has been made to model the macroscopic properties of suspensions in Newtonian fluids in terms of the fundamental particle mechanics. In fact, work can be traced back to Einstein who in 1906 [41, 42] postulated that the addition of spherical particles to a Newtonian fluid leads to a viscosity that should be linearly related to the concentration according to the equation below:

$$\frac{\eta}{\eta_0} = 1 + [\eta]\chi \qquad (2.1)$$

where η is the viscosity of the suspension, η_o is the viscosity of the continuous phase, χ is the volume fraction of the particles, and $[\eta]$ is the intrinsic viscosity. This equation has been found experimentally to only be representative of very dilute, near spherical and nearly monodisperse systems [43, 44].

Much of the early work has been reviewed by Thomas [45] and is has limited usage today. Only a few equations have been established as being useful; the Krieger and Dougherty [46] equation is primary among them and so this relationship is regularly studied and applied.

The Krieger and Dougherty equation is:

$$\frac{\eta}{\eta_0} = \left(1 - \frac{\phi}{\phi_m}\right)^{-[\eta]\phi_m} \qquad (2.2)$$

where ϕ_m is the maximum packing fraction of particles. One of the many advantages of this equation over the Einstein equation is that it (more correctly, when compared to real systems) predicts that as particle concentration increases and approaches this maximum, the viscosity rises to infinity. This equation is often more accurate at describing the behaviour of non-spherical particles and higher particle suspensions. However, this equation is still limited to lower concentrations, of 5-25 % vol, depending on the particle shape [47-49]. Also the equation is only truly accurate when applied to near-spherical particles, when the single particle motion and/or the two-particle interaction dominate [47-49].

At higher particle concentrations than can be used with the Krieger and Dougherty equation (see later notes in this section on Mueller's work) the behaviour of fluids becomes non-Newtonian. This may involve shear thinning behaviour or yield stress, phenomena that can often individually be fitted to a power law or Bingham equation respectively [50]. However, it is not uncommon for both yield and shear thinning to occur in the same fluid hence the Herschel-Bulkley equation is widely as it combines these two features [50-53]. The Herschel-Bulkley equation is:

$$\sigma = \sigma_0 + z\dot{\gamma}^y \tag{2.3}$$

where σ is the shear stress, σ_0 is the yield stress, z is the consistency index, $\dot{\gamma}$ strain rate and y is the flow index (which is between 0 and 1) [52].

A limitation of the Hershel Bulkley in its application to suspension systems is it predicts that the viscosity will approach zero as strain rate goes to infinity since viscosity, η, is given by:

$$\eta = \frac{\sigma}{\dot{\gamma}} \tag{2.4}$$

There are many models in the literature that can be applied to suspension systems [50, 51]. Of particular interest to this author is the Carreau model. It is a simple non-Newtonian model for a shear thinning solution commonly found in the literature relating to suspensions [50, 51, 54]. This model features three regions of interest shown in figure 2.2: a "zero" shear viscosity at low shear rates, a power law, transitional region at intermediate shear rates, and an "infinite" shear regime at high-shear rates and a transitional regime. The equation for the Carreau model is:

$$\eta(\dot{\gamma}) = \eta_\infty + \frac{\eta_0 - \eta_\infty}{[a+(\lambda\dot{\gamma})^2]^{(1-n)/2}} \qquad (2.5)$$

where *n* is a power index, λ is the relaxation time, *a* is a fit constant (often experimentally found to be 1) and η_∞, η_0, and $\eta(\dot{\gamma})$ are the viscosities of the solution at zero shear, at infinite shear and at a given shear rate respectively.

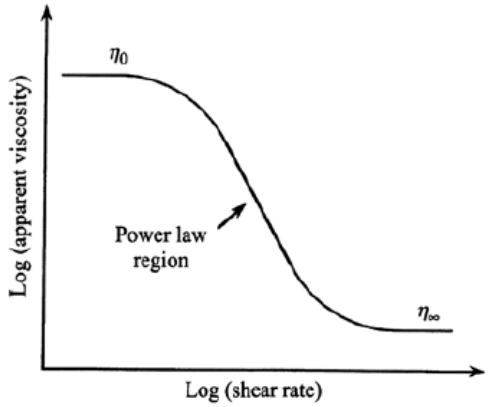

Figure 2.2: Plot of shear rate versus apparent viscosity for shear thinning foods identifying the three separate regions. Often, only data in the power law region are obtained. Taken from [50].

More recently the complexity of the systems being studied has increased. This includes work on more dense suspensions (those in which the average particle separation distance is less

than the particle radius) which typically show shear thickening behaviour [55] and non-spherical studies [41]. It is this later paper by Mueller et al. in 2010 that is of particular interest. Concentrations from a few per cent to over half of the volume are studied. Overall the authors show a clear systematic trend to the Herschel-Bulkley fit parameters used to model the systems (see figure 2.3). They also outline how parameters of the fit used change with concentration and suggest the particle motion underlying the rheology (see figure 2.4). The authors also begin to show how it might be possible to predict other system rheologies and studied not only spherical particles but also angular silicon carbide grit and high aspect ratio wollastonite, amongst other particles to show how to modify prediction for particles with higher aspect ratios. However justification for the use of Herschel-Bulkley equation over similar rheological models is not given. Also there is no way, as yet, to fully predict the rheology of a system as some experiments are required.

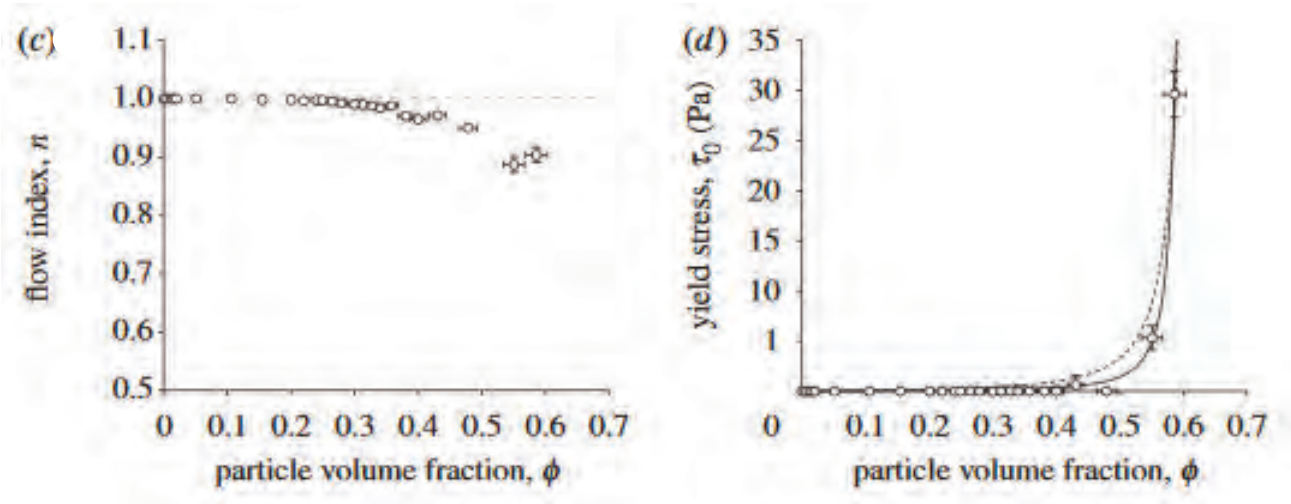

Figure 2.3: Experimental data for suspension of spherical particles taken from [41]. The data shows that at concentrations over ~25 %vol spherical suspensions begin to show shear thinning and at over ~40 %vol a yield stress exists.

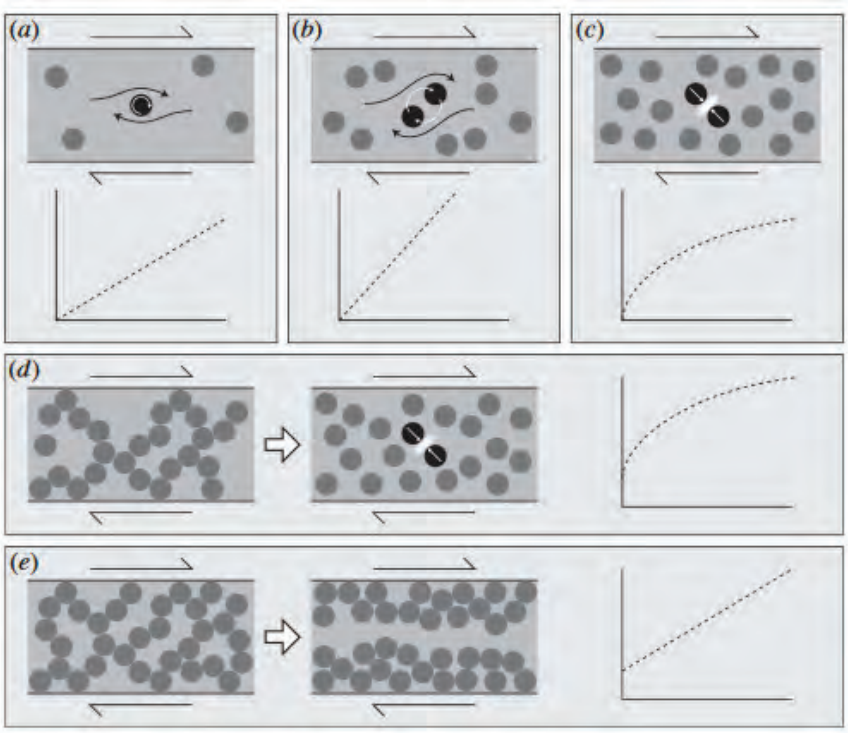

Figure 2.4: Changes in the rheology of suspensions of particles as particle volume fraction increases from (a) to (e). Each regime is illustrated with a sketch showing the expected microstructure controlling the rheology. Image taken from [41].

2.2 Friction and lubrication

The previous section was concerned with the bulk properties of fluids with or without particles in suspension, but it is the behaviour of the flow of these fluids in confined, tribological applications which is of particular interest in liquid abrasive cleaning.

2.2.1 General lubrication

Prior to the discussion of the particular fluids of interest here (i.e. those containing particles) it is worth noting the behaviour of general lubrication systems. As suggested by the thesis overview diagram (figure 2.1) lubrication and friction is a property of the liquid but it is also

dependant the surface. Friction has been around as a subject since da Vinci (1452-1519), though significant progress on the study of lubricants was not conducted until the late 19th and early 20th century. At this time the Stribeck curve, which shows the various regimes of lubrication, was developed [56-58]. A discussion on this curve and its feature is given in figure 2.5.

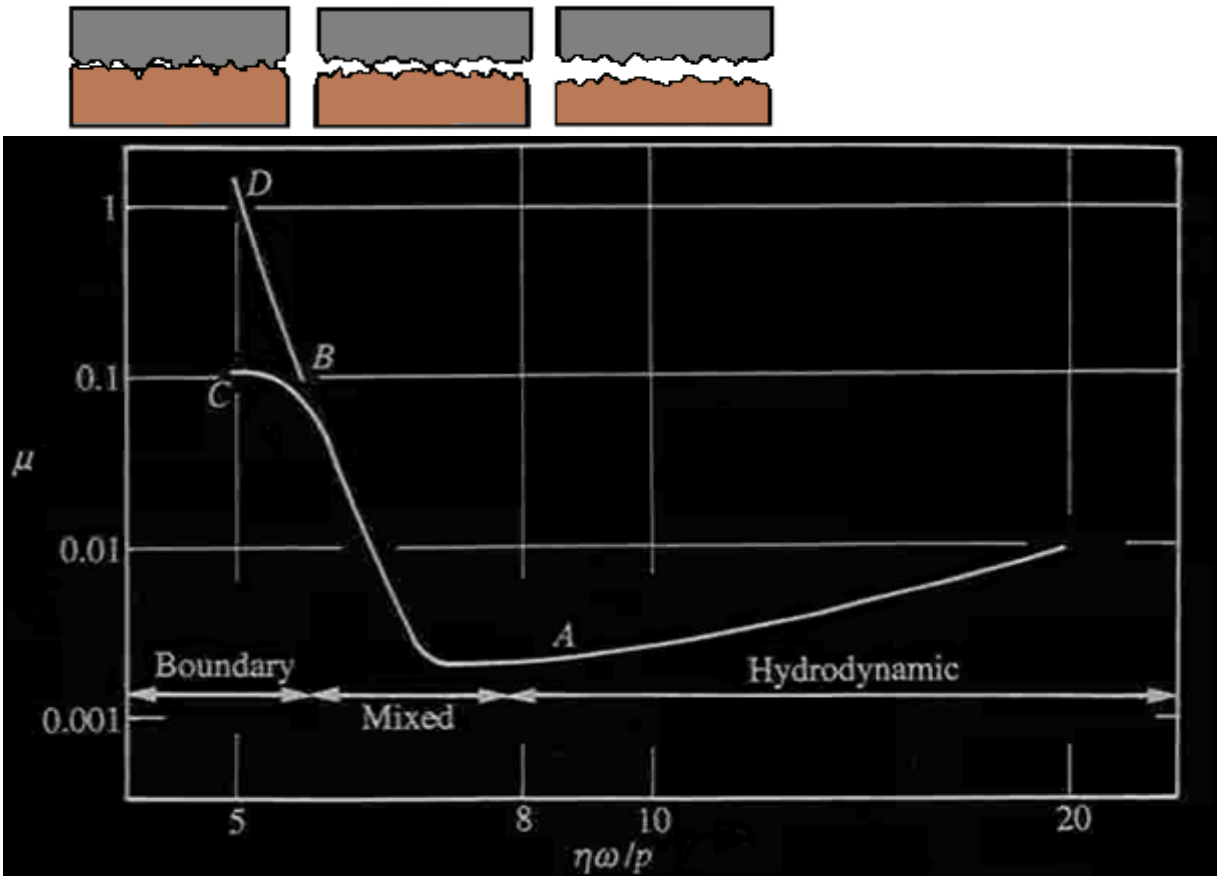

Figure 2.5: The Stribeck curve for friction taken from Engineering Tribology [56]. This curve in particular is for oil lubricating a metal contact. The three diagrams at the top illustrate the contact during the contact between the in the respective friction regime shown in the graph below. The axis show friction coefficient, μ, against the lubrication parameter.

The Stribeck curve illustrates the dependency of the friction on lubrication parameter which includes several key system parameters. The lubrication parameter is also known as the Hersey parameter and is viscosity multiplied by speed divided by load [58]. This parameter contains the main variables that affect fluid film height or separation between the two surfaces. Hence the increase in viscosity or speed (sometimes frequency in rotating system) increases the fluid film height and an increase in load decreases the fluid film height [57].

Hydrodynamic lubrication occurs when the sliding surfaces are separated by a relatively thick fluid film [57]. Viscous forces within the film provide the pressure to support the contact. At the other end of the graph, in dry contact, rough surface may well contain asperity contacts that locally “weld” together. The friction required to break these joins is often quite high, as illustrated by point D in figure 2.5 [56]. In a lubricated contact, and indeed most practical situations, there is a thin, boundary layer of material on the surface that weakens this interface. This leads to the friction coefficient which is much reduced (when compared to dry contact), as illustrated by point C. The exact nature of this boundary layer is not fully understood however in oil based lubrication surfactant molecules are theoretically adsorbed onto surfaces and prevent dry contact.

In between these two regimes mixed lubrication occurs. Hydrodynamic action still occurs but this time the surfaces may come into (elastic) contact, significantly increasing the friction. It is worth noting that the transition to hydrodynamic lubrication often occurs at several micrometers or tenths of micrometers [57, 59]. Note: the transition between hydrodynamic and mixed lubrication regimes may also include a region of elastohydrodynamic lubrication

(EHL). EHL occurs when the hydrodynamic film formation is enhanced by elastic deformation of the surface(s) particularly in non conformal contacts [60, 61]. EHL is not expected to be a significant in the system studied here.

2.2.2 Lubricants with particles

There are many industrial applications of lubricants and circumstances where lubricants contain particles, or where fluids are designed as three-body abrasive systems. Examples include: mineral oils containing dispersed solids, polishing fluids, cosmetics and machining lubricants containing wear particles. As a result much experimental research of the subject has been carried out [57, 58, 62-72]. In particular the application of lubrication in hard contacts, such as occurs between most metal surfaces, draws significant industrial interest due to its relevance in a wide variety of industrial and everyday systems including, but not limited to, moving components for automotive engines, bearings, vessels and pipes in production plants, and hinges. Due to its applications, the wear of hard contacts in metals and steel in particular is an extensively researched area of tribology. As a result it is where the majority of lubricant particulate research has been focused [62-67].

The presence of surfactants in their liquid crystal form is not a significant area for research in the contact of metal surfaces. However, in oil base lubricants many hydrocarbon molecules are present and there are surfactants molecules. In fact much work on the theories of boundary lubrication is based upon the idea of surfactant molecules attaching themselves to the surface and forming a molecular boundary layer [73]. However, the work on boundary lubrication is purely theory based and is not fully understood. The addition of solids to these

systems may be beneficial or detrimental to lubricant performance, depending upon the particle properties and system being lubricated [72]. In the context of LACs lubrication of the calcite over the metal surface is required as damage to the underlying surface is not a desired effect.

In abrasive cleaning, soft contacts such sponges, cloths and brushes are often used. These contacts make the modelling of the fluid behaviour rather difficult as fluid can flow into the applicator. To negate this problem, work in this study work was conducted with an elastomeric half-sphere. This simplification still contains challenges as, by comparison with the work with metals, less is known about the behaviour of particulate lubricants in a compliant contact (contacts where one or both of the contacting surfaces have a smaller elastic modulus than the particles). Examples of the similar lubrication conditions include the mastication of food, abrasive cleaning, the presence of stones in a road-tyre contact, the presence of metallic wear particles in artificial hip joints and the use of particles in cosmetic products applied on the skin [69, 74, 75].

Recently the system of particulate lubricants cosmetics have produced some work that is of particular relevance to this study: Timm et. al [74] investigated the effects of particle concentration and size on the lubrication properties of powder suspensions in a carbopol structured suspension medium. When the tribological contact was fully immersed, the presence of particles in the suspension medium was reported not to have significantly impacted the friction of the system when compared to similar results taken for friction with just the suspension medium. However when the contact was only partially lubricated, a

three-stage friction coefficient curve was observed showing that, as the contact dried, particles were trapped less in the contact and were instead either ejected completely or trapped at the inlet to the contact. By varying the particle size and concentration it was shown that the duration and magnitude of each stage can be controlled. It was observed that the final friction was less than the dry friction indicating the particles themselves often function as lubricants.

2.2.3 Confined flow

Flow confinement studies are less common than the simpler lubrication studies; however they are crucial in focussing on the detailed mechanisms of flow of complex fluids in confinement. Much work has been done previously investigating the flow properties of common fluids that exhibit complex, viscoelastic behaviour. However, it is worth noting that some of these structured fluids may only be approximately viscoelastic: note that in Davies and Stokes [76] work, the authors comment that “carbopol is used as a structured fluid due to its relatively non-thixotropic rheological properties”.

Confined flow studies generally show good correlation between the experimental and theoretical fluids or model pastes [60, 76-81]. However the suspension fluids studied are often simplified to the use of model systems. Although the model of a viscoelastic fluid seems fairly well establish, suspensions in confinement are restricted to single or mono-disperse spheres and the difference an irregular particle or a wide particle distribution of particles or both would make is not clear. Also if (and if so how) the influence of thixotropic properties will translate to real effects in such studies are again a subject that is not covered.

The work that has been conducted falls into one of two subjects: general confinement or squeeze flow. Confinement is often looked at for its applications in both the chemical and biomedical areas and research is concerned with the motion of the suspended particle(s) within a fluid space of characteristic dimensions similar in size to that of the particle [78]. Squeeze flow studies considered often focus on parallel plate or rolling apparatus used to compress and deform a viscoelastic material, often pastes consisting of fine particles or polymers [82]. Neither of these cases has yielded information that can be considered directly applicable to this study. However the investigative techniques and theoretical framework may be of future use.

2.3 Material properties

There are many ways to classify and quantify the properties of a surface. Here the focus is on the topography, imaging and mechanical properties relevant to abrasion and how they are measured.

2.3.1 Topography

Profilometry is a long established technique used to measure surface roughness and map surface topography. Modern profilometers are used for both of qualitative visualisation and quantitative statistical analysis of a surface. A profilometer is defined here as any piece of equipment which is primarily designed around a detector that measures the height (z) of a sample, in relation to the equipment, at points on the surface (as opposed to optical methods that image the surface as a whole). Measurements on a profilometer are normally

taken in a series of line points in the y direction separated by a small distance [57]. By moving the position of the sample relative to the detector in the x direction, using indexing table /motorised stage and performing repeated stylus traversals, a 3D measure of the surface topography can be obtained [83-85].

There are two main types of conventional profilometry: contact stylus and optical stylus. In addition equipment have been developed to take an area scan of a sample to produce a three dimensional map of surface, and some state of the art equipment has been produced by adapting existing setups to provide profile and mapping capabilities. For example profile data could be extracted from focus variation microscopy data [86-88]. These more specific instruments will be dealt with on a case by case basis, as encountered, rather than try and define all such systems together.

Contact profilometers use a stylus (often diamond tipped) of known geometry to trace lines across a surface and the vertical displacement recorded [84, 85]. Stylus shape is often the major factor in defining the limitations of the equipment. In particular, features smaller than the tip radius may be rounded or not measured. However, tips can be produced that allow a lateral and vertical resolution of tens of nanometers. By contrast optical systems have a lateral resolution >200 nm due to light's diffraction limit [85, 88]. The other main disadvantages of contact profilometry are that there is a trade-off between measurement speed and accuracy, the stylus can damage soft materials, and very hard, rough materials can cause damage to the stylus. However the process of using contact styluses is long established and well understood, and often surface standards are written based on contact

profilometry [85, 88]. The other main advantages of contact profilometers are that they are surface finish independent, meaning the colour or reflectivity of a surface (which can cause significant issues with optical techniques) will not affect the results.

Other optical techniques for three dimensional imaging of surfaces have become more common over the years due to the increase in computer power and memory [85, 87, 88]. Previously the application of advanced techniques such as interferometry or confocal microscopy was restricted by the ability of the users to process and collate the resulting data /information. Now such techniques are becoming common place to scan an area of a sample (although they can also be used for either point or line scans). These optical scanners are ordinarily situated within a microscope setup due to the commonality of optics, the ability to visually assess /check the 3D features /data and to increase the ease of use.

The exact process each instrument uses is often dependant on the manufacture however the basic principles are the same. Light (either white or monochromatic) illuminates a surface. The reflection of the light incident on different parts of the surface travel different path lengths depending on the height of asperities. When the light is collected in the instrument and sent towards the detector there is either a restrictive aperture that admits a narrow range of light path lengths (confocal) or reference beam (interferometer) that generates interference fringes based on the path length. These act to filter focused and out-of-focus light. The reflected light pattern is then detected and, by varying the surface height relative to the instrument, used to calculate the surface heights of a sample.

The main advantages of the optical techniques is that they can be applied to a wide range of mechanically different measurement surfaces as the material properties such as hardness and elastic modulus do not impact the technique. Optical techniques are now often faster than contact methods that are restricted to slow scans by their ability to cause damage or generate erroneous data at higher speeds [85, 87, 88]. However, as mentioned above, the optical techniques are often limited in their resolution particularly in the horizontal direction. Also the reflectivity of the surface with respect to the input light can sometime influence the result. Sharp gradients in surface height can also cause problems as light is reflected away from the detector, although often can be captured by refinement of the technique at a cost of measurement time [86]. There is also a problem that the established surface measurement specifications are often defined with contact probes in mind and cannot always be readily applied to non-contact probes. Overall the quality and reliability of profilometry data, particularly modern non-contact techniques is often dependant on the user's skill, available time and the experience of applying a technique to a particular surface.

2.3.2 Imaging

Basic optical microscopy has been around for centuries and can reveal changes in surface topography, wear scars, debris and signs of chemical corrosion on the millimetre to micrometre scale [89, 90]. This technique therefore provides a useful starting point both for damage characterisation and helping the examiner decide on which analytical technique, if any, would be best to apply. The primary problem with optical microscopes is associate with the diffraction limit. This reached at approximately 0.2 μm (dependant on the wavelength of

the applied light) [88, 89]. For higher resolution imaging more advanced techniques such as scanning electron microscopy (SEM) must be employed [90, 91].

An SEM consists of an electron beam, usually from a tungsten electron gun focused using electromagnets to a point on a sample. Electrons from the gun can interact with atoms in a sample target via a variety of elastic and inelastic collisions. The electrons incident on the sample interact with a volume of sample similar to that of a tear drop extending from the point of incident on the surface [92, 93].

Inelastic collisions occur when electrons interact with the elections in an atom. An electron will dislodge one of the inner electrons from its orbital giving and energy will be lost from the incident, primary, electron in order for the electron to be emitted. At the same time a characteristic X-ray is produced (see section 2.3.3). These emitted electrons are termed secondary electrons (SE) and are of low energy: typically 10s of eV, whereas the incident electrons are usually of the order of keV in magnitude. As a consequence of their low energy these electrons will often be conducted away as current for depths greater than ~5nm. Hence the secondary electron detector primarily receives surface topography information. However the likelihood of electron inelastic scattering is often related to the atomic size and so the topological information often has a defect due surface compositional information[90].

The image produced by secondary electrons is only two dimensional. There is some correlation between the “brightness” (in terms of the amount of electrons emitted not light) of a point and height as electrons can be emitted more easily from a peak than a crevice:

due to the fact the surface to volume to ratio is higher at a peak. However no exact method exists for quantifying this effect [91, 94]. It is also worth noting that as the electrons interact with a depth of the sample the resolution is often influenced by incident electron energy. Though reducing the primary electron energy will influence the strength of the signal produced, there is a trade off between "brightness" of the picture and resolution.

Elastic scattering means there is no significant change in the kinetic energy of an incoming electron even though there may be a significant change in the direction of motion of the incoming electrons when they interact with a target sample. Elastic scattering can take place when electrons pass close to or are incident on the nucleus of an atom. Where an electron passes close to the atom it is deflected off its original trajectory by a small amount. The total amount of deflection increases with depth hence a "teardrop" shape of interaction for electrons with a surface [93].

Elastic backscattering is where the electron hits a nucleus "head-on" and bounces backwards on a path roughly opposite to the incoming path i.e. the velocity is opposite upon scattering. These electrons have an energy of several keV and can travel from depths of ~1-2 µm from the surface. They are typically detected either by a ring surrounding the electron beam or a disk near to it. Larger atoms (with a greater atomic number, Z) have a higher probability of producing an elastic collision than smaller atoms because their nucleus has a greater cross-sectional area. The number of backscattered electrons (BSE) reaching the detector is proportional to the mean atomic number of the interaction volume [94]. Thus high BSE intensity correlates with high mass atoms and low signals areas have lower average mass.

BSE produce compositional maps of a sample “surface”. This is made slightly more complicated in the case of crystal structures as packing density will also influence the “brightness” of the BSE signal, as more dense structures will produce a brighter signal and so BSE can be use to look at different crystal phases. Though this process is not to be confused with backscattered electron diffraction; where crystal orientation is obtained.

As with the SE, BSE can only give two dimensional information and SE and BSE images are in black and white because they only record one variable, the electron signal strength at a point [94]. The topography may impact on the BSE image even though primarily the image relates to sample composition. Typically this is only a problem when there is high surface roughness such that the height varies by hundreds of nanometres over small, less than 10 nanometres distance. Having said this, BSE images provide a quick means of determining the number of component phases in a material.

2.3.3 Energy-dispersive X-ray spectroscopy

As mentioned previously the inelastic scattering of electrons off an atom allows electron transitions to occur within the atom. As an electron tunnels from a higher energy level to the lower energy level energy is lost in the form of an x-ray. The x-ray emitted is characteristic to the transition occurring and the element of the atom [90].

One limitation of this technique is that although each X-Ray is, strictly speaking, unique to an element, energy peaks may effectively overlap [94]. This is due to fundamental uncertainty of the energy from Heisenberg’s uncertainty principle and measurement error. Overlap is

particularly problematic at higher energies, where individual peaks may appear to be identical for several different elements. This means users may influence the results by selecting elements to model in the data: ideally this process will be based on prior knowledge of the sample or use of another method to find the information. The process of measuring these characteristic electrons is known as energy dispersive x-ray spectroscopy (EDS). EDS is also known to be imprecise at detecting low (<1%) chemical components. Also light molecules (atomic number less than 11 (sodium)) often have energy signatures that cannot be detected using an EDS [94] and standard methods do not advise on how to measure these light elements [95].

2.3.4 Atomic force microscopy

The first atomic force microscope (AFM) was made in 1985 by attaching a diamond onto one end of a small strip of gold foil [96]. Since then AFMs have been used to investigate and solve many processing and materials problems in a wide range of technologies. Modern commercially available AFMs, such as the NanoWizard II AFM (JPK, UK) used in this investigation, typically use a silicon micro cantilever.

As any two surfaces approach each other they will begin to sense a small attractive force, from Van der Waals forces that increase as the sample gets closer[97]. Eventually the surfaces are so close that the repulsion from the electron shells begins to become of significant magnitude. This force increases more rapidly with decreasing distance than the attractive forces. As a result there comes a point when there are overall no forces on the surfaces. Then, as distance decreases, they begin to strongly repel the each other and are in

contact. The principle behind AFM is that when one of the surfaces is that of a cone or particle attached to a cantilever at its free end (the other end is fixed in place) the angular deflection of the cantilever can be measured. From knowing the mechanical information for the cantilever and measuring the distance from the cantilever to the surface, the Young's modulus and hardness can be calculated. The detection system does not measure force directly. Figure 2.6 shows what happens as a cantilever approaches a surface.

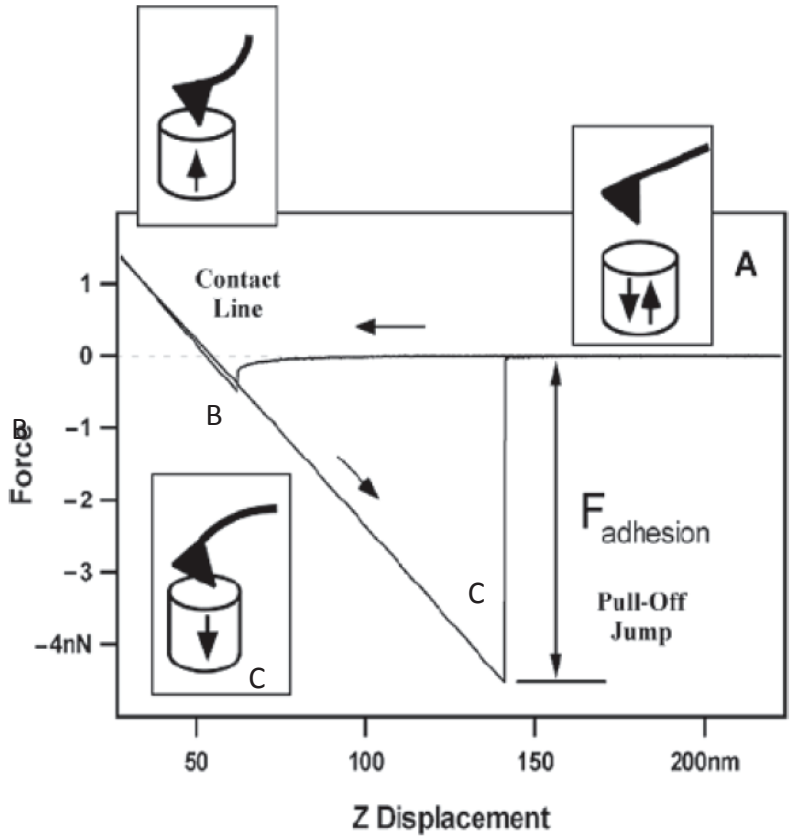

Figure 2.6: Typical force displacement curve for AFM based indentation (taken from [98]). At point A the cantilever is not touching the surface. In this region, if the cantilever feels a long-range attractive force it will deflect downwards but will not make contact with the surface. Provided the attractive force is large enough the probe tip is brought closer it may jump into contact with the surface as represented at point B. This phenomenon is often referred to as snap-in. Once the tip is contacting the surface, deflection increases as the cantilever is brought closer to the sample. Provided the cantilever is stiff enough the probe tip may indent into the surface at this point.

The method used here to measure deflection is a laser beam “bounce” method. This means optical beam from a laser is reflected from the mirrored surface on the back side of the cantilever onto a position-sensitive photo-detector. A deflection of the cantilever will tilt the reflected beam and change the position of beam on the photo detector. As discussed previously this technique can be use as a surface profilometer. For profilometry the deflection is measured whilst trying to keep either the same contact force. Alternatively a dynamic method is used where the tip is vibrated at a given frequency to bring the cantilever in and out of contact. This method avoids high lateral forces from dragging the tip over the surface, this technique is sometimes referred to as “tapping” [99]. Here we are concerned with its use in measuring mechanical properties.

The AFM records the amount of force felt by the cantilever as the probe tip is brought close to and even indented into a sample. This is done indirectly through knowledge of the properties of the cantilever in particular its flexibility or stiffness needs to be measured. Stiffness can either be measured by derivation from the material properties and microscopic measurement of the cantilever or directly by careful nano-indentation of the probe [100]. Once the stiffness is known the deflection of the beam can be related to a force and AFM can be used to measure the attractive and repulsive forces between the probe tip and the sample surface. The rate of approach, magnitude of attractive-repulsive forces to go between, the distance to travel and speed that the AFM cantilever tip travels during the force measurement can be varied.

The slope of the force curve between contact and its maximum value (which is the stiffness of the sample) can be used to calculate the Young's modulus of the sample provided the modulus of the probe is known (see nano-indentation notes in section 2.3.6 for equations). The hardness of the sample can also be estimated provided the shape of the probe is known.

When unloading, the cantilever is withdrawn and adhesive forces between the surfaces surface may cause the cantilever to adhere to the sample some distance past the initial contact point B. Point C on the AFM force curve in figure 2.6, is the point at which the adhesion is broken and this minimum point is called the adhesive force [101].

Taking the slope of the indentation curve to calculate mechanical properties has limitations. This method means that the surface may be allowed to deform both elastically and plastically. Therefore the values calculated from the approach, which assumes elastic deformation, may be incorrect [102]. This method was chosen over using the unload data because the surfaces show a significant amount of surface adhesion on unloading (see later notes). Analysis of the unloading curve is strongly influenced by the material's adhesion via a process comparable to that highlighted for nanoindentation later (see section 2.3.6.1).

AFMs are useful for measuring forces as, depending on the cantilever and experimental setup, they are capable of measuring forces as low as a few piconewtons [99]. Problems can often occur through inappropriate choice of cantilever for the sample as the magnitude of deflection can be too large (off the scale of the photo detector) or too small and the errors may be too large.

The problem of measuring stiffer surfaces arises from a fundamental characteristic of the AFM method. The AFM is a displacement based test setup relying on the measurement of the deflection of a laser beam off a probe tipped cantilever [99]. The resolution of the detector is set by the stiffness of the cantilever and the size and shape of the probe. When a stiff film is placed under the cantilever then its deflection becomes more rapid, and may not be linear or the probe tip itself may deform instead of the surface [92]. Overall if the surface is too stiff compared to the cantilever the fundamental assumptions of the measurement process may not be met. In order to measure a stiffer film there are three basic steps that can be taken: the cantilever needs to be stiffer, the probe needs to be smaller or the approach speed needs to be slower.

As reported in the literature, for silicon-based probes this technique tends to become unfeasible as the surface elastic modulus approaches ~1 GPa [99]. This means that much stiffer metal cantilevers are more suitable for the measurement of harder surfaces. However the use of a stiffer cantilever would limit the ability to measure softer surfaces. Stiff cantilevers are only deflected a small amount by a soft surface. The literature mentions that AFM based techniques are practically limited to measuring materials with stiffnesses varying by up to two orders of magnitude [99].

Another common issue is one of vibration and noise. The cantilever is extremely sensitive to ambient vibration and error can be produced from talking, footsteps and traffic. As such most AFMs are stored in sound dampening chambers and mounted on an isolation table placed on top of a secure, level, robust surface for example a granite block [99]. Atmospheric

conditions may also play a role in affecting the results. High humidity atmospheres (the exact humidity depends on the probe but ~50% relative humidity for 0.5 nm features) may lead to condensation and liquid bridging on contact that will change the adhesion force measured [99].

Finally due to the nature of AFM probes, they cannot normally measure complex or highly textured surfaces [90]. Steep slopes present a problem as only a small area of the probe is in contact. On rough surfaces one must also be careful of overhangs and measuring over air bubbles as they will have elastic properties different to a solid area (as there is an underlying air gap in the sample).

2.3.5 Indentation

Indentation measurements were not carried out as part of this investigation. However prior to a discussion on nanoindentation it is necessary to first introduce the techniques and terminology of what may be termed standard, macro or classical indentation. Indentation is a widely applied process of pressing an indenter tip into the surface of the sample at a known load and the material's resistance to plastic deformation is measured [103]. Deformation is assessed by optical analysis of the size of the indentation mark after testing. The most relevant information is the contact area of the indentation, A, which can be used to find the hardness, H, using:

$$H = \frac{P}{A} \tag{2.6}$$

where P is the maximum load (which in classical indentation can be as little as 0.01 N to over 100 N). The application of these tests is common and is covered in international standards such as ISO 6507 [103] and ASTM E384 [104]. Hardness is a combination of fundamental material properties that combine to form the resistance to deformation caused by a compressive force over a given contact geometry. As hardness is not a fundamental material property it can only be defined by reference to a particular test method [105].

Testing is specific to the test parameters used. These parameters include the maximum load, the rate of loading and unloading, sample preparation, and the number and location of test points [105]. The most important parameter to specify is the indentation tip geometry [105, 106]. The form of the indenter tip are typically either spherical, such as in Brinell and Rockwell testing, or a pyramid such as in Knoop and Vickers testing. The material, form and loading of the tip are historically well defined for a particular range of materials.

Of particular interest is the Vickers indentation tip as it is geometrically similar to the Berkovich tip used in the nanoindenter in these investigations [107]. The Vickers indentation tip is a four sided pyramid with a face angle (the minimum angle of each face and the axis of the tip) of 68 degrees [103, 104]. A Berkovich indenter is a geometrically self-similar three sided pyramid with a face angle of 65.27^0 (76.9^0 from the axis to the edges) [107]. This angle is chosen so that the ratio between the projected area and the square of the indentation depth of the Berkovich and Vickers indentations are both 24.5 making the tests results between tests more meaningful than if another angle was selected [107]. The Berkovich tip is normally preferred for nanoindentation testing because it is easier to grind three sided

pyramid tips to a single sharp point than a four sided pyramid. The contact point of a Vickers pyramid is often a line contact, whereas a Berkovich tips can typically be made with a near spherical tip less than 100 nm in radius [108].

One problem known in indentation stems from the indentation area. Firstly there is the problem that the material in the observed contact area is not illustrative of the total indentation area. The total indentation volume includes material at a distance beyond the contact volume displaced by the probe [83, 84] [109]. There is often quoted figure that the indentation affect approximately 10 times the contact depth and width [109]. However this figure varies between materials. The affects of true indentation volume become particularly relevant to non-uniform materials which includes materials that are coated, multilayered or have a distribution of properties. Interpreting the true mechanical properties from the apparent properties would require a process of mathematical modelling.

2.3.6 Nanoindentation

Nanoindentation is the name given to a variety of techniques used to classify the material properties of surfaces [105]. Indeed even the AFM process described previously can be described as nanoindentation. Nanoindentation is an often studied technique the subject of numerous papers including reviews in the literature [102, 105, 108, 110-115]; as such this review only covers the details required for this work.

In nanoindentation, the indenter – typically a Berkovich pyramid – is continuously pressed into the material being tested with an increasing test load, and then unloaded. The

indentation depth of the pyramid is measured continuously during this penetration process [116]. The hardness value is calculated from the selected maximum test load and the resultant indentation depth. It is typical for the hardness to be based purely on the measured indention depth and a pre-test calibrated tip depth to area function [107]. As stated above, for an ideal Berkovich indenter this projected area, A_P, is:

$$A_P = 24.5I^2 \tag{2.7}$$

where *I* is the indentation depth. In reality the tip will most likely not be perfectly shaped and so the face angle may not be exact or the edges and tip absolutely sharp. It is common for a tip area function to be used to compensate for the imperfections [117]. This means that the area, A_c, of the contact is given by:

$$A_c = c_0I^2 + c_1I + c_2I^{1/2} + c_3I^{1/4} + c_4I^{1/8} + c_5I^{1/16} \tag{2.8}$$

where c_0 to c_5 are constants found experimentally.

This method presents a significant deviation from the classical “macro” indentation as the hardness here may be more accurately defined as measuring the instantaneous deformation of a material due to load [102]. The macro indentation methods are a measure of permanent, plastic deformation of the material. Nanoindentation studies investigate elastic and plastic properties of materials [102, 115]. This means there is likely to be deviations in the results between the two methods. Particular deviations occur for soft elastomeric materials, which classically would not be tested in a Vickers, or similar, test. Deviations are due to the fact that elastomers can show a large degree of deformation before yielding and surfaces may even recover completely after indentation. Therefore as the indentation area, *A*, approaches zero the hardness would approach infinity in these standard tests.

The loads used in nanoindentation range from <0.1 to ~1000 mN and depths of tens of nanometers (up to several microns), which allows for small areas or features within a sample to be measured [102, 117]. The lightest loads allow for the measurement of hardness of thin coatings[111]. It is worth noting that for meaningful measurements there are restrictions on the size and surface finish of samples [118, 119].

2.3.6.1 Quasi-static indentation

Figure 2.7 shows a schematic of a typical simple nanoindentation from the literature [120]. This is a general curve for a viscoelastic–plastic material. The data obtained from this curve can provide information regarding the elastic, viscoelastic and plastic behaviour of a material. Three intercepts are shown: h_{max} is the maximum displacement of the indenter and represents the depth that would be reached by a inelastic material, h_c is the depth of the contact based on the initial unloading, which would be the intercept for a elasto-plastic material and h_r is the residual displacement after removing the indenter from a material with viscoelastic and plastic properties. The exact method to determine stiffness with which to calculate hardness may use either the loading or unloading curve. However in practice it is the unloading curve that is commonly studied [102, 111, 116, 117, 119].

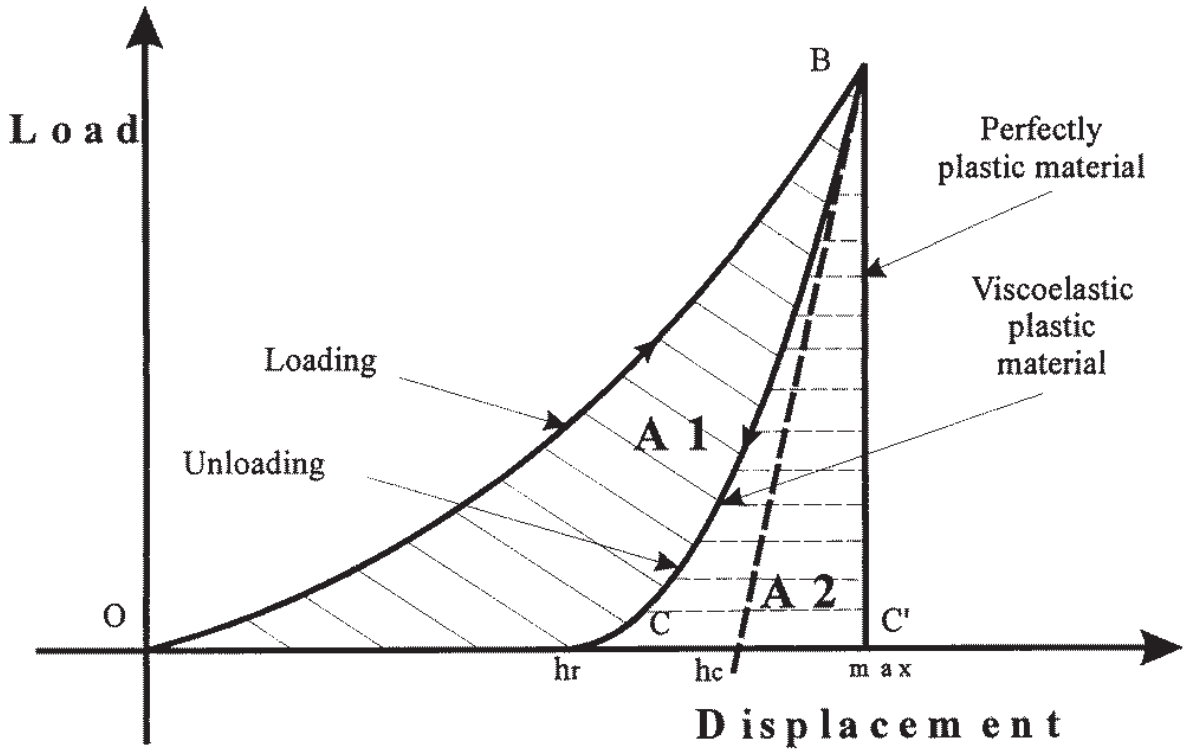

Figure 2.7: Schematic diagram of indentation load–displacement data for a viscoelastic–plastic material taken from the literature [120]. The plastic work done in the viscoelastic–plastic case is represented by the area A1 (OBC). The area A2 (CBC0) corresponds to the elastic work recovered during the unloading segment. In case of purely plastic material, the unloading curve is a straight line (BC').

This diagram is simplified and does not represent a method in which the peak load was held. Holding the load in a viscoelastic-plastic material would cause the tip to creep into the surface, leading to increasing penetration at a fixed load. Not holding the load risks further deformation when the load on the probe is reduced. As a result, viscous or plastic effects commonly cause a "nose" in the data. A data nose is a term used to describe a measurement artefact where during unloading of an indentation tip from a surface the depth appears to increase as force decrease [120].

The most applicable work in nanoindentation and subsequent data analysis found by the author was conducted by Pharr and Oliver. In particular their 1992 paper is the basis of the material properties calculated by nanoindentation instruments [112]. Their work has highlighted many key aspects of nanoindentation [113]. However, the applications of nanoindentation techniques to comparable soft elastomer films are not covered in their work. Nor does other work in the literature detail an established technique of studying the full range of visco-plastic-elastic behaviour found in the soft, elastomer films used in this study. However the application to hard thin films [121-124] and elasto-plastic materials [121, 125, 126] has previously been studied and these provide some insight into possible investigative technique. Many of these investigations also correlate the instrument data to computational modelling to better understand the results in terms of the underlying physical properties of these complex systems [123, 125-127]. This suggests the lack of mathematical modelling in this study limits the interpretation of the results.

Their most significant accomplishment is perhaps establishing a model of the contact [112, 113]. They show that for most physical systems a power law fit with an exponent of 1.5 -2 to the unload curve can be used to measure elastic material properties. This equation has the form:

$$P = \alpha\left(h - h_f\right)^{\beta} \tag{2.9}$$

where P is the indentation load and α and β are the power law fit parameters. α is primarily dependent on the material but *m* is dependent on the contact geometry [113]. From this fit stiffness, $S_{h_{max}}$, is calculated at the maximum indentation depth using:

$$S_{h_{max}} = \frac{dP}{dh} \tag{2.10}$$

This stiffness is required to calculate a reduced elastic modulus, E_r, can be calculated using the equation:

$$E_r = \frac{S_{h_{max}}\sqrt{\pi}}{2\sqrt{A}} \quad (2.11)$$

This modulus not the modulus of the material and

$$\mathrm{E_r} = \left(\frac{1-\nu_s^2}{\mathrm{E_s}} + \frac{1-\nu_i^2}{\mathrm{E_i}}\right)^{-1} \quad (2.12)$$

Hardness can be calculated from the area of the contact

$$H = \frac{P_{max}}{A_c} \quad (2.13)$$

Although approximate values for the power law is often used the exact values for this power law is often dependant on the surface mechanical properties and indentation tip. In particular for Berkovich tips and cones the theoretical value power is 2. In reality the effective pressure distribution does not match the indenter shape and is more convex. A power of approximately 1.5 is often found, akin to a spherical probe [113].

If there is reversible plastic deformation occurring then the fit will not be a measure purely of elastic properties [120]. As such there may be more recovery of the surface than expected based on the elastic properties alone. In order to try and reduce the amount of plastic deformation the load is often held for a long period of time. The length of this hold time is limited by thermal drift in the instrument and the possibility that the materials may strain harden. In the literature finite element modelling has found that work hardening and subsequently pile up is only an issue where the effective modulus is large compared to the yield stress [113]. As yield stresses are difficult to determine from indentation alone it is also

noted that this occurs when the final indentation depth is above ~70 % of the maximum indentation depth.

There other problems associated with measuring the indentation properties from the unloading curve. Typically the curve fit is used data between 20 % and 95 % of the maximum load [117]. In this study the indentation analysis of the film can be influenced by plasticity and adhesion [120]. The influence of the plasticity and adhesion on the response also has an influence on the appropriate fitting region [128].

In adhesive indentation the surface in contact resists the probe's removal [101, 129] [128]. As such areas above the indentation and pile up area may still be in contact with the probe beyond what would be normally expected for a non-adhesive surface. The increase in area does not have a direct effect on the distribution of contact pressure, in terms of spreading the load over a larger area, because the contact area is being assumed from an indentation area tip function and not being measured directly. However the additional contact area will affect the measurement of the mechanical properties as this film surface pulls on the probe. The additional contact material will resist the removal and providing a negative force compared to the normal contact force. The effect of the negative force reduces the overall normal force at a given depth. As a function of depth, the force will drop more sharply than without the adhesive force, meaning the contact stiffness will be higher than expected. Figure 2.8 illustrates this process. The impact of this effect on oscillatory measurements is minimal as the change in depth and therefore area is small. However, if very soft materials

are studied then displacement response to load ratio is likely to be large and therefore the potential for dislocation and error arises.

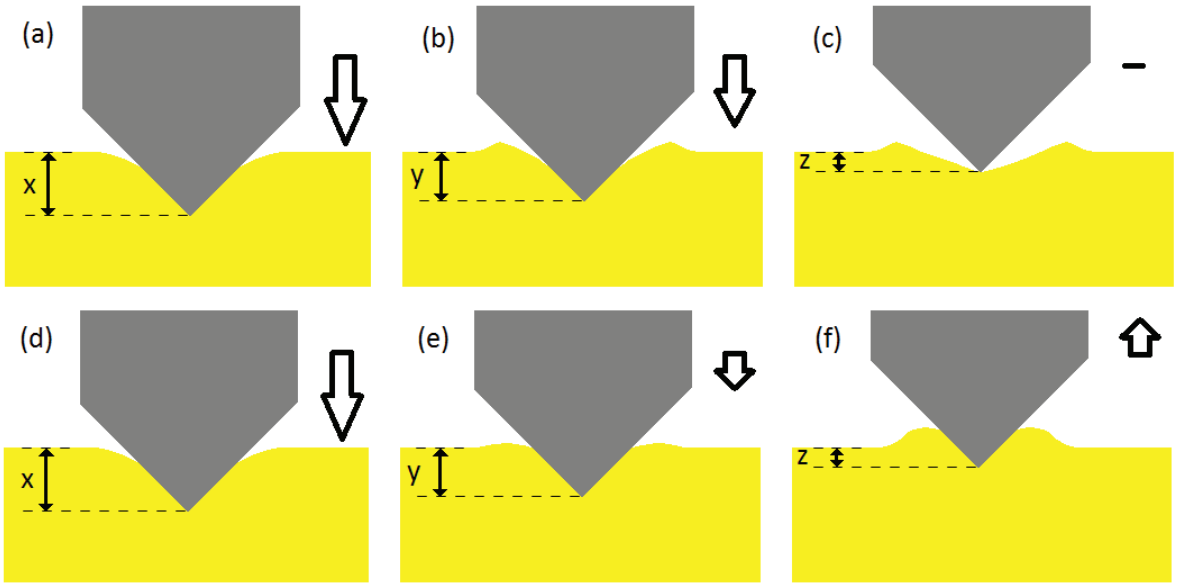

Figure 2.8: Schematic diagram illustrating the effect of adhesion on the surface during indentation. Diagrams a-c illustrate what an adhesion free indentation may look like and d-f show what might be expected with strong adhesion but otherwise identical mechanical properties. The hollow arrows indicate the magnitude of the overall force. The penetration depth is represented relative to the initial contact with x > y, and y > z. At full loading with the same force, a and d, the indentation depth is the same. As the force is reduced, at a given depth the force, is less for an adhesive sample, e, than that of a non-adhesive sample, b. This is because the adhesive force of the sample in part counteracts the normal force. Diagram c shows the point at which a surface without an adhesive force reaches zero force. Pile up is indicated. At the same depth on an adhesive sample, f, the surface is still attached to the probe and the restorative forces result in a negative force being felt.

2.3.6.2 Dynamic indentation

Nanoindenters can be made to not only apply a load and monitor the (quasi-static indentation) but also to oscillate the load on the probe to give continuous mechanical

measurements. Nanoscopic dynamic mechanical analysis (nanoDMA) or dynamic indentation is a way of continuously measuring the apparent mechanical properties of materials as indentation load, depth or time, or oscillation speed is varied. The literature shows it has been used across a wide variety of materials with elastic, plastic and viscous properties [110, 114, 115].

In order to investigate the mechanical properties of a system through dynamic analysis the two component generalised Voigt model is used [110, 130]. Figure 2.9 shows this mechanical model for the system. In dynamic studies an oscillating load is applied and the displacement response is measured. The amplitude of the oscillated load is often small compared to the mean load. This is done to try and ensure that the probe maintains contact with the surface, as mechanical disconnect could lead to erroneous results [110, 114]. The amplitude and phase shift of the resulting curve is measured. A phase shift occurs as a result of a viscous response of the material. A perfectly elastic material would not have a phase shift, δ, and a viscous material would have a 90^{o} shift. As a result materials are classified by a complex modulus, E^*, which is made up of the storage (or elastic) modulus, E' and loss modulus E'' via the equation [110, 130]:

$$E^* = E' + iE'' = |E^*|\cos\delta + i|E^*|\sin\delta = \frac{K_S\sqrt{\pi}}{2\sqrt{A_c}} + i\frac{\omega C_S\sqrt{\pi}}{2\sqrt{A_c}} \qquad (2.14)$$

Additional, it is possible to define the material phase angle for a complex material as the ratio of the storage and loss properties of a material.

$$\tan\delta = \frac{\omega C_s}{K_s} \qquad (2.15)$$

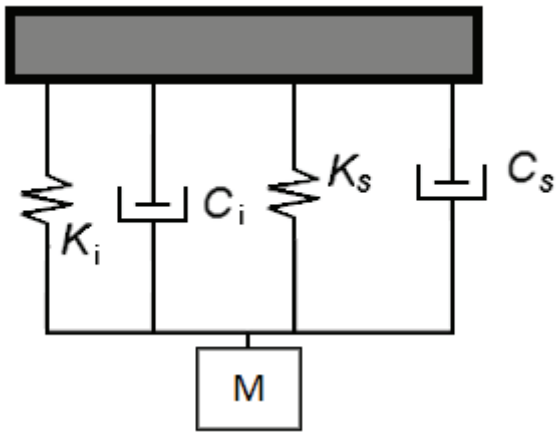

Figure 2.9: Effective mechanical setup during indentation is taken as the two component generalised Voigt model for an oscillating mass, *m*. The indenter setup stiffness and damping constant are K_i and C_i respectively. The specimen surface stiffness and damping constants are K_s and C_s respectively.

It is also of interest to calculate the indentation hardness, which is given by a slightly modified version of the standard indentation hardness definition:

$$H = \frac{F_{max}}{A_{Fmax}} \qquad (2.16)$$

where F_{max} is the maximum loading force and A_{Fmax} is the contact area at this force.

Nano DMA testing may be conducted at constant oscillation frequency and the effect of load or time is studied. Or DMA can be conducted by variable frequency at constant average load and oscillation amplitude. This later technique is has been applied in the study of frequency dependant elastoplastic behaviour in polymers such as polyethylene [131-135]. Frequency dependant behaviour arises because the polymer motion can be stimulated by the force oscillations. Molecular motions may also be limited at certain frequencies due to the vibration of the polymer "locking" the system.

Aside from this direct application of frequency sweeps, the technique is also used in the calibration of nanoindentation systems to obtain the indenter setup stiffness and damping properties [136]. The setup is calibrated in an air indentation method. As the probe is allowed to oscillate freely a resonance occurs and the data can be fitted to obtain the calibration parameters. NanoDMA testing is based on several fundamental assumptions. In particular the calculations of mechanical properties relies on the phase angle of the response being uninfluenced by the resonance behaviour of the surface [114, 115, 121, 130, 136]. The application of DMA is not always thoroughly examined in terms of the effect the forced oscillation may have in terms of the resonance on the system as a whole.

In order to understand this effect the mathematics of the oscillation is outlined [137]. The indenter system is being subjected to forced damped harmonic motion of the form:

$$m\ddot{x} + \zeta\dot{x} + Kx = F_0 cos\ (\omega t) \qquad (2.17)$$

Where m is the mass of the probe, ζ is the overall coefficient of damping, K is the overall stiffness, ω is the angular frequency of the oscillation, and F_0 is the force amplitude. x, $\dot{x}$ and $\ddot{x}$ are is the displacement, speed and acceleration of the sample at time, t.

It can be shown that for a generalised Voigt model that the overall stiffness and coefficient of damping is just the sum of the individual stiffnesses and damping coefficients [110]. In this case:

$$\zeta = C_i + C_s \qquad (2.18)$$

$$K = K_i + K_s \qquad (2.19)$$

If the system is assumed to be in steady state and so transient behaviour can be ignored then the solution to equation 4.1 is:

$$x(t) = A_0 cos\ (\omega t + \phi) \tag{2.20}$$

where ϕ is the phase change and:

$$A_0 = \frac{F_0}{\sqrt{m^2(\omega^2 - {\omega_0}^2)^2 + \zeta^2\omega^2}} \tag{2.21}$$

It is important to note that phase change, ϕ, is not the same as the phase angle of the material, δ, defined previously. The phase change is not a material property but a characteristic of measurement and is given by:

$$\phi = arctan\left(\frac{\omega_0 \omega \zeta}{m(\omega^2 - {\omega_0}^2)}\right) \tag{2.22}$$

where ω_0 is the angular resonant frequency, which is:

$$\omega_0 = 2\pi f = \sqrt{\frac{\mathrm{K}}{m}} \tag{2.23}$$

In the case of air indentation data from the frequency sweep is fitted using equation 2.21 to gain the stiffness and coefficient of damping for the indenter tip[136]. If the sample being indented into is too soft, i.e. the sample properties do not prevent oscillation of the probe tip after excitation, meaning interpretation of the results will be greatly hindered by resonance. However the properties of an underdamped system as a whole (rather than as a function of frequency) could be gained by fitting the curve in a similar way to air indentation and simple subtraction of the calibration parameters as per equations 4.2 and 4.3. Once the sample stiffness is known the modulus can be calculated using:

$$E = \frac{k\sqrt{\pi}}{2\sqrt{A}} \tag{2.24}$$

As described by Pharr the process of repeat indentation removes the plastic deformation [113]. Thus the calculated modulus and stiffness from the holding or unloading is elastic and not storage or complex modulus. That is not to say that the process is free from plastic response. Indeed the surface may yet exhibit frequency or time dependence.

Where the properties of a material are a function of depth the probe is oscillating into the surface, typical during the loading, so that elastic and plastic properties can be measured. There is much work on the application of this technique in the literature [110, 114, 123, 127, 130, 136]. Of particular interest to this project is the application to polymer surfaces [131, 132, 138]. Most of the literature on this subject referes back to a observation by Briscoe [120]. Briscoe studied multiple polymer materials through a series of indentations at increasing loads. The study showed the distance from the material surface has an influence on the material properties. For complex, branched polymeric materials the hardness and modulus data are often seen to vary with the inverse of contact depth. This inverse trend is not fully understood. Linear polymers by comparison do not show a significant trend.

2.4 Particle properties

Proprieties of the calcite can initially be measured by methods similar to surfaces however there are several problems that particles present which are discussed below.

2.4.1 Shape and size

Methods to classify the shape and size of particles traditionally relied on the inspection of particle images in order to measure size and shape [139, 140]. This process has become more automated over the years as this process was slow and the time taken depends on the time needed to process images. Modern dispersal systems combined with rapid imaging and fast computer analysis means that equipment such as Sympatec's QICPIC can now quickly measure the size and shape of a collection of particles [141]. An increase in computing power has also meant that the process of classifying shape has become more sophisticated [142]. However the technique is fundamentally based on two dimensional imaging of the outline of particles and so cannot characterise a single particle shape fully in terms of form and texture.

Laser diffraction is a widely used particle sizing technique for materials ranging from fractions of microns up to several millimetres in size [140, 143]. The traditional method uses Fraunhofer diffraction to classify the particle sizes. This process measures the angular variation in intensity of laser light scattered by particulate sample. Large particles diffract light at small angles and small particles scatter light at larger angles. The light intensity data processed using calculations based on Mie's theory of light scattering by dielectric absorbing spherical particles [144]. Mie theory can and has been adapted for non-spherical particle. However, the interpretation of results from Mie theory can be limited if the complex refractive index is not accurately known or if it is not a homogonous material. The end result is a model of the size distribution of the particles.

As the definition of particle size is dependent on shape the particle diameter is reported in terms of the equivalent diameter for a sphere of the same volume. The application of this technique is best applied to almost spherical particles hence as the technique cannot distinguish size and shape differences when estimating the size the size of high aspect ratio particles. The technique has been very successful and is treated as an established methodology due to speed of the measurement process allowing repeatable results to be gathered in minutes, with little turn-around time required for further measurement.

2.4.2 Mechanical properties

The mechanical properties of small particles are rarely measured or calculated directly. The approach in the literature is either to assume that the particle properties can be described by the bulk material properties, or try to imply the material properties from techniques such as the micro-compressive fracture of the particles [145]. Attempts to measure the mechanical properties directly have been conducted by this research and others, however it was found that the results were generally very variable and the particle properties often depend on the method of measurement. As such the particles properties here have to be assumed to be the same as bulk calcite.

2.5 Wear and cleaning

As mentioned above, much of this project was focused on the tribological behaviour of the LAC system in contact with the soil surface. The frictional data produced by the rubbing provided some useful information on the fluid flow. However, the wear mechanisms, wear

volume and how best to quantify them were key to understanding how the material is being removed.

2.5.1 Wear in hard contacts

The subset of tribology that studies the removal and /or deformation of surface is wear [57]. Wear may occur through many mechanisms and the processes of relevance to this project are those of abrasive wear. Abrasive wear occurs as a result of the mechanical action of a second surface, often termed a countersurface. The science of abrasive wear is usually broken down into the subject areas of two-body and three-body abrasion. Two-body abrasion refers to the wear of material surface by the direct action of fixed asperities on the countersurface. Three-body abrasion refers to the wear of material surface by the indirect action the countersurface through particles that are free to move between the two surfaces.

The longest established wear equation in the literature is Archard's equation [21, 58, 146]. Archard's equation for the total volume of material worn, *Q*, is given by:

$$Q = \frac{kWL}{H} \tag{2.25}$$

where *k* is a dimensionless wear coefficient, *W* is the applied load, *L* is total sliding distance and *H* is the surface hardness. The equation is empirically derived for dry two body contact between the two surfaces [21, 146]. Its applications are often very different from the tribological system it was derived for [57, 58]. The derivation does not include and makes no assumptions about a great deal of parameters that could influence wear, such as the surface topography (roughness), velocity and temperature. These factors are encompassed by the

wear coefficient. Meng and Lundema, in 1995, reviewed 5466 papers and found 182 wear equations containing over 600 different variables defined by the authors [147]. Over 100 of these variables were thought by Meng and Ludema to be distinct parameters that were not equivalent to or significantly similar to variables seen in other work. The applicability of the Archard equation may stem from the fact it is a simple core equation. The coefficient of wear provides a system variable to be found experimentally. Wear should follow the Archard equation provided "conditions" (as Archard referred to them) are kept constant. This equation forms the starting point, if not the basis of most work on wear in the literature [56-58, 147-150]. The fact that it is so widely applied shows its relevance as a fundamental description of wear. However, effects created by the wide-ranging surface properties, particles and fluid here are likely to limit the applicability of the equation.

As stated previously the many uses of hard materials including steel and elastoplastic polymers in tribological applications means that a large amount of research has been conducted into the subject of three-body abrasive wear in hard contacts [57, 151-155]. An experimentally established rule in the wear of metals is that the damage caused by an abrasive particle only becomes significant once the indentation hardness of the abrasive is ~0.8 times the indentation hardness of the surface [156, 157]. The explanation is derived from the fact that the maximum contact pressure for a spherical particle against a flat surface is about 0.8 times the hardness of the particle material. This means that calcite (hardness of ~120 $kgf.mm^{-2}$ from Vickers indentation (HV) or ~2.8 GPa from nanoindentation [158]) acting on SS (200-250 $kgf.mm^{-2}$HV or ~5 GPa [159]) should not cause significant plastic wear damage. However, this hardness is significantly larger than the expected hardness of a

typical polymer (<1 GPa [131, 132]). For this reason this investigation has ignored the damage to the steel and focused on the baked oil film wear. Note: visual inspection of the steel after cleaning confirms that scratching is rare in these experiments and may only occur due to contaminants in the system e.g. silica [22].

As a particle moves over a plastically deformable material the effect it produces depends on many factors. Ploughing is the process where channels form in the material if the particle can penetrate into the surface by a small amount then, as the particle is dragged forward, a ridge of material is formed on either side and in front of the "scratch": the prow in front of the material is pushed forward and under the particle [57, 160]. Material is often not removed in single pass of this type of wear; multiple passes can fatigue the material and cause removal. As the interfacial strength of the surface increases the material under the particle is less likely to be deformed and slip under the material, instead a wedge may form. This wedge formation leads to removal because as the material builds up until it can cut or fall off. At greater attack angles cutting will dominate wear behaviour: typically the transition to cutting occurs when the attack angle is at 40° to 50°. Cutting occurs when the material that would in the previous two mechanisms form a prow in front of the particle is being deflected upwards and therefore out of the channel of attack. As material is moving upwards it can chip off and be removed quite easily [57, 157].

This is not the full picture of hard material wear since other factors can influence the wear of the metals, due to alternate mechanisms of wear, for example wear can be influenced by brittleness and particles with high fracture toughness are less likely to crack [161]. Brittle

fracture is a behaviour is typical of ceramics, but is also seen in some plastics, and heat treated, precipitated and cold worked metals [157, 162]. “Pure” metals, such as stainless steel, have regular lattice structures and high fracture resistance and therefore normally deform plastically. Calcite therefore is unlikely to damage steel through brittle fracture and cracking.

It is also worth noting that, in a lubricated regime, a particle must also be larger than the minimum film thickness, of the lubricated contact, to cause unwanted damage to surfaces [72]. It has been observed that the friction and wear caused by the fluid are not always related, which could result from complications arising from chemical damage from the fluid, wetting of the asperities, heat transfer differences in the fluid or other factors. If there is chemical damage it may become confused with the physical particle damage so experiments of the chemical cleaning of the fluid without particles should be carried out both in tribological and quiescent conditions, and/or “background” areas of stains should be considered.

An effect worth mentioning in this section is that of the size effect: this is where particles show a marked increase in wear rate as their size is increased from several microns to several hundred microns. The size effect in wear is not just not associated with three-body abrasion, but two-body abrasion, erosion, grinding and metal cutting also show this effect [151, 163, 164]. This effect is particularly of interest in polishing.

2.5.2 Polishing

The most studied area of polishing is chemical mechanical polishing of semiconductor materials such as silicone wafers. Studies on household relevant polishing likely to be restricted to internal company documentation. In chemical mechanical polishing it has been found that there is a significant size effect observed on the amount of abrasive polishing: namely that increasing particle size reduces material removal. However the results were found is in the region from nanometres to microns and does not contradict the results that will be presented herein [64, 165, 166]. One recent paper suggests an opposite (increasing material removal with increasing particle size) trend with plastics [167], even though similar work on plastics does not corroborate this result [168]. In all probability the difference in the methodology is responsible for the difference in behaviour: one method restricts the spreading of particles and so ensures particles do not “escape” from being entrained. Although the size effect is not fully understood the most consistent explanation is that of the hard (“debris”) layer model. This model suggests that a surface layer of about 50 - 100 µm work hardens, from applied stresses, more than the bulk of the material. Thus, when small particles abrade the surface, they influence the surface layer and do not affect the material below unlike larger particles, which therefore wear more. Above a critical particle size, the influence of the hard surface will be small, so there is little or no increase with particle size [169].

2.5.3 Wear of baked dehydrated castor oil

As mentioned previously the application of detailed tribological investigation techniques to baked DCO is not something that appears to have been specifically studied before. In fact even mechanical data are not yet established for this system. Work in industry, mentioned in the patent literature [19, 20, 170], typically uses a WIRA (Wool Institute Research Association) instrument. This instrument uses a cleaning cloth tipped probe to trace a Lissajous pattern (a pattern produced by the intersection of two sinusoidal curves the axes of which are at right angles to each other [171]) over the surface of a oil stained sample with cleaning fluid present. The WIRA instrument provides a method of assessing wear in terms of the material removed after a number of Lissajous have been completed. However the complex, changing direction of motion, the single fixed speed and lack of friction measurements limits the possibility of further tribological study.

In its softer liquid form a castor oil soil is just a thin fluid film being acted on by a force, causing a confined flow. Castor oil usually flows as a viscoelastic fluid so the literature studies mentioned previously in the confined flow of the cleaning fluid becomes relevant. Work has been done previously in the behaviour of castor oils in EHL contacts [172] and some work on the spreading of thin oil films [173]. However, transitions to boundary lubrication and the mixing of oil with a LAC system is not mentioned in the literature. The mixing behaviour in particular presents a significant issue in modelling the flow of such soils and there has only been a small amount of work on the process of water/oil mixing in confined flow, and no comparable studies have been reported in the literature on more complex oil/LAC fluid interaction in confined flow.

In this study only results of baked elastomeric and viscoelastic films is discussed. As the DCO is baked on, the carbon chains cross link and form polymer structures that should exhibit similar behaviour to elastomers and soft polymers [174]. Therefore an understanding of the wear of rubbers and, to a lesser extent, plastics should be useful in appreciating the mechanisms used in the in the removal of these stains.

In general, as mentioned previously, wear can be discussed in terms of frictional, plastic and chemical processes based on the interfacial properties of the surfaces and properties of the lubricant. The mechanisms involved for polymers rely upon an understanding of the mechanical properties and it is often found that the wear rate is correlated with a strength, toughness or a fatigue property: these properties are more or less accessible in relatively simple bulk deformation experiments and sensible correlation of wear data and bulk deformation data is sometimes found (though anomalies are common)[175]. Studies of wear in polymers are often based on either model experiments that attempt to study the damage created by single contacts, in which the wear rate itself is not monitored, or wear rate measurements themselves [57, 175].

The general feature of polymer wear processes is that they are governed, in a large part, by the cohesive strength of the polymer. The force on the surface asperity is dissipated through a rather thick surface zone through one of several processes: the interaction of surface forces and the resultant tractive stresses or simply via geometrical interlocking of interpenetrating contacts. The size of the surface zone is defined by the contact geometry

and the contact stresses generated. Typically, these zones will be of a thickness which is comparable to a contact length which can be as large as the particle diameter: perhaps several tens of microns. Deformation processes thus operate within, and are a characteristic of, the bulk polymer. This may not result in an initial wear particle creation as the damage processes is likely to be of a fatigue rather than a unitary nature [175, 176].

Early studies of the damage produced in elastomers by Schallamach drew relatively large rigid indenters over the surface of an elastomer [177, 178]. The damage produced by these 'isolated stress concentrations' depends on the nature of the contact. A sharp needle penetrates deeply into the rubber, and almost periodic tears in the direction of motion are formed (figure 2.10).

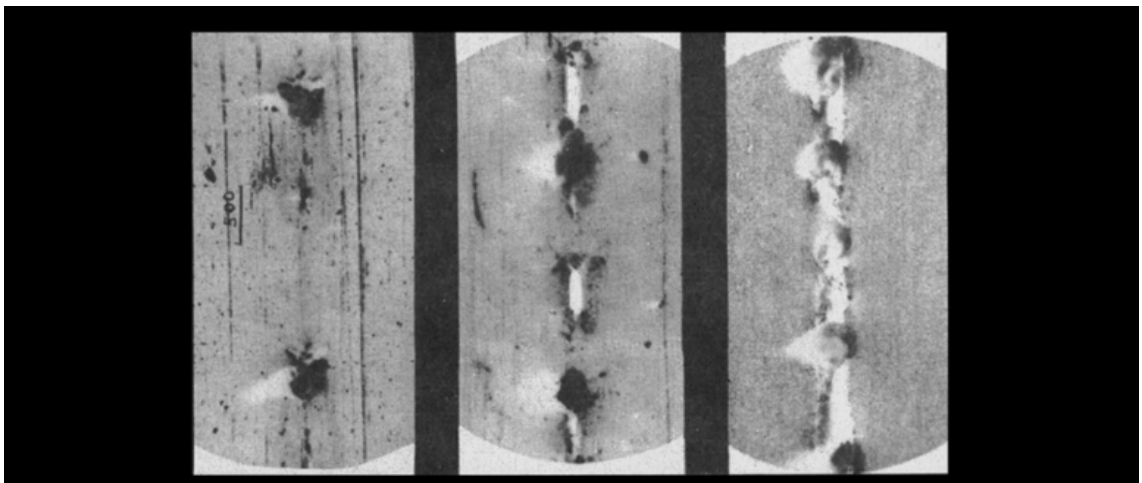

Fig. 10. Needle traces on 3 different vulcanizates of natural rubber. (a), unfilled, E = 11.5 kg/cm², load 80 g, magn. 13 ×; (b), unfilled, E = 18.3 kg/cm², load 50 g, magn. 30 ×; (c), filled with 50 p.p.h. MPC black, load 80 g, magn. 30 ×. Photographs (a) and (b) from ref.[14].

Figure 2.10: Needle drawn on three different vulcanizates of natural rubber, taken from [178].

Schallamach attributed their formation to the result of the needle stretching the surface layers of the rubber at the rear of the contact and pushing forward a prow of compressed rubber in front. A large elastic strain develops in the elastomer and the material ruptures in a direction perpendicular to the sliding direction. When the surface relaxes these flaws are thought to rotate through almost 90 degrees. The sliding motion is intermittent and stick-slip is observed in the sliding force. This process is not associated with wear debris but part of the forward wedge rubber may become detached as the contact slips over the deformed region.

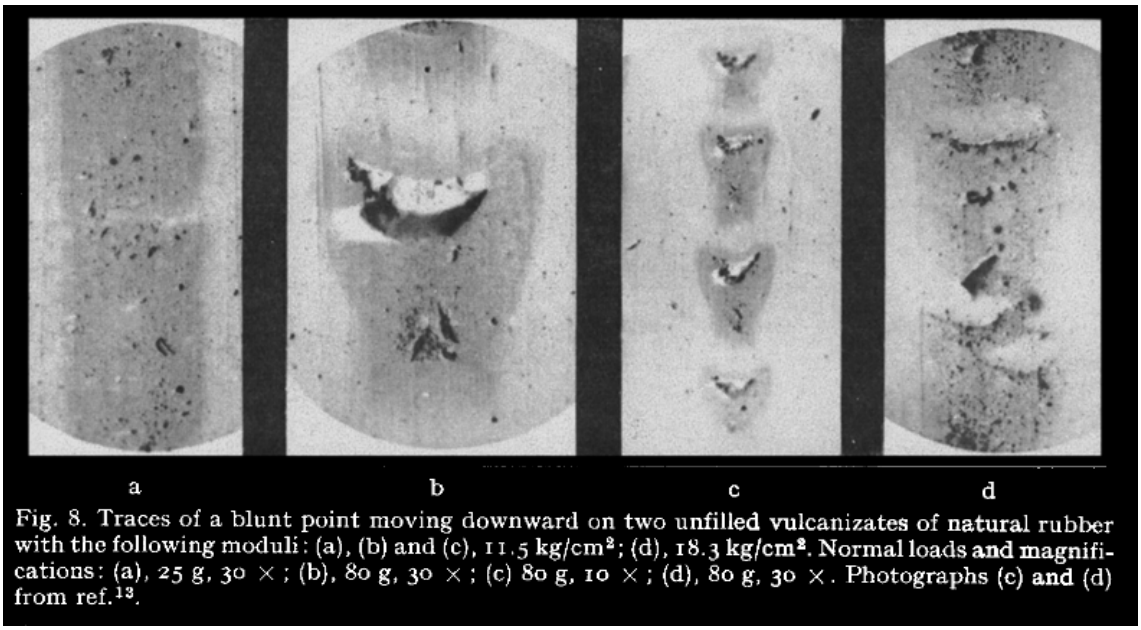

Fig. 8. Traces of a blunt point moving downward on two unfilled vulcanizates of natural rubber with the following moduli: (a), (b) and (c), 11.5 kg/cm²; (d), 18.3 kg/cm². Normal loads and magnifications: (a), 25 g, 30 ×; (b), 80 g, 30 ×; (c) 80 g, 10 ×; (d), 80 g, 30 ×. Photographs (c) and (d) from ref.[13].

Figure 2.11: Traces of a blunt point moving on vulcanizates of natural rubber, taken from [178].

Blunt indenters (see figure 2.11) or sharp indenters with lower loads produce damage in the form of crescents arranged with their concave surfaces facing the direction of motion [177]. Surface tractions are less and tensile stresses at the rear of the contact are present. The

action of the stress also appears to lift or 'tease up' a lip of rubber ahead of the tear. These single contact experiments indicated the importance of a number of variables in the damage process including the role of load, toughness and the tensile nature of the failure process. Schallamach's work main did not specify how material is removed and the exact fatigue nature of the wear process is still not well understood [179].

The wear behaviour of elastomers under multiple contacts is complicated somewhat by the generation of 'abrasion patterns'. Schallamach again worked on this type of abrasion and showed it produces striations perpendicular to the sliding direction and the resultant surface topography resembles that of saw teeth or "Schallamach waves" [179, 180]. The wear which results from this type of process produces relatively large particles of debris and wear in linear motion is greater than with periodically altered or random direction of motion. This increase in wear for linear motion has been suggested to arise from undercutting effects. When the crests of the 'saw teeth' are pulled over by repeat passes a "lip" of rubber is gradually pulled away and a roll of debris is formed which is characteristic of this wear process. The fact that such abrasion patterns form is strong evidence for a fatigue process rather than simple unit rupture. Overall elastomer damage is characterised by the creation of tears perpendicular to the sliding direction. These tears propagate into the bulk of the elastomer and ultimately close through multiple pass and fatigue to form a debris particle [175] (in figure 2.10 in particular the formation of wear debris is apparent).

Rigid polymer wear is also relevant to this project because when the oil is baked for a sufficiently long period it will fully crosslink and form a hard coating. Ploughing grooves and

cracking features, similar to those in glasses, ceramics and metals, are seen in the wear of these harder polymers (see comments above). However, a polymer microstructure is quite different to that of glasses, ceramics or metals, and has many subtle effects on the wear. Glassy polymers are essentially brittle materials in tension with a varying degree of ductility, so material deformation is dominated by fracture and cracking of the surface. Ductile polymers do not show evidence of brittle or low strain fractures. The theories of the deformation of ductile solids by rigid indenters are not exact, mainly because of the progressive change in geometry during deformation. Another wear mechanism seen in polymers is that of adhesive transfer. This is where thin layers are transferred by the counterface and is often, but not exclusively, associated with dry contact between metals and polymers [168, 175, 176, 181].

Perhaps the most relevant papers on the subject of the properties were produced by Lancaster [182-184]. Lancaster showed that harder and more elastic materials are less susceptible to wear than softer materials. In particular that the wear rate was inversely proportional to the square root of the elastic modulus and hardness properties multiplied together. The data showed wide deviations from this trend perhaps due to the wide variety in the properties of the limited number of commercial polymers chosen for the test, subtle effects were lost and the underlying “true” relationship between material properties and wear may be more complicated. However Lancaster’s results were limited to two body abrasion and of bulk materials, and so cannot readily be applied to the three body film abrasion here.

2.6 Summary

There are few direct references that have specific relevance to this study of abrasive household cleaning in the academic literature. This literature review surveys the related knowledge required to understand of the fluid system, the surface properties and wear and polishing with respect to three body abrasion.

The most important aspect of the literature available is the previous studies on wear. In terms of understanding the mechanisms underpinning the wear equation, the work of Schallamach can be singled out as particularly relevant to soft, elastomeric films. There is a standard approach in the literature to the development of a wear equation that means it is often prudent to start with the Archard equation and develop from it. This invariable means the dimensionless wear coefficient is replaced with a more complex term or series of terms. From a scientific perspective the aims of this project may be summarised as first finding if and when the Archard equation can be applied, finding its limitations and adapting k to include viscosity, speed and particle size.

Characterising the films themselves still presents a significant challenge and in this regard much of the fundamental work conducted on nanoindentation by Oliver and Pharr is applicable. However there is not enough work that has been conducted to show how best to measure soft films like those studied in this project.

Finally the work Mueller is singled out as a key for understanding the suspending fluid system. This work shows how fluid properties of suspension can be modelled and related to

the fundamental particle motion. However there are still limitation in the work and a justification of the rheological model is not given.

3. EXPERIMENTAL METHODS

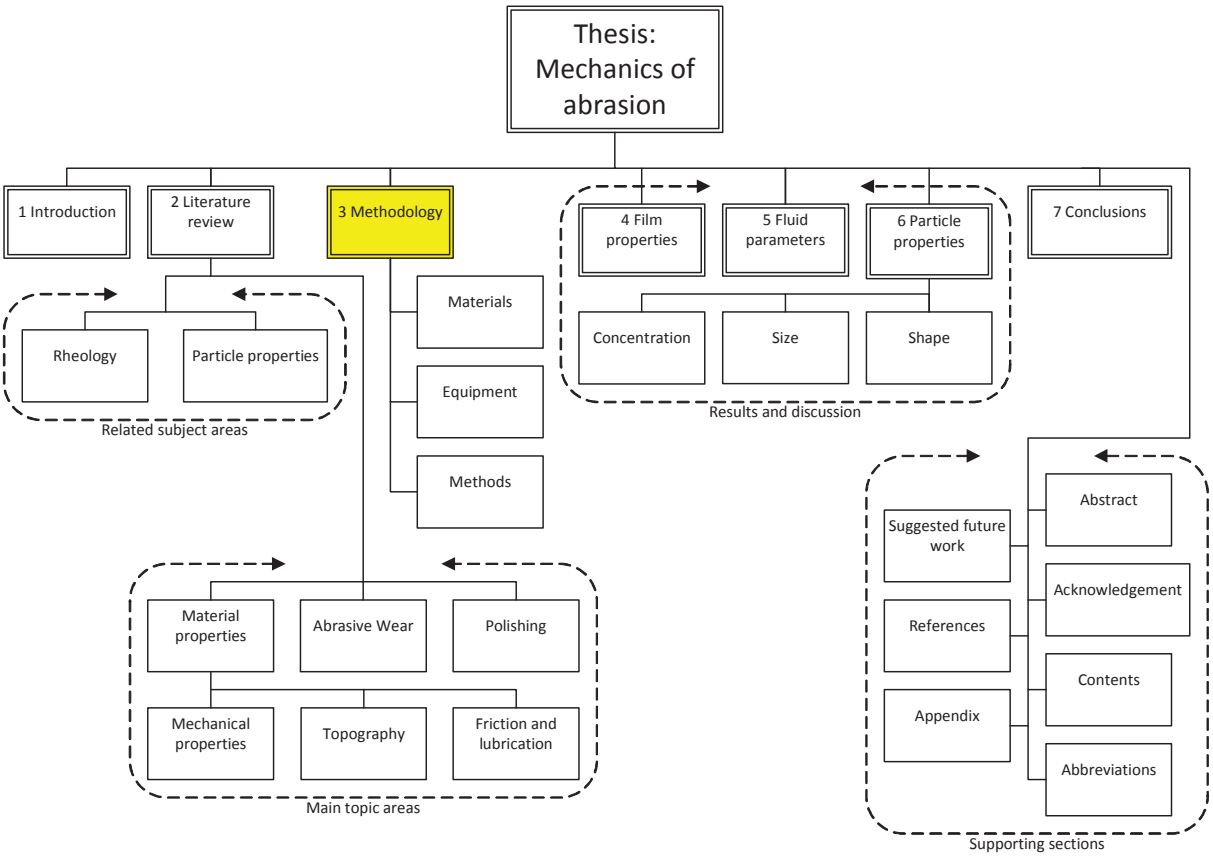

Figure 3.1: Thesis structure overview with the methodology, chapter 3, highlighted

This chapter is to give an overview of the materials, equipment and methods used to generate the results in the subsequent chapters. It aims to outline the tests not fully define them, as some familiarity with the test equipment and processes may be required in some instances. Where possible, equipment parameters for the test are specified in section 3.2. In the detailed method section 3.3, the tribological method steps and measurement specific to this thesis is outlined.

3.1 Materials

3.1.1 Particles

Fine ground natural chalk (FGNC) calcite samples provided by Unilever Research and Development Port Sunlight (URDPS) originated from Omya group through contacts in Italy and the UK. The details of how these samples were produced is proprietary and not known to this author. These samples were further refined by mechanical sieving. A single, circa 2 kg, batch of Omya 65AV calcite was sieved for 60 minutes at 50 hz. The sieves used were 200 mm in diameter and had meshes that were: 45 µm, 53 µm, 63 µm, 75 µm, 90 µm, 106 µm and 150 µm.

3.1.2 Fluids

Any water used during the experimentation was standard distilled water produced by on site at URDPS. A 5 kg second molasses sample, manufactured by Tate and Lyle (also known as black treacle), was purchased and this single sample used for the whole project. Newtonian fluids were prepared using a mixture of the molasses and water.

In this thesis the particle volume concentration is used. Particle solutions were prepared by adding a known mass of calcite particles into a known mass solution and, using the bulk density of calcite [185] from the literature and liquid density (measured prior to testing) calculating the volume concentration.

DCO, from John L. Seaton & Co. Ltd, was provided by URDPS. It is known that the cleaning performance differs between samples. In fact much of the patent literature [19, 20, 170] and industry experiments will contain a reference or benchmark measurement in order to draw conclusions on performance. The castor oil used came from one batch of 2010 oil that was kept in an opaque container within a refrigerator. This batch was therefore in a cold (0-4 ^{0}C), drying environment absent from light minimising ageing reactions, which rely on thermal energy or electromagnetic radiation [11].

3.1.3 Surfaces

Mirrored SS cut into 40 mm by 35 mm tiles originated from Merseymetals Ltd., and were donated by URDPS. The steel samples were provided in one batch, the same size and grade cut from one raw sheet of type 304 steel.

The steel plates were cleaned before use by submerging them into ethanolic potassium hydroxide solution for one hour followed by thorough rinsing with cold demineralised water and drying. This cleaning process should not damage the type 304 steel as it an austenitic steel used extensively throughout industry due to its low cost and good deep draw and welding properties as well as an ability to withstand mildly corrosive conditions [186]. Additionally the work of Sharples et al showed the steel can have a catalytic effect on the oil, accelerating the hardening process [11]. Like all SS 304 is characterised as having a crystallised structure covered in a thin passive chromium oxide film. If the metal is cut or scratched and the chromium oxide layer is disrupted, more oxide will quickly form and recover the exposed surface, protecting it from oxidative corrosion.

Oil surfaces in the tribological study were prepared by baking. Oil was spin coated onto 40 mm by 35 mm tiles. For the tribological experiments an area in the centre of the tile was prepared. This meant the edges of the tile were masked off with 3M Scotch Magic Tape, as shown in figure 3.2. The spin time and speed was fixed at 60 s and 1000 rpm respectively. The spin coater parameters were set such that the tile took approximately 10 s to ramp up and 5 s ramp down in speed. For the majority of experiments the resulting film was then baked in an oven at 100°C for one hour. The sample was then removed and stored in a opaque container in laboratory conditions (20°C, 50% RH) for circa 9 days (see chapter 4 for further notes) to mitigate further photo and thermal oxidation [11].

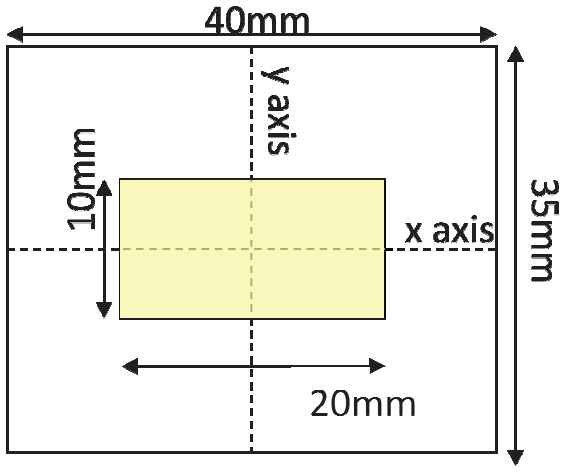

Figure 3.2: A diagram illustrating the typical oil sample prepared for the tribological experiments. The probe travels along the x axis and the sample is scanned in the y axis

A range of temperatures and baking times were used for the oil films. This is because real world oil stains are likely to vary in physical properties. Samples baked at high temperatures for long time periods represent what may be expected to be produced on steel surfaces such

as heater elements, pans and ovens walls. Softer films, baked at lower temperatures and times, are more representative of those found on a splash-back, extractor hood and cooker top.

3.2 Equipment

3.2.1 Tribometer

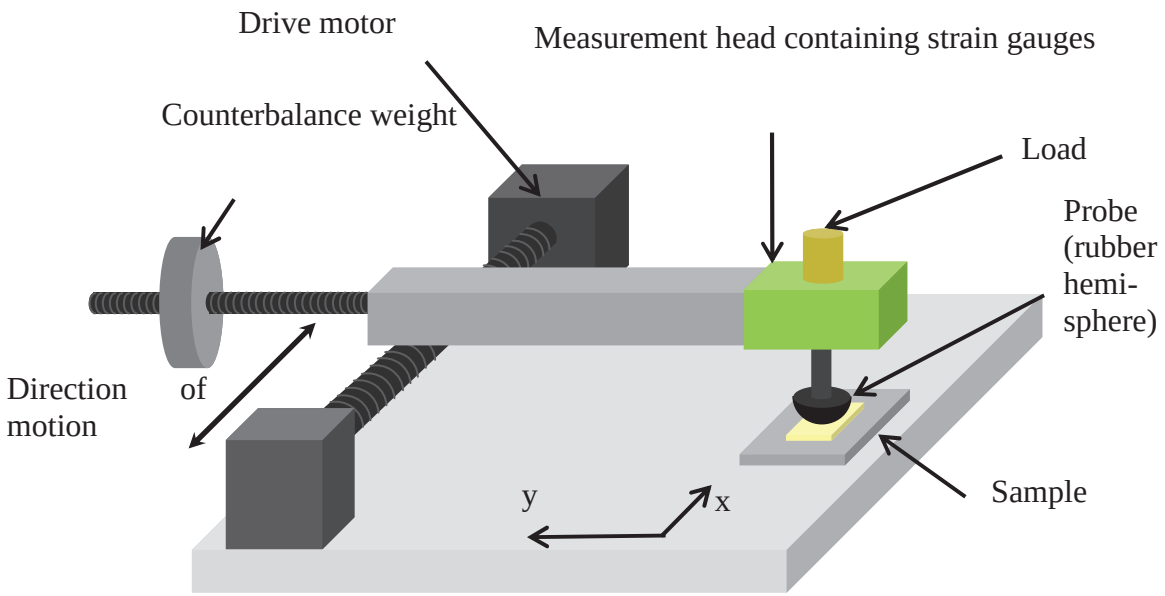

Figure 3.3: Schematic of the Eldredge tribometer used.

The cleaning process used on the samples was carried out used the Eldredge tribometer setup at URDPS (see figure 3.3). This instrument consists of a pivoted lightweight counterbalanced arm driven by a variable speed motor via a screw system. Motion is linear, reversible and the travel distance can be set as required by adjusting the stops. Test surfaces were mounted on the upper surface of a laboratory jack whose height can be adjusted, such that the probe would pass through an area in the centre of the oil sample (for a photograph

of the sample setup see figure 3.4). Before measurement the system was balanced and the height of the sample adjusted such that the arm was horizontal and applying zero force when the sample and probe are in contact. Due to the balancing, when a load was placed directly over the probe holder it accurately represent the normal load applied.

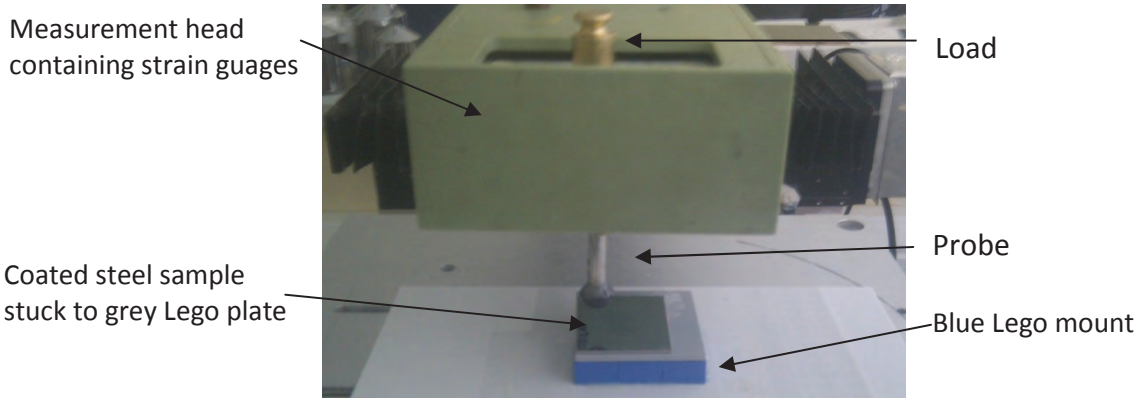

Figure 3.4: Photograph of the sample setup on the Eldredge tribometer prior to wear.

A double beam assembly of thin steel plates is used to connect a probe holder to the main arm. Strain gauges are mounted on these plates which measure the extent of the bending of the plates caused by the frictional force exerted between the sample and the probe. The strain gauges are connected to a Fylde transducer amplifier (359TA) and a passive signal attenuator (gain = 0.1) before low pass filtering using an EG&G pre-amplifier (gain = 10). The conditioned signal is then logged by a PC (Measurement Computing A/D card and DASYlab data acquisition software) in order to record the frictional force as a function of time. The raw data obtained can then be processed and analysed on a separate computer.

The experiments investigated the damage created by running a Viton elastomer half sphere probe, with a 12.7 mm radius of curvature across the centre of the oil track, such that the probe does not leave the oil surface. The probe was selected for the work to ensure that realistic contact pressures could be achieved without the complication of flow through a porous applicator. The probe was mounted via a ¼ inch steel shaft that was attached using a two part Araldite adhesive. This probe was replaced regularly, when visible damage appeared or after a series of tests (a series of tests was a set of tests used to gain one wear rate i.e. sliding distance was varied and other parameters kept constant). In practice this was 5-15 tests. Lego plates are used to mount the sample to the tribometer (see figure 3.4).

3.2.2 Laser profilometry

The laser profilometer was a custom setup shown in figure 3.5. The stylus was a low powered, near-infrared, auto-focusing laser "stylus" (ex Rodenstock). A laser beam was focused, through a moveable lens, on to the surface before being reflected back through the lens and into a detector next to the emitter [90]. Feedback moved the lens in order to keep the light in focus on the detector. If the height of the sample below the laser changed then the lens height adjusted by a proportional amount to keep the beam in focus. The height measurement at each point on the surface was based on the parameters required to focus the laser beam on the surface. As well as this height data, reflectance of the sample was measured but this data has not been used in this thesis.

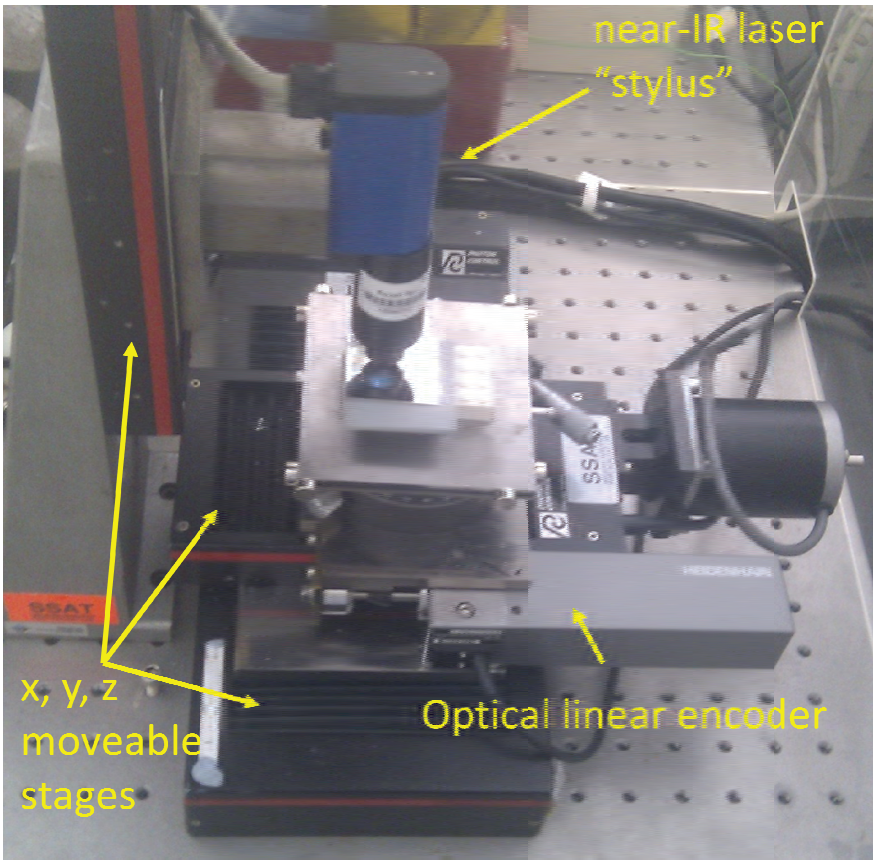

Figure 3.5: Photograph of the sample setup on the profilometer. The image shows the laser on a z-axis stage mounted above the stainless steel sample that has been coated, glued to a grey Lego plate and mounted on to the profilometer lego stage mount. The image also shows the x and y stage

The laser stylus was mounted on a stage moveable in the height (Z-axis) direction. Beneath this, the sample was mounted via Lego to a metal plate fixed onto two further stages moveable in X, Y and rotational axes. In addition, the Y stage was fitted with a Heidenhain optical linear encoder, which was connected to the PC via a linear/rotary encoder selection unit. Once the sample was mounted in place and the centre of the area of interest lined up, the sample brought into focus using the Rodenstock RM600 control box and z axis control.

The raw data obtained was then be removed from the logging computer then processed and analysed separately in MATLAB.

3.2.3 Interferometer

Sensofar S-neox 3D optical profiler with built in Mountains based software was available late in the project [86]. This microscope based profiler was primarily used as a device to characterise the three dimensional properties of the top of a selection of the worn coatings. The blue LED light was primarily used. After focusing the imaging on the top of the surface a scan was run. The upper height limit for the scan was adjusted in order to capture all details or conserve time. However a lower limit of ~7 μm was found due to the fact that eventually the light would focus on the metal substrate and produce an artefact in the results.

3.2.4 Rheology measurements

The purpose of the rheological measurements is to assist in the interpretation of the friction/lubrication experiments in the hydrodynamic regimes, assuming that bulk behaviour persists in this regime (i.e. geometric confinement effects are insignificant). Rheometry is a widely applied science and so the typical method parameters are detailed in this subsection and not specific parameters for each test.

A collection of Newtonian fluids were prepared by mixing molasses and water. The continuous phase and bulk rheological behaviour was characterised. These were initial solutions were used to develop a general method of mixing a series more precise solutions.

These solutions were then measured (and tweaked and re-measured as required) to give the continuous phase rheological systems for the study.

The majority of measurements were carried out on a Bohlin C-Vor rheometer using a serrated Couette cup and bob geometry. The temperature was fixed at 25°C in all experiments. A pre-shear rate, 100 s^{-1}, was applied to the fluid for 60 s before testing in order to try and minimise any effects of "shear history", because a liquid suspected of having thixotropic properties may be sensitive to the pouring /storage just prior to measurement. Where possible each measurement point consisted of 30 s measurement per data point. However for some fluids a shorter 5 s measurement period was taken in order to minimise particle sedimentation. When the fluid became too thin or particle separation became particularly problematic a 40 mm, 1^0 cone on plate or double gap rheological setup was used.

3.2.5 Optical microscopy

Initial optical investigations were carried out on an Olympus BX51 microscope with a Zeiss AxioCam HRc camera for image capture and associated Zeiss Axiovision software for image processing. Additional optical experiments were conducted using a Sensofar S-Neox microscope which is also capable of interferometric and confocal measurements. In all these optical images (throughout the thesis) the tiles were aligned such that the left of the image is the starting point for the motion (i.e. the first pass is always from left to right).

Finally some photographic records were taken to show equipment setup, or give a visual impression of the overall test sample. Hence for some larger scale, photographic images were produced using a Nikon D5000 with 18-55mm f/3.5-5.6 or 40mm macro f/2.8 lenses.

3.2.6 Scanning electron microscopy

The primary SEM used in this investigation was a Model S-3400N from Hitachi High-Technologies Corporation. In addition to the detector features outlined in this subsection, the SEM has an energy-dispersive X-ray spectroscopy (EDS) detector system. The detectors used in this system for detecting electrons are solid state and TV-rate observation systems for SE and BSE respectively. In this investigation EDS data was acquired during SEMs of the steel substrates. The measurement was purely for quality control purposes to characterise the steel surfaces, ensuring the composition was as expected for 304 grade SS. This data has not been included in this thesis as it was not considered novel or significant. Other SEMS were used as required; in particular a benchtop SEM and some cryo-SEM images were obtained.

3.2.7 Atomic force microscopy

The AFM used was a JPK Instruments Nanowizard II at the University of Birmingham. The AFM was used primarily for indentation measurements which were carried out using a 7.6 µm SiO_2 spherical colloidal probe attached to an AFM cantilever with a stiffness of 16.7 $N.m^{-1}$. A 500 nN compressive normal load was applied to film. Drive velocity for the probe was 2 $\mu m.s^{-1}$ and a 2 s hold was carried out when the peak force was reached. Contact radii and

penetration depths were of the order 2 μm and 500 nm respectively. 25 measurements were taken per sample. Elastic modulus and hardness were calculated for each point. The mean and standard deviation of these values calculated.

3.2.8 Nanoindentation

For nanoindentation measurements a Hysitron TI950 Triboindenter was used. A Berkovich tip was used for all indentation experiments. These techniques have previously been discussed in the literature review. Due to the variation in methods available on the triboindenter and the mechanical properties of the materials used varying the exact parameters used for further tests often had to be adjusted. Detail of the parameters used will be discussed with the results in chapter 4.

Dynamic indentation applies a constant strain associated with the geometry of the Berkovich indenter and was done using a 1 mN maximum load with a peak 30 μN oscillation. The frequency is held at 220 Hz. In the case of dynamic indentation frequency sweeps from 3 Hz to 301 Hz. The indentation probe was typically held at an average load of 500 μN and a 10 μN dynamic load applied. For dynamic measurements at least 9 repeat measurements were taken per sample. However analysis was based on a typical curve.

Quasistatic indentation refers to the concept that the probe is moving at a constant speed or being held and is not being influenced by a dynamic oscillation that is a feature of the nano-indentation setup [117]. 25 quasistatic measurements were taken per sample. The mean and standard deviation of the elastic modulus and hardness are used for analysis.

3.2.9 Particle sizer

Particle size was measured using a Sympatec Helos (H1438) laser diffraction particle sizer with a Rodus/M dispersion unit. The Rodus operates at a flow rate of 300 l/min and was fitted with a Vibri feeder and 4 mm dosing line. The detector parameter settings, such the complex refractive index, were setup to measure calcite particles. Due to the range of particle sizes the lens setup used was not held constant, and was instead optimised for the particle distribution observed. The equipment was set to measure the volume density distribution, q3.

3.3 Detailed methods: method for wear and friction measurements

The primary parameter of interest in studying the mechanics of abrasion is the wear volume. This quantity could have been calculated from a contact or non contact profile, in particular interferometer and AFM amongst others. Unfortunately the interferometer setup only became available in the later stages of the investigation and was only used in a limited capacity. The laser profilometer was chosen as the AFM scans during preliminary testing were often significantly affected by thermal deviations and by variation in the surface properties of the sample itself more than was observed using the laser profilometer. Variation in surface properties affects reflection of the laser profilometer, which is measured separately to height. The laser profilometer shares several issues with the AFM in that they cannot measure steep walls or overhangs, and lateral resolution is often limited by the motor. AFM potentially has a high vertical resolution of less than a nanometre, whereas the laser profilometer cannot measure below a few nanometers, and the particular instrument

used in this investigation could not accurately measure heights of tens of nanometers. However the higher speed of the laser profilometer was a significant advantage. Contact profilometry cannot be used as the tip often deforms or causes significant damage to the surface.

As well as this the profilometer data, mass was also measured during some early experiments using a 4 decimal place analytical balance. However, the use of mass data in quantifying wear was found to be impossible due the fact that the amount of material removed during post test rinsing varies. In particular when very low wear had occurred the mass may increase due to material trapped on or under the surface.

Profilometry data of a wear scar is often seen in the literature and typically features a model fit for the background /undamaged surface data. Here the sample is baked leading to significant deviations in the sample surface such that there be topological features (because of the spreading of the oil does not give a perfectly uniform film) but also the exact volume and therefore the height of oil soil varies between samples. The profile must therefore be measured before and after wear on the tribometer. Lego is used to mount the sample to both the profilometer and tribometer in order to produce a relocation profilometer method. The use of Lego parts to produce accurate, affordable mounting system was discovered by Weber [187]. This work alongside follow-on work by Willoughby showed that parts could be precisely relocated using such elastically-averaged alignment fixtures [188]. Relocation profilometry are methods of measuring the surface profile of samples that allow for the

sample to be removed, replaced accurately and premeasured, variations of mounting methods have been used in the literature to achieve this [83, 189].

On top of this the surface of the steel represented may be warped or slanted either due to the production of steel or the metal not being mounted in a truly flat position. This means that even with accurate lateral repositioning the sample may show significant measurement deviations. Software can be used to remove this background feature in both the pre and post wear sample as shown in figure 3.6.

In order to process the data to remove the background data shown in figure 3.6 (a), the areas around the soil are normalised to give a background model shown by the shape in figure 3.6 (b)). In this work a second order polynomial fit in both the x and y directions is used to fit the background data. Subsequently the data without the background effects can be obtained, as shown in figure 3.6 (c). Finally the data are corrected for the refractive index of castor oil (found to be 1.47 at 100 ^{0}C) in order to obtain values for the true height of the oil (see figure 3.6 (d)). Refractive index is corrected for because the height is not being measured directly. Instead the refractive image is viewed as a result of the trans parent nature of the film and the high reflectivity of the steel. In order to ensure that the background distribution of steel (which exists both due to roughness in steel surface and some warping that has not been fully eliminated from the background) or data from pieces of calcite are not exaggerated by this correction only data between 1 µm and 35µm are normally corrected (some user judgement is required in the processing data to confirm these parameters).

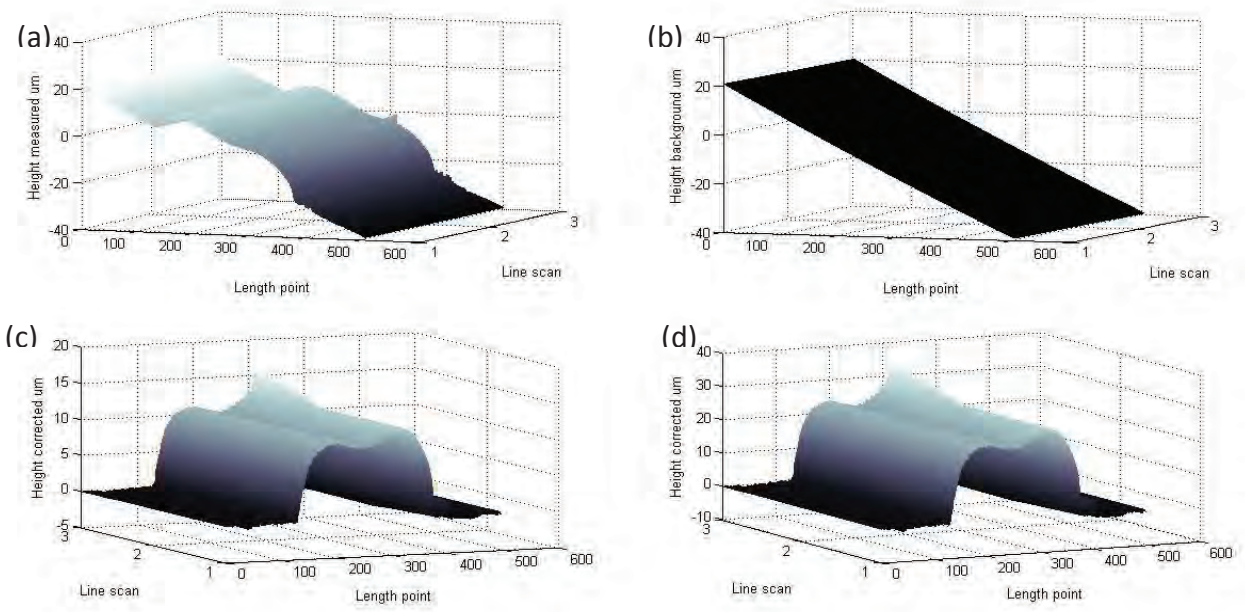

Figure 3.6 Plots from the processing of profilometer data. (a): raw data. (b): background model. (c): data with background removed. (d): refractive index corrected data.

Friction data gathered from the Eldredge tribometer is essentially a square wave, as the change in direction of the probe causes the force to oscillate between forward and reverse friction. Therefore in order to investigate friction a square wave is fitted to the data. The analysis program then takes the midpoint of each flat horizontal section of this waveform and averages the friction about this point (note: data are averaged over ±25% of the square wave line length). This force data can then be divided by the force of the mass acting on the probe to determine the friction coefficient. The final step in processing the data is to invert the negative values and average with the positive values.

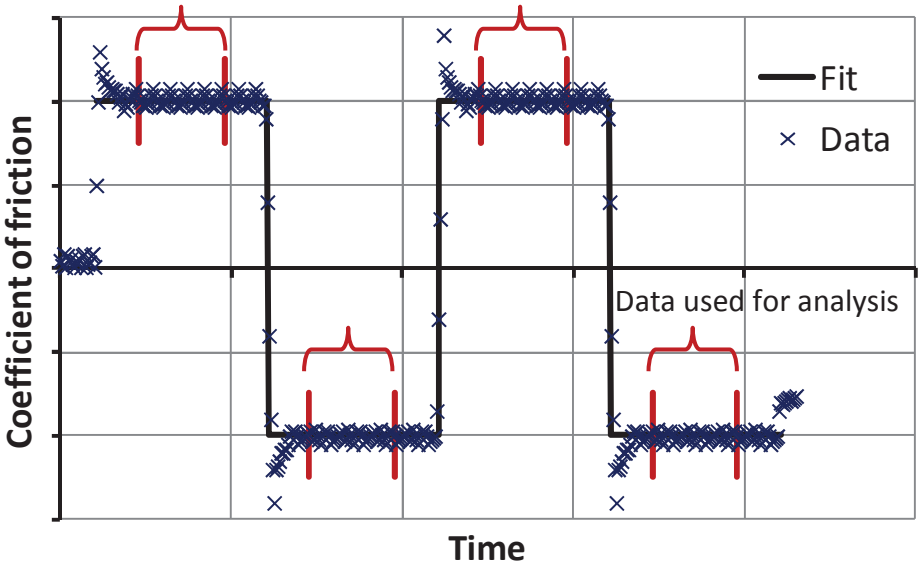

Figure 3.7: Illustration of the features of the analysis process overlaid onto representative raw data. A square wave is fitted to the data and used to find the data for analysis

4. RESULTS AND DISCUSSION: CHARACTERISATION AND INFLUENCE OF FILM PROPERTIES

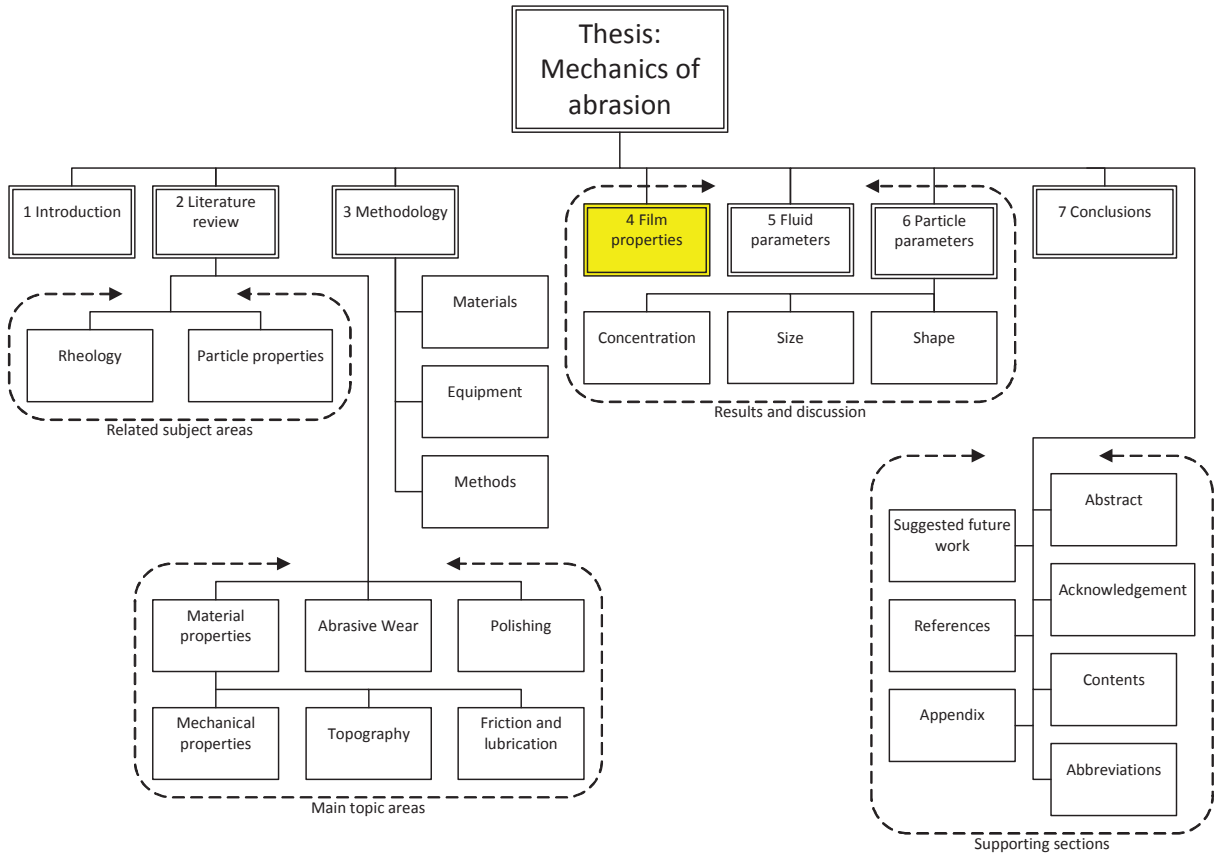

Figure 4.1: Thesis structure overview with chapter 4 highlighted

Fundamentally this chapter investigates the suitability of the linear Archard wear equation for the three body wear of the baked oil films. The Archard wear equation contains three variables: sliding distance, load and surface hardness [21]. Load and sliding distance are trivial variables both to characterise and adjust. However the surface hardness is a more complicated parameter to define for soft polymer DCO films. Hence the first subject that this chapter will address is the measurement of the mechanical properties of baked DCO film.

4.1 Measurement of the properties of baked oil films on steel

It is important to understand how a mechanical property is measured before applying it in an investigation of its effect on wear. The meaning of a material property is often strictly defined in terms of the nature of material and setup of the test. Hardness in particular is not a fundamental material property and can only be truly defined by reference to a particular test method (see subsections 2.3.5 and 2.3.6). Even then there is no single test method to applicable to all materials. Additionally there is no established test method designed to measure the properties of the DCO films in this study. This is because established test methods primarily deal with primary materials not surface films. It is recognised that there are test standards that, theoretically, apply [190, 191] but for soft films on a harder substrate the interpretation in these tests assume the modulus and hardness will decrease as penetration depth increases. As shown in 4.1.2.2, this assumption is not found to be valid. This section will investigate the application of several modern test procedures to measuring the properties of DCO films, outlining the meaning and limitations of the results.

4.1.1 Atomic force microscopy

As discussed previously, AFM is a scanning probe microscope capable, in some instances, of atomic level resolution. Although principally used for high resolution imaging, in this study it is used to detect mechanical properties. Figure 4.2 shows the typical indentation curve of a colloid probe into a soft oil surface baked onto a SS tile. There is a relatively large negative force (-1 μN) produced on the approach due to snap-in. On withdrawal there is a larger negative force due to adhesion (-3.2 μN).

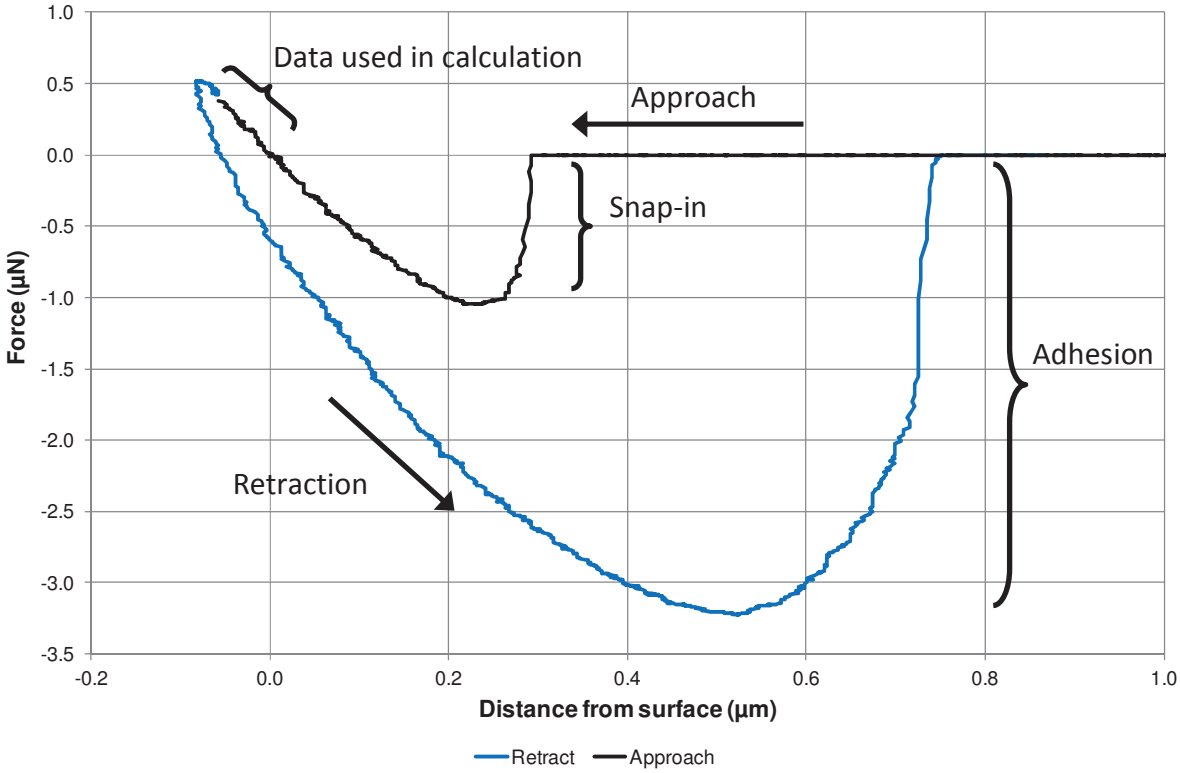

Figure 4.2: Typical indentation of the colloidal probe atomic force microscope tip into a soft baked oil film. The film was baked at 100°C for 1 hour then and indented 164 h after baking. The hardness measured here was 160 kPa and modulus is 7 MPa. Distance from surface is defined by the point at which the cantilever is under no force after snap-in.

Figure 4.3 shows the effect of time after baking on the material properties of DCO films. The trend in the data as a function of time is not significantly different (less than a factor of 40% increase from minimum to maximum hardness and modulus) between batches. Samples gradually become harder and more elastic for the first 200 h. The hardness and Young's modulus peak at approximately 230 h. After this the values appear to decrease with time.

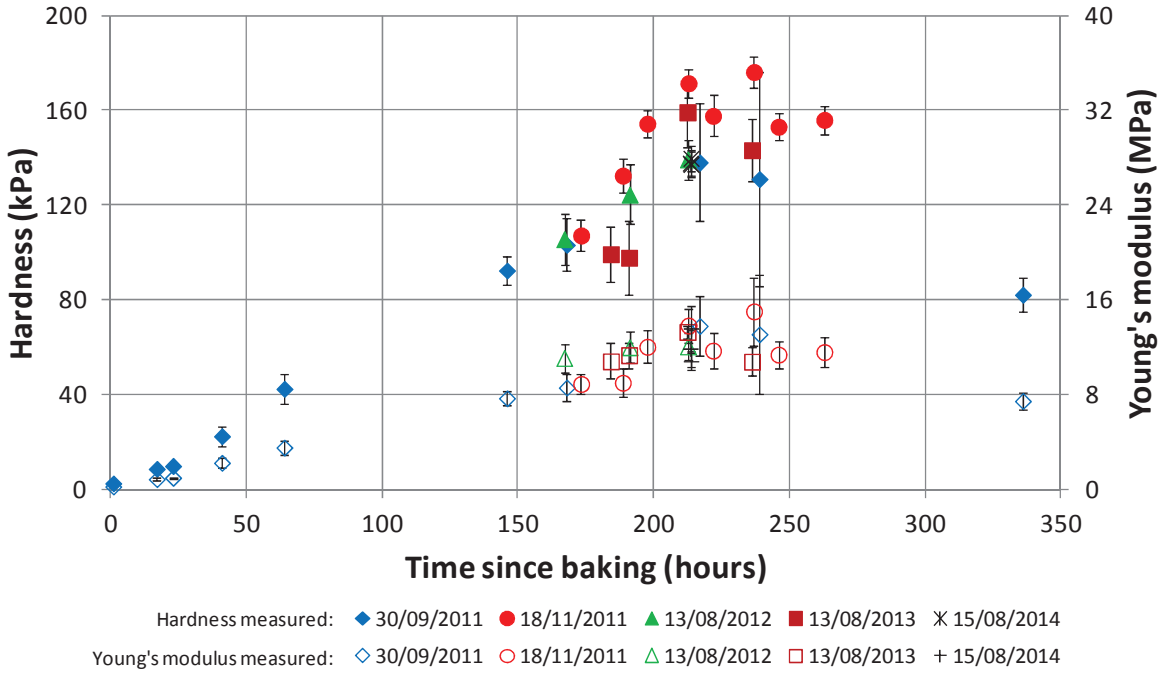

Figure 4.3: DCO film hardness (filled markers) and Young's modulus (unfilled) as a function of time since baking. Measured using AFM indentation. Different markers denote separate oil film samples. 25 measurements were taken per sample and error bars indicate the standard deviation of these values. Note the deviation of some test are larger. This is particularly apparent for the earliest testing suggesting this may be a result of improper sample handling, or unrefined technique in the creation or testing of sample. All oil films sample were baked at 100^{0}C for 60 min.

The trend in the data shown in figure 4.3 suggests that there are competing chemical reactions present in the forming of these oil soils. This is consistent with the literature view point mentioned by Sharples et al [11]. Crosslinking and polymerisation reactions are likely to be driving the hardening of the DCO film. Free-radicalisation reactions are suspected to be softening the film. These mechanisms are driven at different rates and the rates may vary as a function of time. In particular, crosslinking and polymerisation is dependent on the number of free radicals. If the number of free radicals is low the rate of polymerisation and crosslinking reactions will decrease. If the number of free radicals is high the rate of polymerisation and crosslinking reactions will increase. In the results presented in figure 4.3

the overall effect of these competing reactions is that there a peak in the material properties. In the opinion of this author it is expected that if the material properties were continually measured for a longer time period, the material would be seen to oscillate between harder and softer states as the reactions compete. Gradually the material should approach an “ultimate” or equilibrium state. It is noted that there are other oxidisation reactions [11] at work in this material that will affect the ultimate material properties but these are expected to be slower so are seen as being secondary to the processes mentioned above.

According to this oscillation hypothesis the sample should slowly approach an equilibrium state where the mechanical properties are constant as a function of time. This equilibrium state would provide a good experimental substrate. However for practical experimental purposes this state is of little use as the state would take too long to achieve. Given the first peak takes over 9 days to be reached, the process of reaching equilibrium could take months if not years to attain.

For practical purposes it was decided that samples be tested when the material properties reached the first peak shown in figure 4.3. This peak occurs as the softening reactions begin to dominate over the hardening reactions. The peak was taken to be at 9.5 days, though a range of 8 to 11 days was deemed acceptable. The film properties measured by the AFM during this time were an AFM hardness of 150 ± 16 kPa and Young’s modulus of 12.5 ± 1.3 MPa. This range in material properties is due partly to the slow variation over the time

period of acceptable measurements, but also due to random, batch to batch sample variations.

The batch variations may occur in part due to subtle differences in oil and steel properties. Although, these effects should be minimal as thermal and light exposure is controlled and the batches of materials are the same. The more dominant cause in material property differences is thought to be due to slight difference in the preparation method such as temperature variations during baking and dissimilarities in the light exposure, particularly UV, before and after baking. These subtle random sources of error are difficult to control and their effect on the DCO film would require a detailed, long dedicated test program. As such there is a fundamental batch to batch variation in the properties of the films. This effect is not taken into account in the attempts to reduce random and sampling variations for a single batch of DCO films. Most results for a single wear rate used only one batch of baked oil films. Therefore this random fluctuation in properties is a source of error not consolidated in the error calculated for a wear rate when a fit to the wear volume as a function of distance is applied.

When comparing wear rates results between batches it is therefore important to assume that this fundamental variation in the mechanical properties might have an impact. Due to there being 11 % and 10 % variations in the hardness and modulus respectively (calculated from the data between 8 and 10 days shown in figure 4.3), a single wear rate can never be less than 11 % accurate. Therefore, if the fit of the wear volume data gives a wear rate with an error of less than 15 % this is always discounted in favour of a higher 15 % error. The

nominally higher value of 15 % is chosen here over 11 % as the sample variation is not the only source of error.

For the softer baked oil films the atomic force microscopy process, discussed previously, is an effective means of measuring and classifying the materials. The method described was used extensively to characterise the soft DCO films used in the experiments reported in sections 4.2, 4.3 and more extensively in chapters 5 and 6. However there are subtle effects that the method is not evaluating /excluding. When it comes to classifying a range of DCO films produced by a variety of baking conditions, the limitations to the method becomes more apparent.

The first limitation is that the method looks at the approach of the probe to the surface and measures the deflection of the cantilever. This method means that the surface may be allowed to deform both elastically and plastically. Therefore calculations from this method, which assumes elastic deformation, would not be accurate. This method was chosen over using the unload data because the surfaces show a significant amount of surface adhesion on unloading (see figure 4.2). Analysis of the unloading curve would be influenced by the material's adhesion (see subsection 2.3.4).

Secondly the AFM method uses a fixed load and loading rate for the indentation (note: the method settings were found during proprietary work prior to the start of this work). As seen in the literature many methods show sensitivity to both the load and loading rates [96, 99, 100, 192, 193]. The results provided by this method cannot readily be compared to other

results using a different method(s). A difference in material properties may arise from a change in the measurement technique used [96, 99]. However, the method may need to change in order to measure the properties of a stiffer film.

The resolution of the detector is dependent on the stiffness of the cantilever and the size of the probe. It the surface is too stiff, compared to the cantilever and tip, the fundamental assumptions of the measurement process may not be met [96, 99]. In order to measure a stiffer film there are three basic steps that can be taken: the cantilever needs to be stiffer, the probe needs to be smaller or the approach speed needs to be slower. Such changes to the methodology will have a direct impact on measured mechanical properties and cannot be used to compare samples that are only subtly different (see subsection 2.3.4). The results from different methodologies may be useful in order to gain an approximate understanding of the difference between surfaces if there is a large difference in mechanical properties. However, even with this approximate understanding of the material differences, another source of error can arise if the stiffness of the film is similar to or greater than the stiffness of the probe. Silicon based probes this technique tends to become unfeasible as the surface modulus approaches ~1 GPa (see subsection 2.3.4). This means that much stiffer metal cantilevers are more suitable for the measurement of harder films.

However the use of a stiffer cantilever would limit the ability to measure the softer films. As stiff cantilevers are only deflected a small amount by a soft surface. AFM based techniques are limited to measuring materials with stiffnesses varying by up to two orders of magnitude (see subsection 2.3.4). This means that a set of cantilevers would need to be used in order to

measure the mechanical properties of a wide range of surfaces with hardnesses from less than 1 MPa up to several GPa on an AFM. As AFM cantilevers are created to be a somewhat disposable item they are subject to large manufacturing differences in their geometric and physical properties [96, 99]. Each new setup would need to be characterised in terms of stiffness and shape in order to find a suitable set. Errors would arise from comparing the results of different probes as each probe shape and/or cantilever stiffness is different. In practice rather than continually modify the AFM technique to match the required surface measurement nanoindentation techniques were used to characterise different surfaces.

4.1.2 Nanoindentation

Nanoindentation equipment is designed to cover a wide measurement range with the same measurement head and tip. In this case the Hysitron 950 triboindenter with DMA head can be used at forces from approximately 30 nN (below which noise prevents accurate contact force detection) up to just over 8 mN. Also it can indent from approximately 30 nm (this limit due to the radius of the Berkovich tip) up to 5 µm[117, 194]. Although nanoindentation provides a wide range for measurements, there are practical considerations and limitations on the results, so measuring a range of materials does present several issues. As discussed previously the setup of an individual material is often specifically optimised (see subsection 2.3.6). The primary advantage of the nanoindentation measurement over AFM is therefore the symmetry in the test setup in terms of indenter shape and setup. This advantage is particularly significant when a Berkovich tip is used.

4.1.2.1 Quasistatic trapezoidal indentation

The initial AFM based technique was designed to characterise very soft, almost liquid, films with <1 MPa modulus up to soft films of ca. 10 MPa. The AFM method was used to ensure that there was a suitable time period for reproducible films to be tested. It is possible to do a similar simple trapezoidal load verses time indentation profile on the nanoindenter. The key difference being that on the nanoindenter the load is the control parameter not the displacement. As such, a simple indentation keeps the loading rate constant as opposed to the approach speed, which was kept constant on the AFM.

Figure 4.4 shows a typical trapezoidal, quasistatic indentation of a DCO film with the nanoindenter. The unloading rate is relatively high and the hold time is deliberately long. This is to try to prevent a “nose” in the data created by viscoelastic effects. The mechanical properties are measured from a curve fit to the unloading curve. The curve fit used data between 20 % and 95 % of the maximum load, here giving the hardness as 9 MPa and the elastic modulus as 600 MPa. There are problems associated with measuring the indentation properties from the unloading curve. The problems arise in fitting the unloading curve from the assumption that the response is perfectly elastic. In this example the indentation analysis of the film can be influenced by plasticity and adhesion. The influence of the plasticity and adhesion on the response also has an influence on the appropriate fitting region. As the appropriate fitting region is decided by user preference, the measurement of properties between users may change. Even an individual may vary their approach to fitting based on a particular data set.

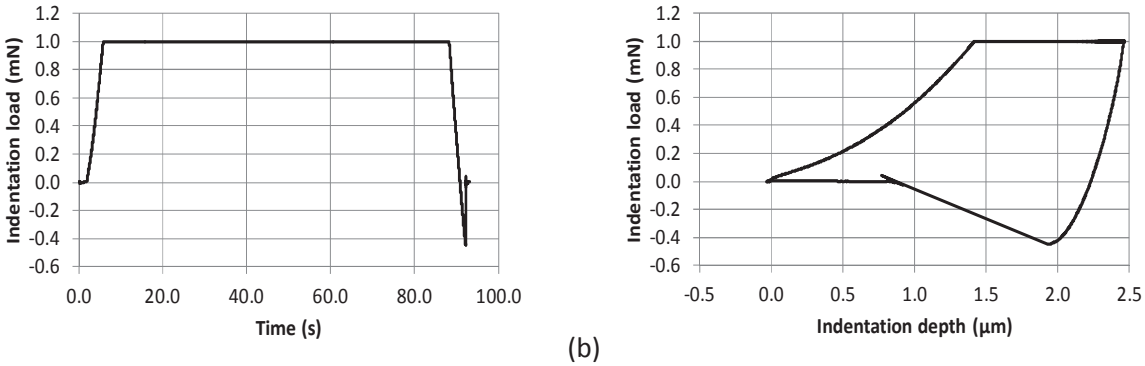

(a) (b)

Figure 4.4: Trapezoidal nanoindentation of a DCO film with strong surface adhesion using a diamond Berkovich tip on the Hysitron triboindenter. The load as a function of time (a) shows a 1 mN load applied in 6 s, held for 80 s and then unloaded to zero in 6 s. The force goes negative indicating an adhesive force. The indentation profile (b) shows the load as a function of penetration depth. This oil film was baked at 180^{0}C for 1.5 h and measured after 9 days. The straight line in the unloading curve (b) from 1.9 µm to 0.8 µm is an artefact due to adhesive failure not captured by the measurement process

Under non-adhesive unloading the surface contact area decreases as the indentation probe is removed. Even if the unloading is perfectly elastic on unloading, the best model of the curve could involve several approaches. In particular the initial unloading of an elastic surface is often linear regardless of tip shape due to reversible deformation near to the contact. After this initial unloading the power law relationship between load and distance can be found. Although approximate values for the power law are often used the exact values for this power law are often dependant on the surface mechanical properties and indentation tip. If there is reversible plastic deformation occurring then the fit will not be a measure purely of elastic properties [126, 131]. As such there may be more recovery of the surface than expected based on the elastic properties alone. In order to try and reduce the amount of plastic deformation the load was held a long period of time.

In adhesive indentation the surface in contact resists the probe's removal. As such areas above the indentation and pile up area may still be in contact with the probe beyond what would be normally expected for a non-adhesive surface. The influence of this additional contact area and the affect the measurement of the mechanical was discussed previously in subsection 2.3.6.1. The additional contact material will resist the removal and providing a negative force compared to the normal contact force.

The Young's modulus is proportional to stiffness and might be expected to increase with the stiffness. However the elastic modulus is also inversely proportional to the root of the contact depth. The contact depth is taken as the point at which the curve fit reaches zero. If the fit follows the curve to the point where the curve is equal to zero then, due to adhesion, this contact depth will be higher than the true value for the system. Overall the effect of contact depth may reduce the calculated modulus and hardness such that the terms "measured" modulus or hardness may more accurately relate the fact that these are measurement specific values.

In order to measure the impact of viscous and plastic effects further, the unloading curve can be separated out and compared to other films. Figure 4.5 shows the unloading curves for DCO films with various mechanical properties. The properties have been altered by changing the baking conditions. It is possible to fit a power law to the unloading data, as done in other work, however analysis of the data requires there to be an offset for the final indentation depth. Ordinarily this would be the point at which force reaches zero (1.5 µm for the 180°C data here). However adhesion has adversely affected the curve meaning the final

indentation depth could be as low as 1.25 µm, where the force is minimum and the adhesive response is about to fail. Therefore it is only possible to give a range for the depth.

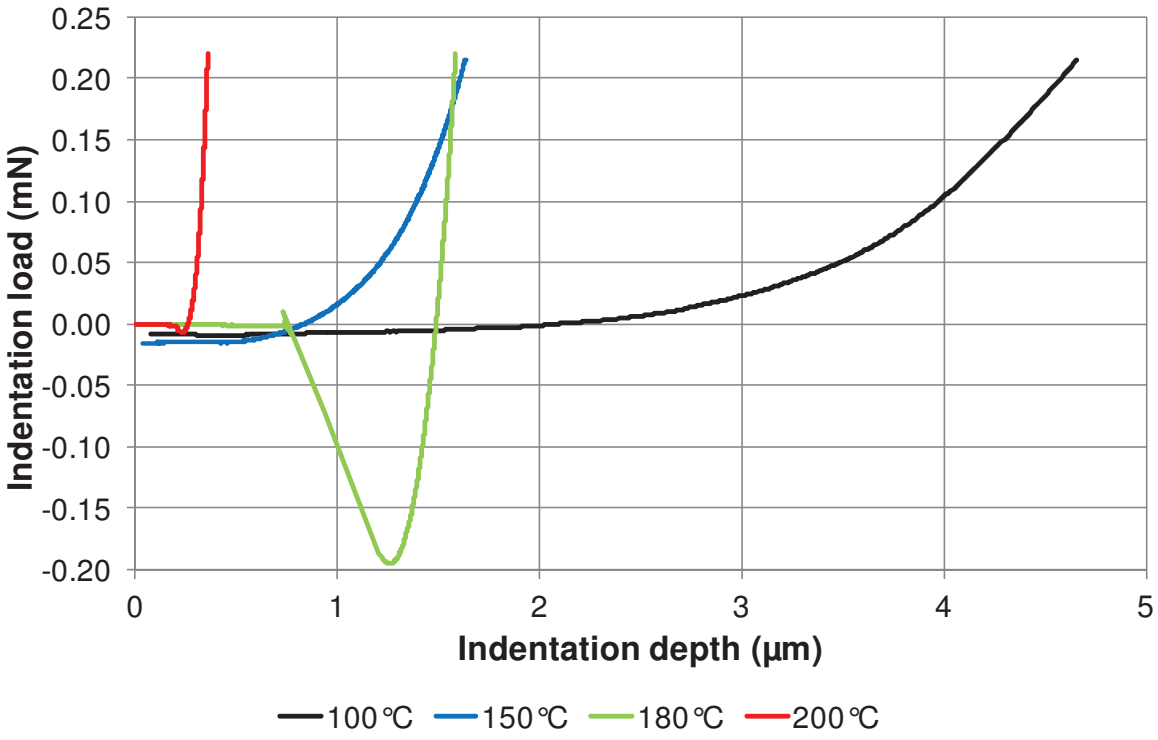

Figure 4.5: Unloading curves from the nanoindentation of DCO films with different mechanical properties using a diamond Berkovich tip on the Hysitron triboindenter. All measurements use the method outlined in figure 4.4. All samples were baked for 90 min and stored for 8.5 days before measurement. Mechanical properties were varied by changing the baking temperature.

A smaller range in depth can be gained for the film baked at 200°C. The graph shows the 200°C baked film to be stiffer, more brittle and less adhesive than the one baked at 180°C. These observations suggest at the highest temperature the film may be becoming a hard, glassy polymer. The larger amount of deformation and adhesion for the film baked at 180°C shows viscous and/or plastic effects are significant. For the softer films it is not possible to determine a minimum final contact depth, as indicated by the fact that the 100°C and 150°C

curves do not reach a minimum. It appears as though the film is maintaining contact as the probe moves towards the original contact point. This suggests that the soft films have a viscous component and can flow back into shape.

However, the problem of not knowing the indentation depth is inconsequential, as the curves do not readily fit a power law with an index between 1 and 2 unless a very restrictive sample length of data is used. As discussed previously the expected power law index is 1.5 (see subsection 2.3.6.1). Using a more restrictive length does not seem appropriate as such a fit would increase the contact depth. As discussed above the contact depth is expected to be lower, not higher, than zero in the curve. For the whole unload curves powers of 2 to 3 (closer 3 for very adhesive curve from the 180^{o}C baked film) would give an acceptable fit but this does not have a physical significance. It might be possible to use a fit to establish the mechanical properties if it were possible to prove the result was related to another measurement of the mechanical properties (see subsection 4.1.2.3). In reality the problem arises from the fact that the films are adhesive and elasto-visco-plastic and therefore deformation is dependent on the rate and magnitude of the unloading.

Figure 4.6 shows the corresponding loading curves to the unloading curves shown in figure 4.5. An interesting point is that the final indentation depth of the films baked at 150^{o}C and 180^{o}C, after holding the load, were similar even though the loading curves are different. As the film baked at 180^{o}C should be more cross linked, as it has a steeper loading and unloading stiffness and therefore has a higher apparent hardness and elasticity. Yet at the higher temperature (200^{o}C) the loading curves are at a much lower depth. An explanation

for this behaviour is in terms of the viscous or plastic nature of these films. The 150^{o}C film has a low "viscosity" and this can be seen by investigating the creep behaviour during the holding segment of the indent, shown in figure 4.7. During the holding time the probe creeps into the surface. The rate of creep is slower for the 150^{o}C film than the 100^{o}C but significantly slower than the 180^{o}C film, which may be creeping due to irreversible plastic deformation not viscous flow which may be reversible.

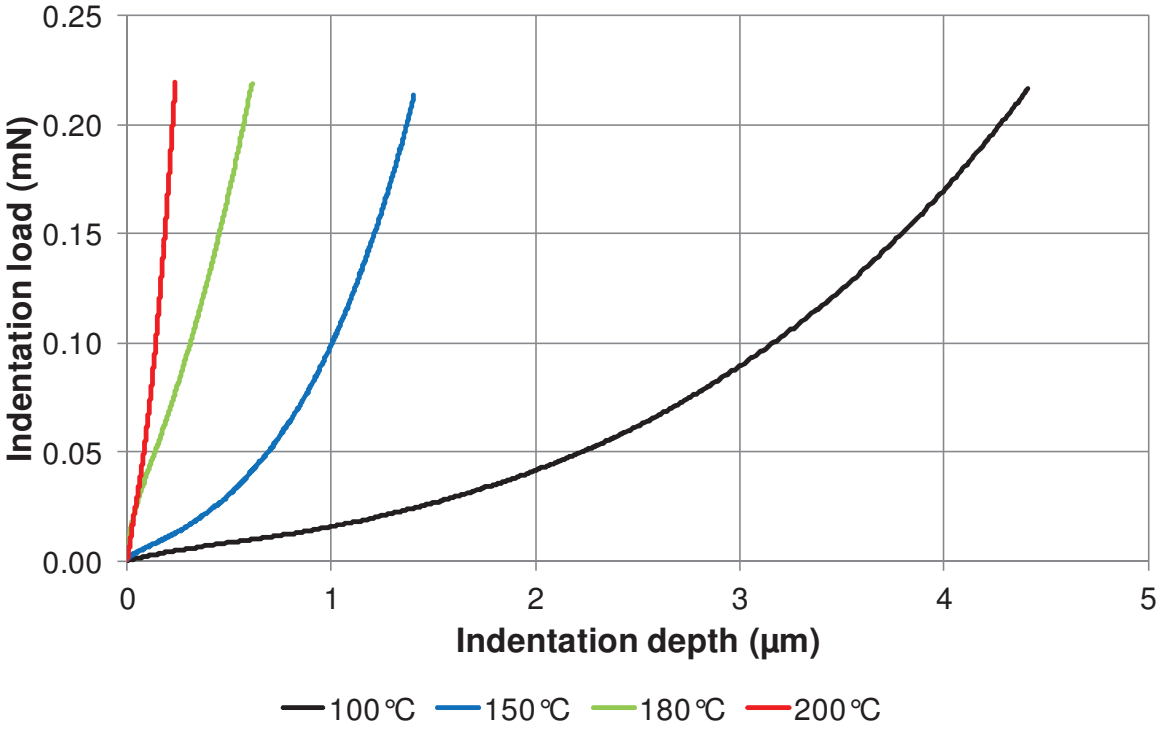

Figure 4.6: Typical loading curves from the nanoindentation of DCO films with different mechanical properties using a diamond Berkovich tip on the Hysitron triboindenter. All measurements use the method outlined in figure 4.4. All samples were baked for 90 min and stored for 8.5 days before measurement.

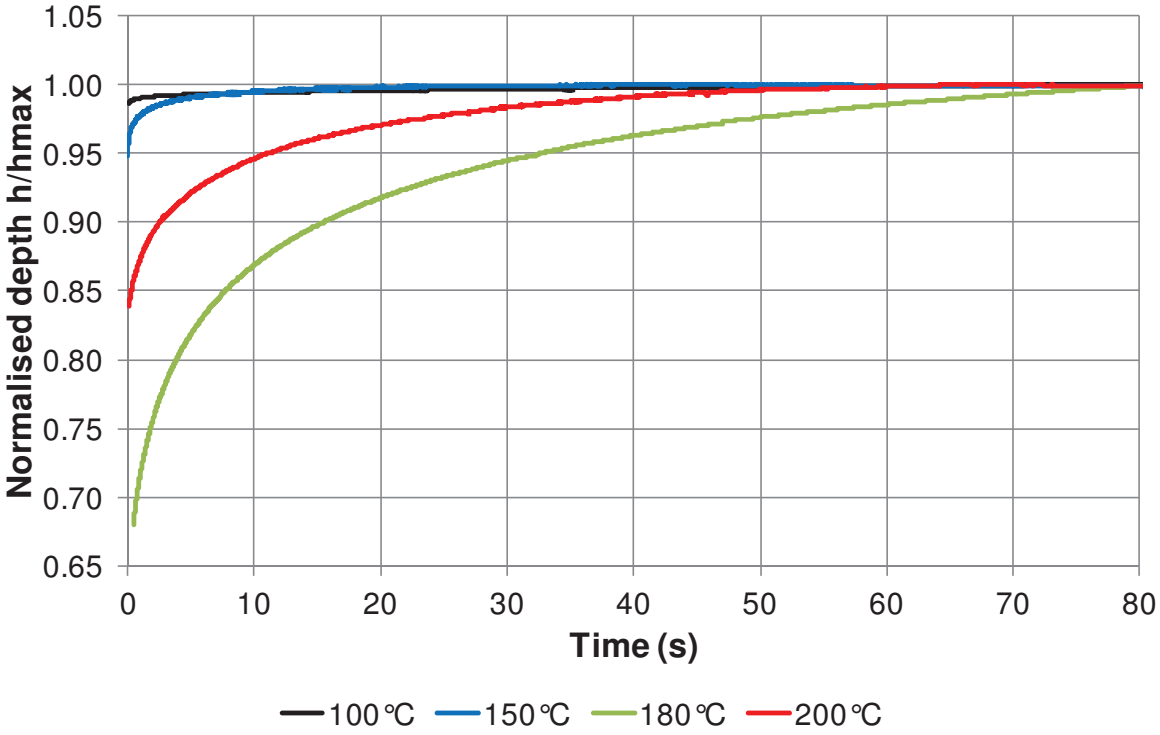

Figure 4.7: Relative holding curves from the nanoindentation of DCO films with different mechanical properties using a diamond Berkovich tip on the Hysitron triboindenter. All measurements use the method outlined in figure 4.4. All samples were baked for 90 min and stored for 8.5 days before measurement.

The data indicates that increased baking temperature affects not only the elastic properties of the films but also the visco-plastic properties. The fact that the relative creep is so large in some of the results shows how the results derived by properties such as the maximum penetration depth can be influenced by the user choice of indentation parameters. The 200^{o}C data shows less creep than the 180^{o}C and seems to represent a film that is becoming more of a solid, brittle material, less viscous and likely to deform after yielding.

Overall a quasistatic loading technique is a straightforward and fairly simplistic method which can give a way of differentiating between the baked oil films. However the results

gained from this technique have been shown not to be reliable for understanding fundamental mechanical parameters. The test is not designed to be used to detect subtle properties of the film. Of particular note is that these results represent one fixed load. Meaning that for each film the penetration depth will remain relatively constant. Between test samples the penetration depth is not consistent. This creates a problem because, as discussed previously, Briscoe [120] and other authors [131] have highlighted that investigation of polymer surfaces show that they often exhibit surface properties that differ from the bulk material. Additionally the work of Sharples et al [11] on castor oil mentions the production of a large array of oxide products at the air film interface. It is therefore likely, even expected that the properties of these films may differ at the surface.

4.1.2.2 Dynamic indentation: oscillating the loading force

Nanoscopic dynamic mechanical analysis (nanoDMA) or dynamic indentation is a way of continuously measuring the apparent mechanical properties of materials. In this subsection the nanoDMA is applied during the loading of the indentation in order to measure the apparent mechanical properties as a function of depth. The literature shows it has been used across a wide variety of materials with elastic, plastic and viscous properties [102, 110, 114, 131, 135]. Therefore it represents a promising technique to apply when trying to understand the polymeric nature and oxide layer of these baked oil films.

Figure 4.8 and figure 4.9 show the apparent properties of two baked oil films measured as a function of depth via nanoDMA indentation. The apparent or measured hardness and storage modulus are plotted. There is an extremely large apparent surface effect. For the

first 500 nm the data for both modulus and hardness could be modelled as a function of the inverse of penetration depth. This inverse law is in agreement with the results summarised by Briscoe [120]. The inverse trend is not fully understood however for complex, branched polymeric materials the hardness and modulus data is often seen to vary with the inverse of contact depth. Linear chain polymers (those with little or no side chains) do not show a significant trend. The complex reactions during baking are thought to cause complex branching of the molecules in castor oil hence the oil could not expected to be made up of linear molecules.

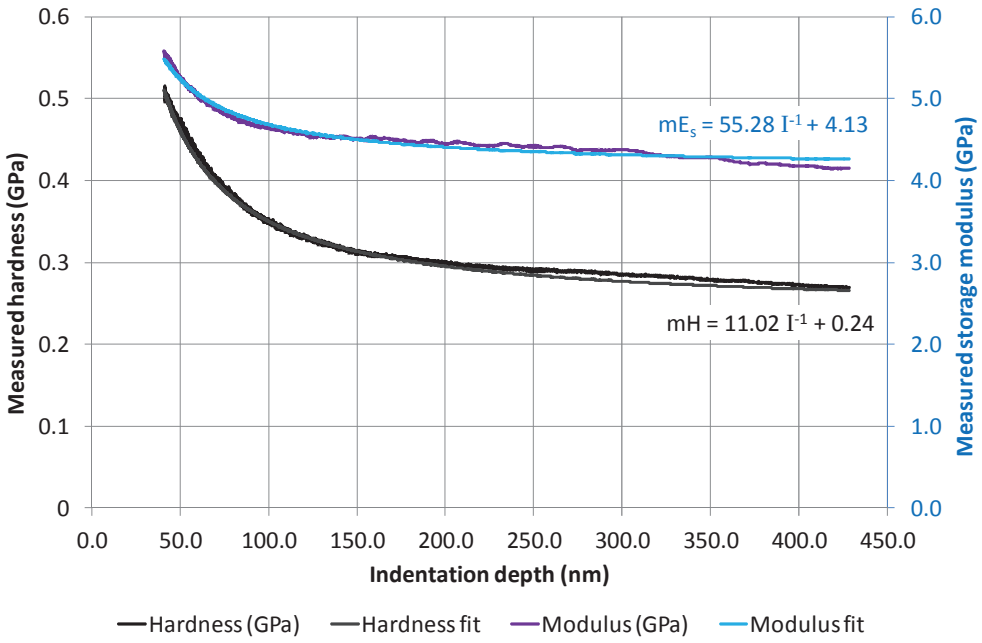

Figure 4.8: Measured DCO film hardness and storage modulus as a function of indentation depth for a hard baked oil film. The measurements were made using a DMA method set out in the method subsection 3.2.8 up to a maximum load of 1 mN. The oil film was baked at 200^{0}C for 1.5 h and measured after 9 days. The film was measured by the laser profilometer to be 20 µm thick

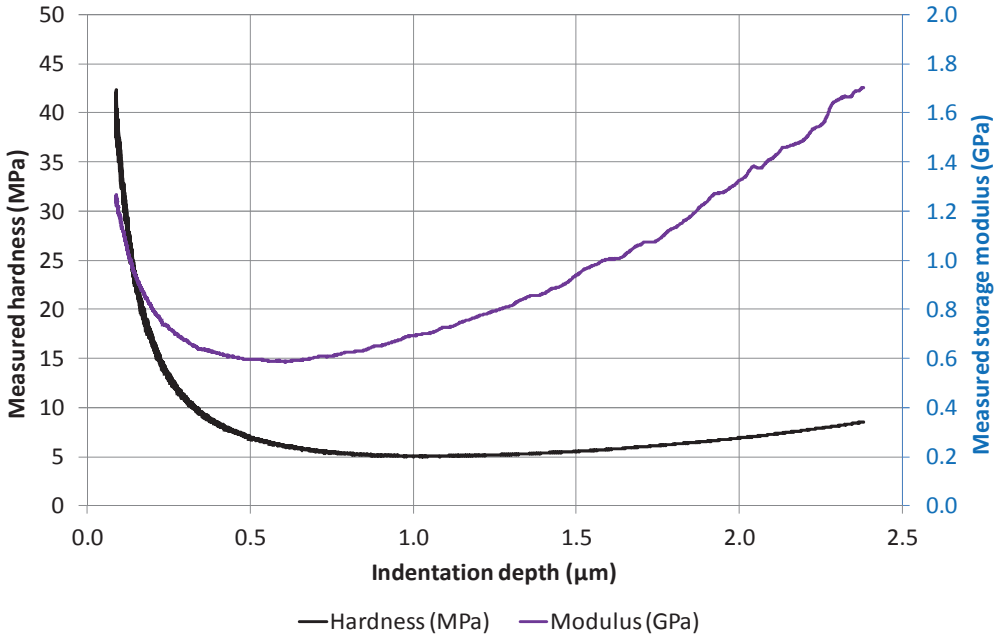

Figure 4.9: Measured DCO film hardness and storage modulus as a function of indentation depth for a soft baked oil film. The measurements were made using a DMA method set out in the method subsection 3.2.8 up to a maximum load of 1 mN. The oil film was baked at 150^{0}C for 1.5 h and measured after 9 days. The film was measured to be 24µm thick

At greater than 1 µm the mechanical properties shown in figure 4.9 are best described as increasing with the square of the penetration depth. The square of the penetration depth is an area. The most likely cause for the rise in properties is that the interaction with the underlying substrate is beginning to impact the results. These measurements of the mechanical properties of soft polymers as a function of depth require closer examination as there are three primary erroneous effects that could be influencing the trend seen in figure 4.9.

Firstly there is the problem that the material in the contact area is not the true indentation volume. This point was discussed earlier in subsection 2.3.6 and means that total

indentation volume includes material at a distance beyond the volume simply displaced by the probe. This is often quoted as being approximately 10 times the contact depth and width. The stiffening of the surface with depth at >1 μm suggests that this effect might be significant for this film. However the effect may be due to the fact the film itself is getting stiffer with depth. Such an effect may be possible if the catalytic effect of the substrate [11] leads to stiffer material close to the surface of the metal. Interpreting the true mechanical properties from the apparent properties as a function of depth would require a process of mathematical finite element modelling. This process is complex but is possible and would require a significant research investment in order to insure that the tip and surface are properly modelled. This work is outside of the scope of this project. Overall gaining an appreciation of what will be terms as "the apparent" mechanical properties was deemed the most important task. This approach is taken because the apparent mechanical properties are the ones that a wear particle will experience, which is of primary interest to this project.

Secondly there is a possible problem of adhesion. Again this is a phenomenon that has been discussed previously. However adhesion is likely to be an insignificant problem here as the relative motion of the indentation probe used in DMA is only a small fraction of the indentation depth. This means that the change in volume is likely to be minuscule meaning any adhesion effect is likely insignificant.

The third problem with indentation test arises with the use of DMA testing. DMA testing is based on several fundamental assumptions. In particular the calculations of mechanical properties relies on the phase angle of the response being away from the resonance

behaviour of the surface. To illustrate this problem a soft film was measured via nanoindentation, as shown in figure 4.10. The hardness data is negative for depths -1.4 µm. It is clear that this is not a real effect. The behaviour of the phase angle shows that the response of the probe is out of phase with the input force, showing the system is oscillating past a resonant frequency.

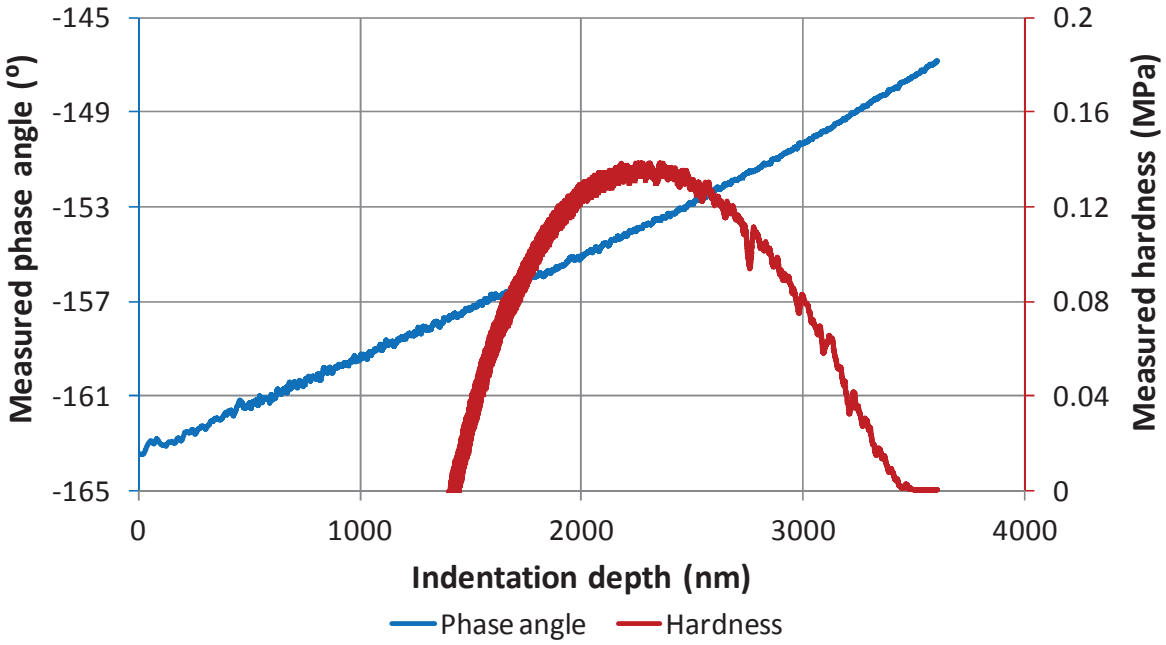

Figure 4.10: The measured phase angle and hardness of a soft film measured by dynamic indentation. The measurements were made using a DMA method set out in method subsection 4.1.2.2 up to a maximum load of 1 mN. The oil was baked for 60 minutes at 100 ^{0}C and measured after 74 hours. The film was measured to be 24µm thick.

4.1.2.3 Dynamic indentation: frequency sweep during the holding segment

As both loading DMA and standard unloading curve fitting present potential problems, a frequency sweep method is investigated. This method uses the frequency sweep function in order to derive a material stiffness and subsequently calculate a mechanical modulus.

Frequency sweeps on polymer materials are commonly used to investigate materials that exhibit frequency dependant elastoplastic behaviour such as polyethylene. This behaviour arises because the polymer motion is stimulated by the force oscillations. Molecular motions may also be limited at certain frequencies due to the vibration of the polymer "locking" the system. In order to measure the elastoplastic frequency response, the frequency is varied and the corresponding mechanical properties calculated from the phase angle and amplitude of the response (see section 2.3.6.2). This technique could be used to measure the mechanical properties of the hard baked oil films, such as those shown in figure 4.11.

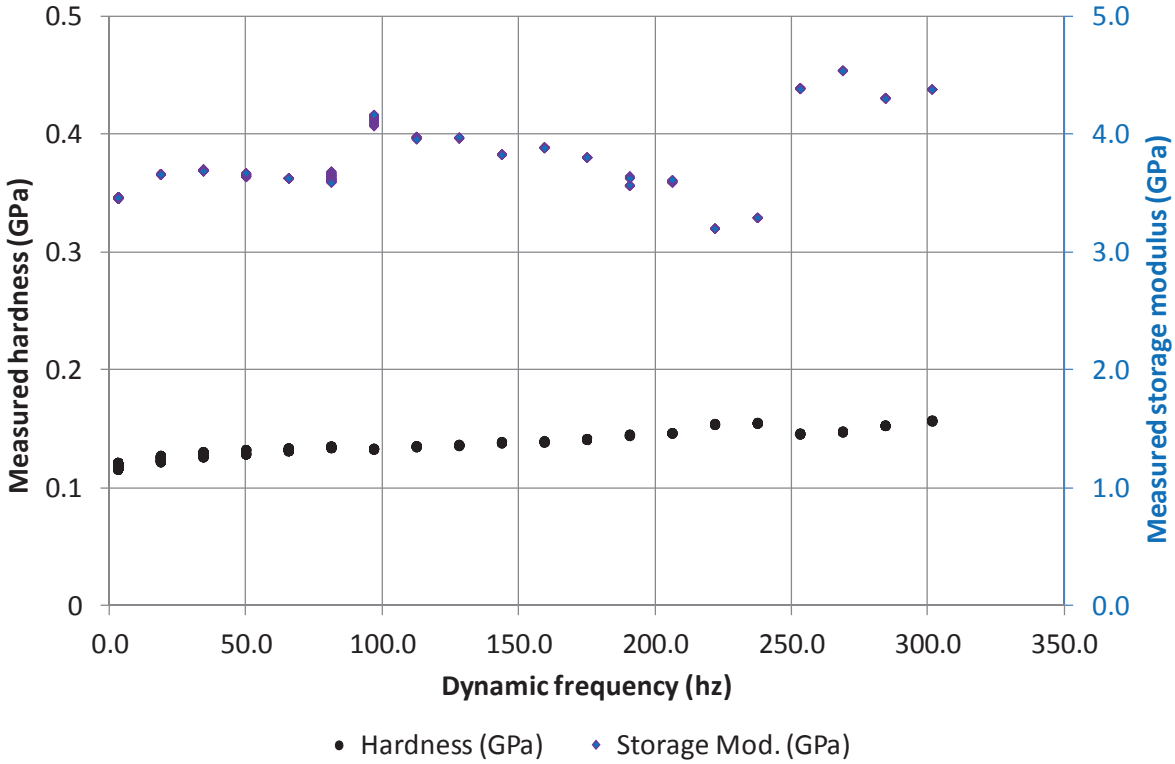

Figure 4.11: Measured DCO film hardness and storage modulus as a function of indentation frequency with a static 1 mN load. The film is representative of a hard baked oil film. The oil film was baked at 200^{0}C for 1.5 h and measured after 9 days. The film was measured to be 20 µm thick and is the same film used to collect the data in figure 4.8.

Figure 4.11 shows that at high frequency (> 250 Hz) the modulus is similar to the modulus of figure 4.8. However at other frequencies the data is not comparable and the hardness is consistently below the previously calculated values. The hardness appears to increase as a function of frequency. There is a general increase of modulus as frequency increases; however there is a discrepancy in this trend at 100 Hz and between 200 and 250 Hz. In order to investigate the information gathered by a frequency sweep further a soft film is indented, as shown in figure 4.12.

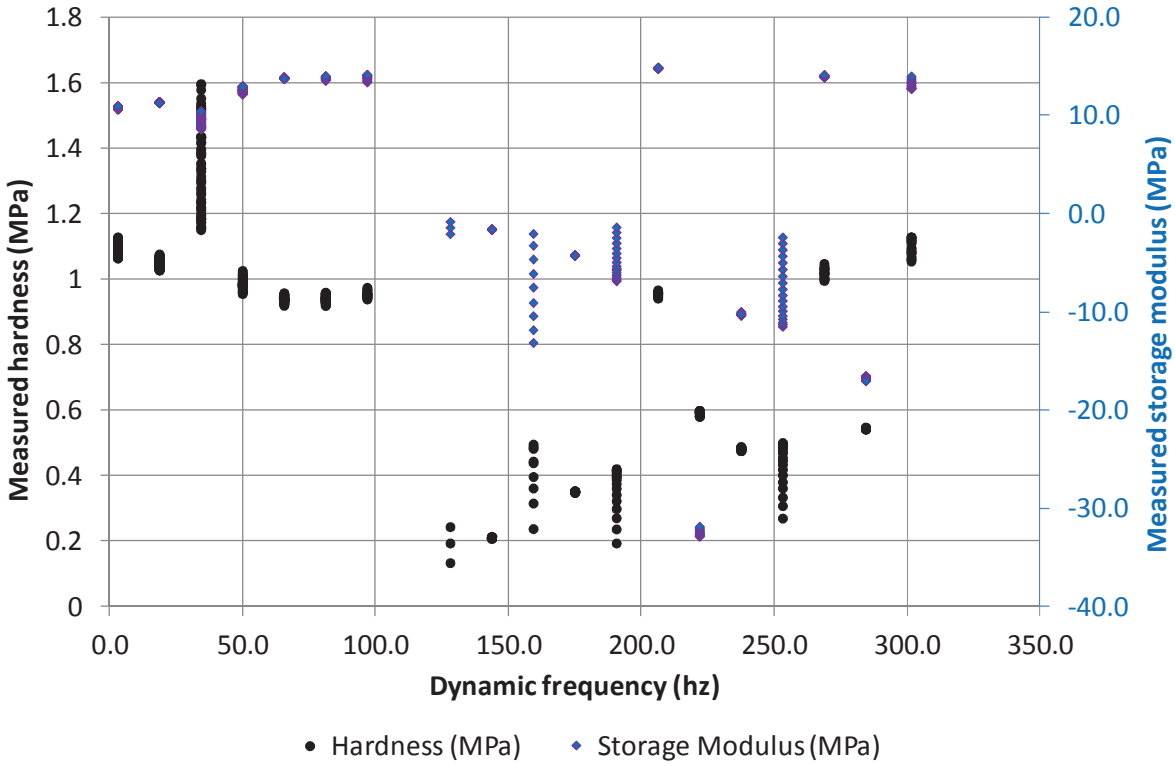

Figure 4.12: Measured DCO film hardness and storage modulus as a function of indentation frequency. Data taken with a static 1 mN load. The film represents a soft baked oil film. The oil film was baked at 100^{0}C for 1.5 h and measured after 9 days.

Figure 4.12 clearly shows that the application of a nanoDMA frequency sweep to a soft film does not seem to work as well as for the harder films. This may suggest that, similar to the indentation nanoDMA in the previous section, the method is not suited to dynamic measurement. However the corresponding phase shift and displacement amplitude data in figure 4.13 suggests a known phenomena. In particular the forced oscillation is impacting a resonance on the system as a whole.

As mentioned previously the process of DMA calibration automatically generates values for the stiffness and coefficient of dampening of the indenter using an air indentation method. In order to find the properties of the surface a similar method is used. The probe is first indented at a fixed load. The load is held to try and allow for creep into the surface. An oscillation is applied. In this case the frequency of apllied oscillation starts at 301 Hz and is reduced to 3 Hz.

The raw data is first filtered to remove outliers and anomalies. In particular anomalies present in the contact depth are removed. Indentations that are more than an order of magnitude above or below the average penetration depth are removed. The penetration depth may be become unusually large or small due to disconnect between the indenter tip and the surface. This problem occurs near to the resonant frequency and above. The most probable reason for the probe disconnecting from the surface is the phase angle between the input force and displacement being large. Disconnect between the probe and surface presents a problem in two ways. Firstly when the probe disconnects from the surface it is free to move with low impedance and so the displacement may be larger. Secondly when

the probe reconnects with the surface its phase and amplitude are not in equilibrium. The indenter is therefore subject to transient oscillatory behaviour and the measurement response is not readily predictable. Measured properties such as amplitude in this case are effectively random because the system tries to measure a steady state oscillation.

Filtered data from the frequency sweep is fitted to gain the stiffness and coefficient of dampening. Then the sample stiffness and dampening can be gained by simple subtraction of the calibration parameters. Once the sample stiffness is known the modulus can be calculated.

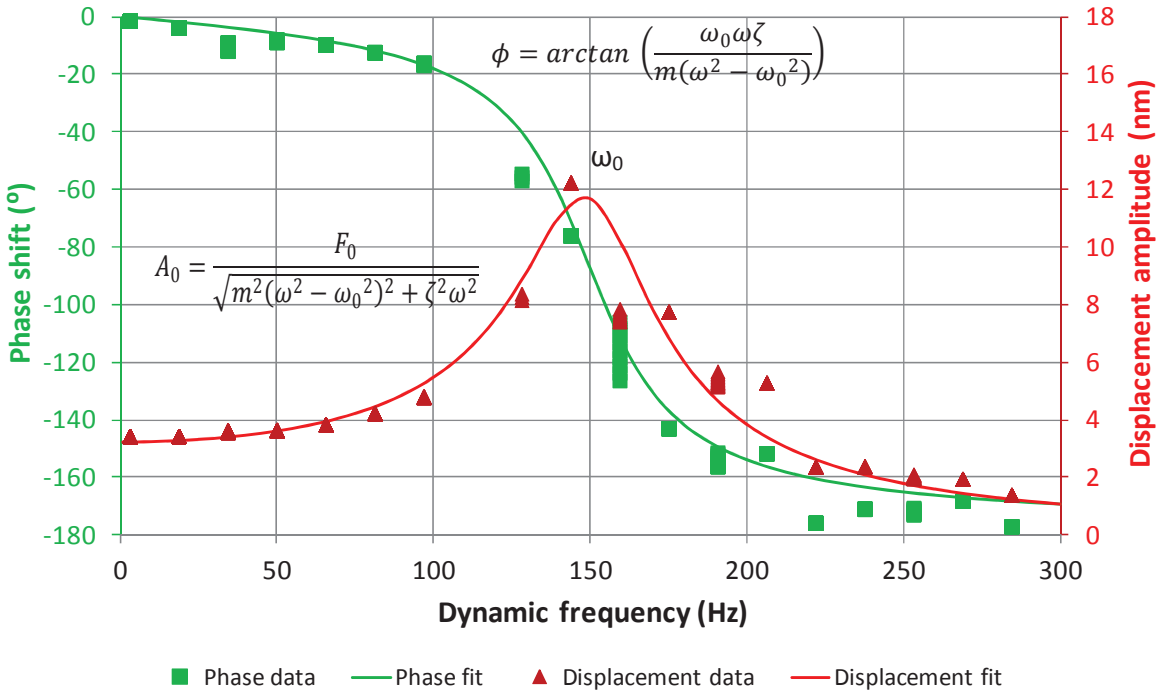

Figure 4.13: Measured phase difference and displacement amplitude as a function of indentation frequency. Data taken during a static 1 mN load for a soft baked oil film. The oil film was baked at 100^{0}C for 1.5 h and measured after 9 days.

An example of this fitting technique is shown is figure 4.13 for the raw data used in figure 4.12. The fit shown to the data shows an elastic modulus of 11.3 MPa and a calculated

hardness would be 0.14 MPa. For comparison a 20 % - 95 % fit to a quasistatic unloading curve would give an elastic modulus of 10 MPa and a hardness of 1 MPa. Clearly the modulus data is in good agreement, though the hardness is not comparable.

The most likely cause for this discrepancy is that the probe is held under oscillatory load for a long time in this test. This allows the probe to creep into the surface and increase the area used for the calculation of hardness. It is assumed that the modulus and stiffness response calculated here should be purely elastic, there are two reasons for this. Firstly the probe is held to allow for plastic creep. Secondly the probe is oscillating into the surface, a process of loading, unloading and reloading. As described by Pharr the process of repeat indentation removes the plastic deformation [113]. Thus the calculated modulus and stiffness is elastic and not storage or complex modulus. That is not to say that the process is free from plastic response. Indeed the surface may yet exhibit frequency dependence. However, given the prevalence of the macroscopic resonance curve in this data a different method would be required to properly measure the effect of oscillation frequency on the elastoplastic properties. In particular, in order to measure the elastoplastic frequency response, the resonant frequency needs to be much higher than the study frequency in order to limit the effect of resonance on the results. Given the relation in equation 4.7 the obvious solution would be to use a lighter indenter tip and/or finding a stiffer setup. However finding such a setup is difficult as the design of ever smaller tip configurations is limited by mechanical constraints. With the current arrangement only a limited section of the softer film or a harder DCO film can be studied in this way.

Referring back to figure 4.12 a region of 3 Hz to 97 Hz is seen to be relatively clear of measurement defects. However, even here there is also a subtle problem just below 50 Hz where a slow drop in modulus and increase in hardness. Whilst dismissing the 34 Hz data, the modulus and hardness is seen to vary from 10 to 14 MPa and 0.9 to 1.1 MPa in this region respectively. Overall this data is in broad agreement with both the indentation technique and the modulus from the sweep technique. In order to identify the best values for the mechanical properties to use it is necessary to consider the response of harder DCO films to see how the results compare.

Figure 4.11 shows the typical data for a hard film. It does suggest a small increase in hardness as frequency increases. Though given the magnitude of the effect is only a 36% change in frequency of two orders of magnitude so the effect is much smaller than other systems that have been reported in the literature, such as LDPE. Specifically the data here suggests indentation hardness may best be described by a power law, albeit with the low index of 0.045. It is not possible to get a reasonable harmonic motion fit, similar to the method demonstrated in figure 4.13, to the frequency sweep data for these hard films. This is because the key parameters if the data are best studied near to the resonance and the data is too far away from the resonance of the system to get a reasonable fit. As the harmonic fit data cannot be taken for hard films, measurement of mechanical properties will focus on indentation and frequency calculations.

The calculated mechanical properties from the frequency sweep method shows good agreement with the quasistatic indent measurements for hard films. A fit to the unload

curve of the 200 ^{0}C data in figure 4.5 (which was prepared in the same way as the data in figure 4.11) gives a hardness and modulus of 0.12 GPa and 3.3 GPa respectively. This is not comparable to the range of 0.12 GPa to 0.16 GPa and 3.2 GPa to 4.5 GPa seen in figure 4.11 . In particular the value of the indentation properties is almost identical to the low, 3 Hz, frequency data.

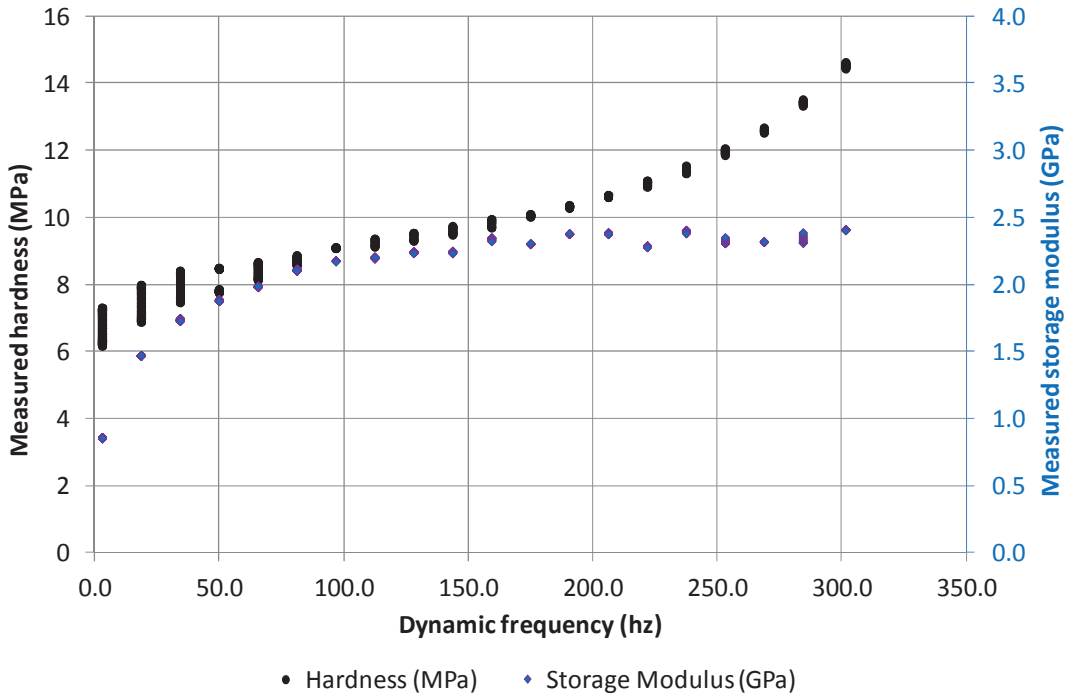

Figure 4.14: Measured DCO film hardness and storage modulus as a function of indentation frequency. Data taken with a static 1 mN load. The oil film was baked at 180^{0}C for 1.5 h and measured after 9 days.

For completeness the method needed to be applied to the transitional films produced at intermediate temperatures. Figure 4.14 shows the frequency sweep data for a film baked at 180^{0}C. The data shows a much larger range of values than in previous films modulus and hardness ranges being 0.85 GPa to 2.4 GPa and 6.2 MPa to 14.6 MPa respectively. This is in comparison to the quasistatic values gained from the data in figure 4.5 of 0.51 GPa and 7

MPa for the modulus and hardness respectively. Although the hardness at low frequency is comparable to the quasistatic indention, the elastic modulus is half here. This result may be due to the large adhesive effect seen at 180^{0}C. The adhesive effect makes calculation of the contact point during unloading harder (as discussed earlier). The large range may well be expected given that this film also showed a large deformation during the quasistatic hold period presented previously in figure 4.7. It further shows that the plastic deformation is most significant in this transitional film, compared to the soft elastomer films and hard glassy polymer films.

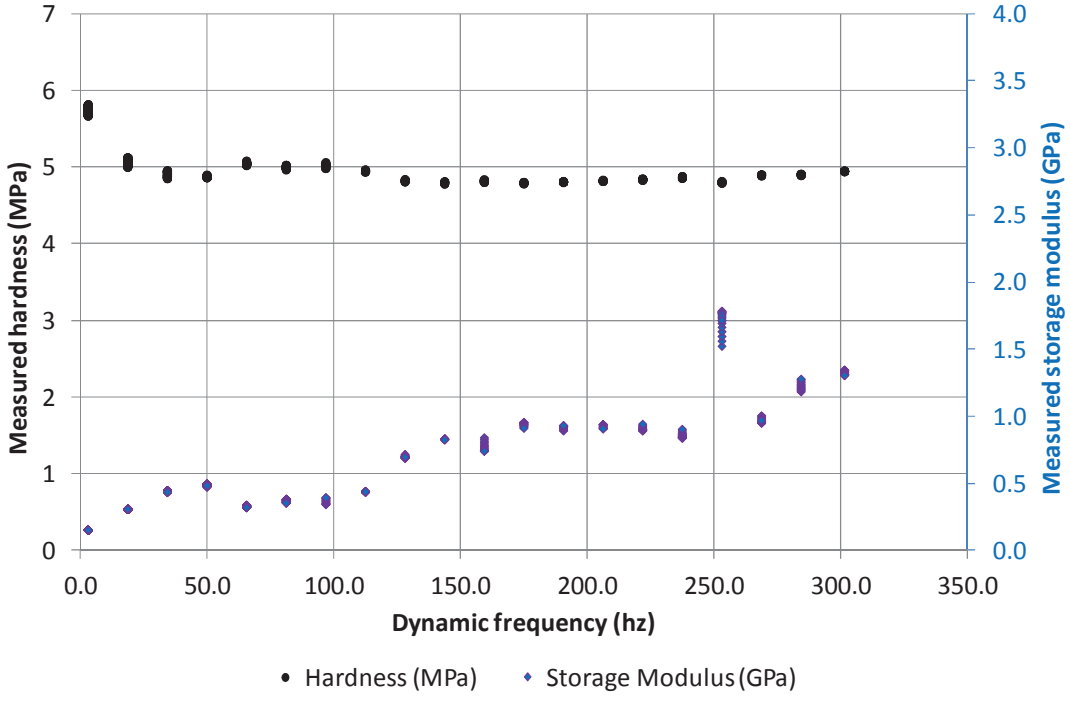

Figure 4.15: Measured DCO film hardness and storage modulus as a function of indentation frequency. Data taken with a static 1 mN load. The oil film was baked at 150^{0}C for 1.5 h and measured after 9 days.

It is also worth investigating the behaviour of films at 150^0C. Figure 4.15 and figure 4.16 shows oscillatory nanoDMA mechanical properties of DCO films baked at 150^0C for 90 and 60 minutes respectively. It is apparent that between these two baking conditions the films go from being too soft and exhibiting harmonic motion, to possessing sufficient stiffness to avoid harmonic motion. In both cases the modulus appears to increase with frequency. For 90 minutes of baking the quasistatic indentation data in figure 4.5 gives an elastic modulus and hardness of 95 MPa and 6.5 MPa respectively. The corresponding data in figure 4.15 has a range for the elastic modulus and hardness of 0.11 GPa to 1.6 GPa and 4.8 MPa to 5.8 MPa respectively. An equivalent quasistatic indentation for the 60 minute film gives a modulus and hardness of 19 MPa and 1.7 MPa respectively and the ranges in figure 4.16 (prior to harmonic motion effects i.e. 3 Hz to 82 Hz) are 15 to 25 MPa and 1.4 MPa to 2.2 MPa. At 150^0C the quasistatic indentation and frequency sweep, though not identical, show relatively good agreement particularly at low frequency.

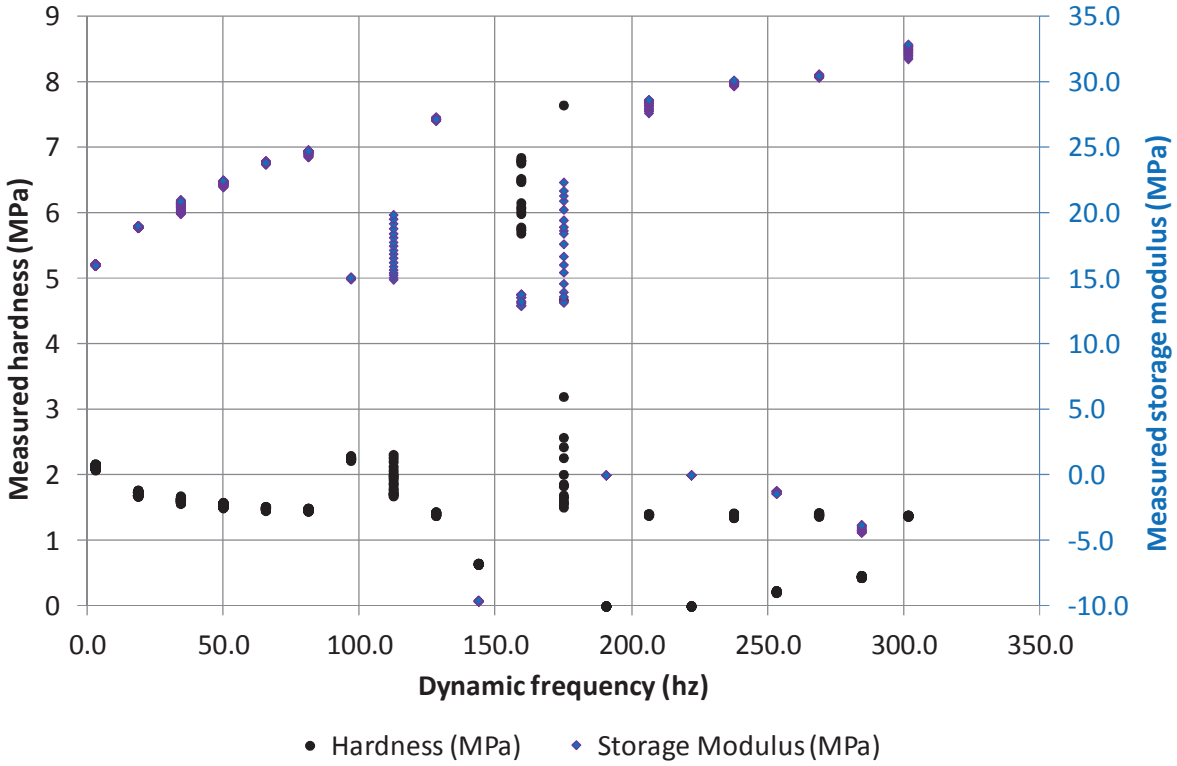

Figure 4.16: Measured DCO film hardness and storage modulus as a function of indentation frequency. Data taken with a static 1 mN load. The oil film was baked at 150^{0}C for 1 h and measured after 9 days.

Overall it has been shown that the low frequency sweep data (below 82 Hz) is in good agreement with quasistatic indentation. There is a significant problem with measuring the mechanical properties based purely on static indentation technique though due to adhesion. Adhesion appears to be a significant problem for the harder transitional films (as illustrated in the 180^{0}C data). Therefore the method of choice for quoting data is the frequency sweep method. In particular quoted mechanical properties will be based on the 3 Hz data. It is recognised that although (within the confines of these experiments) the low and high temperature films show a limited variation in mechanical properties, and conform to values typical of elastomer and glassy polymers respectively, the mid temperature films show a

wide variation. As the mechanical properties are variable in these intermittent DCO films care must be taken to not overly rely on the absolute values of the mechanical properties found.

4.1.3 Properties of films as a function of baking temperature

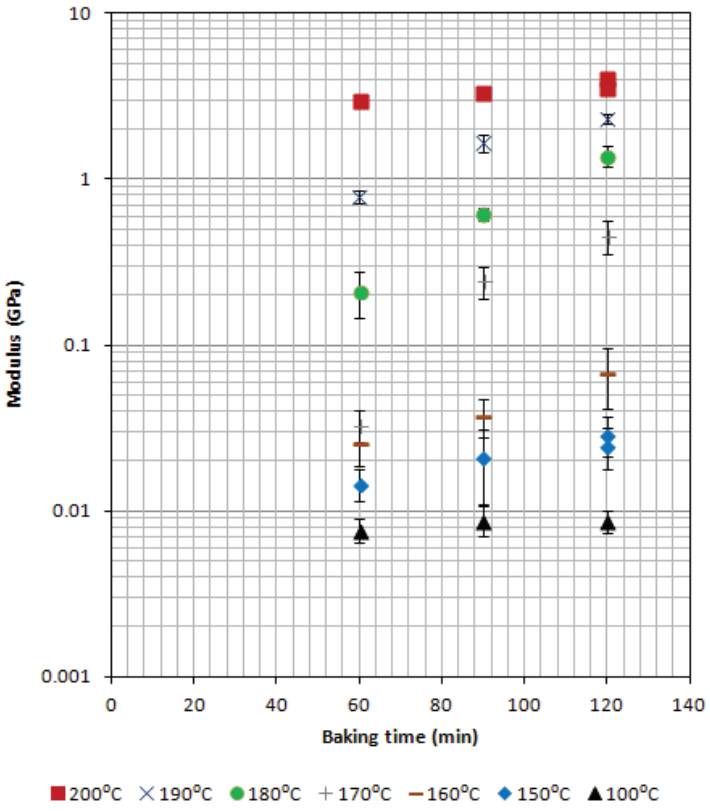

Figure 4.17: The effect of baking time and temperature on the storage modulus of the DCO film. Data used was low frequency, 3 Hz, dynamic oscillation measurements at a fixed load taken on the Hysitron 8.5 days after baking.

Figure 4.17 shows the measured storage modulus of the baked oil film. Figure 4.18 shows the corresponding hardness data to the modulus data presented in figure 4.17. Overall

elastic modulus increases as a function of baking time and temperature. At 100^{0}C the effect of time is very small and can easily be accounted for when the errors of the measurement are considered. The modulus is <10 MPa and hardness of ~1 MPa is comparable to that of a hard synthetic elastomer. The data suggests the 100 ^{0}C baked oil films are composed primarily of molecules with limited cross linking in the structure. Weakness in the structure may come not only from a low number of cross links but also contaminants such as oxides formed in the film.

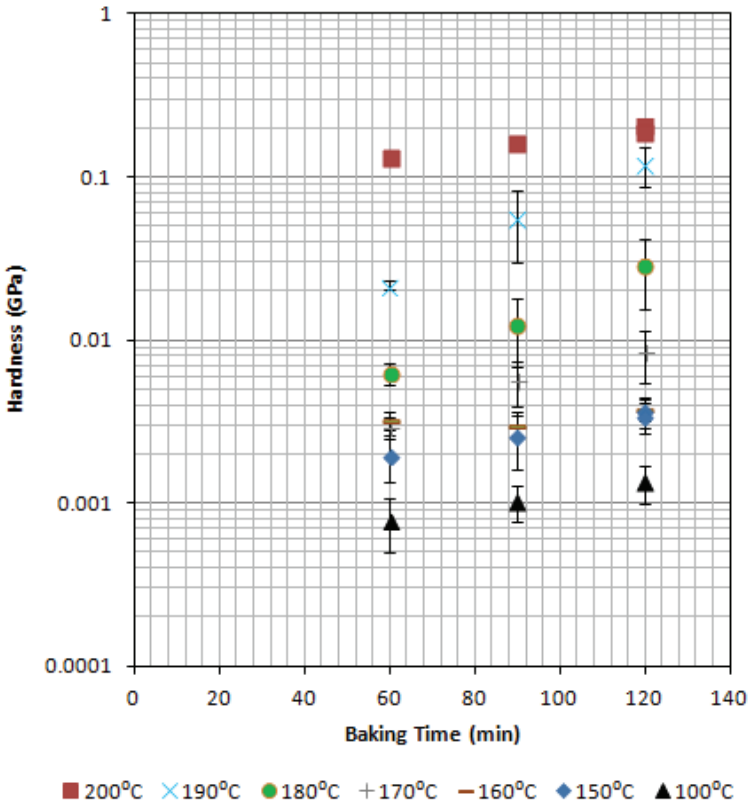

Figure 4.18: The effect of baking time and temperature on the indentation hardness of the baked oil film. DCO film indentation hardness corresponds to films used in figure 4.17

At 200^{0}C there is a steady increase in hardness and modulus as time increases. These trends cannot be accounted for purely by the standard deviation of the measurements. Although it is possible that the effect may be reduced when consideration is given to the repeatability of producing the oils films is considered i.e. the sample variation error will typically be ~20%. The modulus is >1 GPa and hardness of >100 MPa is representative of a hard plastic either crystalline or thermoset polymer. As the lower temperature film is elastomeric in behaviour, and the explanation of oil hardening is in terms of crosslinking, the film is most likely similar to a thermoset polymer in nature.

At 150^{0}C and 160^{0}C there is a more substantial effect of time on elastic modulus. Though the hardness at 150^{0}C and 160^{0}C is substantially higher than 100^{0}C, the effect of baking time and temperature is not substantial. However although the increase in hardness and modulus observed is within the sample deviation, the variation is large. This indicates that the film is transitioning, as discussed previously, so the film's measurement and even film production may not be as consistent as at other temperatures. Again it must be stated that the absolute values for these films may not be reliable. It is at 170^{0}C to 190^{0}C that is there is a major change in both the hardness and modulus as a function of time. The significant increase at circa 180^{0}C suggests the activation energy for a thermosetting reaction is surpassed.

Overall oil films baked at 100^{0}C, 150^{0}C, 180^{0}C, and 200^{0}C present a suitable range of material properties for further testing in this chapter. As the patent literature [19, 20, 170, 195] contains references to oil films baked at 100^{0}C for 60 minutes this represents the primary focus for the later sections of this thesis. However, the 100^{0}C and 60 minute baked oil film here was left for a much longer time (~9 days) than samples in the literature cleaning

tests: indeed the cleaning tests in the literature were often conducted on the same day, with a sample aging for only 1-5 hours. Figure 4.3 shows that films used after a short time are much softer than the films used here. However, problems with making and conducting a repeatable experiment after only a few hours confirm the decision to test multi-day aged samples.

4.2 Wear of a baked oil film

The discussion so far has concerned the mechanical properties of the baked oil film as they are deemed to be of primary interest. Aside from the change in mechanical properties, changing the baking conditions influences other properties of the DCO films in particular the density and optical properties. Due to the nature of the measurement density cannot easily be measured directly. It would require a full scan of both the steel surface and the DCO film surface to get a total oil volume for the density and be of limited value. Therefore it has not been quantified in this investigation. Hence the wear is measured purely as a volume method. It is worth noting that there are two primary methods for determining a wear amount, mass and volume. It should be clear therefore that when comparing two DCO films prepared in different ways that the wear rate in terms of mass may show a different trend. Also the results should not be compared to wear data that relies on mass without care being taken to ensure that the measurements are comparable. The volume method is dependent on refractive index and so the optical refractive index were quantified for this investigation prior to their use in the analysis.

4.2.1 Basic wear behaviour

Before the wear behaviour as a function of mechanical properties can be understood it is important to understand the basic wear behaviour of the DCO film. Hence this first investigation looks at the wear as a function of its primary variable: sliding distance.

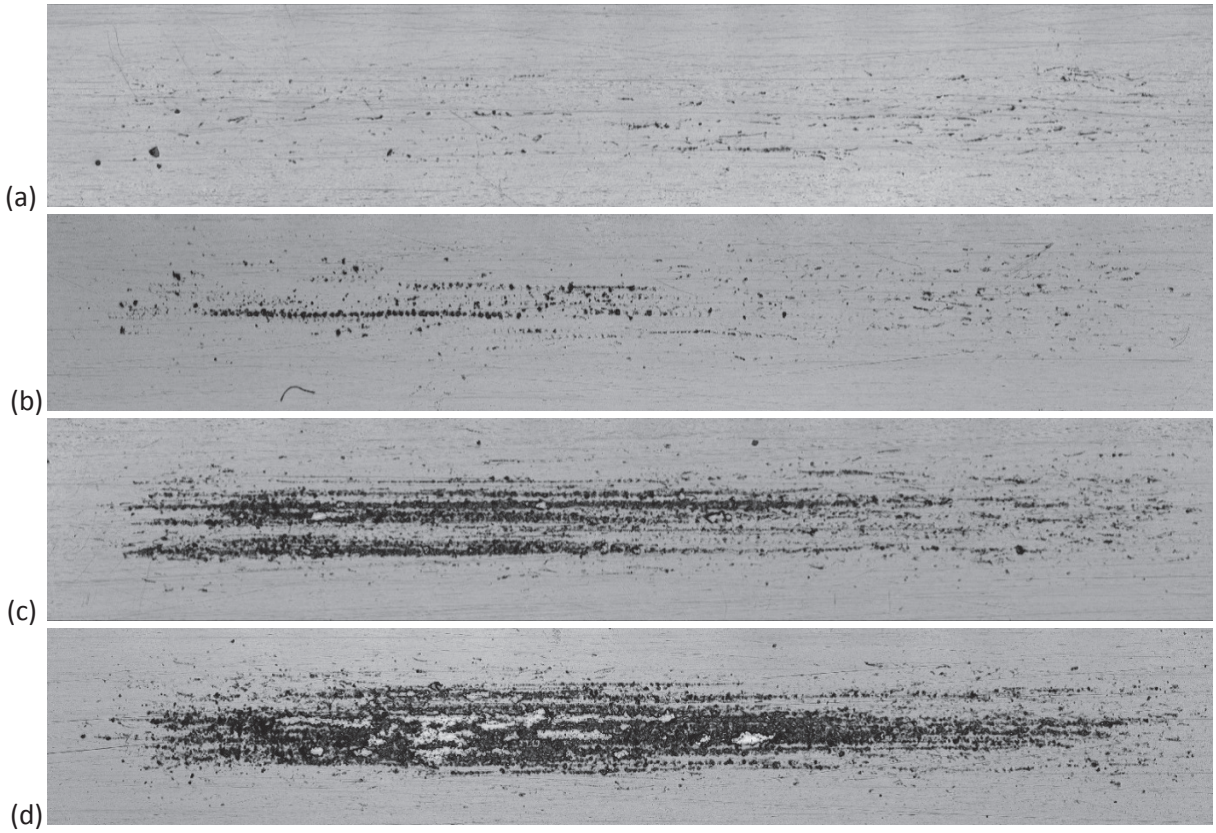

Figure 4.19: Optical microscopy of damage at different sliding distances. Sliding distances are 12 mm (a), 60 mm (b), 120 mm (c), and 240 mm (d). All images are to same scale: the horizontal field of view is 13.6 mm. d = 62 μm, η_0 = 0.02 Pa.s, W = 0.196 N, u = 7.6 mm.s^{-1}, and C = 8.4%.

Figure 4.19 shows that an increase in sliding distance results in more visible wear on the surface of a baked oil film. In all these optical images (and throughout the thesis) the left of the image is the starting point for the motion and seems to show slightly higher amount of wear. This may be as a result of an increase in wear rate when the motion is initiated.

Figure 4.20 shows the corresponding profilometry data to the images in figure 4.19. Data is gathered by scanning a 1.2 mm section in the centre of the sample using seven equally spaced lines. The accuracy of the experiments can be improved by increasing the number of scan lines. However, increasing the number of line scans increases the time needed to scan a sample. Overall the number of line scans is a trade off between the amount of time to scan a sample for accuracy and maximising the number of samples studied.

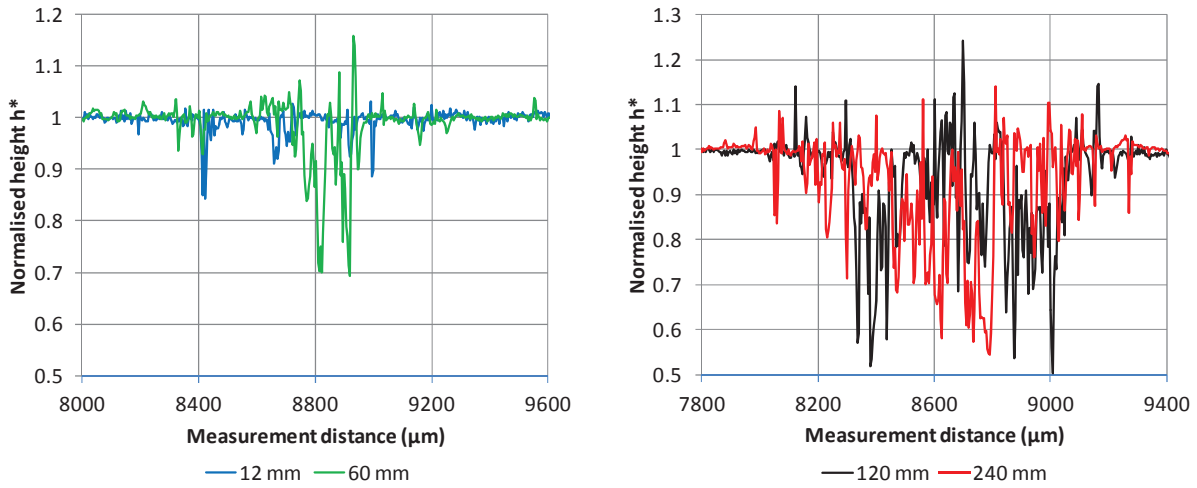

Figure 4.20: Cross-sectional profile of the averaged (over 7 lines) and normalised damage at different sliding distances. d = 62 µm, η_0 = 0.02 Pa.s, W = 0.196 N, u = 7.6 mm.s^{-1}, and C = 8.4%.

As expected, figure 4.20 suggests a longer sliding distance gives an increase in the amount of damage. The data is quoted in terms of a normalised height rather than a true height before and after wear. The true height of the oil film before wear varied between 20 and 25 µm and may contain height defects or waviness, which may be confused for wear features. To aid clarity the height before wear is set to one at each point and the wear scaled by this data. Hence the resulting data is in terms of normalised height, h*.

The data from figure 4.20 can be quantified in terms of a wear volume. A wear volume is calculated taking each line as containing a representative sample of the height change. Each height change is summed over the wear track width to give an area removed. The area removed is multiplied by the length of a single stroke to give a wear volume. Then an average wear volume is calculated from the set of volume data. Variance in the data can be calculated as the standard deviation of the volume removed. Measurements of the volume of material lost are repeated for multiple samples at different sliding distances. Samples are not reused as it would introduce a variability that would be hard to quantify i.e. multiple start ups, wetting, drying and other influences on system evolution. Measurement distance shown in the graphs is the distance from the start of the laser scan profile and is arbitrary. Due to the repeatability of film production and positioning the wear pattern often shows little shift between measurements. The graph in figure 4.21 shows the effect of repeated sampling at different sliding distances for data, including that shown in figure 4.20.

The wear rate of a sample is the gradient of the linear region in the wear data. This approach is not only the most straightforward to apply but it is also supported by being the foundation of wear equations in the literature, principally the Archard wear equation (see section 2.5). Linearity was found to occur in the data after a few initiation cycles and continued until the wear process reached an end point. The graph in figure 4.21 shows a typical example of these wear stages. Once the linear region is found data is fitted and a standard error calculated using a least squared method. Figure 4.22 shows the corresponding friction data gathered during these wear experiments.

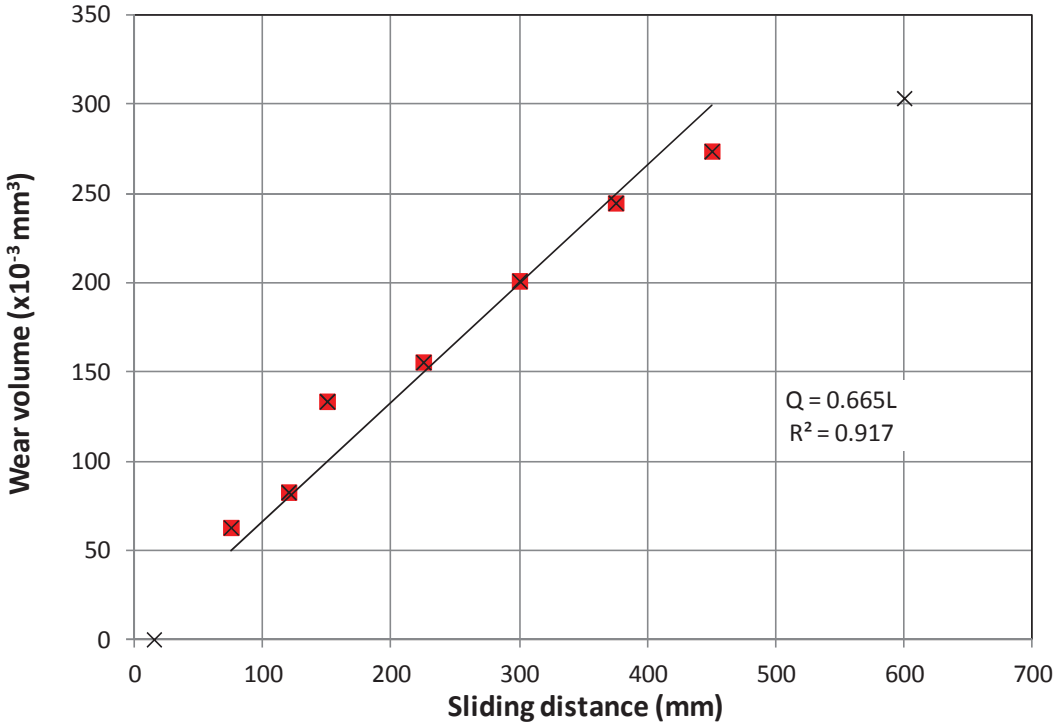

Figure 4.21: Wear volume as a function different sliding distances. Highlighted data points are used for the fit and other points are excluded from the fit. d = 62 µm, η_0 = 0.02 Pa.s, W = 0.196 N, u = 7.6 mm.s^{-1}, and C = 8.4%.

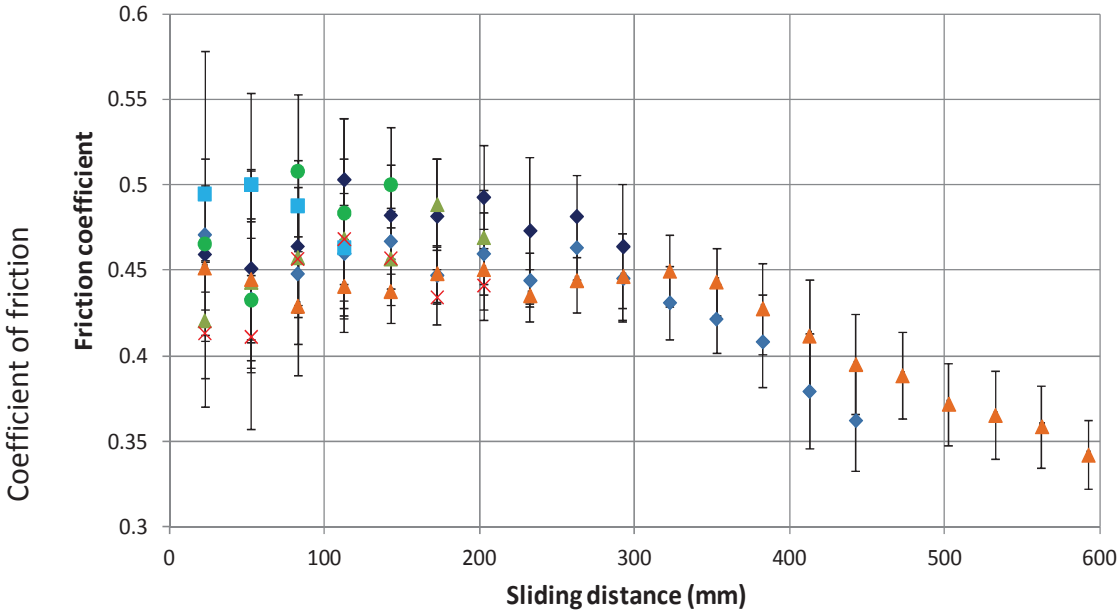

Figure 4.22: Coefficient of friction as a function of sliding distance. The different sets of points denote the friction obtained by separate wear experiments. d = 62 µm, η_0 = 0.02 Pa.s, W = 0.196 N, u = 7.6 mm.s^{-1}, and C = 8.4%.

In the literature wear rate multiplied by load is characterised by either a volume removed per unit sliding distance or an area of material removed per pass or cycle [57]. As the wear volume is calculated with a factor of the length of a sliding distance, the wear rate given here in terms of volume removed per unit sliding distance and is equal to the area of sample removed per number of passes. In order to make it clearer the exact sliding distance, which is fixed and recorded at the start of a series of tests, is set at 12mm though in reality there was approximately a 0.5mm deviation in the length. In reality it is only the number of passes over the central measurement region that is important. Where the total sliding distance, *L*, is quoted the number of passes can be calculated easily by divided by 12mm.

There was often an initiation stage observed during this investigation, where very little material is removed or in some instances material appears to be added. Instead observations of the first few passes often show that material is being displaced rather than removed. This suggests that the process of wear requires some amount of “conditioning” of the surface in terms of roughing and /or introducing surface strain and /or tearing. The data in figure 4.20 and figure 4.21 suggests that this has occurred in the example data, as the first (15mm) point shows practically zero wear. However it is clear from the data in the main trend can be fitted through the origin. The point is treated as an anomaly as the deviation is negative indicating at least one of the height profiles shows a build up of material.

This initial stage is also characterised by a greater variation in the friction as shown in figure 4.22. The variation is likely due to the indeterminate nature of the initial wear. The

coefficient of friction then becomes steadier as the wear becomes more linear. Finally the end process is characterised by a reduction in the friction, indicating fewer wear events or rather and smoother motion of the probe.

In the literature an initial transient is seen [196-198]. However the behaviour described is that wear rate decreased with sliding distance. This work is not immediately comparable as the behaviour was found in erosion rates for hard brittle ceramic and glass material, which are expected to be quite different to the three body abrasion of soft polymers here. However the work is of interest as the authors theorised that the reason for the initial high wear rate was that many of the surfaces contained pre-existing cracks or a surface roughness features different to those produced by the erosion. Once the wear was is a steady state the erosion relied on those cracks and asperities produced by the erosion process, hence the wear rate changes. For the oil surfaces in this study there it is unlikely that the virgin oil surfaces contain any surface defect, limiting the initial wear. Later the wear rate can develop linearly as grooves and asperities give purchase for the wear particles to operate on, whilst the wear produced new grooves and asperities to operate on.

The fact that the data enters is a linear trend is interesting. In the more widely studied subject of two-body wear the Archard equation is derived from a simple asperity contact theory for the contact between two surfaces. Three-body wear relies on particle capture by the countersurface before the wear process can begin. This means that fundamentally, the mathematical nature of the wear process is dependent on the nature of the particle capture. Capture of particles intuitively seems to be a statistical process, dependant on the flow of

the fluid, and concentration and size of the particles. In particular it relies on particles repeatedly being drawn into the contact zone and /or not being permanently pushed out of the sliding path of the probe. As a linear wear relationship is observed it suggest that a significant number of particles are not lost from the sliding path and that particles are repeatedly drawn into the contact region. This particle capture cannot be witnessed directly due to the opaque nature of the surface, fluid and countersurface. However the role of particle capture was investigated further and will be discussed in a later section. As schematic diagram summarising the possible wear mechanisms is shown in figure 4.23.

This random nature of the wear provides an alternative explanation to the initiation behaviour. As the wear relies on a random particle /surface interaction the lack in wear material at low sliding distance may be due to either a low number of interactions or a low sample of the interactions. The former hypothesis means that the first passes do not create enough wear to impact the measurement. Investigating this would require direct observation of the wearing, which is not possible due to the opaque nature of the components parts involved in the wear process. The later explanation would mean the phenomena are a result of the relatively low number of lines in the sample size. This explanation is easy to investigate as it only relies on inspecting a selection of samples with more lines to check the wear is being characterised correctly. As part of the preliminary work to this investigation the number of scan was varied and found not impact on wear rate significantly once ~4 lines were taken in a 1 mm track length.

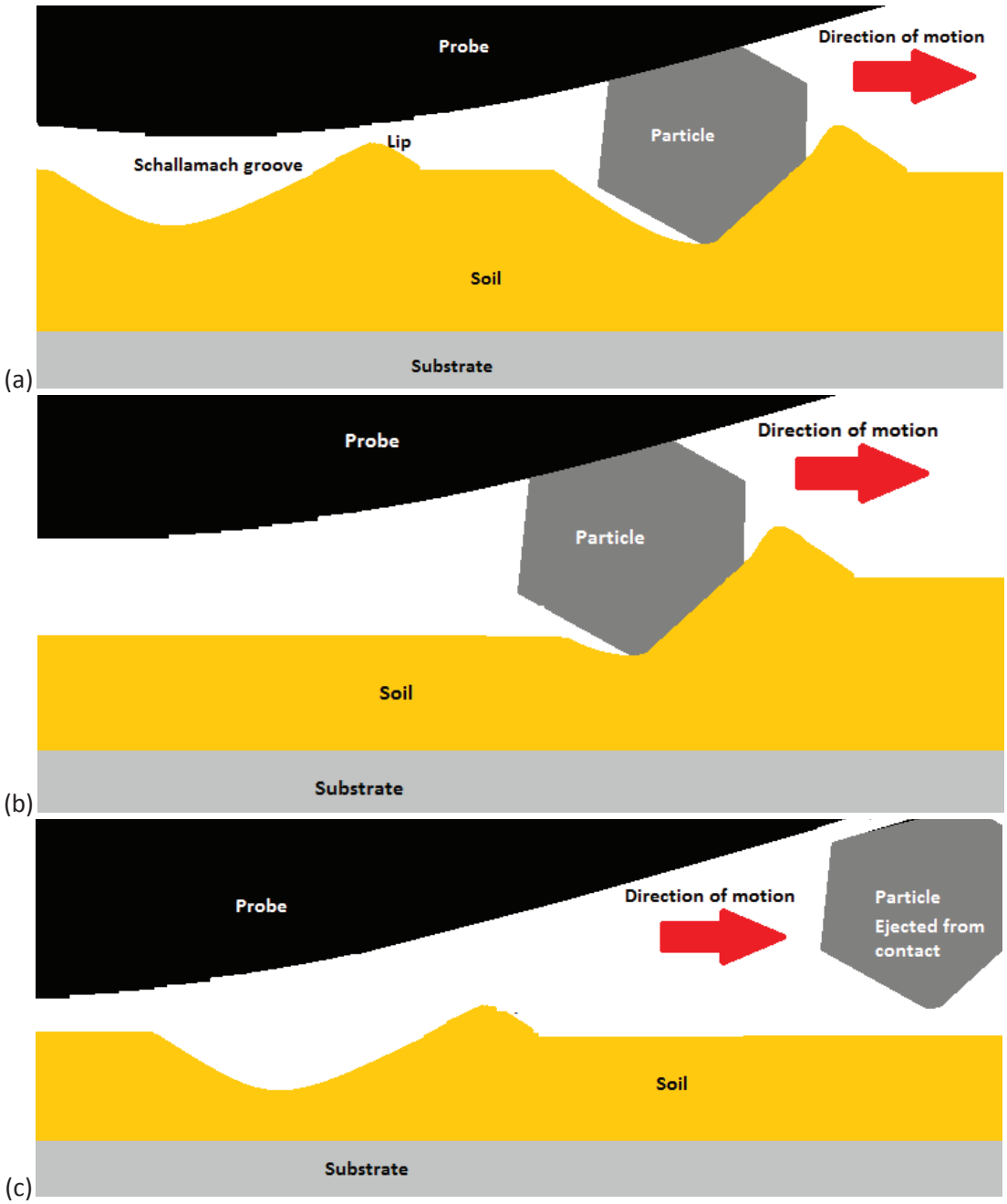

Figure 4.23: Schematic diagrams of main particle wear mechanisms expected in this three body abrasion. All diagrams are in cross section. (a) Representation of Schallamach wear. Material is deformed plastically and once the pressure in front of the contact is sufficiently high the contact particle slips and the wear process starts again. (b) May be cutting or plowing wear. This type of wear is only expected in harder materials, where the particle is firmly held. In plowing material is being pushed away from the contact, forming ridges. Cutting gives continuous material removal. (c) Shows the possibility of single wear events followed by material removal. In softer materials this may be a Schallamach grove. If the material were more brittle the particle may chip the surface instead.

Two forms of end processes can occur, either a gradual limitation in the amount of material removed or a sudden increase in the material removed. Continual, linear wear until the film was removed was not observed in this investigation. A sudden increase in the amount of material removed is characteristic of delaminating of part or all of the baked oil film. Pure delamination can only occur if the shearing force from the particle is greater than the adhesive force binding a section of the oil to the steel surface. A limitation in the wear volume removal is seen to be reached in figure 4.21. Limitations occur because the wear material is finite and therefore it is less likely for particles to impact and remove the remaining material. It may be noticed that this is referred to as a limitation not a plateau. This is because although the amount of material is limited the process of removal is likely to occur stepwise i.e. when the amount of material is removed in discrete pieces rather than as a gradual, continuous process.

4.2.2 Effect of load on DCO wear

Archard theorised that the volume of material removed by wear is proportional to the load. It was suggested in the previous chapter that during a “middle” sliding distance the wear is linear and therefore possibly “Archardian”. Although the wear in part of the sliding distance appears Archardian, the overall wear equation is not and would require a modified form to account for particle capture and fine material effects. However, if this basic relationship underpins the wear of the three-body wear of a baked oil film, the wear volume should be proportional to load.

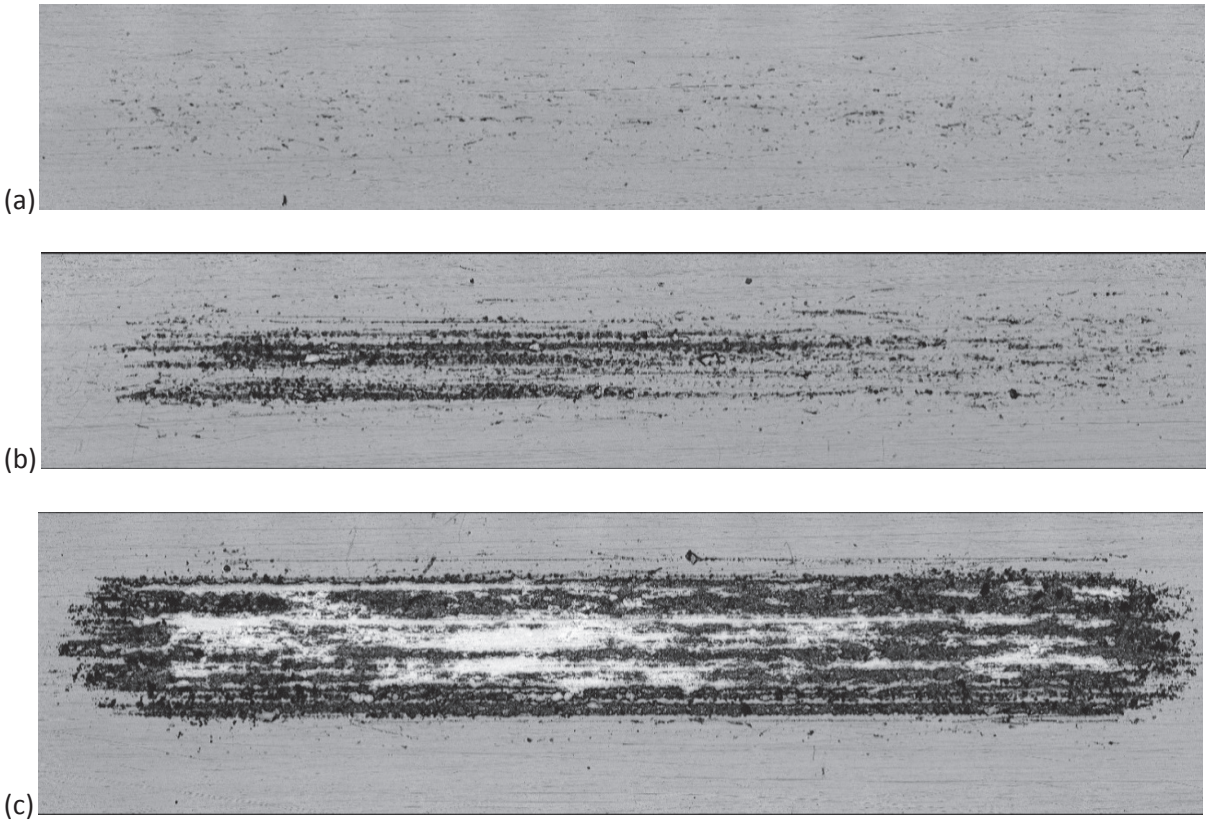

Figure 4.24: Optical microscopy of damage at different loadings. Loadings are 0.049 N (a), 0.196 N (b) and 0.981 N (c). All images are to same scale: the horizontal field of view is 13.6 mm. L = 120 mm, d = 62 μm, η_0 = 0.02 Pa.s, u = 7.6 mm.s^{-1}, and C = 8.4%.

Figure 4.24 shows the visual appearance of baked oil film wear produced by different loads in otherwise identical sliding conditions. These images show that an increase in load has a significant impact on the amount of wear. The images also show that as the load increases the nature of particle capture changes. Figure 4.24 (a) shows that at low load particles are only entrained for short distances of a few millimetres and do not maintain a continuous contact with the surface and countersurface. By contrast figure 4.24 (c) shows evidence of extended entrainment at high load, in some instances for 100 mm. Figure 4.24 (b) is an intermediate measurement both in terms of the load and the entrainment distances observed.

(a)

(b)

(c)

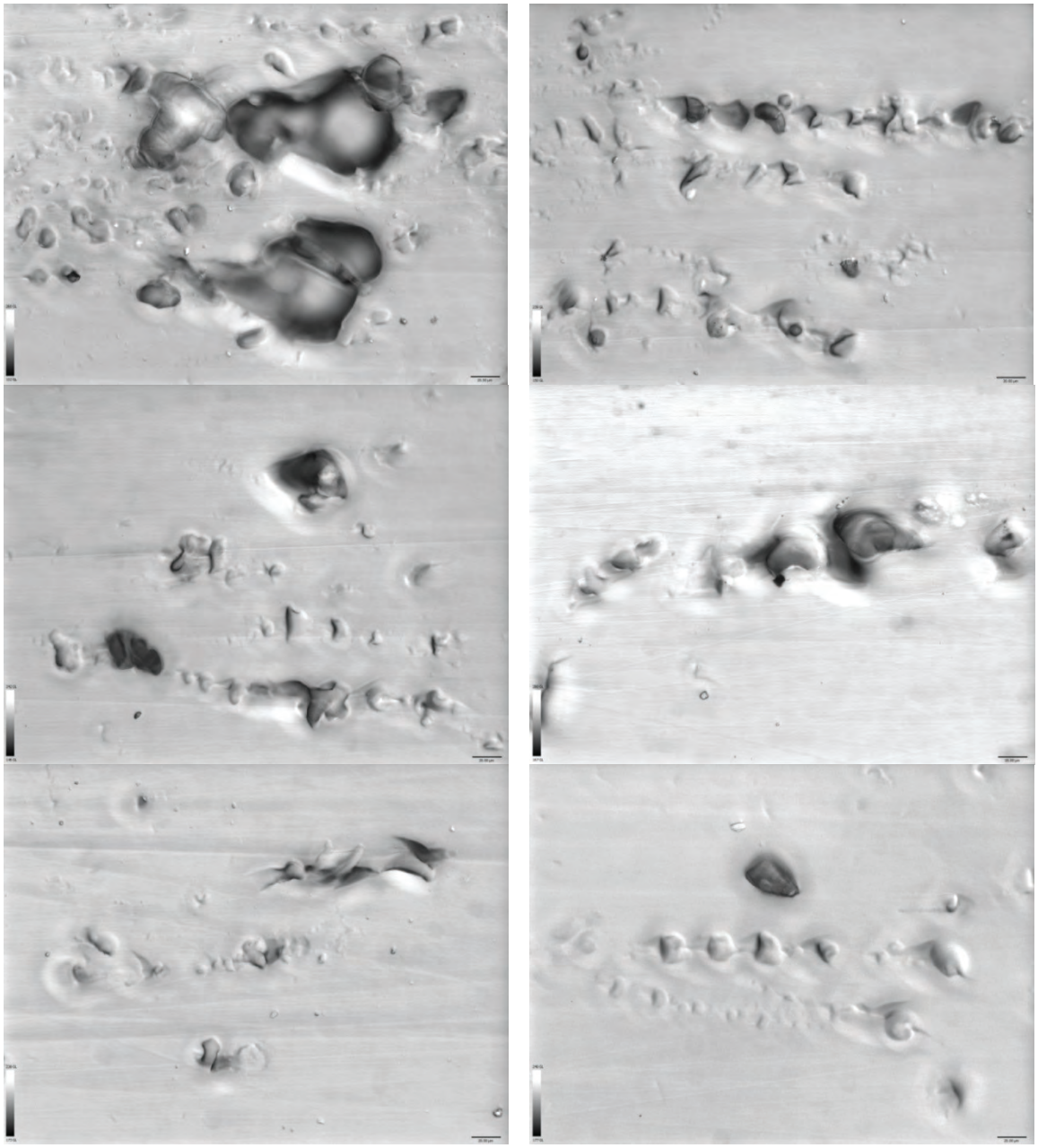

Figure 4.25: A collection of images showing typical wear features seen on the samples. Images are taken on samples where the sliding distance is less than 60 mm. All images show wear with d = 62 µm, u = 7.6 mm.s^{-1}, T = 100^{0}C, t = 1.5 h, C = is 8.4% and η_0 = 0.02 Pa.s. Values for W are: 0.196 (a), 0.098 (b), and 0.049 (c). The scale bars are 20 µm.

To further investigate the physical damage individual wear events are observed at a low number of passes. Typical images of the wear events are shown in figure 4.25. At low load figure 4.25 (c) shows material deformation in the form of ridges that are developed behind

the contact point. Some tearing may also occur in front of where the contact was expected to be. There are many events where some material was removed from the surface during contact. These features typically have a large amount of material build up in front of the removal where the deformed material had accumulated in front of the contact before a section of material is removed. As load increases this material deformation becomes more severe and more material appears to be deformed during contact. More of the material surface is removed when a plastic deformation event occurs as both the width and depth of the deformation increases.

There are many repeated wear events seen where repeated plastic deformation and material removal occurs. The process of repeated deformation is reminiscent of Schallamach's observations of wear on rubber (see section 2.5.3). In particular the regular patterns of material removed and build up is reminiscent of the pin on disc patterns. This may be expected as the oil film baked at 100^{0}C has be characterised as an elastomer. Schallamach wear patterns are not observed for all wear events, as individual wear incidents occur. Also rather than being regular patterns across the sliding length they are often cut short and show changes in wear direction when particles move in and out of contact. This shows that fundamentally the wear is consistent with typical, Schallamach rubber wear. However the wear shows contacts being created and stopping due to the fact this is a 3 body, not a 2 body system.

As previously carried out in section 4.2.1, the wear of a sample shown in figure 4.24 can be measured using profilometry the height normalised to give a profile as shown in figure 4.26.

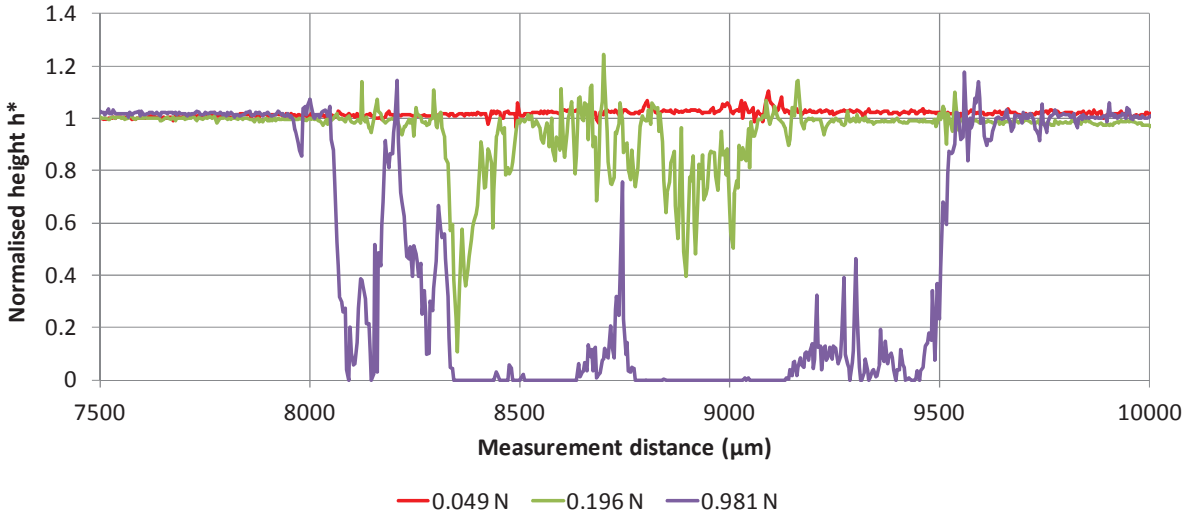

Figure 4.26: Cross-sectional profile of the damage at different loadings. L = 120mm, d = 62 µm, η_0 = 0.02 Pa.s, u = 7.6 mm.s^{-1}, and C = 8.4%.

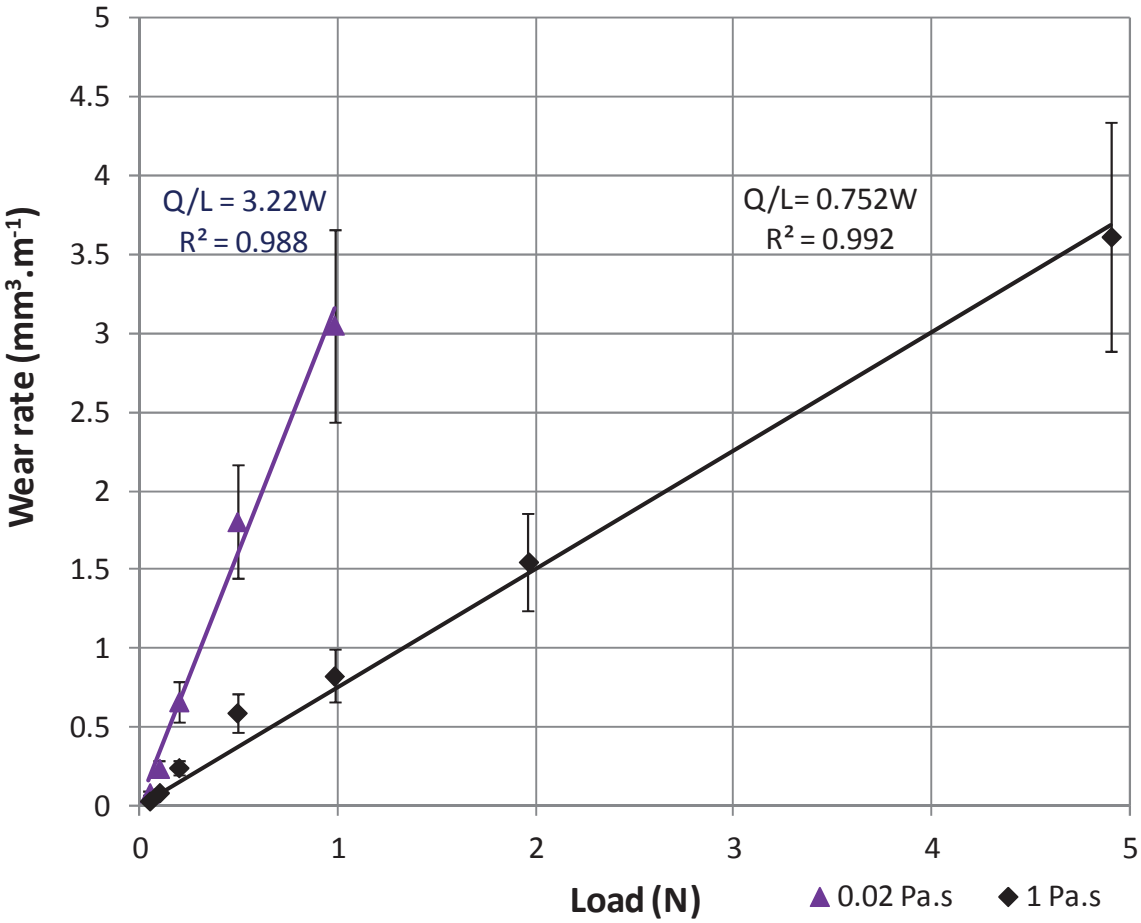

Figure 4.27: Wear rate as a function of load at two viscosities. d = 62 µm, u = 7.6 mm.s^{-1}, and C = 8.4%.

The experiments that produced the data in figure 4.26 are systematically repeated at different sliding distances to gather a series of wear rates. Further wear rates are gathered under other loading conditions in order to quantify the effect of load. Wear rate is preferred over pure wear volume as the variable to study. Firstly this is because there are conditions where the linearity does not hold as demonstrated in section 4.2.1. Measuring the rate of wear also means that the trends are based on multiple measurements rather than a single value, reducing the variance in the results. Figure 4.27 shows the effect of varying load on wear rate. A linear fit through the origin is shown. The data clearly indicates that wear rate is proportional to load, as expected. Two different continuous phase viscosities are chosen to illustrate the effect is consistent even as other parameters of the system vary. A fuller investigation into the effect of viscosity will be given later.

Figure 4.28 shows the corresponding friction data to the wear data shown in figure 4.27. Frictional data is taken from the average of 4-20 passes or until linearity is no longer seen in the wear. This is to minimise the impact of initiation variation and end effects. Figure 4.28 shows a general increase in the coefficient of friction with load. This may indicate that the increase in wear results in an increase to the friction. However the increase in coefficient of friction is small compared with the variation in the measurements and so may not be as a result of a physical change in the friction. Indeed it may be that the coefficient of friction is broadly independent of load.

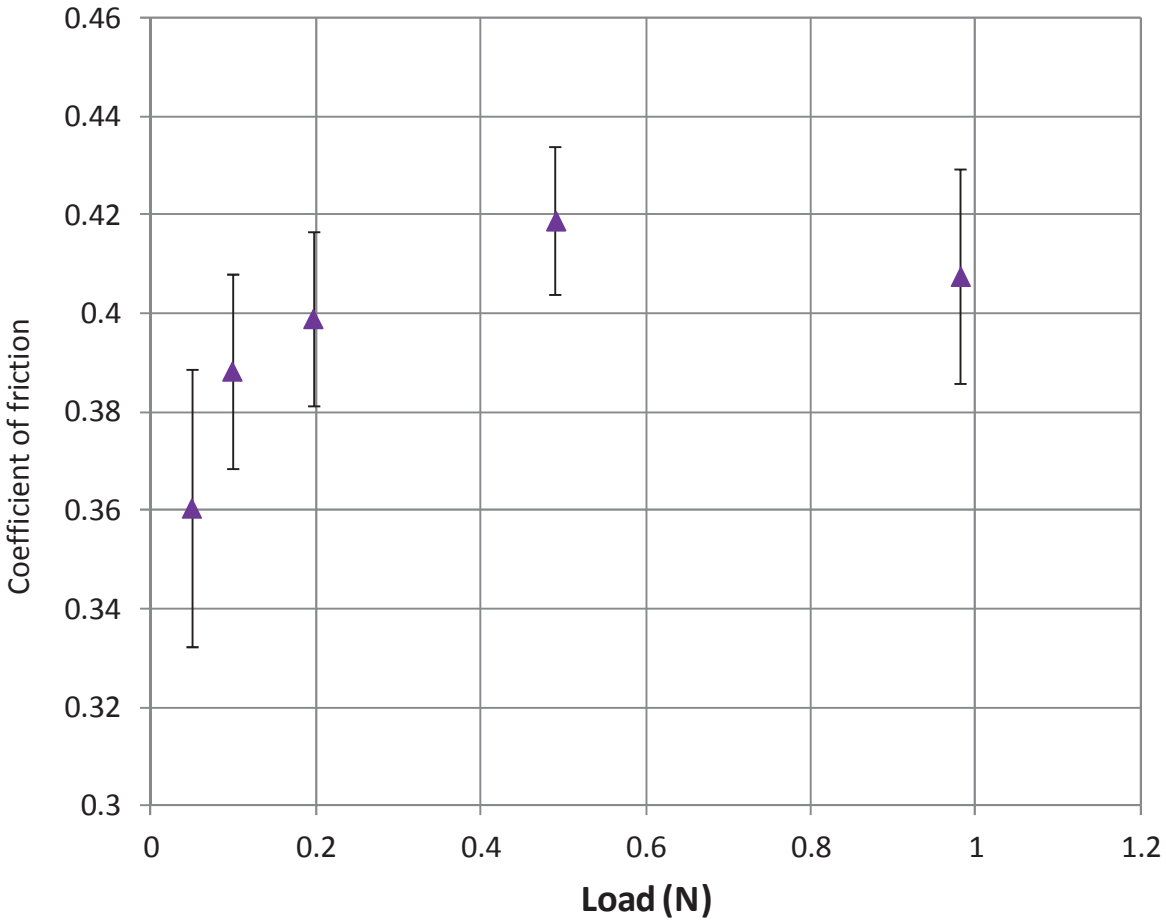

Figure 4.28: Coefficient of friction as a function of load. This data corresponds to the data shown in figure 4.27. d = 62 µm, u = 7.6 mm.s^{-1}, C = is 8.4% and η_0 = 0.02 Pa.s.

4.3 Effect of surface properties on baked oil film wear

The final variable in the Archard wear equation in hardness. This subsection will investigate the impact material properties have on the wear. The material properties of the DCO films were investigated previously in subsection 4.1. Final results that show the influence on baking conditions on hardness are summarised in figure 4.18.

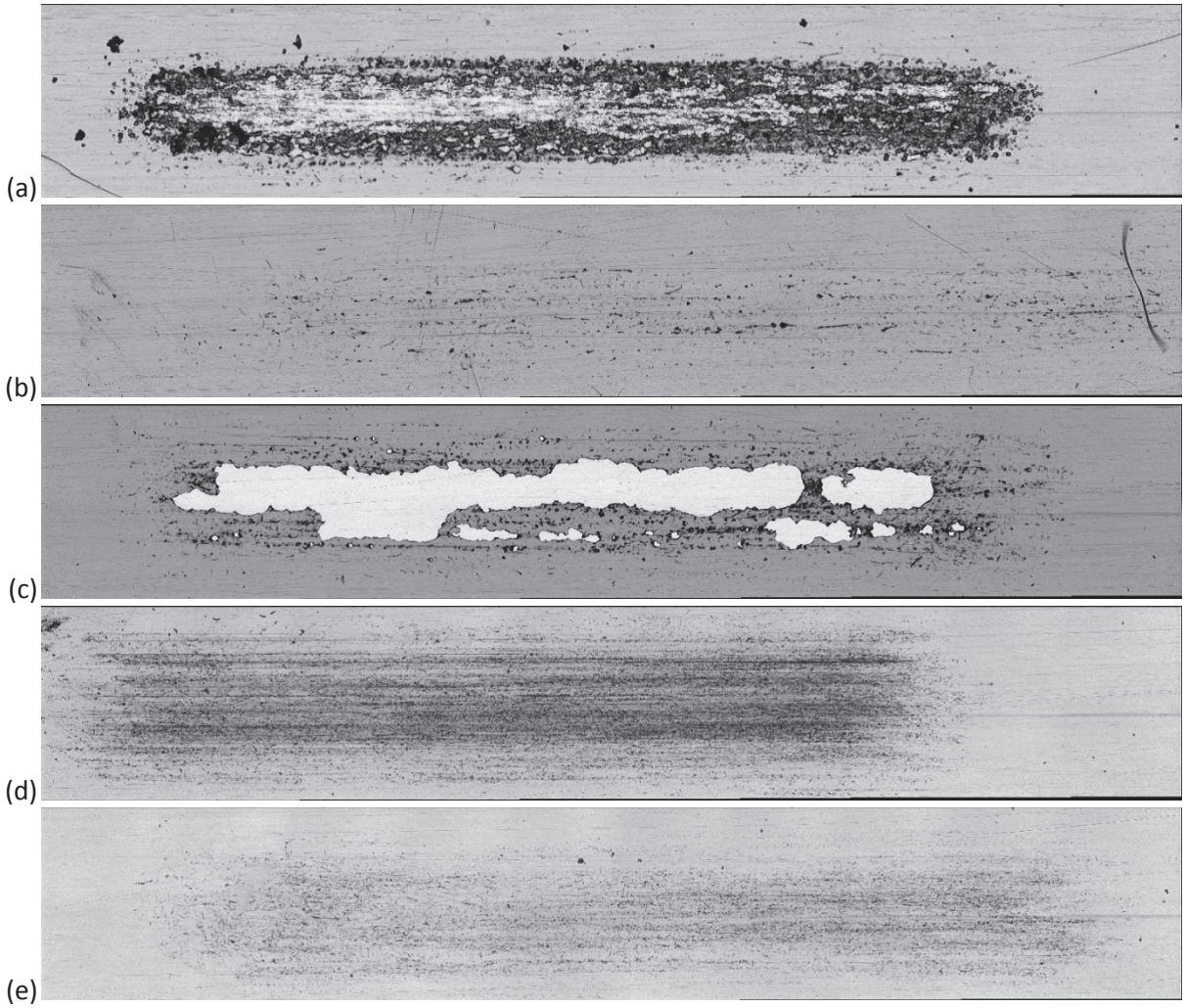

Figure 4.29: Overview of damage of baked oil films with different hardnesses produced by optical microscopy. All images are to same scale: the horizontal field of view is 13.6 mm. L = 120mm, d = 62 µm, η_0 = 0.02 Pa.s, u = 7.6 mm.s^{-1}, and C = 8.4%. T, t, and W are: 100^{0}C, 1.5 h, 0.49 N (a); 150^{0}C, 1.5 h, 0.49 N (b); 150^{0}C, 1.5 h, 1.96 N (c); 200^{0}C, 1.5 h, 1.96 N (d); and 200^{0}C, 1.5 h, 1.96 N (e).

In order to investigate the effect of surface properties on wear, sets of DCO films were produced with a range of material properties. These DCO films were then worn at a series of sliding distances to produce wear rates. Figure 4.29 shows an overview of the wear of DCO films at different hardnesses and loads after ten passes. The load is varied in these images as conducting experiments at a single load was problematic. This is because the wear rate at low hardness and high mass are too rapid to be measured and the wear rates at low masses

and high hardnesses are too low for a series of experiments to be conducted in a reasonable time frame to achieve a significant amount of wear. Thus the load was increased as hardness increased. Rather than studying the wear at fixed loads the load was varied on each series of DCO films in order to ensure the results linearly proportional to load. The wear rates divided by load produced are plotted as a function of inverse hardness in figure 4.30. Wear rate is plotted against inverse hardness as, according to the Archard equation, this should be a linear relationship.

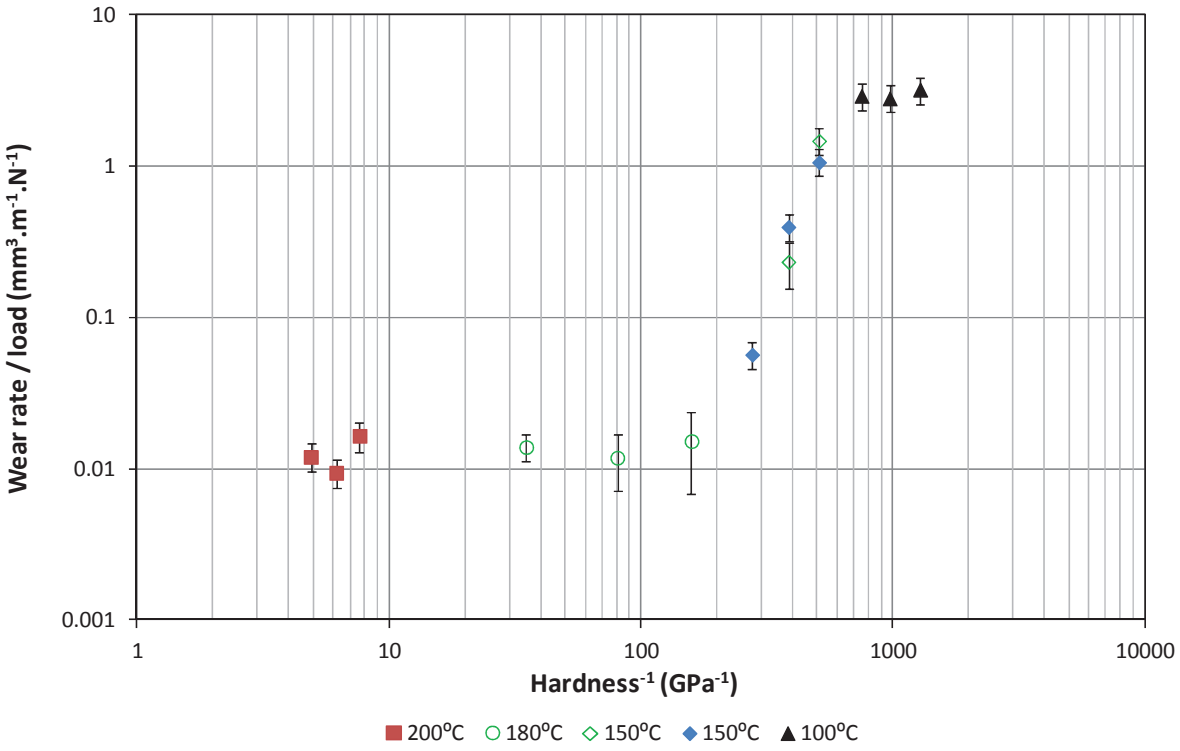

Figure 4.30: Wear rate divided by load as a function of the inverse hardness. Data points collected via the original profilometer method are shown in filled markers. Data points collected via the interferometer method are shown with unfilled markers. Baking time was also varied and times of 60, 90 and 120 minutes. An increase in baking time corresponded to an increase in hardness; as shown in figure 4.18. η_0 = 0.02 Pa.s, u = 7.6 mm.s^{-1}, d = 62 µm, and C = 8.4 %vol. although straight lines could be fitted to the three regions of the graph this in practice was not done due to the limited data points and large errors (in comparison to the gradient of a fit).

The data for oil films baked at 180^0C, shown in figure 4.30, are taken by a different height scanning method to the primary, profilometry method. The relocation profilometry method is used extensively with respect to the measurements presented as it was the only feasible method for collecting data at the start of the investigation. The interferometer method only became available late on in the project. Setting up and repeating measurements with a new test method would have been impracticable. However, reliability issues with the relocation profilometry equipment meant that the interferometer provided the only feasible method for data collection. The details of the interferometer method are given in section 3.2.3.

Several samples that had already been scanned by profilometer were rescanned to show the comparison between the two methods. These data points have been included in figure 4.30. The new method collects more data and therefore should in theory give a reduced error compared with the profilometer. However the profilometer includes a pre-scan of the surface, which allows a direct measurement of the removed oil volume to be made. Time did not allow for a complete method development and so the original film height was unknown. The original film height and therefore the volume of material removed were estimated. As the data relies on estimates there is a larger error in the results.

The wear imaged in figure 4.29 shows a clear decrease in the amount of wear as hardness increases. The wear as a function of hardness data shown in figure 4.30 supports the observations. However the wear rate divided by load clearly shows a non-linear behaviour that is not in line with the Archard wear equation. Instead there are three regions of wear.

Films that are about 10 MPa or softer have wear rate more dependent on hardness than those harder than 10 MPa. At about 2 MPa there appears to be a second deflection in the trend. There is a sharp change in the wear rate from about 2 MPa to 10 MPa but a lower change in wear rate below approximately 2 MPa. This suggests there are three regimes; a lower elastomer wear regime, a high thermoset regime and a transition regime.

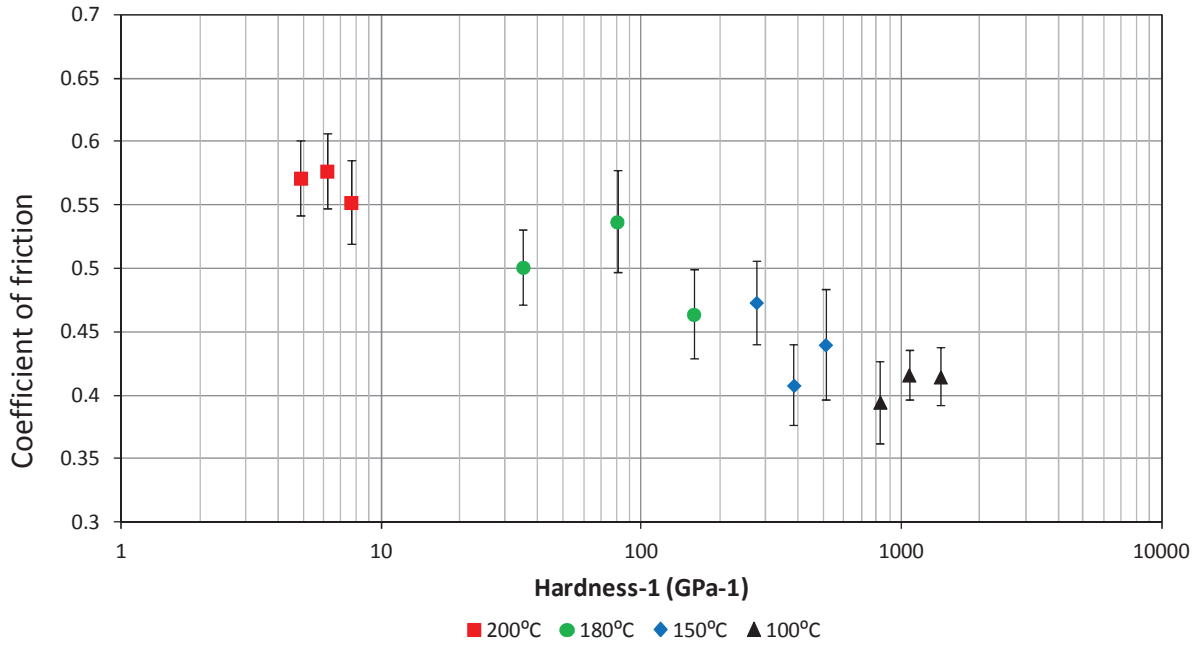

Figure 4.31: Coefficient of friction as a function of DCO film hardness. Corresponding to the data in figure 4.30. η_0 = 0.02 Pa.s, u = 7.6 mm.s^{-1}, d = 62 µm, and C = 8.4 %vol.

Corresponding coefficients of friction to this hardness data is shown in figure 4.31. There is a general increase in the coefficient of friction, from 0.4 to 0.6, as hardness increases from 0.7 MPa to 200 MPa. However it is difficult to assume a fit to this data as there are many models that predict friction and many of the data show large errors compared to the trend. This deviation is most likely due to averaging frictional data with a signification noise generated by the random particle motion and wear events. The frictional data may also support the

idea of there being three wear regimes. However figure 4.31 would indicate both the 180^{0}C and 150^{0}C belong to the transitional regime, whereas the impression from figure 4.29 is that the 180^{0}C belongs to the thermoset regime. This may be a limitation in the way 180^{0}C data was collected giving a larger deviation in the measurement and lowering the average wear. However the idea that 180^{0}C data is part of the transitional regime is supported by the measurement of modulus presented in section 4.1, and would mean the transitional regime upper limit is at approximately 50 MPa.

Although elastic modulus was studied when characterising the baked oil films previously, data is not shown in terms of the modulus. This is because it is not the primary variable expected as it is not in the Archard equation [21], and also due to the large deviations seen as a function of frequency in section 4.1 it is difficult to establish the true elastic modulus of the DCO films.

To further investigate the process of hardening's effect on wear the images in figure 4.32 and figure 4.33 were collected. Figure 4.33 shows three dimensional images gathered on the Sensofar instrument at the end of the project and not widely applied across this thesis. The method used scanned the top of the DCO film and is not without limitations, as the range of the measurements must be selected such that substrate reflections do not influence the results. Typically this means that the depth of a wear event cannot be greater than 7 μm.

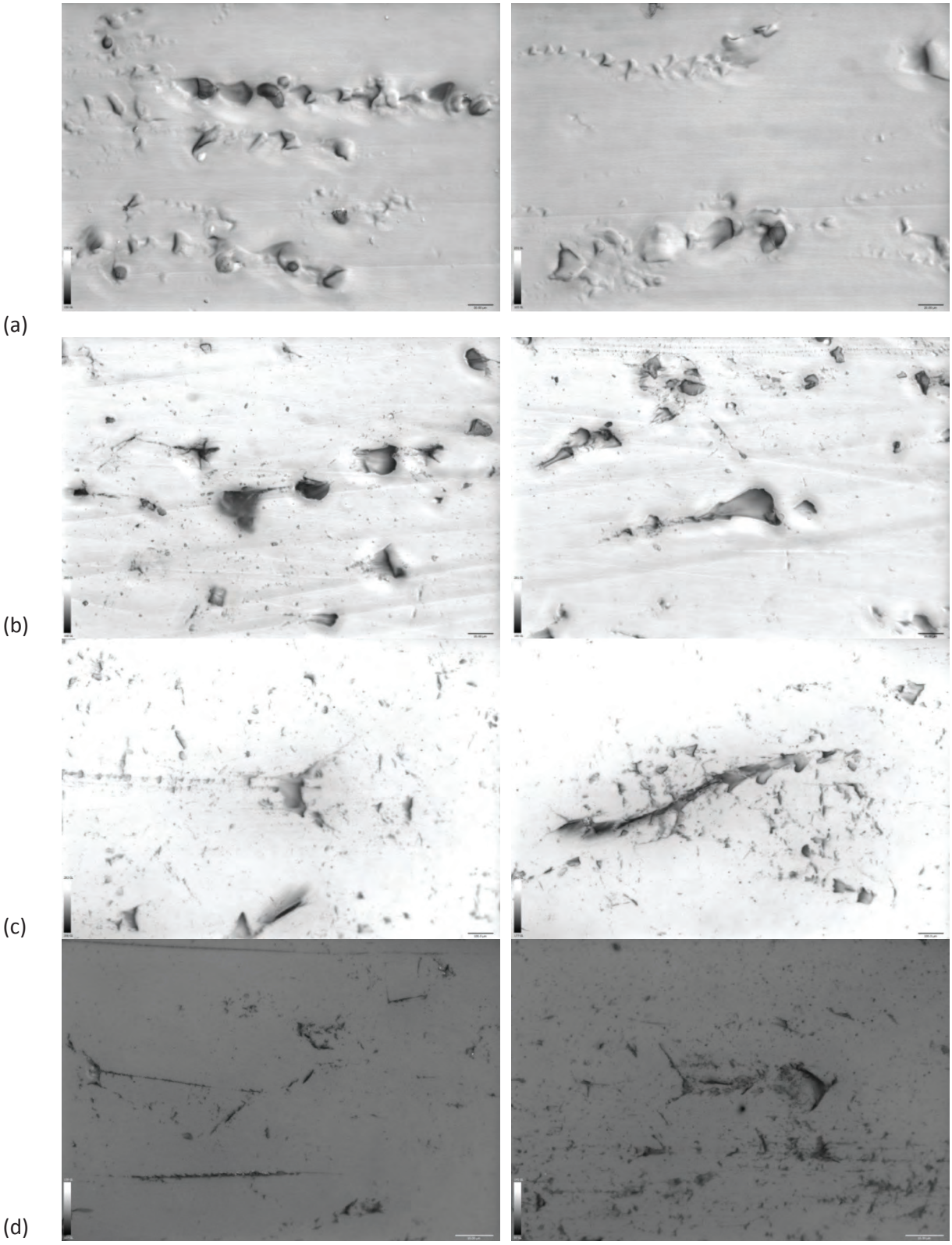

Figure 4.32: A collection of images showing typical wear features seen on the samples. All images show wear with d = 62 µm, u = 7.6 mm.s^{-1}, C = is 8.4% and η_0 = 0.02 Pa.s. T, t and W are: 100^{0}C, 1.5 h, 0.196 N (a); 150^{0}C, 1.5 h, 0.981 N (b); 180^{0}C, 1.5 h, 4.91 N (c); and 200^{0}C, 1.5 h, 4.91 N (d). The scale bars are 20 µm (a), 20 µm (b), 10 µm (c) and 10 µm (d).

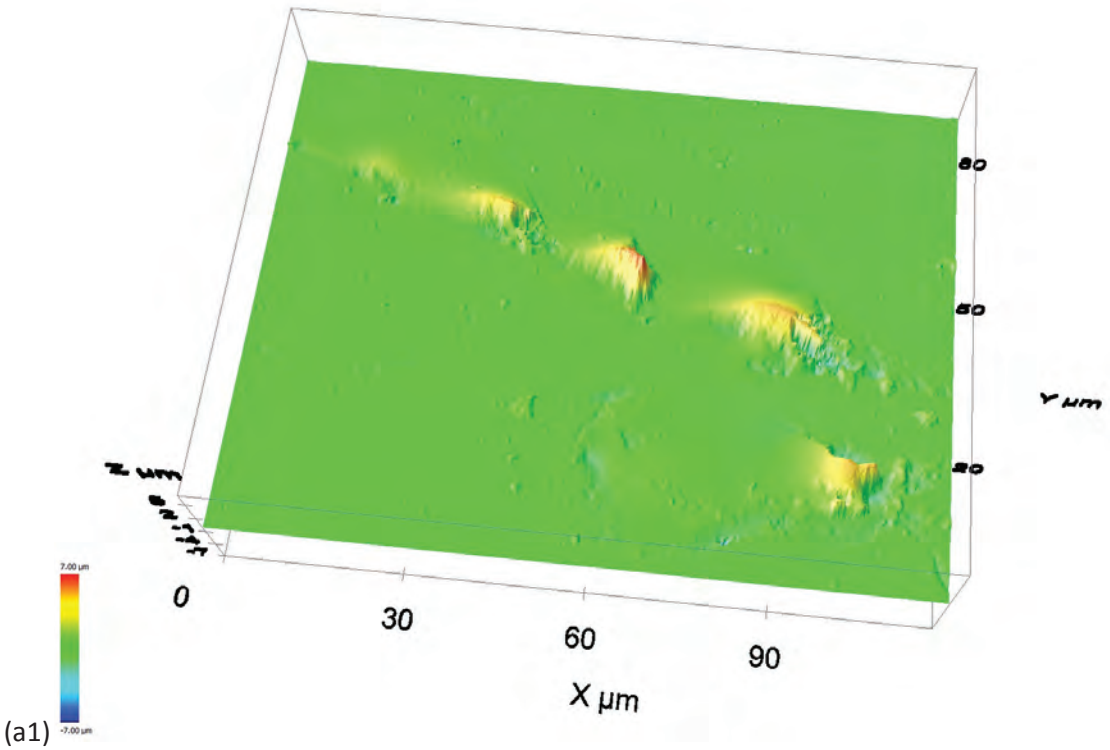

(a1)

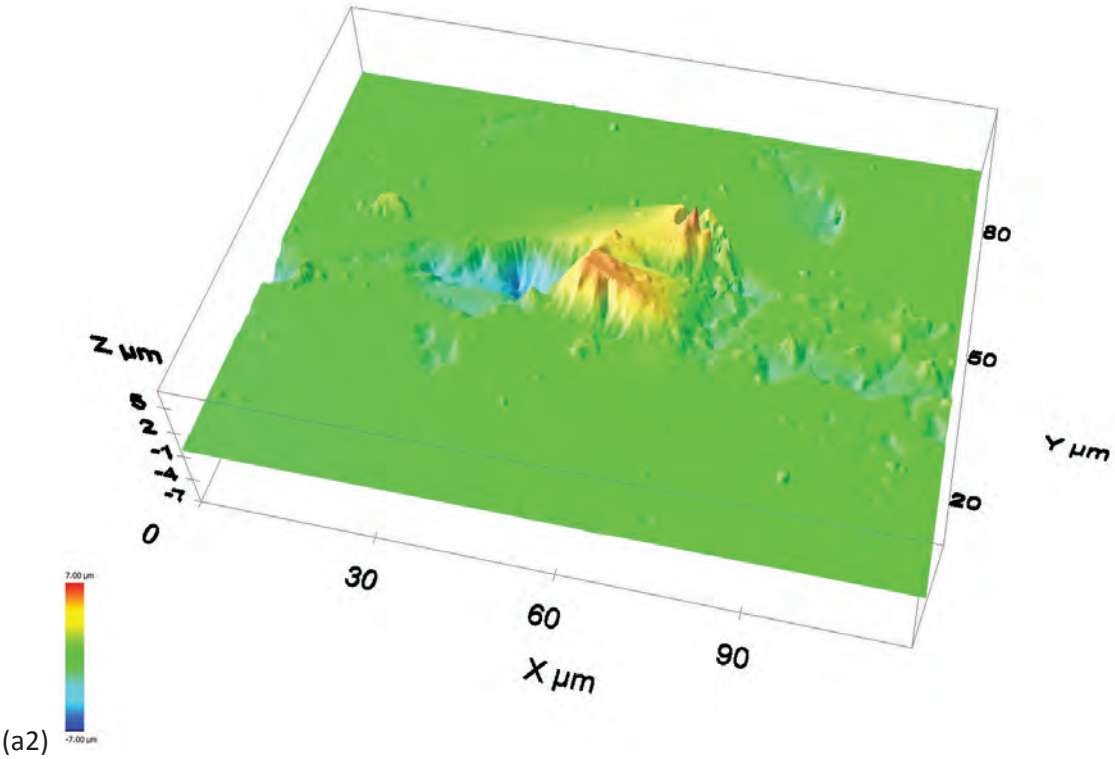

(a2)

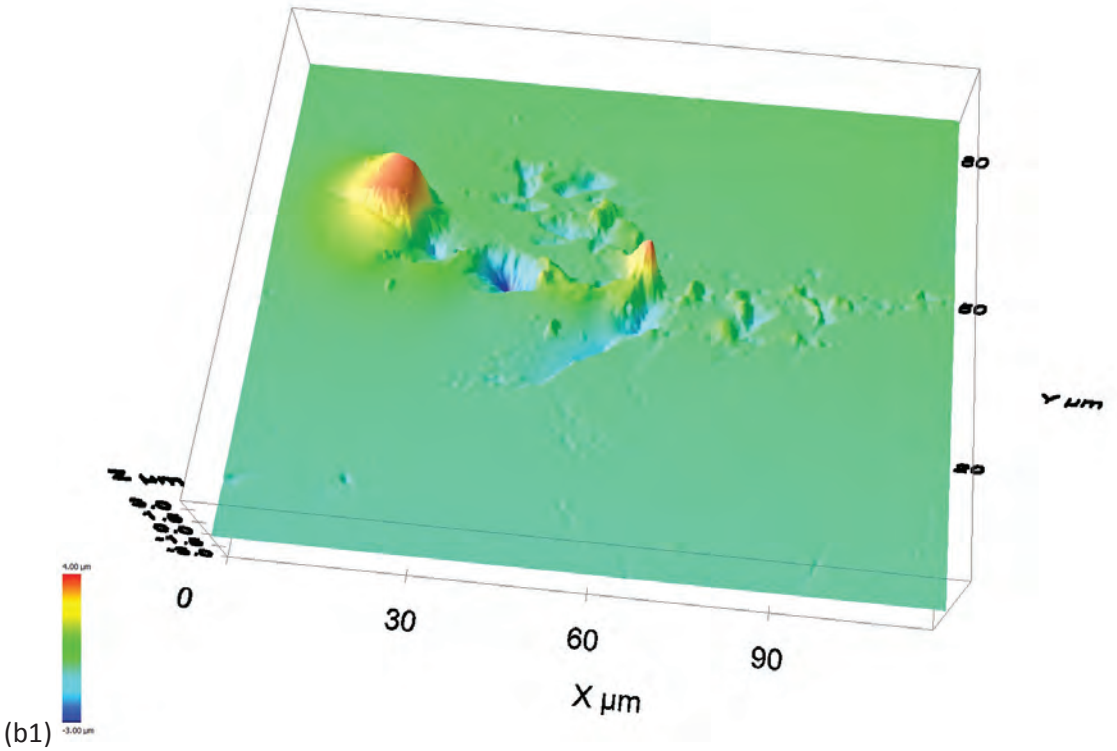

(b1)

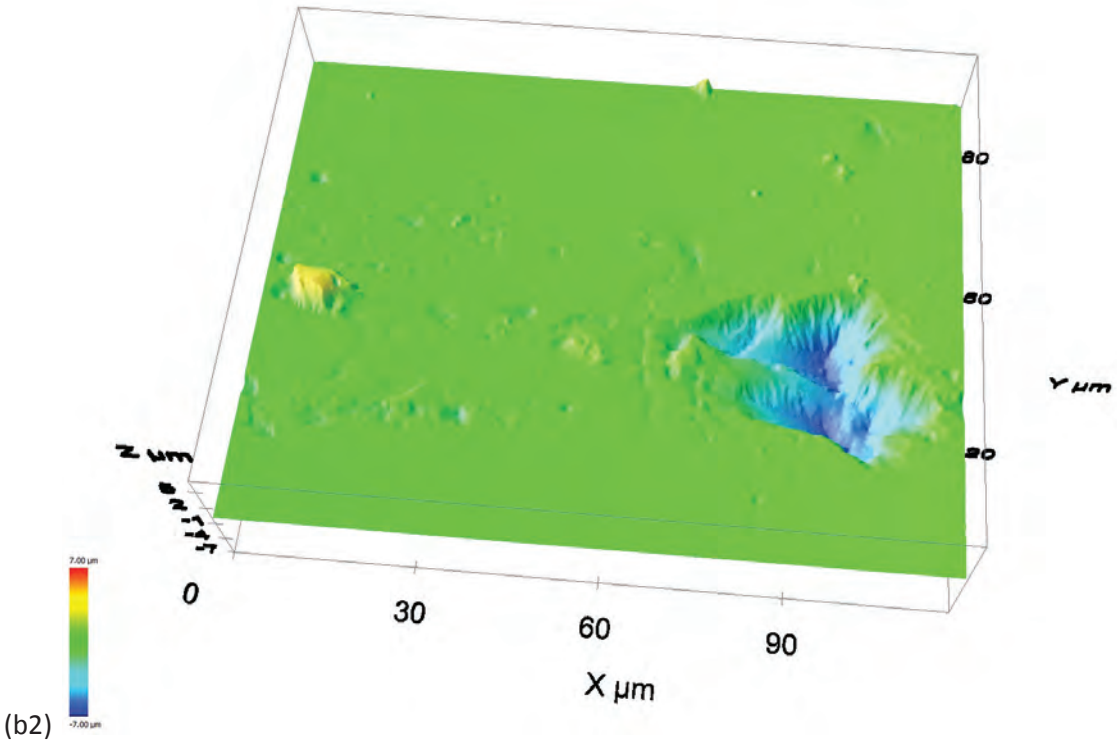

(b2)

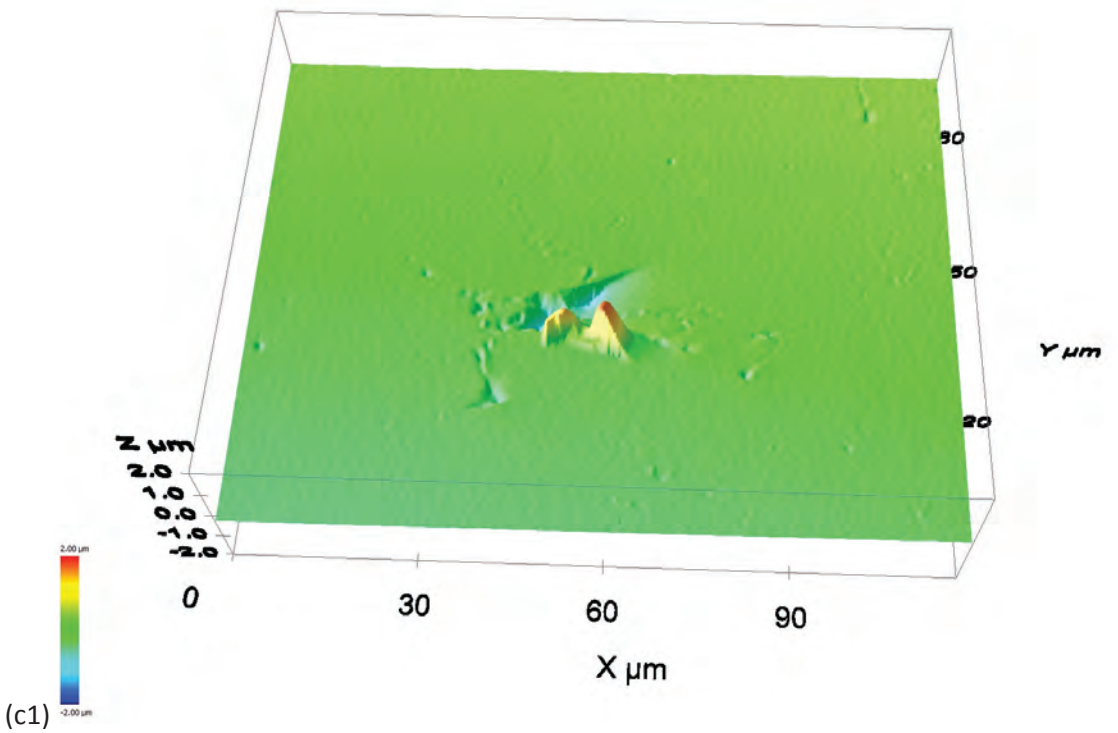
Z µm
2.0
1.0
0.0
-1.0
-2.0
0
30
60
90
X µm
Y µm
50
20

(c1)

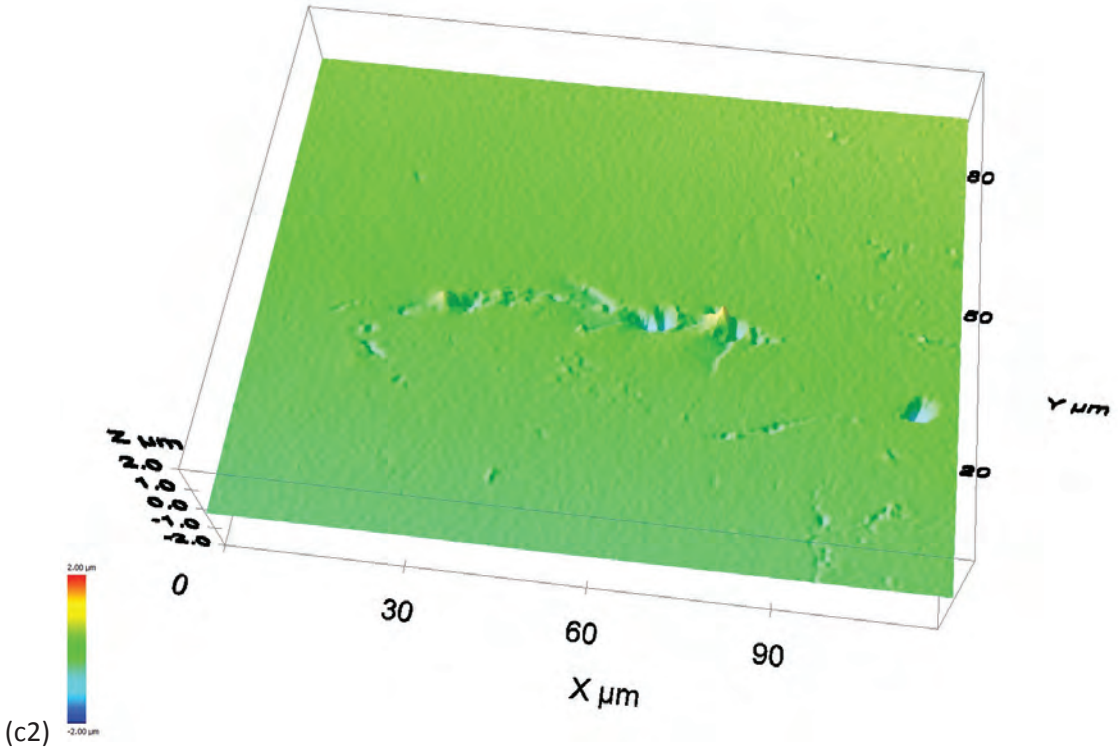
Z µm
2.0
1.0
0.0
-1.0
-2.0
0
30
60
90
X µm
Y µm
80
50
20

(c2)

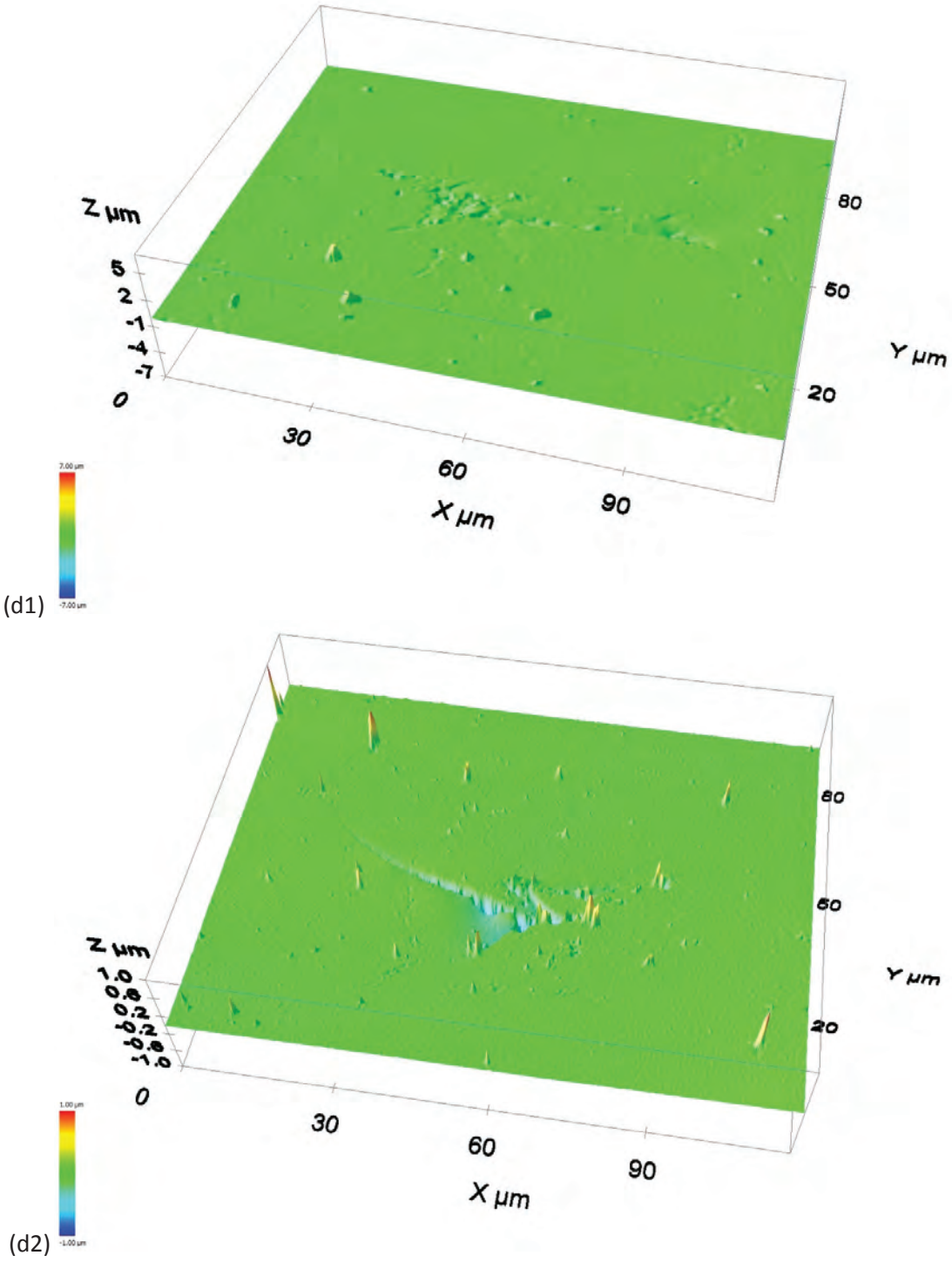

Figure 4.33: A collection of topographical images showing typical wear features. All images show wear with d = 62 µm, u = 7.6 mm.s^{-1}, C = is 8.4% and η_0 = 0.02 Pa.s. T, t and W are: 100^{0}C, 1.5 h, 0.196 N (a); 150^{0}C, 1.5 h, 0.981 N (b); 180^{0}C, 1.5 h, 4.91 N (c); and 200^{0}C, 1.5 h, 4.91 N (d). The scale bars are 20 µm (a), 20 µm (b), 10 µm (c) and 10 µm (d). Note the veritical ranges are: -7 to 5 (a) (b) (d-1), -2 to 2 (c), -and 1 to 1 (d-2)

The images of a soft film, for example the film baked at 100^{0}C shown in figure 4.32 (a) and figure 4.33 (a), show the same wear processes seen in section 4.3. Figure 4.33 (a) clearly illustrates how the deformation is both results in pile up and ridges of material that is displaced. The wear of an oil film baked 150^{0}C, shown in figure 4.33 (b) shows a similar amount of pile up. However the repeated soft elastomer, Schallamach patterns are rarely seen with oil films baked at 150^{0}C. Also the material appears to be more brittle as the wear seems to include some tearing of the surface prior to material removal. This means the deformation and ploughing is reduced. After baking at 180^{0}C the wear shows a limited amount of soft deformation of the surface, resulting in only a modest amount of pile up seen in figure 4.33 (c). Primarily the wear behaviour for films baked at 180^{0}C is dominated by tearing, cracking and some brittle chipping of the surface. When the film have been baked at 200^{0}C there is no evidence of pile up or soft deformation of the surface. The wear events are also both smaller and shallower than those baked at 180^{0}C. Wear of films baked at 200^{0}C is very brittle and consists primarily of cutting and cracking. Chipping seems rare for film baked at 180^{0}C and 200^{0}C so it is the repeated crossing and cracking that is removing the material. This effect is even more significant due to the fact the images were taken of wear at higher mass. As such the significant drop in the wear rate seen in figure 4.30 may be understood not just as the point at which the system is limited in its penetration into the surface due to the high hardness. The transition also occurs because particles in this range of tribological conditions are limited in their ability to cause a significant number of heavy wear processes due to the cohesive strength of the film and the film's resistance to deformation. Rather the material removal relies on the repeated damage to the surface.

Fundamentally the mechanisms involved in the wear of materials also change with the wear rate. This constitutes a change in the conditions of the test. The Archard equation groups system specific parameters into the wear coefficient, k. As such the fact that Archard equation does not model this behaviour does not mean that the wear is not Archardian. Rather this trend shows that the wear coefficient needs to be modified to accommodate widely different material properties.

4.4 Summary

The first step in this investigation was to establish a repeatable method of oil film production. An AFM technique was used to show that repeatable baked DCO film production was possible. However, this AFM setup could not be used to measure a wide range of surface properties without modifying the indenter to better measure each film. In practice rather than continually modify the AFM technique to match the required surface measurement nanoindentation techniques were used to characterise different surfaces.

Nanoindentation by quasistatic loading technique is a straightforward and fairly simplistic method which can give a way of differentiating between the baked oil films. However the results gained from this technique have been shown not to be reliable for understanding fundamental mechanical parameters. Dynamical indenting the material during loading gives erroneous effects particularly when used on the soft films. Overall data obtained during a frequency sweep at low frequencies (below 82 Hz) seems to be the most reliable and is in good agreement with quasistatic indentation. There is a significant problem with measuring the mechanical properties based purely on static indentation technique though due to

adhesion. Therefore the method of choice for quoting data is the frequency sweep method. In particular quoted mechanical properties will be based on the 3 Hz data.

Again this is what is predicted by Archard. Oil films baked at 100^{o}C, 150^{o}C, 180^{o}C, and 200^{o}C and baked for 60, 90 and 120 minutes presented a suitable range of material properties for testing the applicability of the Archard in this investigation. Films baked for 100^{o}C for 60 minutes will be the DCO films used in the later sections of this thesis.

The second and third section of this chapter focussed on investigating the first aim of this thesis: to understand how the wear of a model baked DCO soil depends on Archard wear parameters of sliding distance, load and surface hardness. When sliding distance was varied the oil films exhibited a region of linear wear predicted by the Archard equation, albeit with some limitations at low and high sliding distance. The slope of this straight line is the wear rate. The wear rate was found to be linearly dependant on load, as predicted by the Archard equation. Experiments were repeated at a different viscosity to change the test conditions and wear rate was again linearly proportional to load.

The behaviour of the oil film wear as a function of the surface hardness was not found to follow the trend predicted by the Archard equation. Instead there are three regions of wear; a soft material wear regime, a high hardness regime and a transition regime. Fundamentally the mechanisms involved in the wear of materials also change with the wear rate. The Archard equation groups system specific parameters into the wear coefficient, k. The wear

rate as a function of hardness trend shows that the wear coefficient needs to vary to accommodate the different material wear mechanisms found for these films.

5. RESULTS AND DISCUSSION: INFLUENCE OF FLUID PARAMETERS

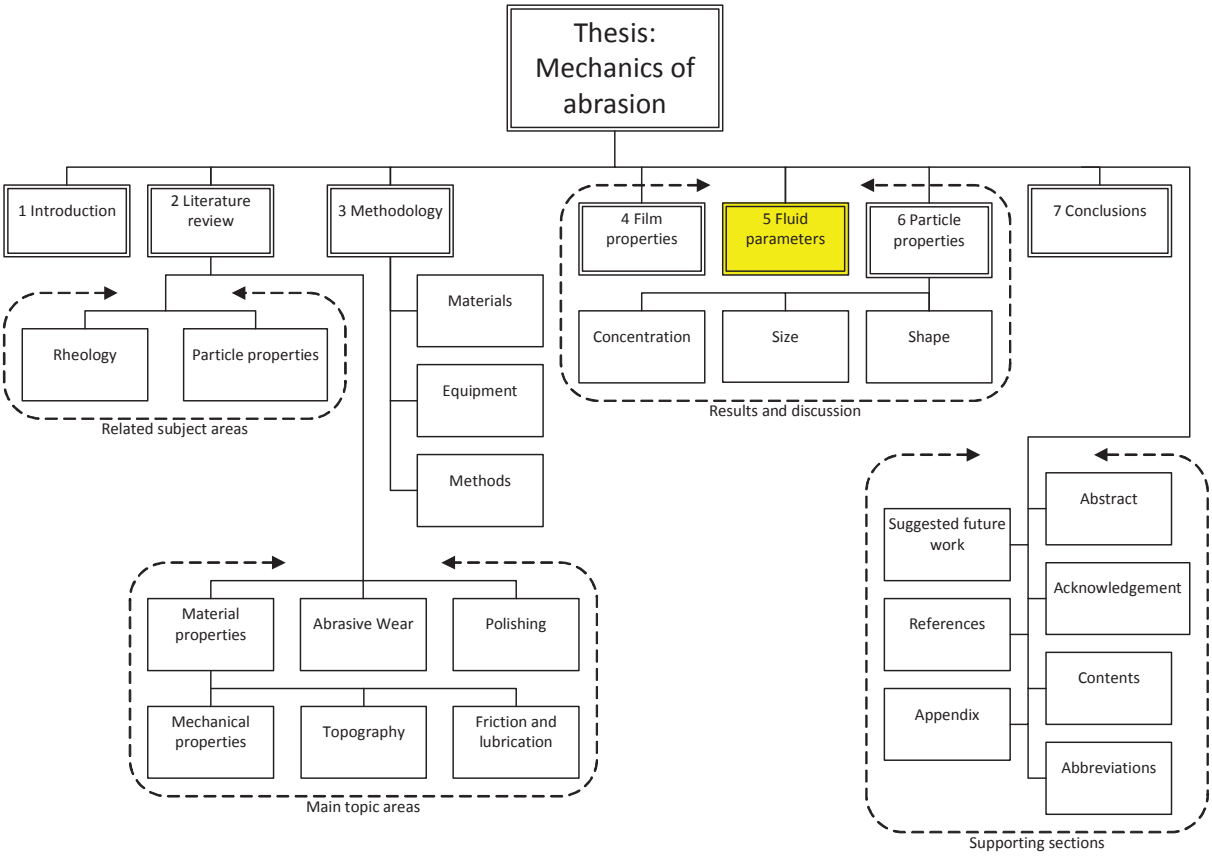

Figure 5.1: Thesis structure overview with chapter 5 highlighted

In the previous chapter the variables of the Archard linear wear equation were investigated with a particular focus on the film surface hardness. There are many parameters that are not included in the basic wear equation. Researchers have proposed their own, mainly empirical, wear equations in the literature which take into account more variables [147]. However, as discussed in section 2.5, it is apparent that each equation is derived to explain a specific tribological problem and do not seem universally applicable. This chapter will look into two other parameters of interest: speed and viscosity. These two parameters have been linked

together by the fact that they are expected to influence wear via their impact on the "lubrication" of the system.

5.1 Fluid Properties

Prior to measuring the effect of the fluid on abrasion it is first necessary to define the fluid properties both in terms of the bulk rheology and the behaviour in confinement i.e. lubrication.

5.1.1 Rheology

The raw rheological data of the continuous phases are shown in figure 5.2. These were created in accordance with the methods discussed earlier (subsection 3.1.2). Calcite particles were then added to these solutions to give the test slurries and the corresponding response for these slurries are also shown in figure 5.2. It was only possible to measure the properties of 0.2 Pa.s or thicker solutions as a series of rheology points. This is because as viscosity is reduced the time taken for particles to begin to settle out of the solution reduces, making accurate measurement of the rheology problematic. In order to measure the rheology of low viscosity calcite suspensions fewer points can be measured over a given time accurately. Hence the data at lower viscosities is measured using single points. Viscosities were calculated from this data and these values are shown in figure 5.3.

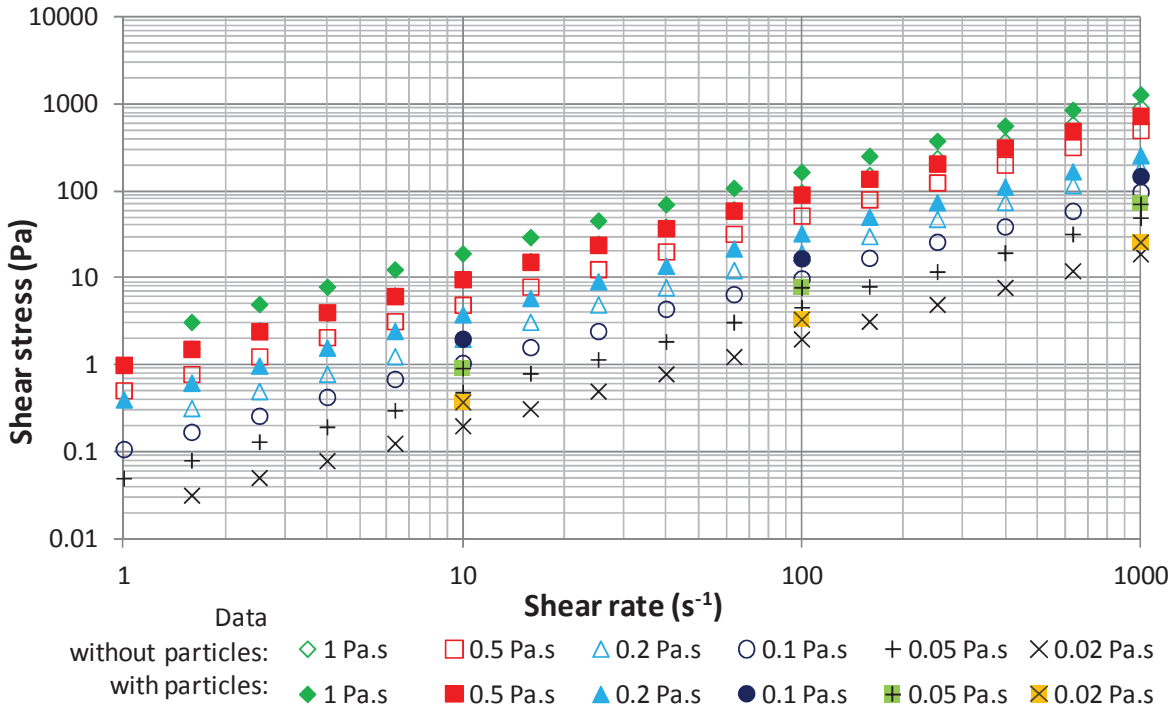

Figure 5.2: Raw rheological data for the continuous phase solutions and test solutions containing 62 µm particles at a concentration of 8.4% by volume.

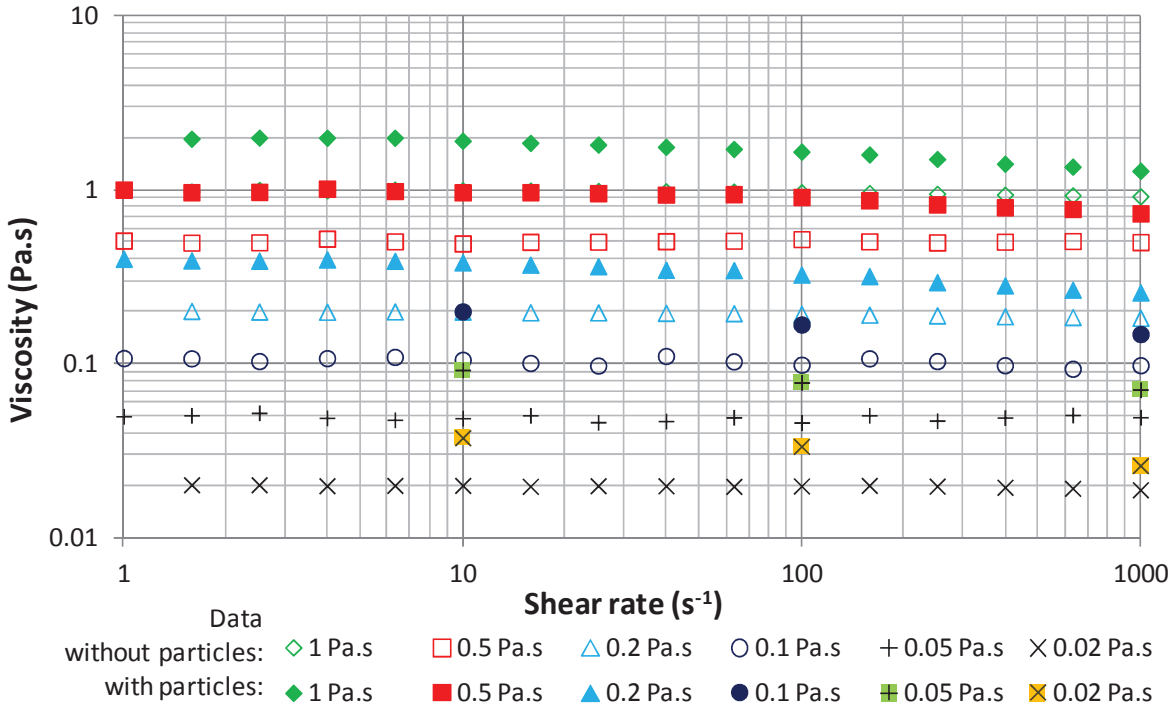

Figure 5.3: Calculated viscosities for the data shown in figure 5.2.

Most of the continuous phase data appears to show Newtonian behaviour. The highest viscosity sample, measured as being 1 Pa.s, does show some shear thinning at shear rates over 100 s^{-1}. However the effect is minimal, only reducing the viscosity by 10% over the measured range. It is not clear if non-viscometric flow phenomena such as viscous heating or hydrodynamic instabilities described in the literature [199-201]. As such the rheology is taken to be approximately Newtonian and suitable for this study.

When the 62 µm particles were added to the solutions it resulted in a shear-thinning dispersion, as indicated in the data. If the viscosity of the calcite slurry is divided by the continuous phase viscosity a relative viscosity of the suspension can be calculated as shown in figure 5.4. This relative viscosity of a solution with the calcite particles can be modelled by a modification of the Carreau equation (eqn 2.5 in subsection 2.1.1).

$$\frac{\eta(\dot{\gamma})}{\eta_0} = \frac{\eta_\infty}{\eta_0} + \left(\frac{\eta_0 - \eta_\infty}{\eta_0}\right)[a + (\lambda\dot{\gamma})^2]^{(n-1)/2} \qquad (5.1)$$

The choice of Carreau equation is appropriate because it predicts three key regimes: a low shear regime, a high shear regime and a transitional regime. Data in figure 5.4 appears to show a low viscosity regime, where the viscosity is double the continuous phase, and a transition. There is no high shear viscosity data. A high shear viscosity is predicted by the fact the fluid has an approximately Newtonian continuous phase. This logically means that the fluid cannot shear thin indefinitely and must reach a limit as the shear rate approaches infinity; hence a Herschel-Bulkley equation was not used. At infinity the data here has been fitted such that the fluids will approach the continuous phase viscosity. Intuitively, the fluid

viscosity at infinity should either approach or be slightly higher than the continuous phase viscosity (in finite particle effects cannot be ignored).

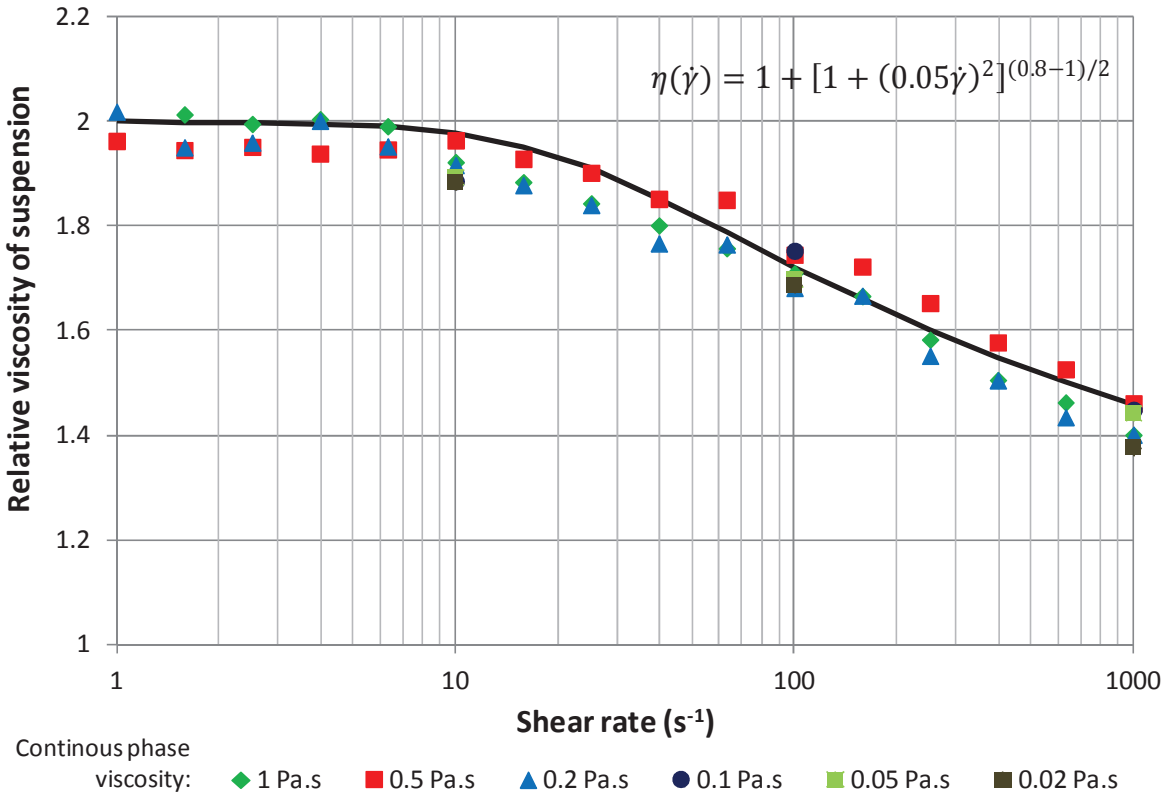

Figure 5.4: Relative viscosity of the calcite suspension as a function of shear rate for multiple continuous phases. Note the fit values in the equation have been rounded from the optimum values.

The suitability of the Carreau equation over other rheological models will not be fully discussed here as it is outside the scope of this investigation. The main purpose of this model is to show the symmetry of the fluid systems, whilst beginning to model the key features expected by the fluid. The fact all the fluid systems can be reduced to this model suggests that, at any given shear rate, the viscosity of the whole systems are related. Specifically they

are related by the ratio of their continuous phase viscosity to their suspension phase. A study like this, where the continuous phase viscosity is varied, will also be studying the effect of the bulk viscosity. It is worth noting that there is a change in the nature of the shear thinning when a different particle size or shape distribution is used which will not be discussed in this thesis.

This approach of just using the continuous phase viscosity to define the difference between fluid systems has a fundamental flaw. The viscosity of interest in a tribological study such as this is the viscosity in the contact region. This viscosity is defined by the shear rate in the contact. The shear rate is related to the lubrication parameters and the effective probe height. A viscosity change will change the lubrication parameters, changing the film height and therefore impact the shear rate on the fluid. Hence a change in fluid will mean the system is not being studied at a single, given shear rate. Instead a change in fluid means a more complex change in viscosity than can be related by just the ratio of the continuous phases. This effect is not to be fully studied here as the presence of the particles will limit the development of a complete understanding. In particular the true fluid film height is likely to vary as particles are trapped and released by the probe.

Another reason for using the continuous phase as the study variable is that it is easier to measure and understand. The measurement of the continuous phase can be done simply on a rheometer as it is a uniform flowing mixture. However in order to measure the properties of the bulk fluids care has to taken as the particles in these solutions are not suspended. As has already been stated the continuous phases are Newtonian and do not suspend particles.

Even in the thickest solutions, the particles (which are denser than the solution) will be slowly settling under gravity. Therefore any results for measurements of the rheology of the bulk solution must be studied carefully in order to ensure the system properties are being captured appropriately. Even if it were possible to measure a trend in the fluid systems through a rapid measurement it is unlikely that the most appropriate points will be captured. Rheometers available to this project were built to study fluids up to a shear rate of the order 10^3 s^{-1}. The shear rate in the contact between the particle and the surface is likely to be of the order 10^6 s^{-1}. As such any representative viscosity for the asperity contact zone would only be inferred from the trends at much lower viscosities and is likely to be erroneous.

5.1.2 Stribeck curve

In order to understand the behaviour of lubricated tribological contacts it is important to know and understand the lubrication regime. Stribeck's work in 1901 outlined the standard graphical features of a lubrication curve and established the key regions of interest. Figure 5.5 shows the Stribeck curve for the system in this study. The curve was taken using two particle free, Newtonian fluids to lubricate a probe passing over an oil surface. Figure 5.5 shows the three areas of lubrication and the expected friction behaviour in each region.

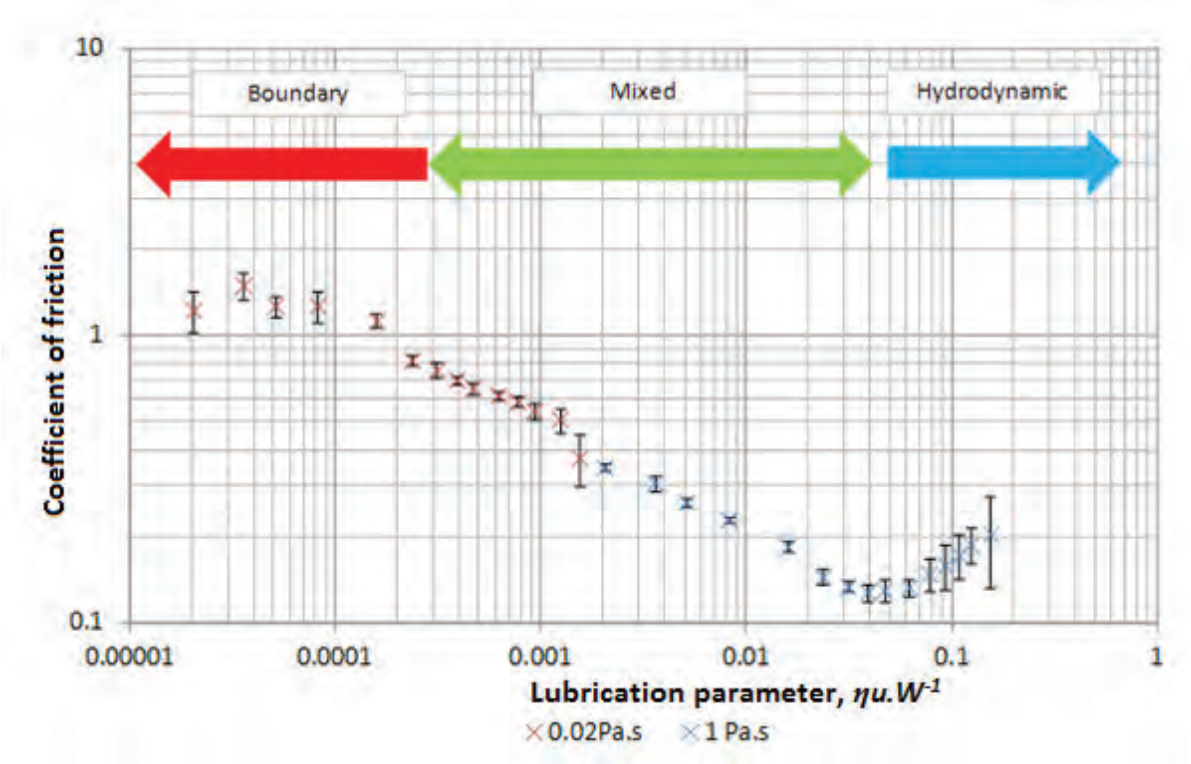

Figure 5.5: Stribeck curve taken for the system, measured using 2 Newtonian solutions to lubricate the probe passing over the oil surface. As the fluids are without particles there was no damage recorded. Load was 0.196 N and the speed was varied from 0.4 mm.s^{-1} to 30 mm.s^{-1}.

The data suggests that in the absence of other effects, the majority of the data gathered for this investigation should be in the mixed regime. The parameters chosen for the experiments in the previous chapter, 4, correspond to a mixed lubrication regime. Only with the appropriate combination of low mass, high speeds and high viscosities will the data become hydrodynamic. Conversely only when a solution is subjected to a mixture of low speed, low viscosity and high mass will the lubrication be boundary due to the fluid.

It is important to note that this graph does not predict the lubrication for the system as a whole; it merely gives an indication of the lubrication. This is because the friction recorded

during the wear experiments will be influenced by the presence of particles. Particles will modify the behaviour of the solution in two ways: rheological changes and a physical discrete breakup of the fluid system. As indicated in subsection 5.1.1 the addition of particles results in a viscosity greater than the continuous phase viscosity. Hence if it is the full solution viscosity that is of interest then the system will be closer to the hydrodynamic regime than if the continuous phase is the overriding influence. Provided the predicted gap height is approximately equal to the mean particle size or less is not believed that the solution viscosity is of primary influence due to the physical influence of the particles.

Each particle can physically either be trapped between the probe and the film surface or rest on one of the surfaces, reducing the possible gap size and influencing the physical properties of the surfaces in the contact zone. In both cases the particles in solution in the contact region will be reduced; in the former case it is because the particles that are smaller than the minimum film height will be trapped at the front or entrance to the contact. Therefore particles will be either pushed forward or around the contact reducing the number of particles in the contact region. As the concentration of particles is reduced the viscosity will reduce (this effect will be discussed in a later results chapter). It is also worth noting that the particles trapped will increase the film height as the particles can physically be pushed onto and thus raise the probe height as the particles are pressed down due to the curve of the probe.

5.1.3 Lubricant film height

As has already be suggested it is the height of the fluid film in relation to the particle size that is expected to dictate the amount of wear. There are many equations for calculating a lubrication film height [202-204]. However none of the equations are designed for this complex system of an elastomer contacting a thin, soft film covering a steel substrate with a particulate suspending solution for lubrication. Hence any calculation can only be used to provide an approximate value for the lubrication. For the purpose of this thesis the equations of Hamrock and Dowson are used for calculating film thickness [204]. A full justification for this equation over other film height equations is not given here as the calculation is used only as an indication of the relative size of the film height to the particles. Hence this section has not been included in the literature review.

The calculation is carried out for the contact between the probe and the steel surface. The oil surface is not chosen as it is thought that the bulk material properties of the steel would dominate the material behaviour. Plus a calculation involving the DCO film would require a more complex and time consuming calculation, which may not provide a significant benefit for this project as the equations are not designed for the complex fluid system used here.

As a ball on flat the contact has an ellipticity of 1 and by consultation of the literature can be described as being isoviscous elastic contact [204]. Depending on the contact parameters the lubrication can be either be hydrodynamic or elasto-hydrodynamic. For hydrodynamic lubrication the minimum film thickness, h_{min}^{HL}, is given by:

$$h_{min}^{HL} = \frac{72}{25}\pi^2 R^3 (\eta_0 u)^2 W^{-2} = 28.4 R^3 (\eta_0 u)^2 W^{-2} \quad (5.2)$$

where *R* is the radius of curvature of the contact, which in this instance is equal to the radius of the spherical probe. The equation for the minimum EHL lubrication film height is:

$$h_{min}^{EHL} = 1.78 E'^{-0.44} R^{0.77} (\eta_0 u)^{0.65} W^{-0.21} \quad (5.3)$$

where *E'* is the reduced modulus.

In order to investigate the influence of lubrication on wear the speed and viscosity will be varied. Load is the third parameter assumed to influence lubrication. However the effect of load was investigated in the first results chapter.

5.2 Effect of speed

According to the derivation of the Archard wear equation, speed should not influence the volume of wear material produced. Archard's wear equation was derived for dry, two body contacts. As such not only is speed a readily available parameter to vary, the influence of speed on the wear of a three body fluid system is of merit.

Figure 5.6 shows images of the wear produced by varying the speed of the probe running over a DCO film whist keeping all other parameters constant. The images show that as speed increases the number of particles entrained for a long distance decreases even though the total number of entrained particles appears to increase. The particles being entrained also show a larger deviation from linear motion as speed increases i.e. the wear path goes from a linear at 3.1 $mm.s^{-1}$ to wavey at 60.4 $mm.s^{-1}$. It is suggested that as speed increases the

depth of wear decreases by the fact there are less bright wear scratches where particles appears to have cut near to the steel surface. In order to investigate this further the height is measured by profilometry, as detailed in the previous chapter.

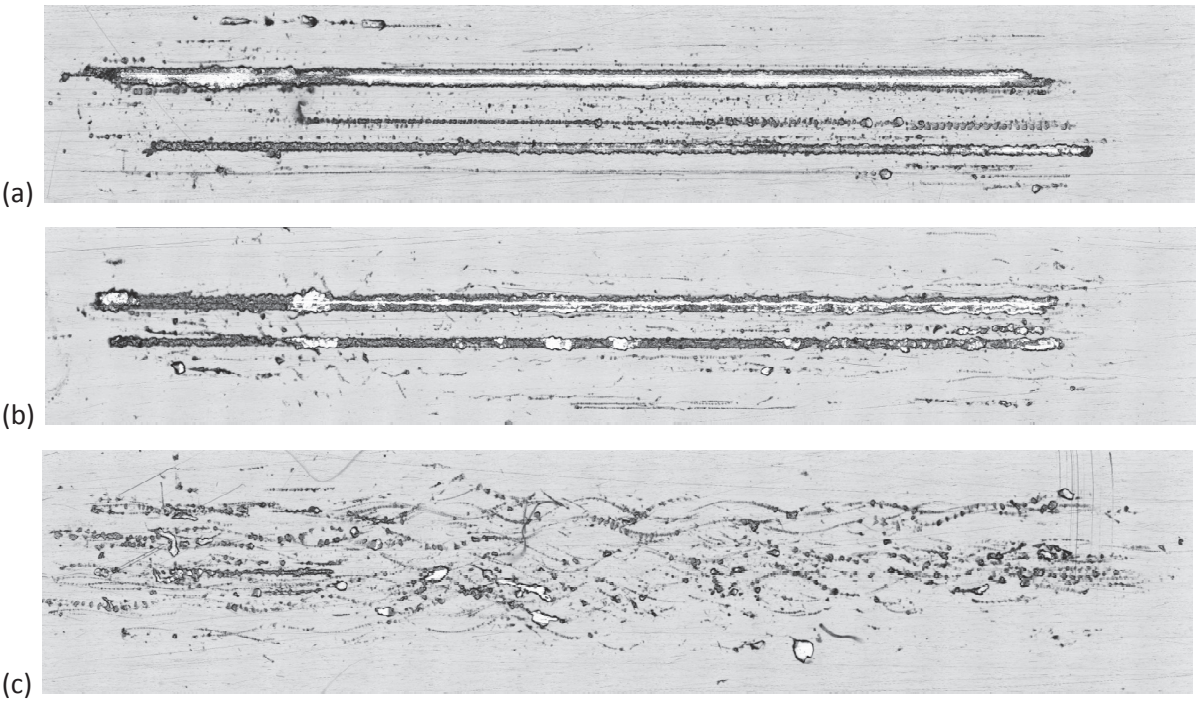

Figure 5.6: Optical microscopy of the overall damage at different probe speeds. Speeds are 3.1 mm.s^{-1} (a), 15.2 mm.s^{-1} (b), and 60.4 mm.s^{-1} (c). All images are to same scale: the horizontal field of view is 13.6 mm. d = 62 μm, η_o = 1 Pa.s, W = 0.196 N, L = 150 mm, and C = 8.4%vol.

Figure 5.7 shows the average height data collected via profilometer scans on the surfaces shown in figure 5.6. At 3.1 mm.s^{-1} the wear is dominated by 2 deep scratches which reach to the steel surface, and there are three shallow scratches and a small amount of surface roughening. The 60.4 mm.s^{-1} data shows 10 shallow scratches and a large amount of surface roughening.

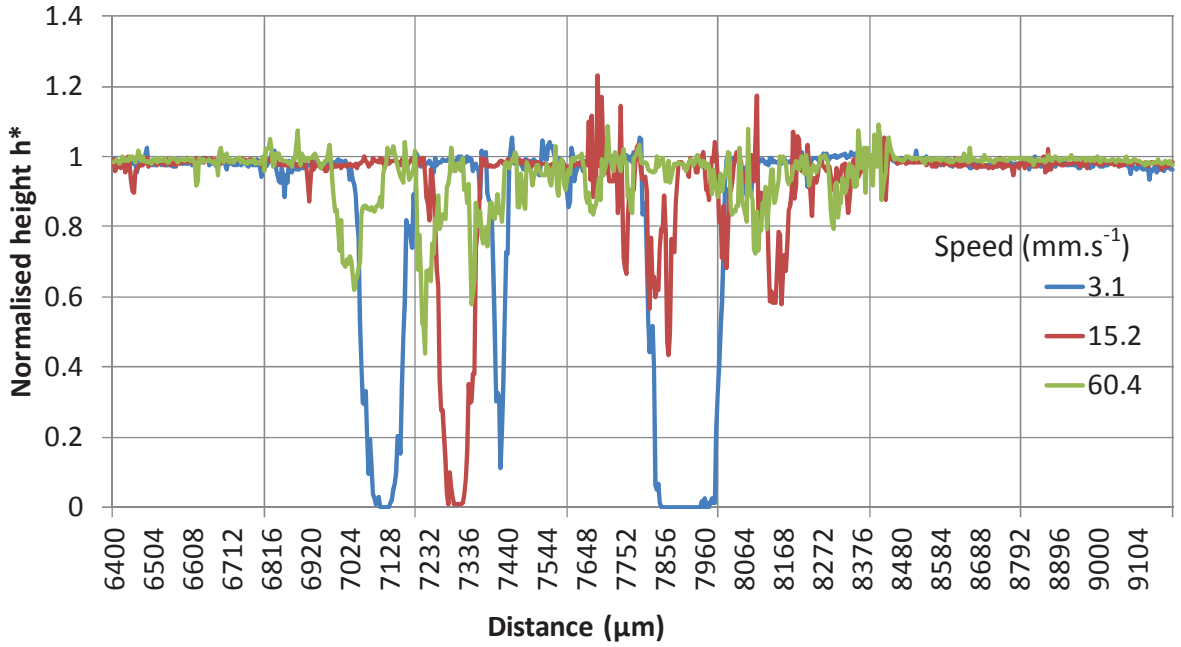

Figure 5.7: Profile of damage cross-section at different probe speeds. d = 62 µm, η_o = 1 Pa.s, W = 0.196 N, L = 150 mm, and C = 8.4%vol.

The observations of the wear, as shown in figure 5.6 and figure 5.7, suggests that as speed decreases there are fewer particles being captured. However individual wear events caused by these particles seem more severe as the penetration depth and wear lengths are greater. At higher speeds more particles seem to be captured. These particles are entrained for only short distances and do not penetrated deep into the surface. At all speeds there are small "pits" in the surface which appear to be where particles have impacted the surface but not caused significant damage. Overall increasing speed appears to aid particle capture but decrease the wear volume per interaction. To investigate this further individual wear events are imaged after short sliding distances in figure 5.8.

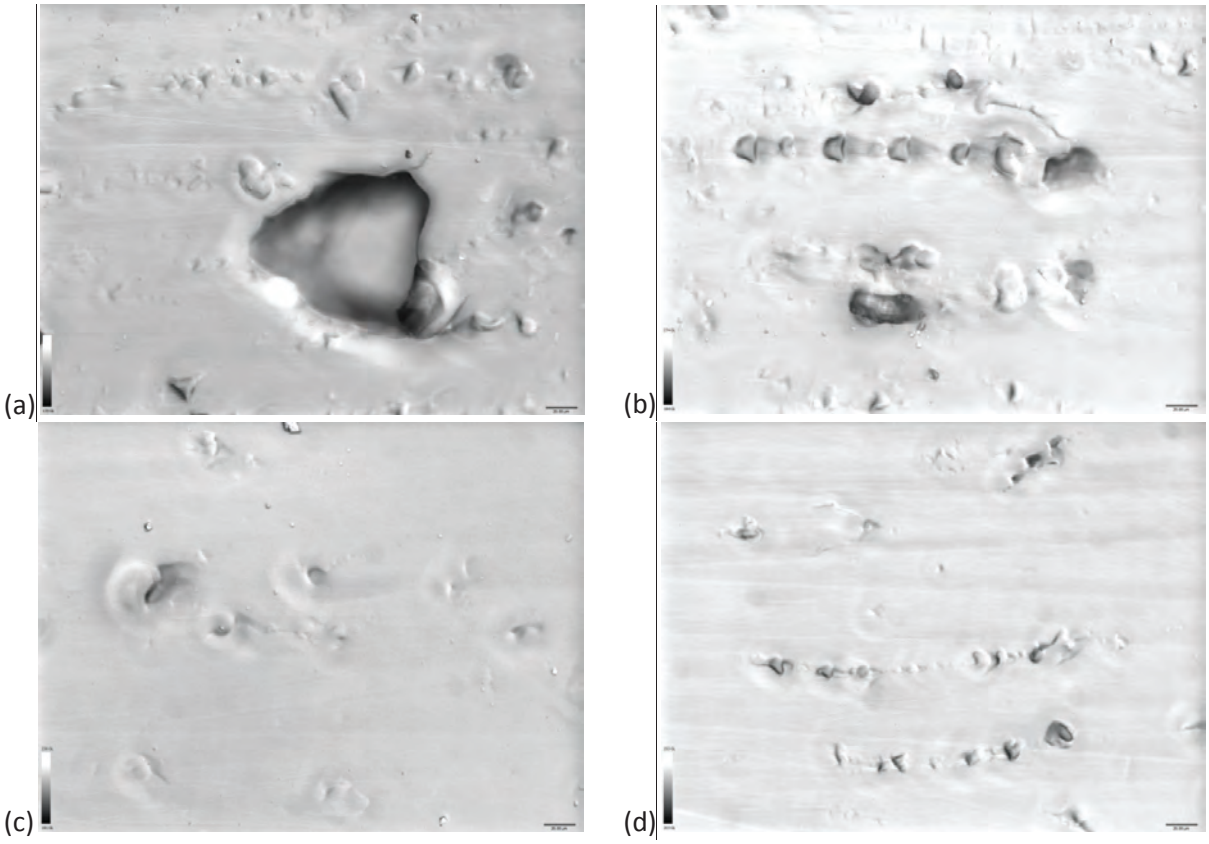

Figure 5.8: Optical microscopy of damage individual wear events different probe speeds. Speeds are 7.6 mm.s^{-1} (a) and (b), and 60.4 mm.s^{-1} (c) and (d). All images are to same scale and the small bar in the bottom right of the image is 20 μm. d = 62 μm, η_o = 1 Pa.s, W = 0.196 N, and C = 8.4%vol. Images (a) and (b) were found on L = 15 mm sample and (c) and (d) on a L = 90 mm sample.

Figure 5.8 (a) shows a deep individual wear event where a large amount of material has been cut out of the surface. By comparison the image in figure 5.8 (c) shows little material removal. There is a large amount of deformation in (c) and some tearing in the surface. The repeated damage in figure 5.8 (b) and (d) shows a similar trend of build up and release in the contact seen previously and comparable to the Schallamach patterns in the literature. Damage in figure 5.8 (b), which may be due to a smaller particle than the damage in (a), shows a mixture of material removal and pure deformation. The repeating width is roughly the same, suggesting the particle doing the damage is firmly held. By comparison, the

repeating damage observed at higher speed in (d) is dominated by deformation only events and the width of the wear is less consistent. It is also noticeable that the direction of particle motion is less linear at higher speed, as seen previously in figure 5.6. Overall this suggests that at low speeds particles can build up pressure and cut into the surface and chip out material. At higher speeds the particles are not drawn as deeply, into the same area of the contact, and less firmly held in contact, resulting in less damage. It is noticeable that figure 5.8 (a) and (b) show no evidence of the heavy wear seen in figure 5.6 at low speeds. This is not unexpected as the roughening of the surface as an initiation step was discussed earlier. It is likely that the heavy wear comes as a result of particles being caught in the roughened surface and deepening of the wear tracks as sliding distance increases.

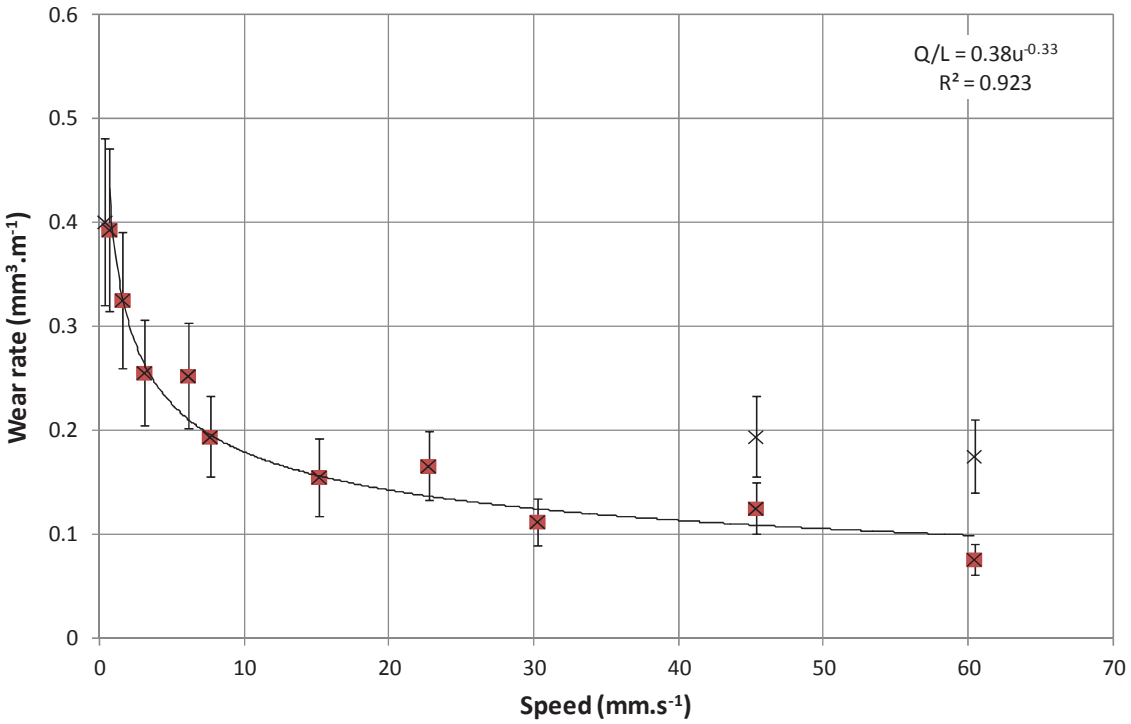

Figure 5.9: Wear rate as a function of probe speeds. d = 62 µm, η_0 = 1 Pa.s, W = 0.196 N, and C = 8.4%vol. The calculated minimum fluid film becomes hydrodynamic at 18 mm.s^{-1}. Minimum fluid film equals average particle size at about 32 mm.s^{-1}. Non-highlighted data points were not used in the fit.

The profilometer data are quantified in terms of a volume removed and experiments are repeated to produce wear rates at multiple sliding speeds. Wear rates are shown to clearly decrease as a function of speed in figure 5.9. An inverse power law has been fitted to the data and shows a good correlation. This behaviour may be explained in terms of the particle size and lubrication height.

For the system in figure 5.9 the point at which the fluid film height is equal to the mean particle size is calculated to be 32 $mm.s^{-1}$. It is noticeable that wear rates for speeds less than 30 $mm.s^{-1}$ are significantly higher than the wear produced at greater speeds. The particles are not monodisperse as such there is a distribution of particles lower than (and above) the mean. As the mean is based on a q3 volume density calculation, the number of particles declines rapidly as particle diameter increases because the volume is proportional to the diameter to the third power. At ~32 $mm.s^{-1}$ half of these particles, in terms of volume or mass are too small to be captured and go through the contact region unhindered. Even those particles with a diameter near to the film height are unlikely to cause significant damage. This is because the entrainment force of the probe will only hit the top of the particle and so force will predominantly be directed parallel to the surface rather than normal to it. Without a significant normal force particles should be driven to either slide or roll without significant damage, although the exact shape will also impact this effect.

As the probe is spherical rather than a cylinder or flat, particles not aligned with the central contact region may also be forced away from the centre of the wear path. This is because force applied by the probe will have a component perpendicular to the direction of motion

and normal force. If the particles were perfectly spherical the force would be expected to cause the particles to be rolled away from the contact zone with minimal indentation into the surface. These particles are angular and so the dynamic behaviour is hard to quantify.

At low speeds the angular nature of the particles means that particles both near to and away from the centre of the contact may be entrained and cause a significant wear through ploughing, with some repeated plastic removal, as can be seen in figure 5.6a. As speed increases the probe is lifted higher from the surface. A higher probe height means more particles can slip through the contact uncaptured and the probe will contact larger particles higher than at lower speeds. These conditions for wear of the captured particles are “worse” in the sense that the contact will have a smaller normal force, reducing the likelihood of the highly damaging ploughing wear. Instead the wear at high speed is primarily through tearing and multiple pass fatigue and the removal of ridges in the surface, as seen in figure 5.6c. As the normal stress is reduced and the contact point is higher, the particles have a greater freedom to move and shorter contact time, hence as speed increases the particle movement becomes less linear as particles can be moved perpendicular to the probe’s travel direction. Figure 5.6c shows particles not only being regularly moving away from the contact zone but also towards the contact zone. The movement towards maybe in part due to a pressure void behind the contact pulling the particles back into contact but also it maybe due to the particles having an irregular shape. The wear tracks also appear to get shorter with speed this is because the increase in fluid height would also allow particles to be pushed out of contact or rotate and go under the contact more easily.

It is argued above that increasing speed should lead to wear patterns that are less harsh and shorter in length. However increasing speed appears to give an increase in the number of particle damage events to the surface, as shown in figure 5.6. This may be due to a reduction of the impact time of the collisions between the probe and the particles, and /or an increase in the amount of material blocking the particles from causing damage. At low speeds it might be expected that particles are slowly drawn into the contact zone. As such each particle has more time to either be entrained or roll out of the contact. Also at high speeds the probe may be passing more energy to the particles. At high speeds particles may not be able to roll out of contact and so are more easily entrained. However as the contact is not ideal the damage is less severe than at lower speed. These explanations of higher energy and more particle interaction would also explain why higher speeds are associated with higher friction (see figure 5.10).

Another explanation is that the smaller particles are being drawn into the contact without damage at low speed but are sufficient to block the entrainment of larger particles. This blocking would mean that the smaller particles must also cause some damage. This may be the small pits seen across the surface, however the pitting damage may also be due to low impact rolling of particles. Overall the particles cause less damage at speed because, although there are more events, the mechanism of wear is significantly less severe.

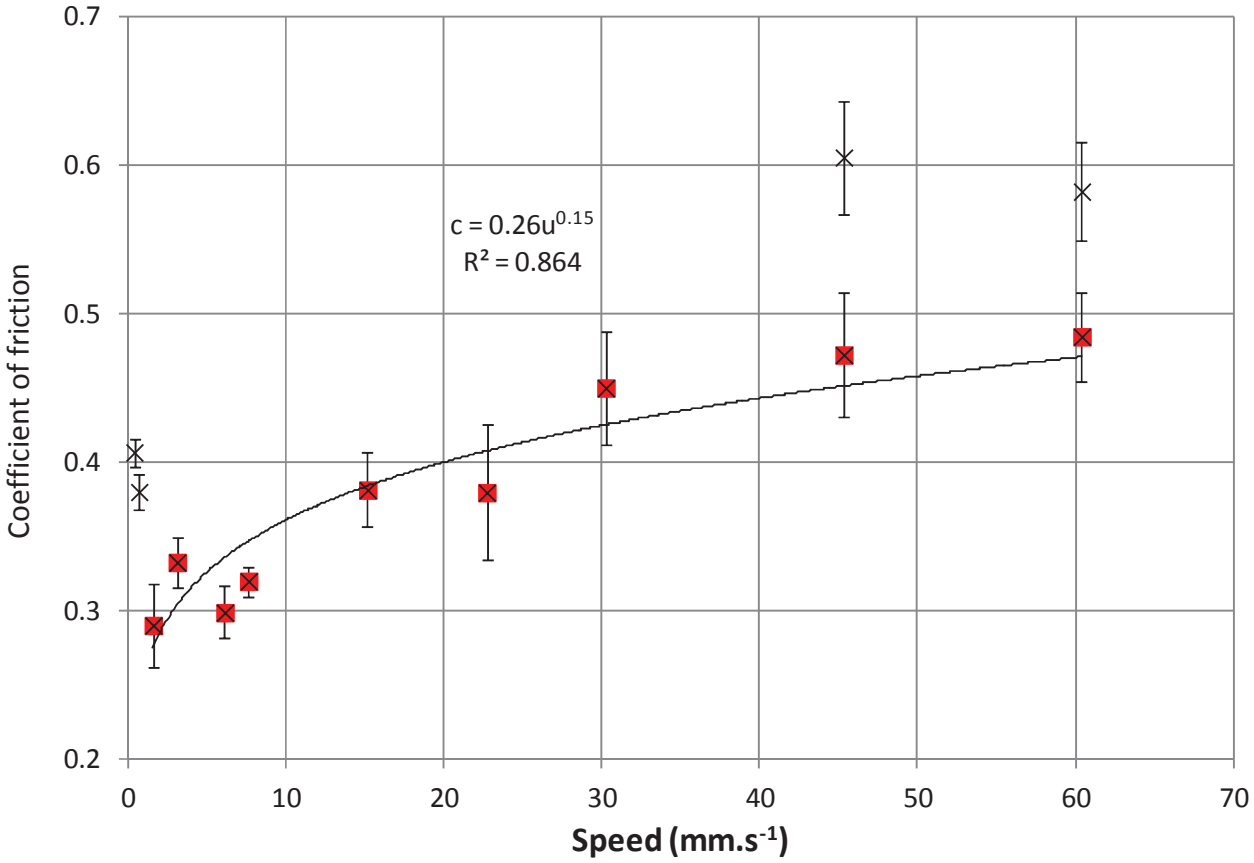

Figure 5.10: Coefficient of friction as a function of probe speeds. d = 62 µm, η_0 = 1 Pa.s, W = 0.196 N, and C = 8.4%vol. Non-highlighted data points were not used in the fit.

At low speeds there appears to be a plateau in the data where the two wear rates are practically identical. This plateau also corresponds to a deviation from the trend in the friction seen in figure 5.10. This lower limit is likely to be due to a system entering a high contact stress state where the lubrication film is so thin that the probe effectively almost always wants to be in contact with the surface. This means there is no drop in height as the speed decreases and the forces applied by the probe become effectively constant. The low speed also will have very little effect on the ability of particles to move out of contact or build up in the contact. Instead the build up and /or particle movement into or out of

contact is similar for all low speed systems. As the fluid is no longer influencing the system it becomes speed independent, which is an Archard system, and maybe termed as a three body “boundary” regime.

There are multiple points of data presented at the higher speeds. Some of the data has been declared erroneous and the remaining data has been measured using a slightly different method. The quantified erroneous data is shown in figure 5.9 and corresponding friction data in figure 5.10. An image of the damage is seen in the erroneous data is shown in figure 5.11. There is a clear pattern of repeated high and low wear on the surface. Prior to this the only inequality in the wear behaviour over the surface was between the centre and edge of contact zone and between the start middle and end points. These differences have been discussed earlier. The pattern of wear here is clearly different. Observation of the probe during the wear process gives an indication of the origin to pattern seen here.

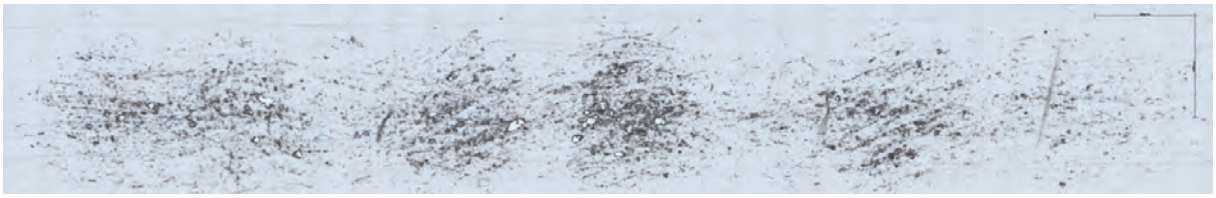

Figure 5.11: An optical microscopy image of the overall damage at high probe speed. The scale bar on the right is 1 mm. d = 62 μm, η_o = 1 Pa.s, W = 0.196 N, L = 300 mm, C = 8.4%vol, and u = 200 mm.s^{-1}.

For each pass the probe carriage is required to switch direction and begin moving in the opposite direction almost instantaneously. At very low speeds the process is observed to be slow and there is a noticeable “turnaround” in the raw frictional force data. This turnaround

is characterised by a slope in the raw friction data (see figure 3.7) as the direction changes followed by a peak in the initial points of friction force after reversal (see section 3.3). The slope is most likely due to compression, bending and flexing in the system particularly in the probe holder. The peak in the friction force appears to come when there is to the sudden change in direction. This jolt means that the probe springs back as it turns around and can bounce, moving vertically, modifying the wear parameters and therefore the friction. As the speed increases the carriage is observed to hit the turnaround harder. This means the slope in the friction is steeper as the probe has less time to change direction. Also the initial peak in frictional force increases in magnitude and the reversing motion less smooth as speed increases. At high speed the reversal in motion not only jolts the arm, it also causes a series of disturbances to the motion. This oscillating motion means that the applied force is not constant and hence the observed damage is not constant across the length. Instead there appears to be sections of high and low wear where the probe has impacted over the surface. Indeed at extremely high speed the reversal of the motion not only seems to cause the probe to oscillate but can cause the entire instrument to vibrate.

In order to minimise the effect of this impacting force the length of the sliding distance can be increased as was done in order to gather the high speed data in figure 5.9. By increasing the sliding distance this allows a greater distance for the wear to occur in and a greater distance for the probe motion to settle; such that at the centre of the wear track the motion is smooth and oscillation free. As a result the wear from samples with a longer sliding distance was seen to follow the trend in the other data in figure 5.9.

Following on from the arguments above it is thought that eventually there will be a limit to the trend when the wear rate drops to almost zero. The trend in wear rate against speed appears to be caused by a limitation in the number of particles larger than a specific size; the size of the gap between the probe and the surface. This gap will increase with speed and the number of particles decreases rapidly with size: therefore there must come a point where the gap is so large that there are a limited number of particles that have the potential to be captured. Unfortunately the data cannot be gathered at such high speeds, with parameters similar to those in figure 5.9, due to limitations in the equipment: specifically vibrations in the tribometer and the track length allowed on the steel samples.

Figure 5.12 summarises the description of the effect of speed on wear described in this section.

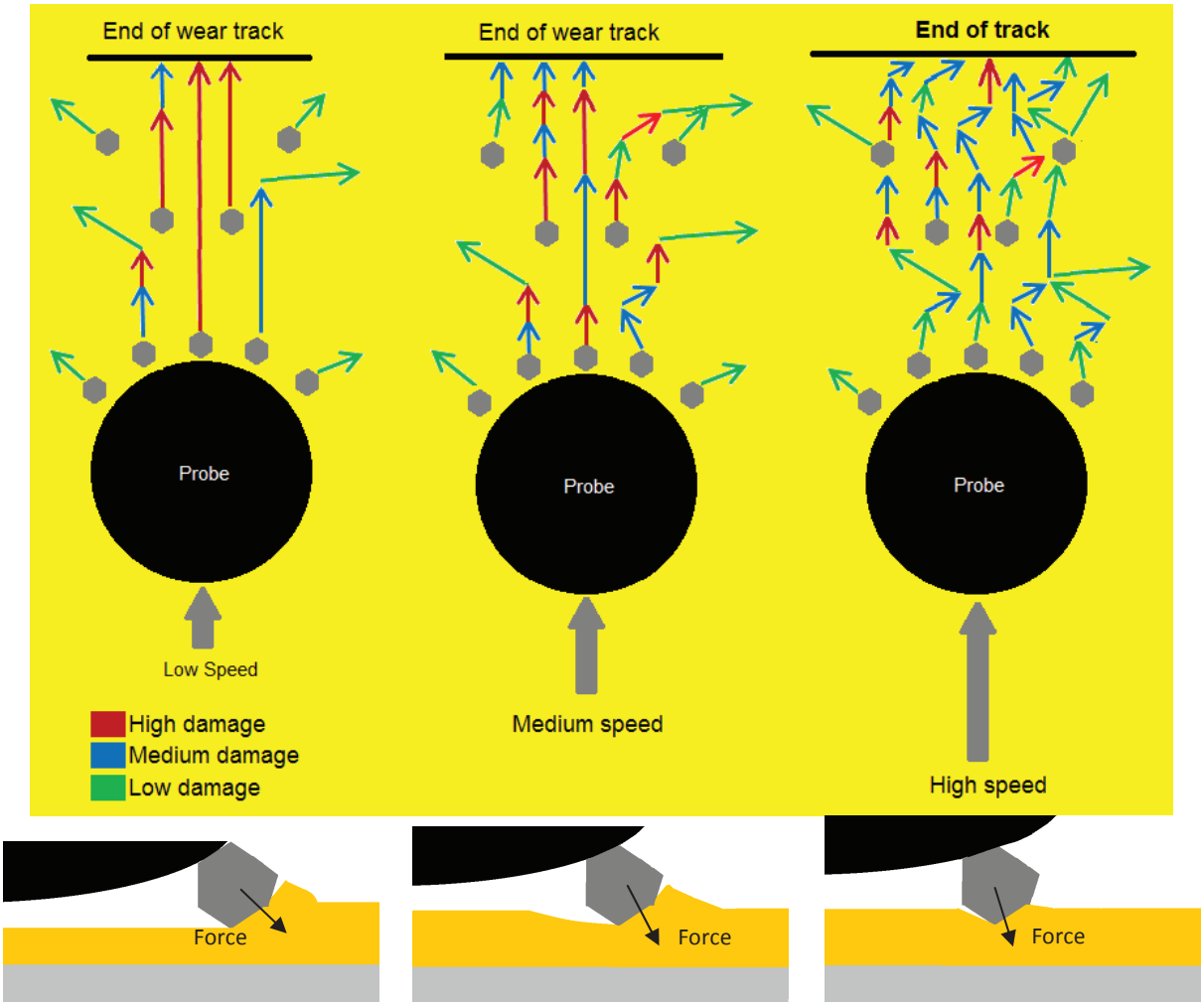

Figure 5.12: Schematic diagram of the effect of speed on expected particle motion and contact geometry. As speed increase the particles move less linearly, the probe height increases and less wear occurs. At low speed the motion is more linear with particles fixed in contact. At high speeds particles are less firmly held and so less wear occurs as particle move less linearly. As will be shown in 5.3 increasing viscosity is expected to have the same effect on the particle capture geometry but the particles motion will not become less linear as viscosity increases.

5.3 Effect of viscosity

In the first part of this chapter the influence of fluid lubrication was studied indirectly from the effect of speed. This section will look into the properties of the fluid and study their influence on the lubrication of the system and consequently the wear of system.

Figure 5.13 shows the visual impact on a wear pattern caused by changing the viscosity, whilst keeping other parameters constant. There is a clear increase in the amount of damage caused by decreasing the viscosity. All images show long, linear repeating or constant wear scars. However, the length of the wear scars increase as viscosity decreases. This indicates that, as viscosity decreases more particles are drawn into the contact zone and / or fewer particles are being lost to the contact zone. This is supported by the optical microscopy in figure 5.14 where lower viscosity leads to an apparently deeper wear depth. However the shape and other features of the wear are similar.

(a)

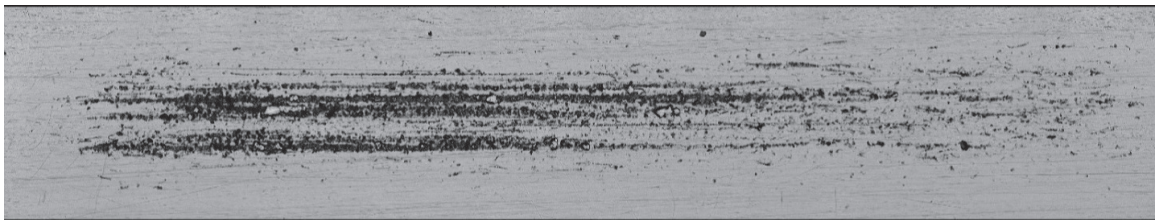

(b)

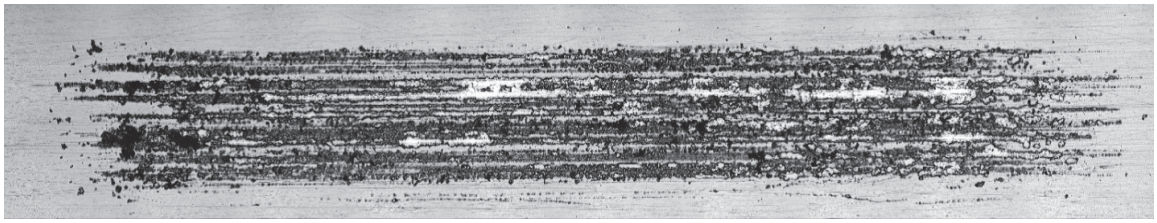

(c)

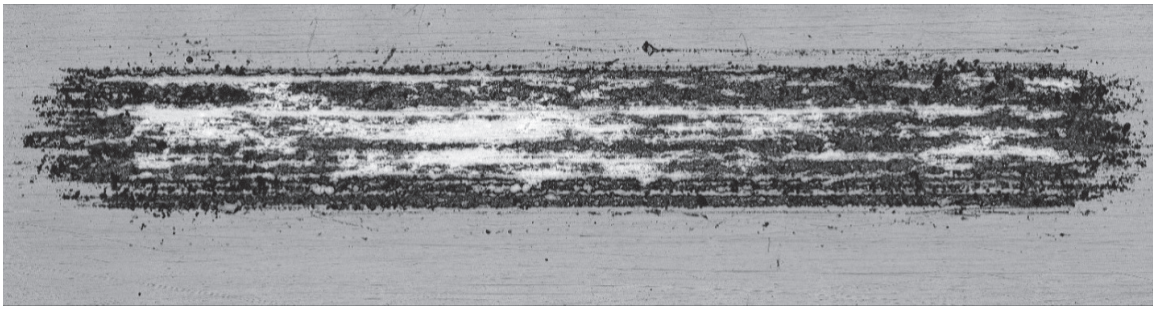

Figure 5.13: Optical microscopy of damage at different continuous phase viscosities. Viscosities are 1 Pa.s (a), 0.2 Pa.s (b), and 0.02 Pa.s (c) respectively. All images are to same scale: the horizontal field of view is 13.6 mm. W = 0.196 N, d = 62 µm, C is 8.4%vol, u is 7.6 mm.s^{-1}, and L is 150 mm.

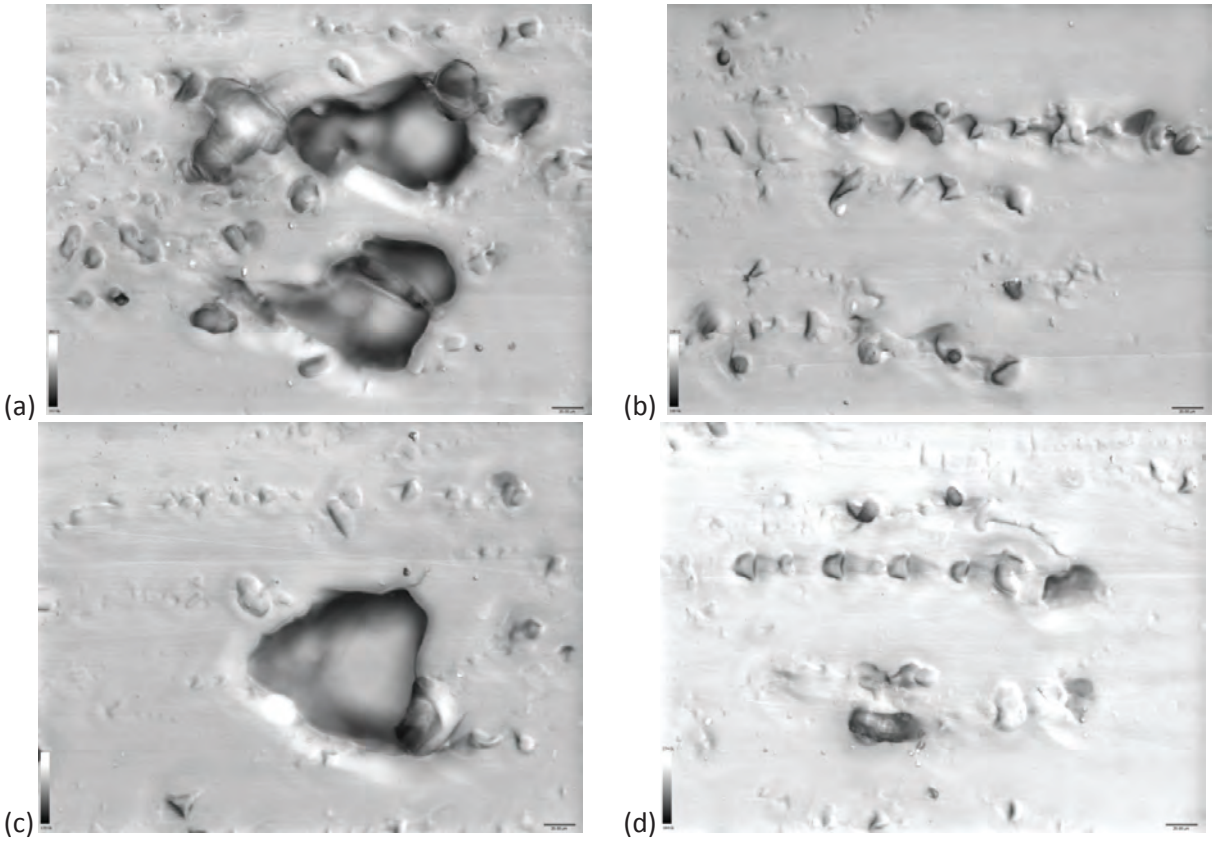

Figure 5.14: Optical microscopy of damage individual wear events different continuous phase viscosities. Viscosities are 0.02 Pa.s (a) and (b), and 1 Pa.s (c) and (d). All images are to same scale and the small bar in the bottom right of the image in 20 µm. W = 0.196 N, d = 62 µm, C = 8.4%vol, u = 7.6 mm.s^{-1}, and L is 15 mm.

In order to understand this process it is necessary to go back to the lubrication equation 5.3. The gap of the probe is proportional to viscosity and speed to the same power, 0.65. The fluid gap increase means that the contact between the probe and appropriate particles becomes greater and more particles slip through the contact. With fewer particles impacting the surface fewer wear scars are seen. The nature of the wear also changes with viscosity. At high viscosity the particles' contact points are higher and so the particles are more likely to chip into the surface. At lower viscosities the particles can be more heavily forced into contact and so, higher damaging, ploughing damage can be seen.

The fact that an increase in film height leads to a decrease in the severity of the major cause of wear damage, means the result of increasing viscosity is similar to an increase in speed. However the visual evidence, in figure 5.6 and figure 5.13, and corresponding height data, in figure 5.7 and figure 5.15, shows two key differences: the amount of low impact wear, which causes the surface to roughen, and the linearity of the wear pattern. As the amount of severe wear decreased with speed there was an increase in mild wear. Increasing the viscosity does not give a secondary wear process. It is also noticeable that the wear of the surface is significantly less linear with an increase in film height due to speed. Whereas the increase in film height due to viscosity caused many of the particle to deviate off the linear path. Therefore it is the short contact time and /or an increase in particle energy caused by increasing speed that is expected to be driving both these processes seen previously, not the lubrication film.

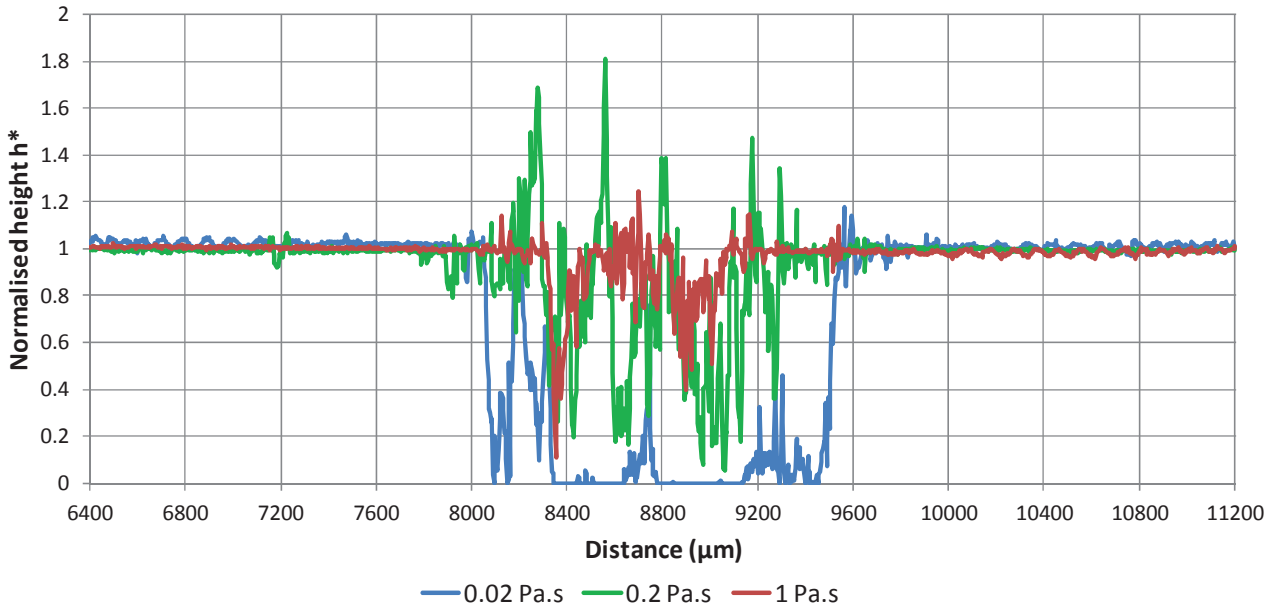

Figure 5.15: Profile of damage cross-section at different viscosities. Viscosities are 1 Pa.s (a), 0.2 Pa.s (b), and 0.02 Pa.s (c) respectively. d = 62 µm, C = 8.4%vol, u = 7.6 mm.s^{-1}, and L = 150 mm.

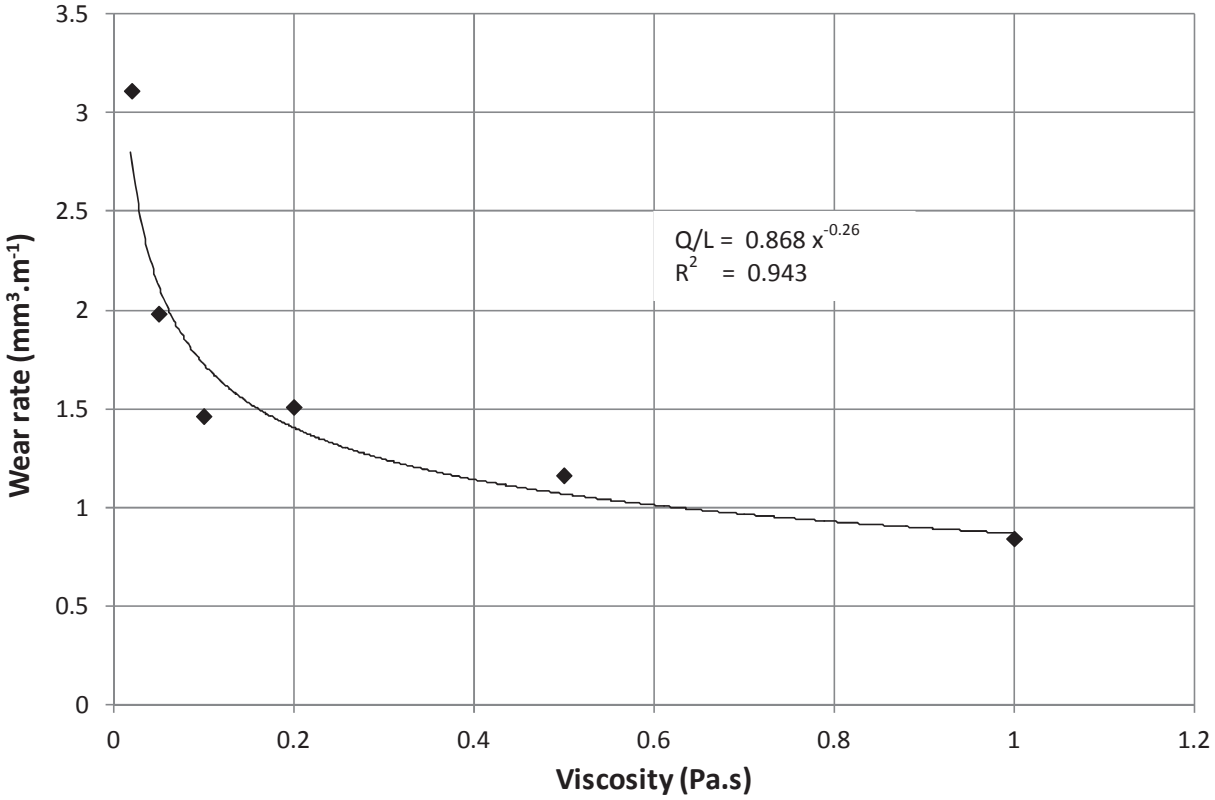

Figure 5.16: Wear rate as a function of viscosity. W = 0.981 N, d = 62µm, u = 7.6 mm.s^{-1} and C = 8.4%vol.

Figure 5.16 shows the effect of viscosity on wear rate and figure 5.17 contains the corresponding friction data. There is a decrease in wear as viscosity increases. This also leads to a reduction in the friction coefficient. The increase in viscosity has an associated impact on the film height. Therefore as viscosity increases fewer particles can be brought into the contact and therefore as seen previously the result is lower wear.

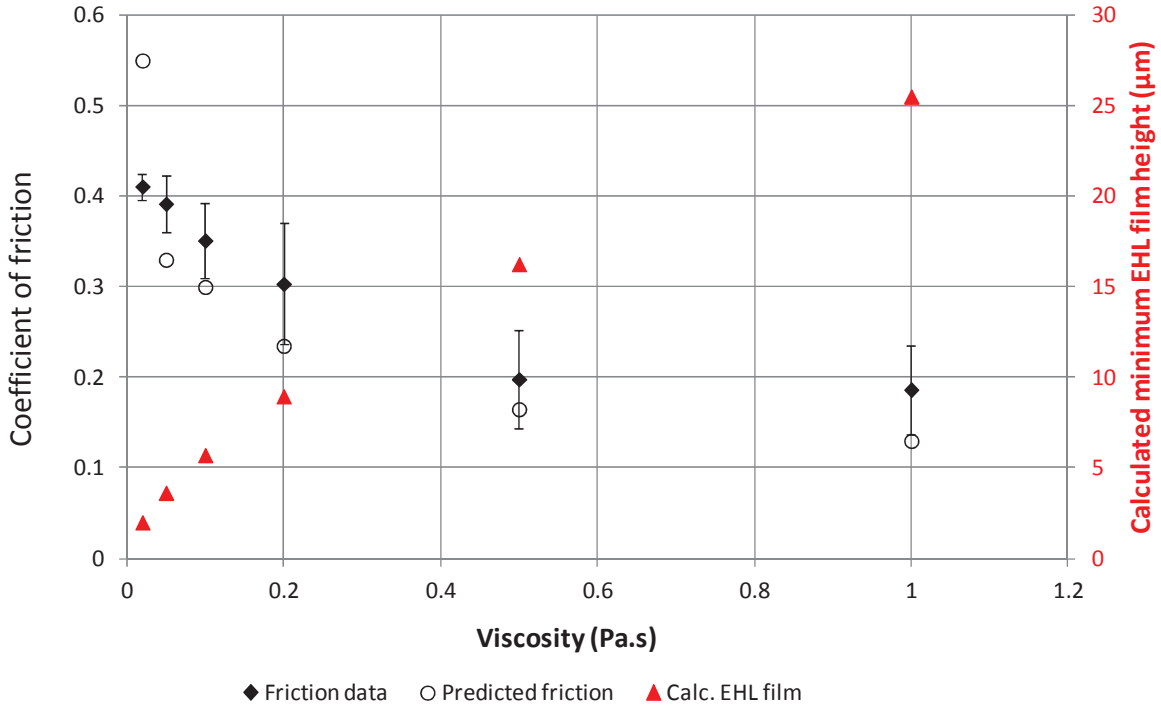

Figure 5.17: Friction coefficient as a function of continuous phase viscosity. W = 0.981 N, d = 62µm, u = 7.6 mm.s^{-1} and C = 8.4%vol. Also shown is the calculated film height for reference

In order to more fully study the viscosity effect, the load has also been varied, as shown in Figure 5.18. As expected there is a decrease in wear as viscosity increases. The curves fitted to the viscosity data shows a relationship of -0.26, compared to -0.33 for the speed data (figure x). This may be due to the equation not describing the lubrication film accurately however it is a typical feature of lubrication film equations that viscosity and speed have the same power. Here it seems the lower trend in wear rates due to the increase in viscosity, when compared to a speed increase, might be due to the lack of a secondary wear process. This secondary wear is from the particle impact as it is moves out of contact. The change in viscosity will only influence the contact point of impact not the momentum or energy

imparted. However, higher speed means a higher energy impact. Hence the change of speed may give rise to a secondary wear effect.

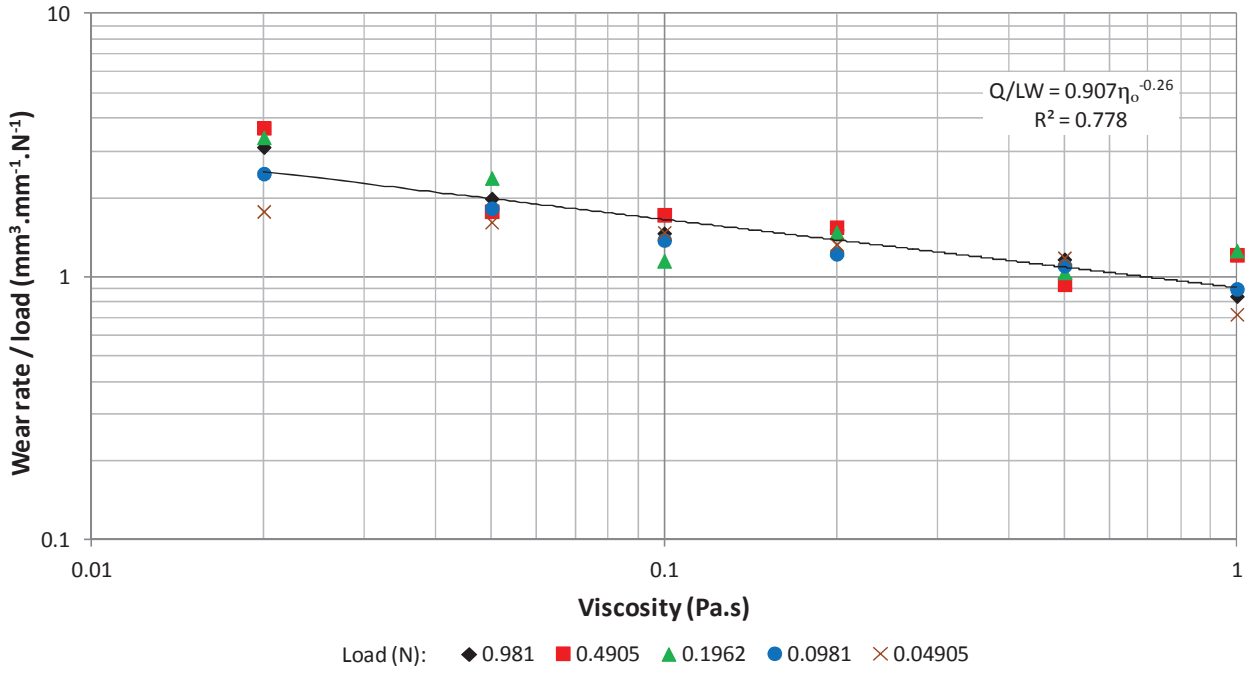

Figure 5.18: Wear rate divided by load as a function of viscosity at multiple loads. d = 62µm, u = 7.6 mm.s^{-1} and C = 8.4%vol.

5.4 Summary

The fluid properties of the continuous phase and slurries were measured. The molasses solutions used were Newtonian within the limitations of the equipment used. The slurries could be modelled using a version of the Carreau equation. It was found that with a fixed particle size and concentration the viscosity at each shear rate could be scaled by the Newtonian, continuous phase viscosity.

The aim of this chapter was to investigating the second aim of this thesis: to characterise the behaviour of the soil wear in response to changes in the flow properties of the suspending fluid. The effect of speed and viscosity were both was found to influence the wear. The wear rate data for speed could be fitted with a power index of -0.33. Similar analysis for viscosity found a power law index of -0.26. Repeat measurements at different loads confirmed a power law index of -0.26.

Overall these two terms can be incorporated into the Archard equation with the result that the equation becomes:

$$Q = \frac{k_{H^* u\eta} WL}{H^*} \eta^{-0.26} u^{-0.33} \qquad (5.4)$$

where H^* is used to donate the fact that hardness effects should only be considered over restrictive range, such that the mechanism of wear does not change. $k_{H^* u\eta}$ is a modified wear coefficient that must have units to compensate for viscosity and speed power laws. It must vary according to the hardness and wear mechanisms prevalent during particular abrasive process conditions.

6. RESULTS AND DISCUSSION: INFLUENCE OF PARTICLE PROPERTIES

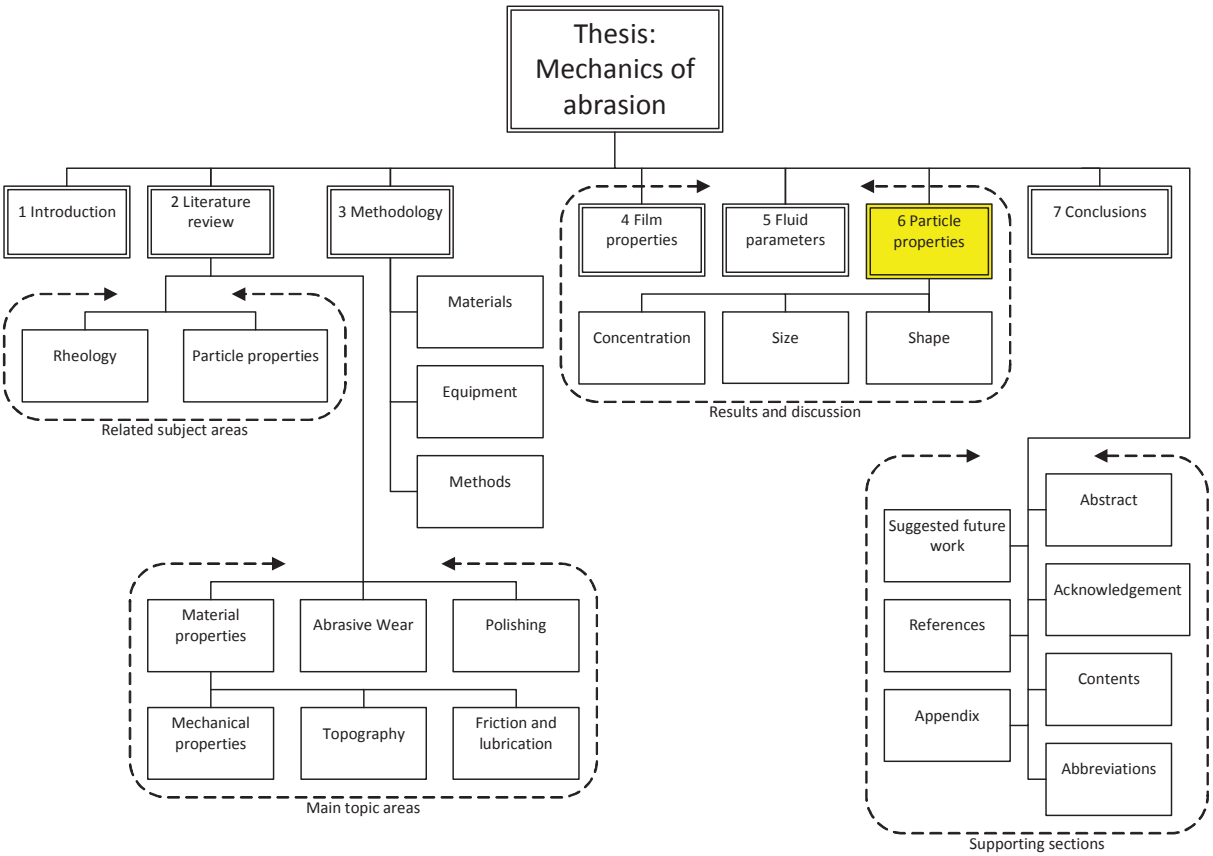

Figure 6.1: Thesis structure overview with the particle properties chapter, 6, highlighted

Results so far show the effect of the multiple parameters included in the standard Archard wear equation, as well as speed and viscosity. These parameters are to a lesser or greater extent outside of the design parameters available to liquid abrasive fluid designers and are controlled by the consumer. This chapter will focus on the more design controllable parameters of particles. Particle properties are also regularly a subject of study in the literature [160, 205-209]. It would be impossible to truly study all the ways a distribution of particles may vary. In this study the aim was to try and gain an insight into how readily

available particles, relevant to the application, can influence the DCO film wear. Further on, following discovery of the unusual behaviour of high aspect ratio particles, the investigation also looks into the phenomena of polishing in the context of household cleaning.

6.1 Effect of particle concentration

The simplest parameter with respect to the affect of particles to vary is their concentration. There are multiple methods that can be used to define of the concentration of the system, particularly by the number of particles, their volume or mass. In this thesis the particle volume is used, which is in line with many previous studies in the literature [42, 45].

Figure 6.2 shows that an increase in particle concentration causes the damage across the whole contact area to increase. It is noticeable at low concentrations that wear patterns shown in figure 6.2 (a) and (b) suggest some initial non-linearity in the particle motion. This may not happen at higher concentrations as there could be physical blocking of the particles coming out of contact, ensuring linear motion. Figure 6.3 shows the profilometer data corresponding to the images in figure 6.2. The graphs show an increase in both the number and depth of wear events as the concentration increase. Figure 6.3 also shows a noteworthy general increase in both the symmetry and “roundness” of the overall two dimensional wear pattern seen as a function of depth. This seems to suggest that as the concentration increases the wear becomes less random and the probability of wear begins to follow the contact stress distribution of the probe.

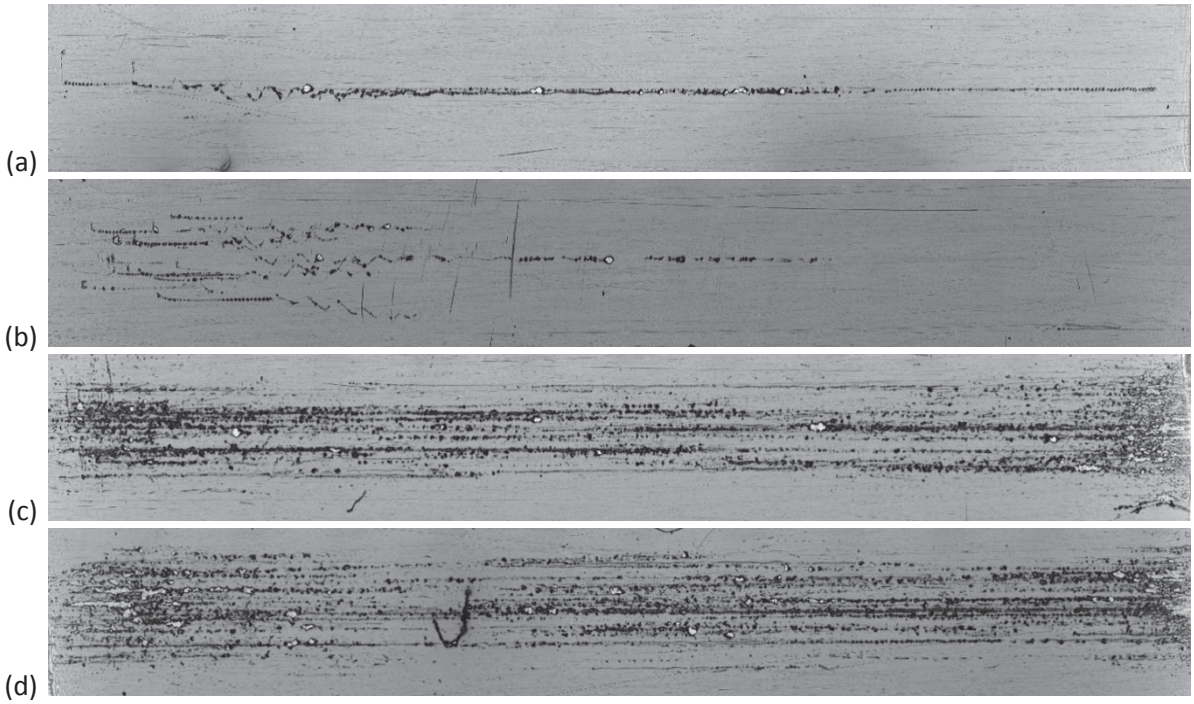

Figure 6.2: Optical microscopy of the overall damage at different particle concentration levels. Concentration levels are 0.4% (a), 1.9% (b), 13.7% (c) and 19.7% (d) by volume. All images are to the same scale: the horizontal field of view is 13.6 mm. d = 62 µm, $\eta_{0=}$ 1 Pa.s, W = 0.19 N, u = 7.6 mm.s^{-1} and L = 150 mm. Soils were baked at 100^{0}C for 60 minutes and tested after 1 week.

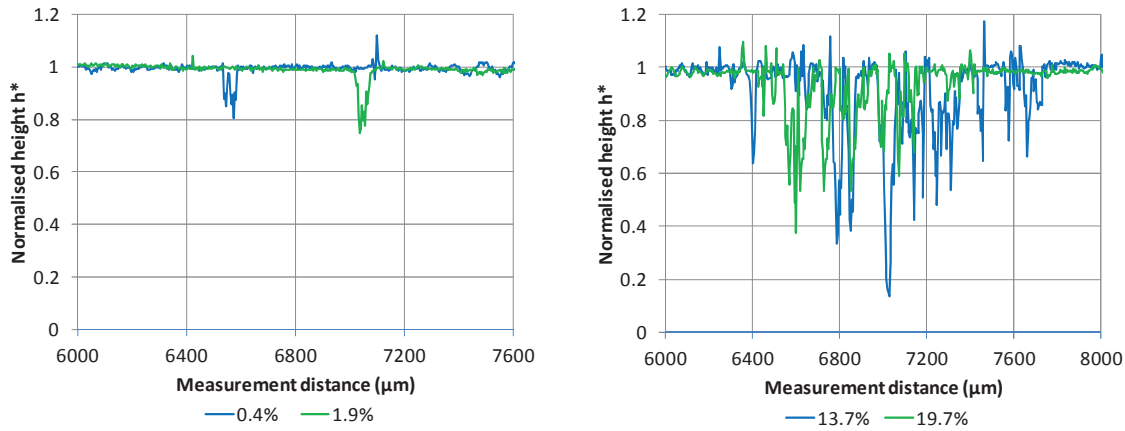

(a) (b)

Figure 6.3: Average, normalised profile of damage at different particle concentration levels. d = 62 µm, $\eta_{0=}$ 1 Pa.s, W = 0.19 N, u = 7.6 mm.s^{-1} and L = 150 mm.

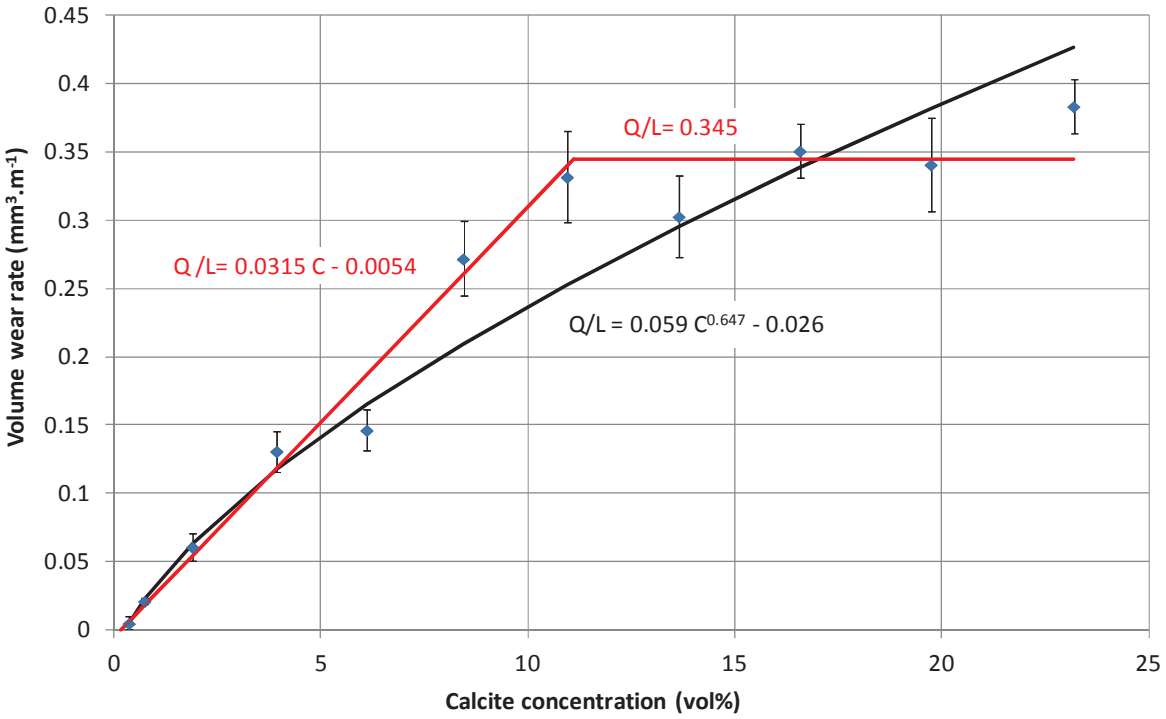

Figure 6.4: Wear rate as a function of particle concentration. d = 62 µm, η_0 = 1 Pa.s, W = 0.19 N, and u = 7.6 mm.s^{-1}.

Figure 6.4 shows the effect of particle concentration on wear rate. As particle concentration increases the wear rate increases. The result is logical as more particles should mean more particles are available to be captured and subsequently wear. The trend may be modelled as either a power law or a two region system. At 8.4% or less there is almost linear increase in the wear rate. At greater than 8.4% there is another linear trend in the data, with a much shallower gradient than the first trend, that here is treated as a constant wear rate. Both this two stage wear trend and the power law suggest the same rationale. Initially wear increases as the number of particles increase because there is a proportional increase in the particles available to be captured and subsequently entrained. At higher concentrations the addition of particles does not have as significant an effect as the contact zone fills. Additional particles are not entrained and are blocked or deviated from the contact. This two stage

process can be used to explain the fact that at high concentrations the particles begin to form a spherical wear pattern. The second stage of wear is a saturated regime, where the contact is expected to be equivalent to a ball with a rough calcite surface. Here this region is referred to as a saturated regime. At lower concentrations the wear is more random as the particle capture is inconsistent and is referred to as the stochastic regime.

Figure 6.5 shows more detailed images of individual wear events. At low concentrations figure 6.5 (a1 and a2) shows the similar repeated Schallamach wear seen previously at higher concentrations such as figure 6.5 (b1 and b2) in terms of deformation and pile up. However the penetration depth appears to be much less and the amount of material removal is much less. This shows that the decrease in concentration is reducing both the number of wear events and severity of wear processes. At higher concentrations figure 6.5 (c1 and c2) shows similar material removal to figure 6.5 (b1 and b2) in depth. However the surface area affected by the chipping does appear more random at the higher concentration (in terms of the surface area of damage seen), which means that each wear event is less consistent suggesting more random, less entrained particles. However there are more of these wear events to detect supporting the idea that more particles in the contact. Overall there are more particles but also more particle-particle interaction which hinders smooth entrainment.

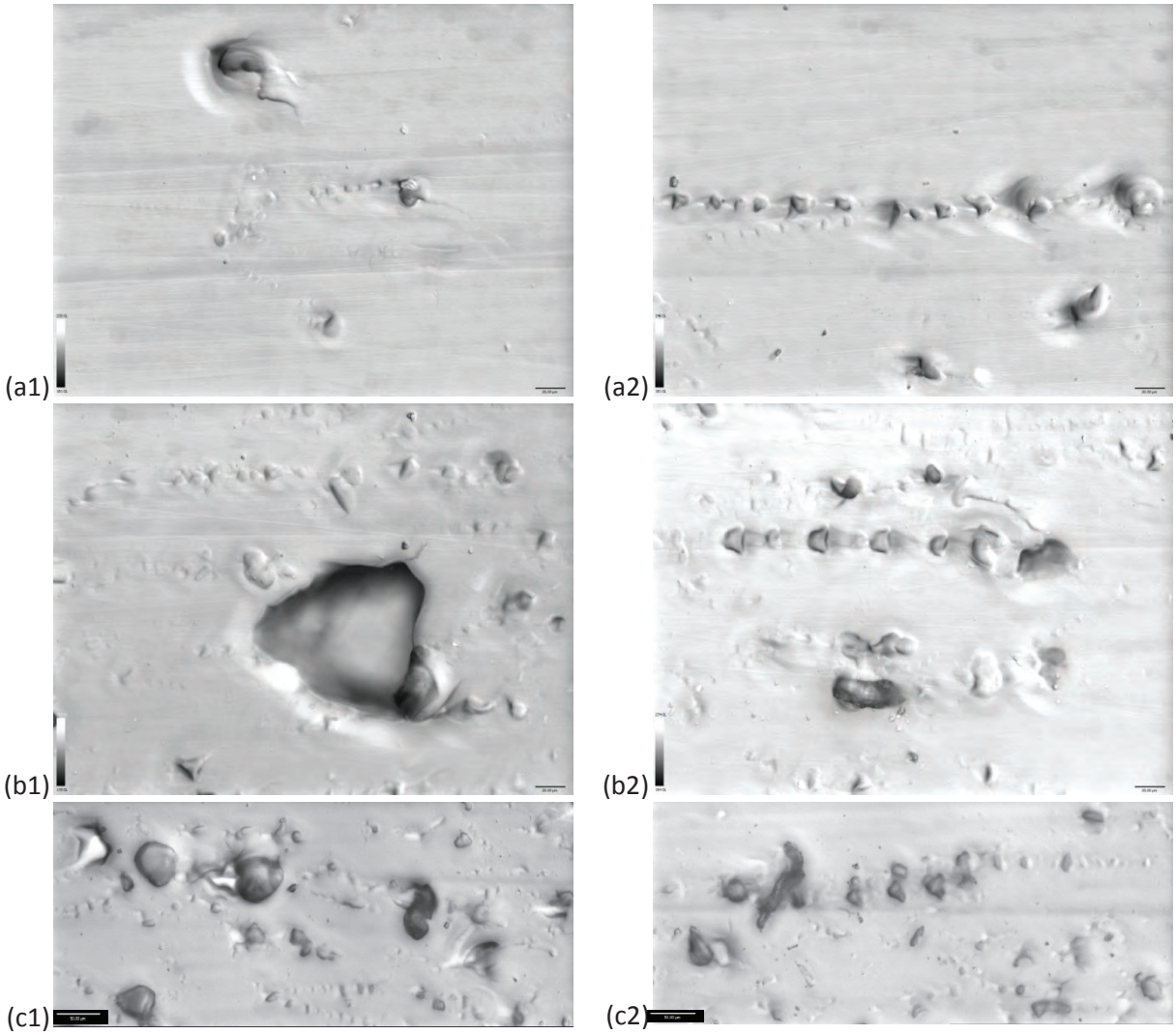

Figure 6.5: A collection of images showing typical wear features seen on the samples at different particle concentration levels. Images are taken on samples where the sliding distance is less than 60 mm. The scale bar on images a1, a2, b1 and b2 is 20 µm. Images c1 and c2 were taken by stitching two images together and the scale bar is 50 µm. Concentration levels are 1.9% (a1 and a2), 8.4% (b1 and b2) and 19.7% (c1 and c2) by volume. d = 62 µm, η_0 = 1 Pa.s, W = 0.19 N, u = 7.6 mm.s^{-1} and L = 150 mm.

The corresponding friction data to the wear data is shown in figure 6.6. The data shows a clear increase in friction with concentration that can be fitted to a power law. However it is possible, given the errors that at greater than 15 %vol the data almost reaches a constant with a large amount of noise, agreeing with the two stage system suggested in figure 6.4. It

is worth noting that the friction predicted between the probe and surface from the previous chapter is approximately 0.15. This suggests that at low concentrations the particles aid lubrication. This must means particles are being trapped and rolled in the contact region. There is visual evidence in figure 6.2 and figure 6.5 that some particles do roll at low concentration. The reason why friction increases with concentration is probably due to particles beginning to fill the contact region preventing free motion of particles and aiding entrainment. At higher concentrations the contact region is likely to be packed with particles so the coefficient of friction is dominated by the effect of particle-particle interactions. This may mean the particle concentration reaches a limit as the particle system is locked in front of the contact. It is unclear if this limit is at 11 %vol or at a much higher value.

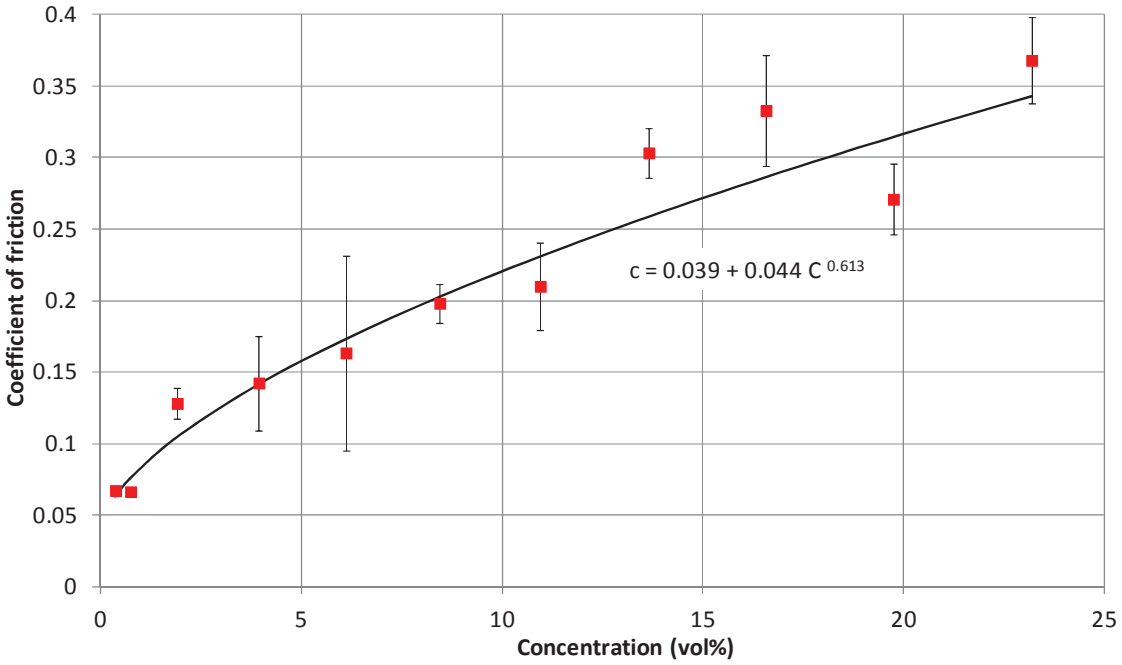

Figure 6.6: Friction as a function of particle concentration corresponding to the wear data in figure 6.4. d = 62 µm, η_0 = 1 Pa.s, W = 0.19 N, and u = 7.6 mm.s^{-1}.

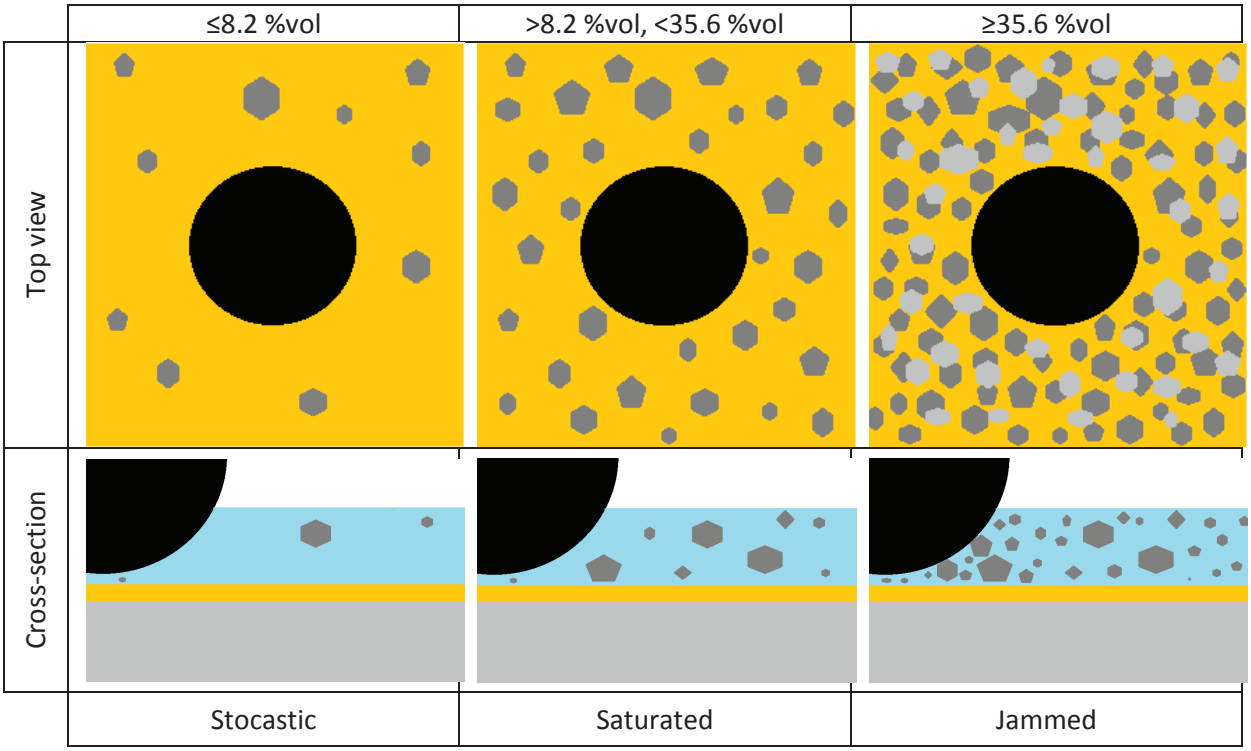

Figure 6.7: Schematic diagram summarising the expected effect of concentration on the contact that results in the observations seen in this section. At low particle concentrations interactions are rare and the wear relies on random interactions. As concentration increases the particle interaction become more regular wear increases until the number of is high enough that particle wear is independent of particle number. Eventually there are too many particles, as particles will jam between the contact and surface, preventing wear.

At a very high particle concentration, 35.6 %vol it was found that the particle system formed a thick paste that did not readily flow. Attempts to use the paste appeared unsuccessful and very little wear was created, with a wear rate of 0.007 $mm^3.mm^{-1}$. Observation of the probe during the wear showed that the low wear rate was due to the fact that the probe was sliding near the surface of the paste and barely penetrating into the "liquid" layer. Essentially the particle system had become fully jammed and did not readily flow. This system was designated as not of interest to the project as it is not a reasonable system due to the fact it could not flow and commercial household LACs are generally <25 %vol abrasives. However

the result does mean that at very high particle concentrations the wear rate should approach a peak value and then drop to zero as the system jams. The schematic in figure 6.7 summarises the explanation of the effect of particle concentration on wear described in this section.

6.2 Effect of particle size

There are a significant number of commercially available particles that can be chosen for a LAC system. The selection of appropriate particles for research purposes would ideally be between monodisperse uniformly shaped samples of different sizes such that custom distributions could be used with tightly controlled parameters. However, the production of such a collection of particles would either be prohibitively expensive for any practical experiment and /or impossible to acquire on an appropriate time scale. Therefore the selection of an appropriate set of particles was between commercially available samples. By far the most common material used for LACs are fine ground natural chalk (FGNC). A collection of FGNC particles with different size distributions were acquired. Each sample is designated by the expected mean particle size. In order to produce a narrower, more precise distribution of particles for the tribological studies the 65 AV particles (see subsection 6.2.1) were sieved and the resulting sieve fractions investigated.

6.2.1 Particle size measurement

As the exact information on the FGNC particles is not known and the parameters quoted in product documentation is measured on a random section of the bulk production, each

sample used was imaged and measured for this project. Figure 6.8 shows SEM images of the ground calcite. The images show that the particles are angular at all size ranges and suggest a wide size distribution. As detailed previously the measurement of particle size and shape is not a trivial one and there exists, to this author knowledge, no way of fully classifying the three dimensional size and shape of these particles in full. Instead any shape measurement would rely on a measurement of a two dimensional projection of the area of the particles. Classifying the size of the particles used laser diffraction method. The size distribution data for this data is shown in figure 6.9.

Figure 6.9 shows that the unmodified particle sizes have wide and complex distribution (it would not be possible to fit all the data to the same simple model). The data also indicates how increasing the size of the particles rapidly reduces the number of particles in a given area or volume. In reality these samples are not ideal to work with to investigate size effects as they have a significantly large size variation.

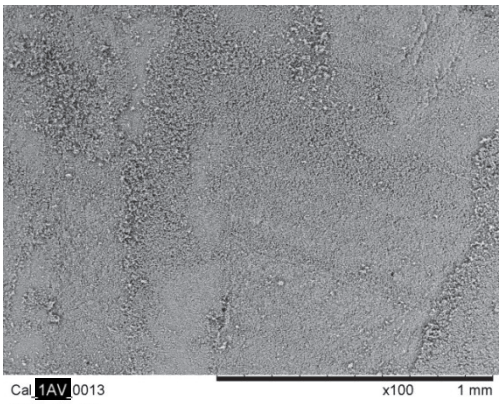

(a1)

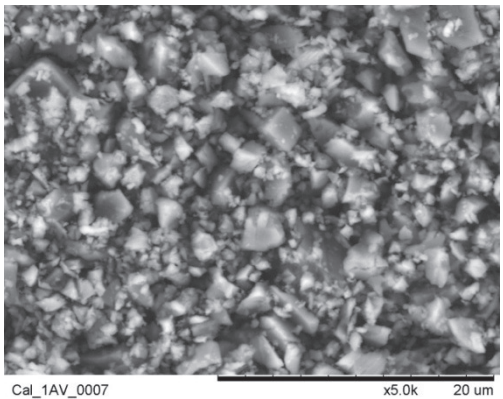

(a2)

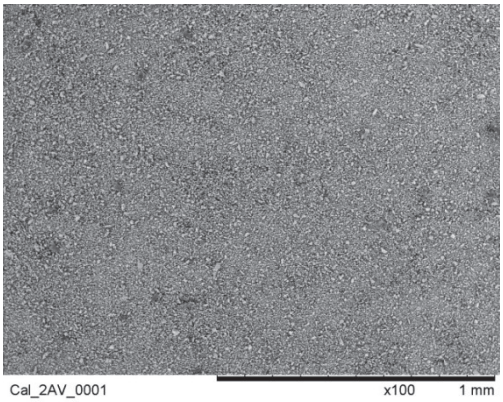

(b1)

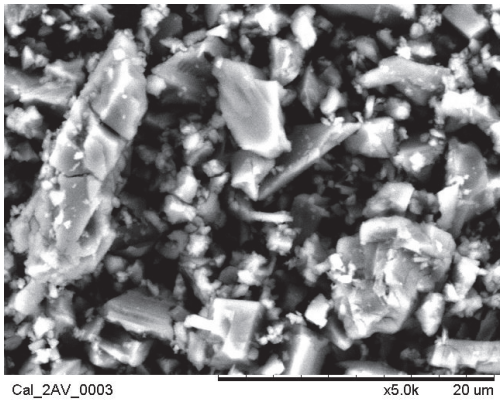

(b2)

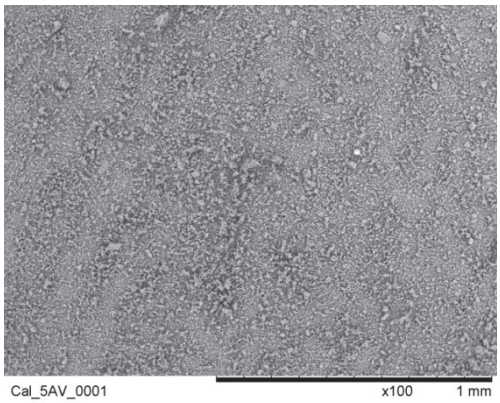

(c1)

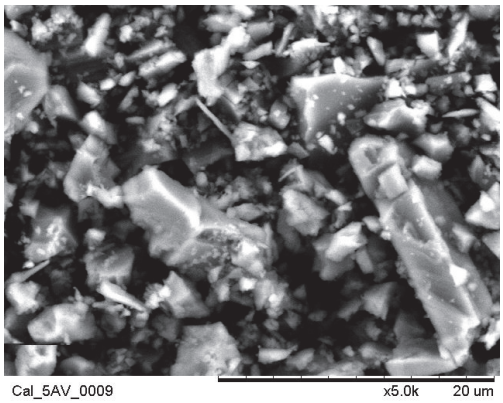

(c2)

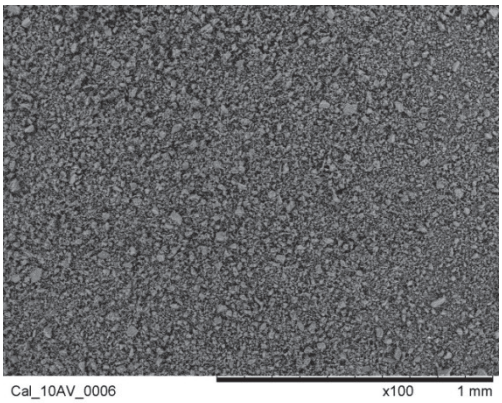

(d1)

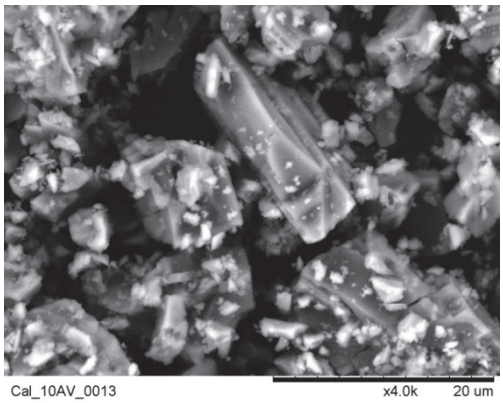

(d2)

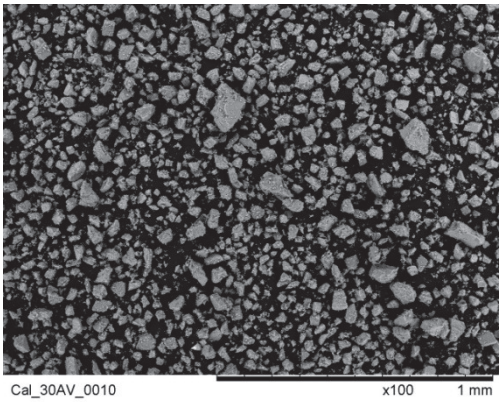

(e1)

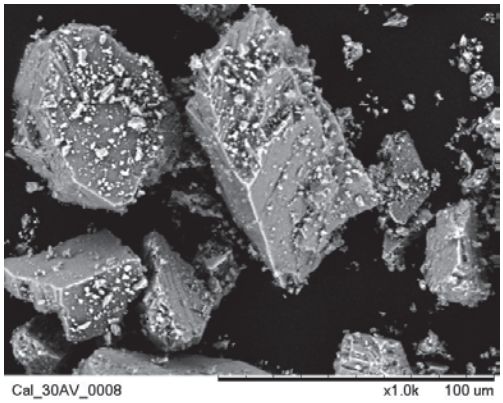

(e2)

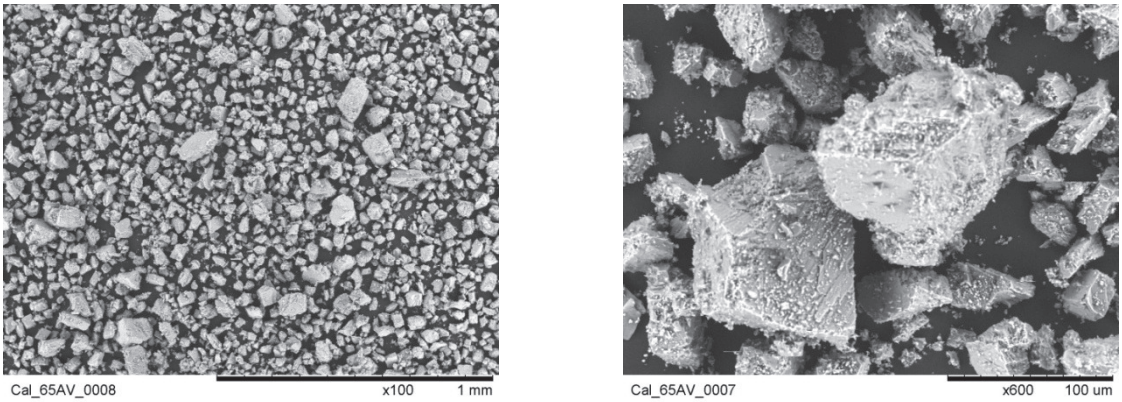

(f1) Calcite Particles (f2) Calcite Particles

Figure 6.8: A collection of SEM images showing the raw, milled but not sieved, calcite particles used. Note: the left hand images are all at x100 magnification to aid comparison of the sizes.

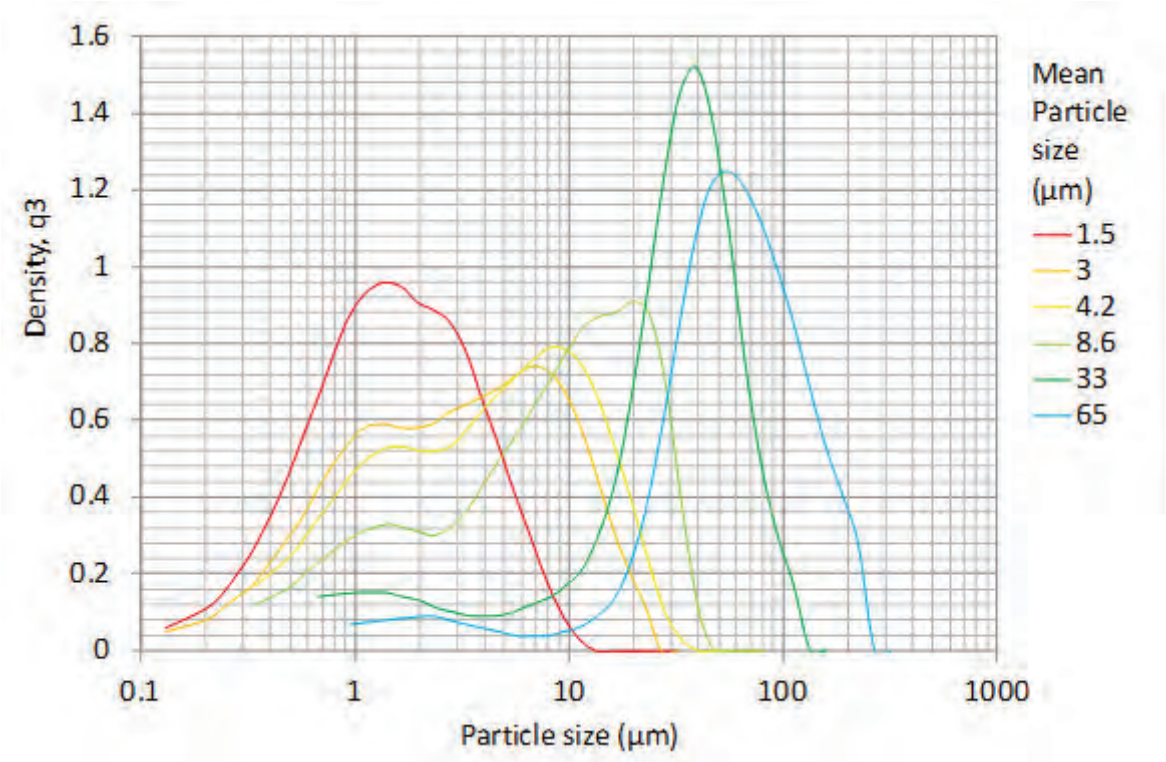

Figure 6.9: Particle size distribution of the milled particles shown in figure 6.8

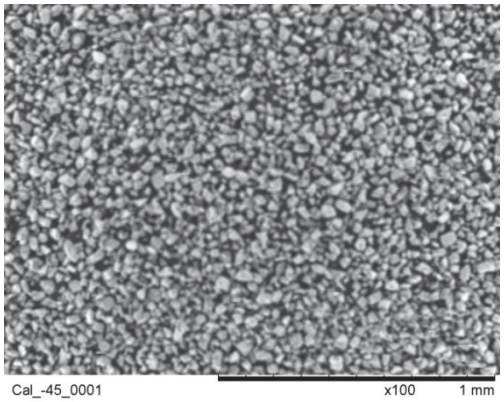

(a1) Calcite Particles

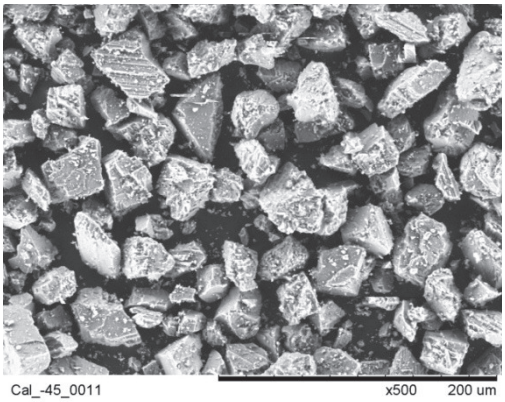

(a2) Calcite Particles

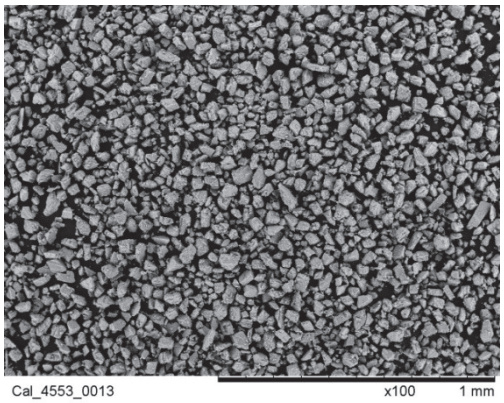

(b1) Calcite Particles

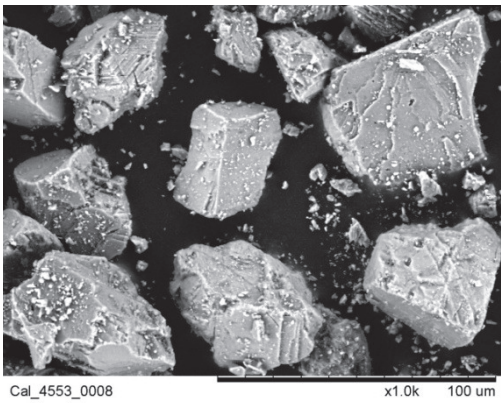

(b2) Calcite Particles

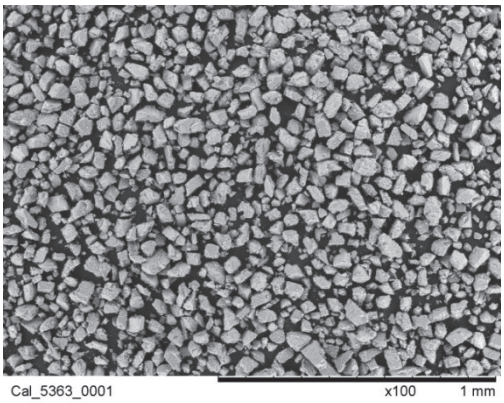

(c1) Calcite Particles

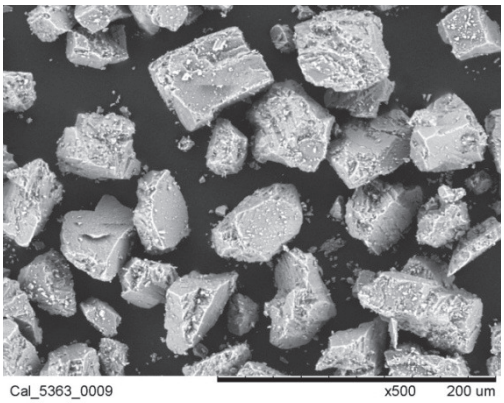

(c2) Calcite Particles

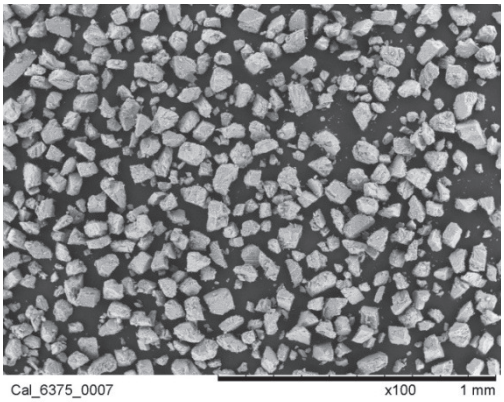

(d1) Calcite Particles

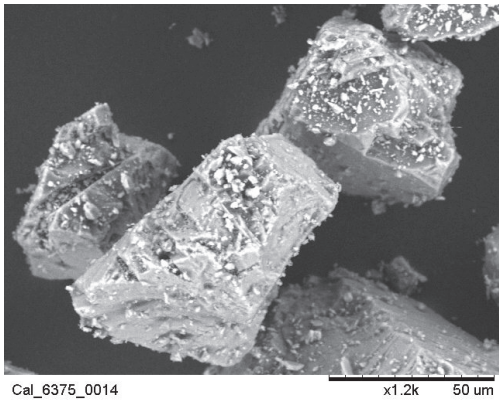

(d2) Calcite Particles

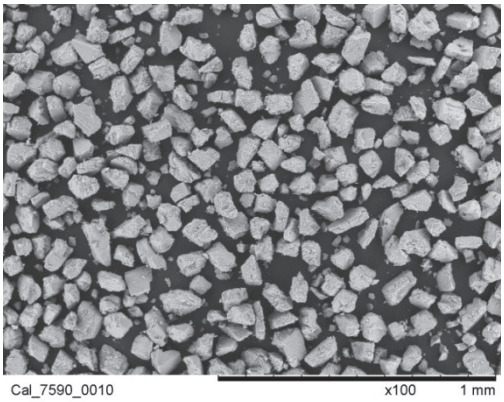

(e1) Calcite Particles

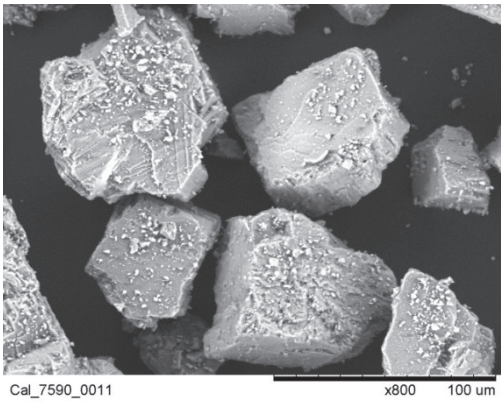

(e2) Calcite Particles

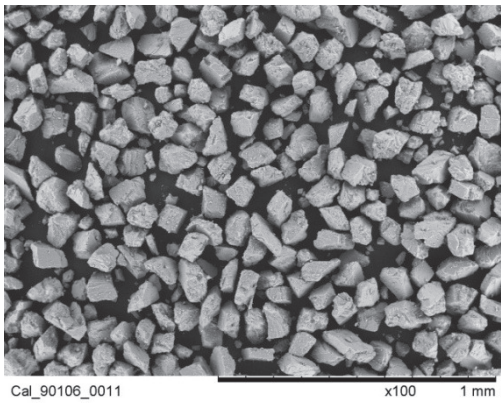

(f1) Calcite Particles

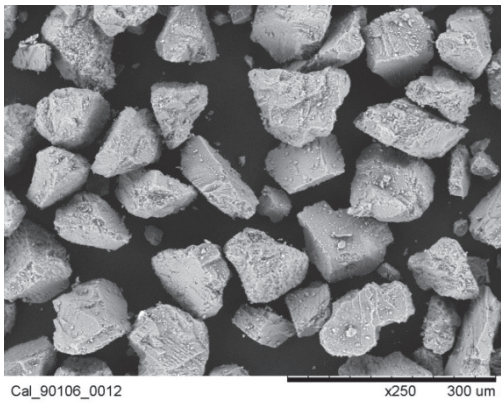

(f2) Calcite Particles

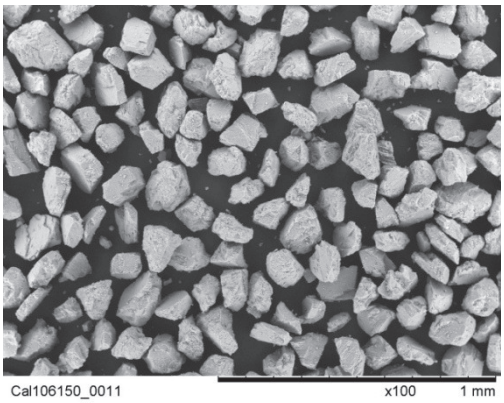

(g1) Calcite Particles

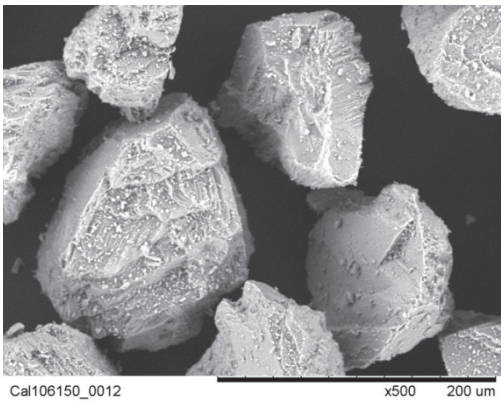

(g2) Calcite Particles

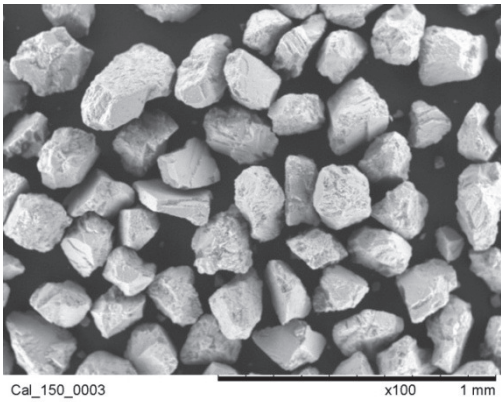

(h1) Calcite Particles

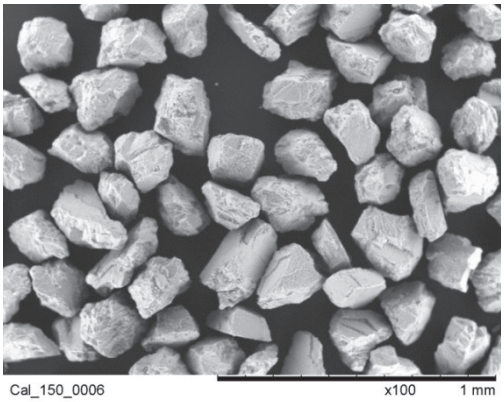

(h2) Calcite Particles

Figure 6.10: A collection of SEM images showing the particles produced by sieving 65av particles.

Figure 6.10 shows SEM images of the sieved particles. The images show, as expected, that an increase in lower grid size in the sieve column corresponded to an increased particle size and a reduction of particle number. Visually all the samples appear to show angular, blocky particles of different sizes. The shape of these particles have not been fully categorised, however these visual images show no significant deviation in the overall shape. It is arguable that the larger particles become more rounded with smoother facets. However, if this perceived change in shape is fully representative, the effect is expected to be too subtle and difficult to quantify. This subtle change in shape would also be largely irrelevant as it is not possible to acquire particles with such subtly different shape derived from the same base material (and therefore mechanical properties).

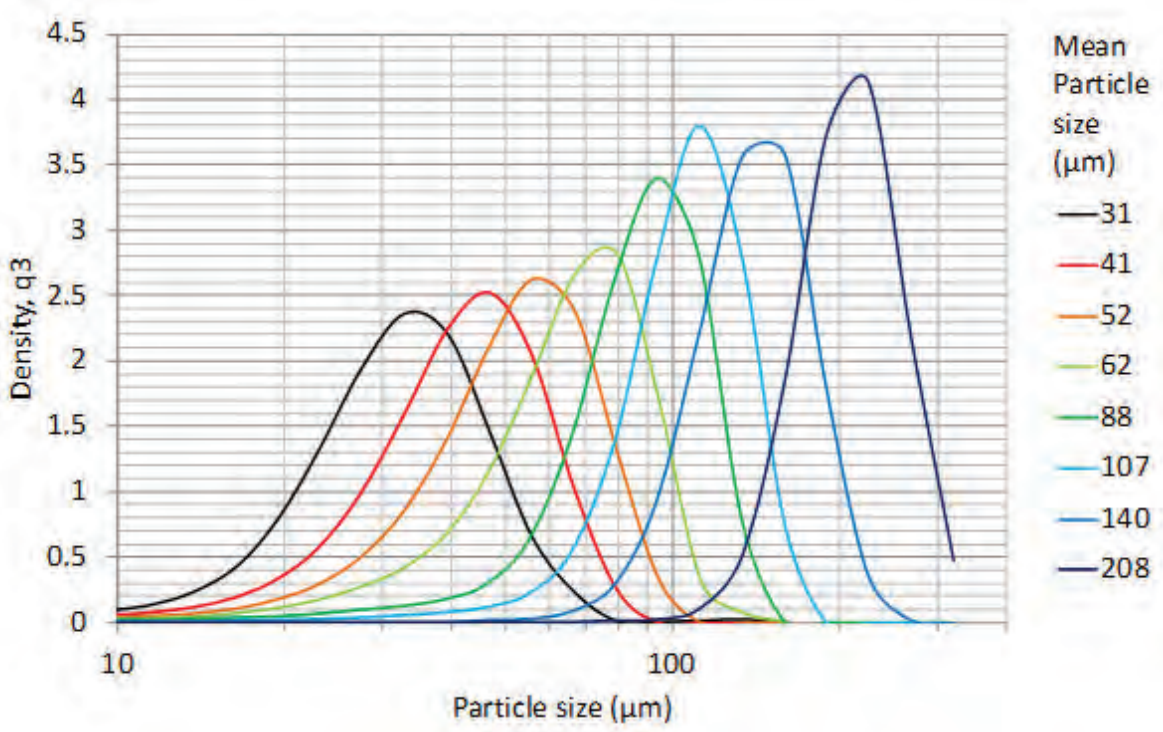

Figure 6.11: Particle size distribution of the sieved particles shown in figure 6.10

Figure 6.11 shows the corresponding size distribution data to the imaged particles in figure 6.10. Predictably there is an increase in particle size as sieve size increases. It is noticeable that the graphs are very smooth and none show a significant cut off in any of the distributions at either high or low sizes. At the lower size end of the distribution it might be expected that some smaller particles go “unsieved” and therefore remain to be measured. At the higher end it might be supposed that some of the particles that go through the sieve are re aligned before measurement to allow for a greater size. However this smoothing is more likely part of a measurement artefact, as it is expected that there should be a sharp drop in the number of particles going through the sieve when the appropriate sieve size is reached. The process of measuring the samples takes a scattered light distribution and models it to an appropriate particle size distribution. Many assumptions and processing steps are taken by the software that may not be appropriate when there are possibly distinct bands of particle sizes. Unfortunately the algorithms controlling this calculation equipment are proprietary and the software cannot be adjusted; so it is not possible to refine the data to try and define a more accurate size distribution for each of the particle samples.

Overall the data in figure 6.11 primarily shows that a series of particle distributions have been made that are distinct from each other, and have a different mean particle size. A summary of these particles is shown in table 6-1. Although it would be possible to model the data to a distribution, this would not be beneficial as the distribution would be calculated from potentially erroneous, estimated particle size calculations.

Table 6-1: Summary of the particles used. All numbers are sizes in µm

Manufacture quoted raw particle size	Lower sieve	Upper Sieve	Measured mean particle size, $D_{4,3}$
1 AV	N/A	N/A	1.5
2 AV	N/A	N/A	3
5 AV	N/A	N/A	4.2
10 AV	N/A	N/A	8.6
30 AV	N/A	N/A	33
65 AV	N/A	N/A	65
65 AV	N/A	45	31
65 AV	45	53	41
65 AV	53	63	52
65 AV	63	75	62
65 AV	75	90	88
65 AV	90	106	107
65 AV	106	150	140
65 AV	150	N/A	208

6.2.2 Impact of particle size on wear

Using an 8.4 %vol concentration, as used in the previous chapters, the overall visual impact on particle size on wear is indicated in figure 6.12. Primarily the sieved particles were used. As there were no sieved particles below 30 µm, to capture low size data some raw FGNC particles were used. These images show that there is a general trend of increasing damage as particle size increases. The corresponding profilometer data are shown in figure 6.13 and supports this observation. However, the distinction between 62 µm and 107 µm is less clear.

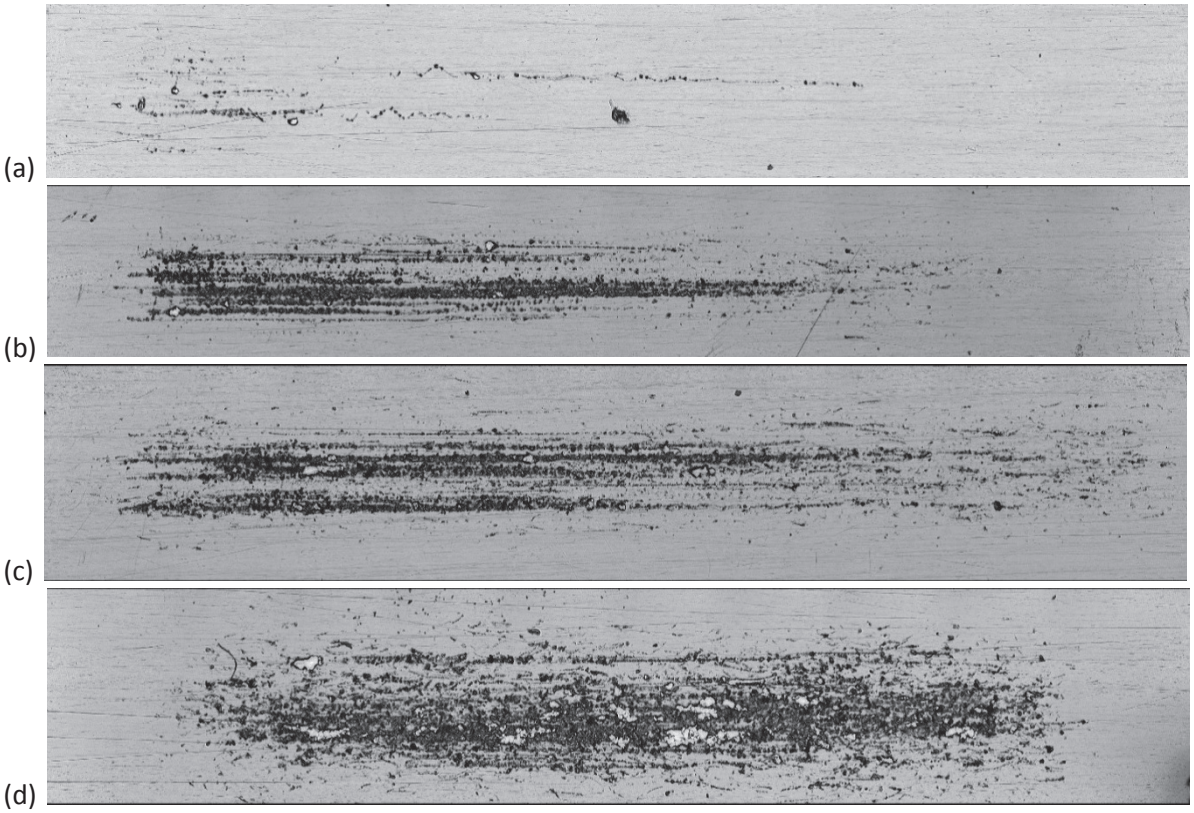

Figure 6.12: Optical microscopy of the overall damage from different particle sizes. Particle sizes are 8.6 µm (a), 41 µm (b), 62 µm (c), and 107 µm (d). All images are to same scale: the horizontal field of view is 13.6 mm. η_0 = 0.02 Pa.s, C = 8.4%vol, W = 0.196 N, sliding u = 7.6 mm.s^{-1}, and L = 150 mm.

In particular the profilometer data figure 6.13 (b) shows two different types of wear. At the lower 62 µm the wear shows a collection of 5 distinct large wear paths that are also seen visually in figure 6.12 (c). The data suggests that at this concentration particles are being captured, entrained and are causing wear in a similar manner to that seen previously. By comparison figure 6.13 (a) shows two wider wear paths with rough surfaces and in figure 6.12 (d) it is hard to make out the individual wear paths of single particles. Instead the image shows a roughened surface where multiple particle and surface interaction have taken place. This observation means that either there are more particles interacting with the surface or each particle is interacting with the surface more times.

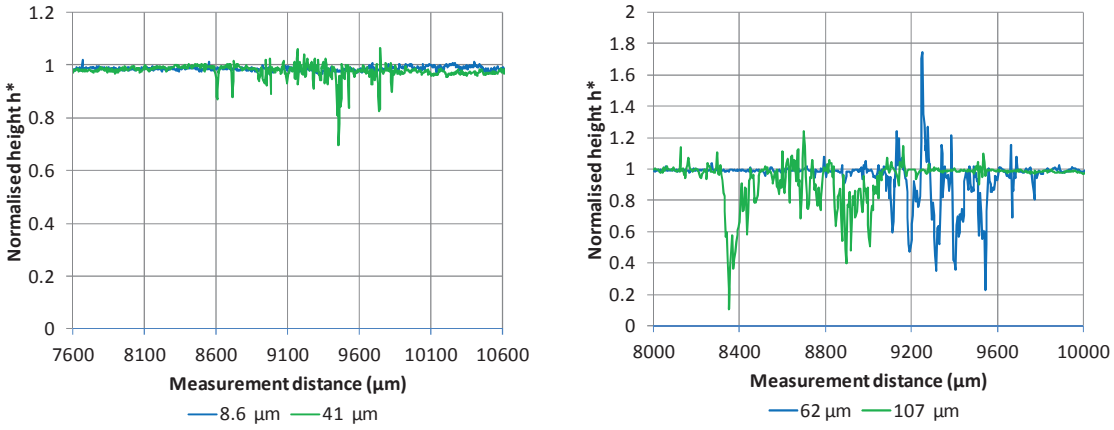

(a) (b)

Figure 6.13: Average profile of damage at different particle sizes. η_0 = 0.02 Pa.s, C = 8.4%, W = 0.196 N, u = 7.6 mm.s^{-1}, and L = 150 mm.

The profilometer data in figure 6.13 are quantified into wear rates by varying the sliding distance. Further particle sizes are studied in order to study the wear rate as a function of particle size in figure 6.14. Figure 6.14 shows three different regions of wear. There is very low wear for the particle distributions with a mean size below 8.6µm. Then there is a significant increase in wear rate up to 140 µm. At 208 µm the wear rate actually appears to have dropped.

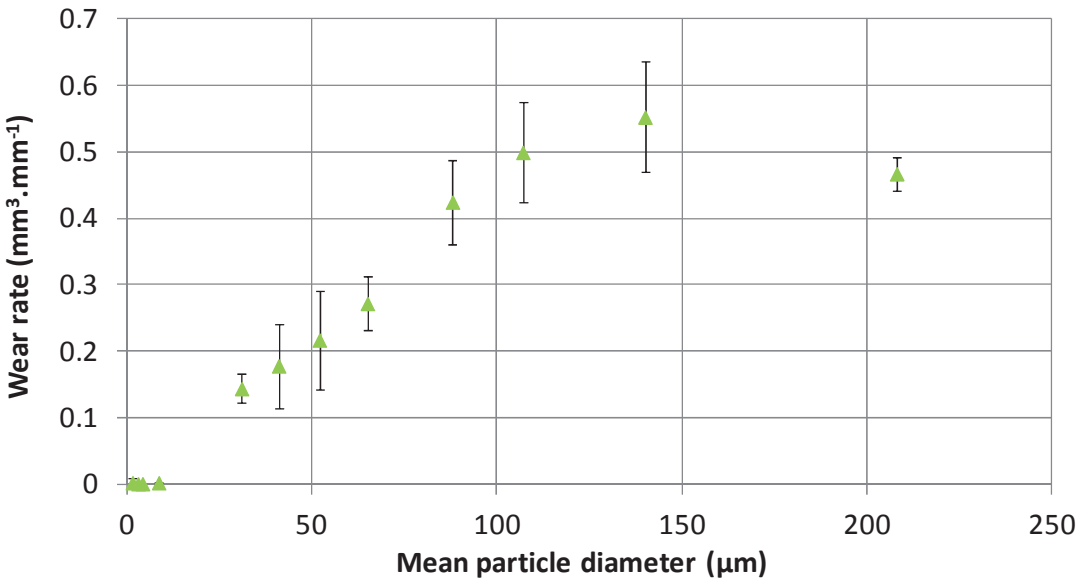

Figure 6.14: Wear rate as a function of particle size. η_0 = 0.02 Pa.s, u = 7.6 mm.s^{-1}, W = 0.196 N and C = 8.4%vol. The calculated minimum lubrication film thickness is 2 µm.

The very low wear rate for small particles (particles below 8.6 µm in size) is of the order 0.001 $mm^3.mm^{-1}$. Much of the data is not reliable and is provided for indication only. This is because the experiments to produce the wear rate will have only measured low wear volumes that are expected to be near to or below the limit of detection. At these extremely low wear rates either few or no particles are interacting with the surface and /or the particles in the contact are causing little damage. Figure 6.12 (a) suggests both these effects are occurring. The reason for the low particle capture and wear may be explained by examining the expected film height. The expected film height is 2 µm. It is therefore reasonable to assume that for particles near to this size a significant number of particles may pass through the contact unaffected. Those particles larger than the gap size will be contacted at a high up on their form, hindering capture.

The significant increase in wear rate up to 140 µm is what might be expected. Increasing the particle size means there is a majority of particles significantly larger than the film gap, so particles can be more readily captured. The drop at 208 µm is not expected but can be explained. Increasing the particle size may mean that the particles are more likely to be captured but it also means the number of particles will be dropping. With the volume density constant, the number of particles will fall as the third power of particle diameter. If the particles were monodisperse, then there would be a third less particles at 208 µm than at 140 µm. Figure 6.11 shows the particle distribution and it suggests that there is a narrowing of the size distribution with increased size. This most likely because of the surface attraction effects between the particles themselves and between particles and the sieve mesh increase as size decreases. This means that mechanical energy required to make

particles pass through an opening increase, so more finer particles that should pass through the mesh are above the mesh. It also means that the particles that pass through the sieve. The 208 µm sample would have very few particles below 100 µm, whereas the 140 µm sample will have many particles in the 50 µm to 100 µm size range. The narrowing of the size distribution would be expected to exaggerate (i.e. give a sharper peak in the data) the effect of the mean size increase on the number density. However without a selection of samples with a range of narrower distribution particles it is not possible to study this effect further.

Figure 6.15 shows more detailed images of the wear features seen when the size is varied. At low size figure 6.15 (a1 and a2) shows that particles only just indent into the surface and there is a minimal amount of deformation and damage or material removal is minimal. In fact much of the deformation results in no material removal. By comparison when the size is increased figure 6.15 (b1 and b2) shows a significant increase in number of entrainment events and the deformation includes more material removal, resulting in more wear. At very large particle sizes, 208 µm, figure 6.15 (c1 and c2) shows there is often a significant amount of material damage but often little material removal. This suggests particles are not held fully in the contact and a free to move. However, multiple passes will cause significant damage because any damage appears to be deep into the surface.

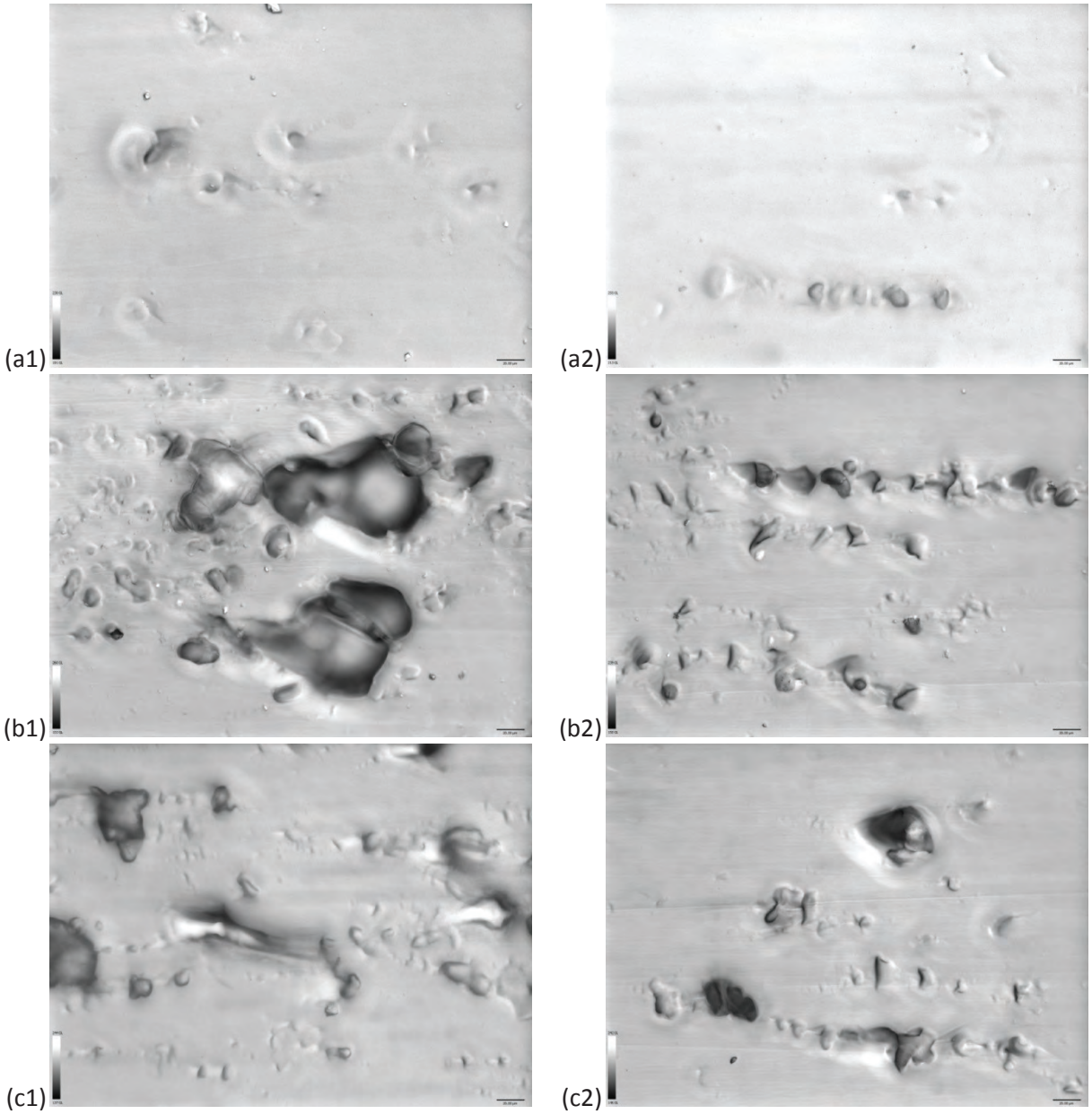

Figure 6.15: A collection of images showing typical wear features seen on the samples at different particle sizes. Images are taken on samples where the sliding distance is less than 60 mm. The scale bar on the images are 20 μm. Particle sizes are 8.6 μm (a), 62 μm (b), and 208 μm (c). η_0 = 0.02 Pa.s, C = 8.4%vol, W = 0.196 N, and u = 7.6 mm.s^{-1}.

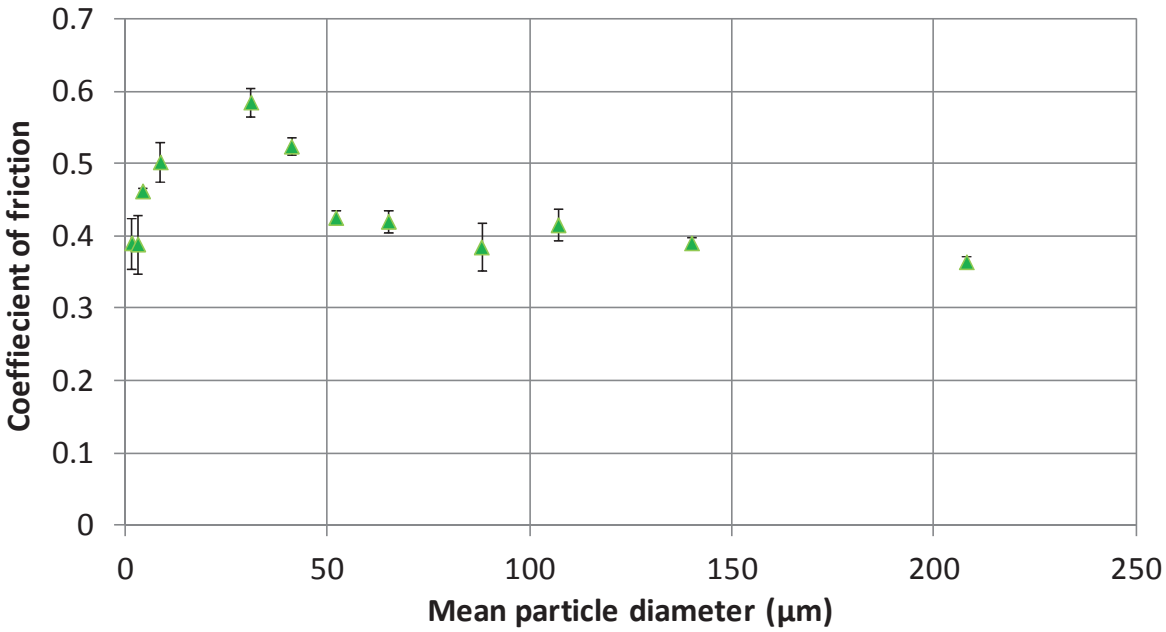

Figure 6.16: Coefficient of friction as a function of particle size. η_0 = 0.02 Pa.s, u = 7.6 mm.s^{-1}, W = 0.196 N and C = 8.4%vol. The corresponding coefficient of friction based on the continuous phase is 0.70.

The corresponding friction data to this wear data is shown in figure 6.16. For low particle sizes, going from the mean particles sizes of 1.5 µm to 31 µm, there is an increase in the coefficient in friction from 0.39 to 0.58. Given a predicted film height of 2 µm and the distributions in figure 6.11 and figure 6.9, this region is expected to be going from a contact in which many particles pass through the contact without being captured to one in which most particles would be expected to be entrained. The equivalent fluid only coefficient of friction is approximately 0.7 and the system is expected to be in a mixed state of lubrication, the friction may be in line with this behaviour by being below this maximum friction for probe surface contact. At small particle sizes few particles are captured and only act mainly to thicken the fluid. Thickening the fluid increases the film height of the system, and moving the system away from the boundary lubrication regime reducing the friction coefficient. As

particle sizes increase, the particles stop acting as part of the fluid as particles bridge the contact between the two surfaces, resulting in wear and an increase in friction.

At 31 µm the friction coefficient reaches a peak. It is also noticeable that although the friction gradually increases the wear rate is practically zero until 31 µm particles are used. This seems to suggest that entrainment point or penetration depth below a mean particle size of 31 µm is too low to result in significant damage. At around 31 µm more significant wear processes can begin to take place, resulting in greater material removal. Below 31 µm the entrainment of particles results in material deformation but the parameters do not allow for the force to build to its peak which will occur just before material removal through chipping. Above 31 µm the high friction drops as particle size increase as the chipping process has already been established. Although more particles can penetrate and particles can penetrate deeper and longer so more wear can occur, friction is independent of the contact area and the images in figure 6.12 show little increase in wear events between 41 µm and 62 µm. This suggests only the largest particles cause wear and other particles are either blocked, roll out of contact or cannot be entrained as the contact is lifted by the particles causing wear.

Over 52 µm the friction coefficient is practically constant at 0.4. There may be a slight reduction as the particle size increases. The error bars in figure 6.15 indicate the average of the measured deviation in the coefficient of friction and sources of error, such as batch variations, are not included. As such this apparent slight reduction may not be a true reflection of the actual wear. The factor of three differences in the wear rate for these large

particle sizes is not seen in the friction data. This may not be due to the same effect suggested by the images (shown in figure 6.12 and figure 6.15): more particle interactions and an increase of random particle motion as size goes from 62 µm to 208 µm. This may be a result of the particles finding it easier to roll and move out of contact with increased size due to the particles-probe contact moving further forward of the centre of the contact and reducing the contact point, meaning the force is more longitudinal than vertical. Wear rate is still high as the particles are large (much larger the film height) and so can penetrate deep into the surface whilst being moved by the probe. However wear rate is not increasing due motion of particles instead of entrainment. The schematic in figure 6.17 summarises the explanation of the effect of particle concentration on wear described in this section.

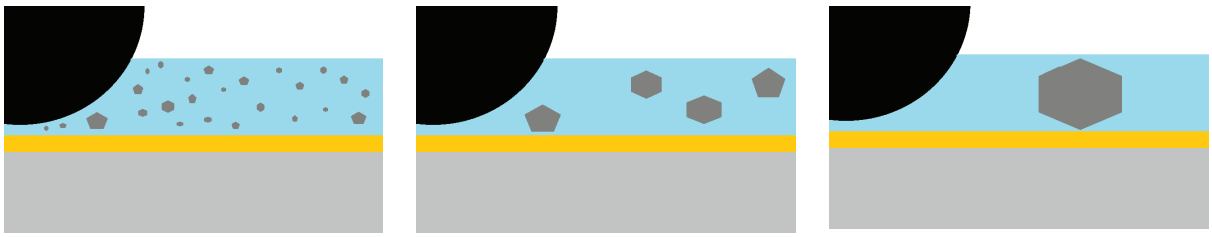

Figure 6.17: Schematic diagram summarising the expected effect of particle size on the contact that results in the observations seen in this section. At low particle size capture is rare as many particles are too small to be captured. As concentration increases the particle interactions with particles large enough to cause wear becomes common. As size increases further the number of particles drops until there are too few particles, and particle interaction is infrequent. Although the increased size particles can, individually, cause more wear than smaller particles.

6.2.3 Further assessment of the impact of particle size on wear

The effects of particle size seen so far can be interpreted as being due to lubrication and particle number. To further assess the effect of particle size on wear, the viscosity and speed were varied as these lubrication parameters should influence the entrainment of particles at different sizes. Figure 6.18 shows the effect of speed and particle size on the wear rate. Firstly it is immediately apparent that the wear rate drops with increasing speed. The data can be divided by speed to the power of -0.33, as shown in figure 6.19, due to the speed effect discussed in section 5.2.

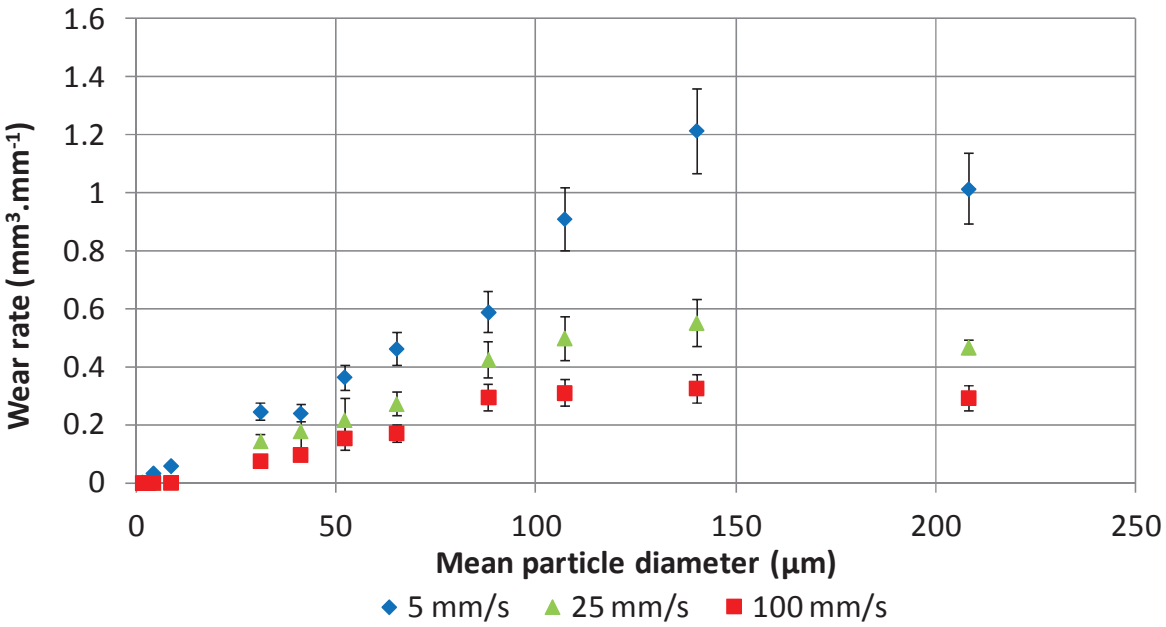

Figure 6.18: Wear rate as a function of particle size at multiple speeds. η_0 = 0.02 Pa.s, W = 0.196 N and C = 8.4%vol. The calculated minimum lubrication film thickness is 0.7 µm, 2 µm and 5 µm at 1.6 mm.s^{-1}, 7.6 mm.s^{-1} and 30 mm.s^{-1} respectively.

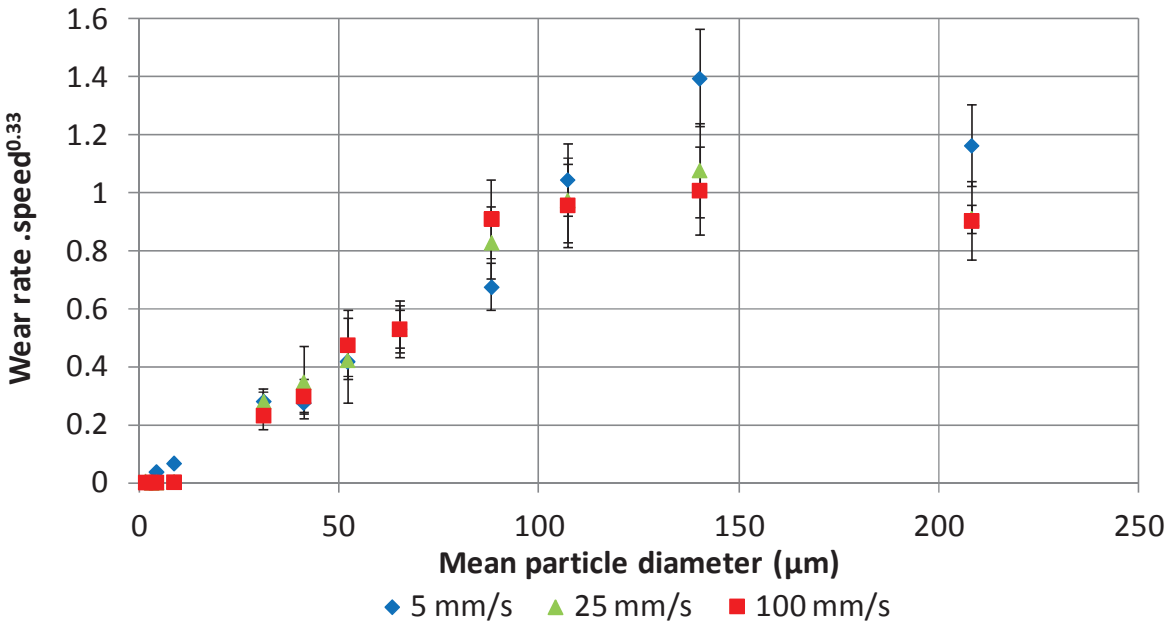

Figure 6.19: The wear rate as a function of particle size at multiple speeds, from figure 6.18, divided by speed to the power -0.33. η_0 = 0.02 Pa.s, W = 0.196 N and C = 8.4%vol.

There are two regions where the wear behaviour that is not explained by the previous speed and size data at large and small particle sizes. In particular the peak in the wear at 140 µm shows a significant decrease in wear as speed increases and there is a slight drop at 208 µm. At large diameters the wear is behaviour is expected to be due to the number of particles. At low speed the gap between the probe and the surface is less than a micron and expected to be fundamentally a boundary system. It might be expected that as speed decreases the few particles that are present are more likely to be entrained both because of the low separation and because the speed is low it becomes difficult for particles to be rolled or knocked out of contact. At low speed, higher viscosities show no significant wear. However there is a small amount of wear, circa 0.05 $mm^3.mm^{-1}$ at 5 $mm.s^{-1}$, which again may be due to the low gap size or slow speed preventing particle entrapment.

The corresponding friction is shown in figure 6.20. The data for mean diameters above 52 µm shows a relatively consistent coefficient of friction of 0.4. At 5 $mm.s^{-1}$, from 52 µm to 107 µm there is a small drop in the friction coefficient relative to the higher speeds. This may be due to an underestimation of the error meaning that the small deviation is not significant or it may be an extension of the small size behaviour. At small particles sizes, less than 52 µm, there is widely different friction behaviour dependant on size and velocity. The lower speed of 5 $mm.s^{-1}$, the system shows an increase in friction as particle size decreases. The system is expected to be fundamentally boundary lubricated and so as particle size decreases the artificial particle height created by the particles decreases. Hence particles processes such as rolling are likely to decrease as well. There is also the possibility that at low particle size the particles may jam into the surface and lock the system, increasing friction.

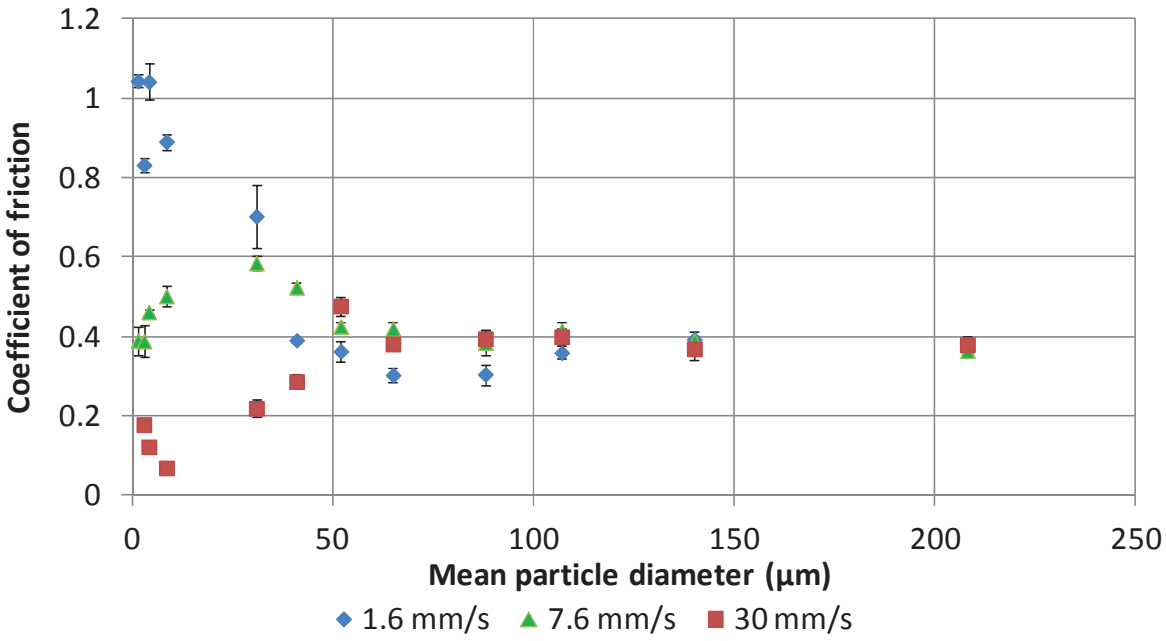

Figure 6.20: Coefficient of friction as a function of particle size at multiple speeds. η_0 = 0.02 Pa.s, W = 0.196 N and C = 8.4%vol. The data corresponds to the data in figure 6.18. The corresponding coefficient of friction based on the continuous phase is 1.32, 0.70 and 0.41 at 1.6 $mm.s^{-1}$, 7.6 $mm.s^{-1}$ and 30 $mm.s^{-1}$ respectively.

At 100 mm.s^{-1}, the expected particle-free coefficient of friction is expected to be 0.4 (from data in figure 5.5), identical to the high particle size friction coefficient. However there is a dip in the data at sizes less than 52 µm. This may be explained in part by the particles becoming small relative to the gap size, so they become part of the fluid system and increasing the viscosity of the system and lowering the friction. However this would not truly explain the fact at very low (<10 µm) particles sizes the friction begins to increase as particle size is reduced. Therefore it must be the particle behaviour that is driving the friction relationship. At 8.6 µm the mean particle size is only just greater than the minimum predicted gap size, 5µm, and so particles are expected to just pass or roll through the contact if there is any interaction. If the particle size increases more particles are fully entrained, increasing friction until the contact is full. As the size increases further, the jammed contact then forces rolling and sporadic chipping of the surface in front of the contact. A decrease in particle size from 8.6 µm size means most particles can pass through the contact unaffected and thus the system approaches its particulate free fluid friction coefficient of 0.4.

Figure 6.21 shows the effect of continuous phase viscosities and particle sizes on the wear rate. For clarity viscosity to the power -0.26 is used to simplify the relative wear rate in figure 6.22. The 0.02 Pa.s data shows unusual behaviour compared to the other two samples at the relatively low size of 31 µm, and high sizes of 140 µm and 207 µm. At high particle size it might be that the large particle sizes are dropping out of solution faster and so making wear easier, particularly as the number density is dropping, thus reducing the likelihood of probe-particle interactions.

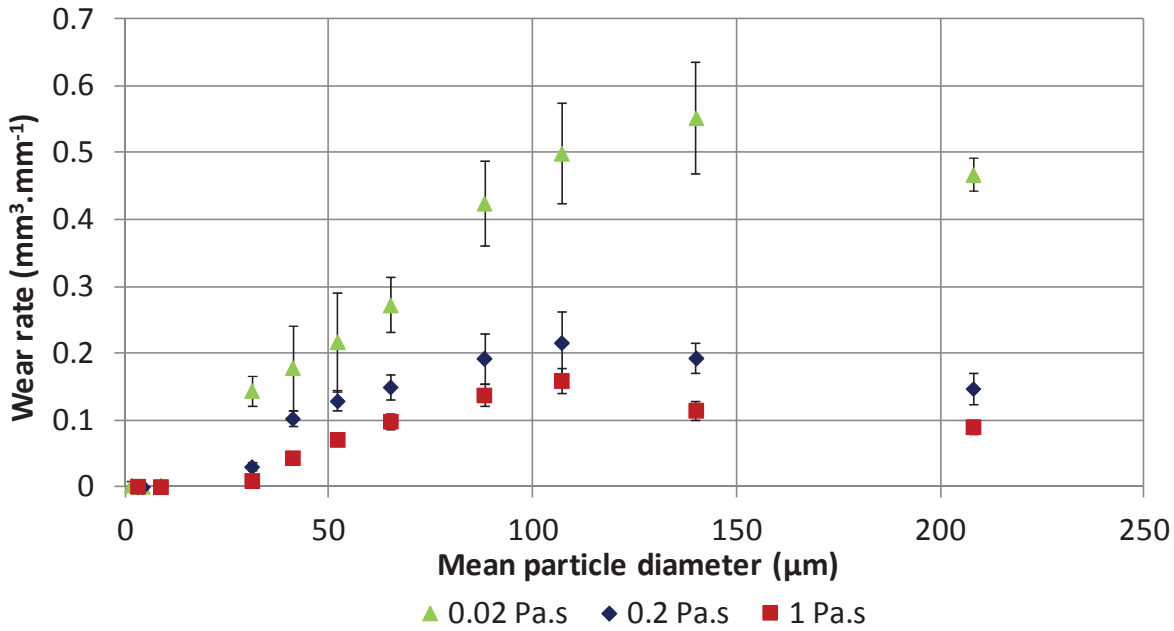

Figure 6.21: Wear rate as a function of particle size at different continuous phase viscosities. u = 7.6 mm.s^{-1}, W = 0.196 N and C = 8.4%vol. The calculated minimum lubrication film thickness is 2 µm, 9 µm and 26 µm at 0.02 Pa.s, 0.2 Pa.s and 1 Pa.s respectively.

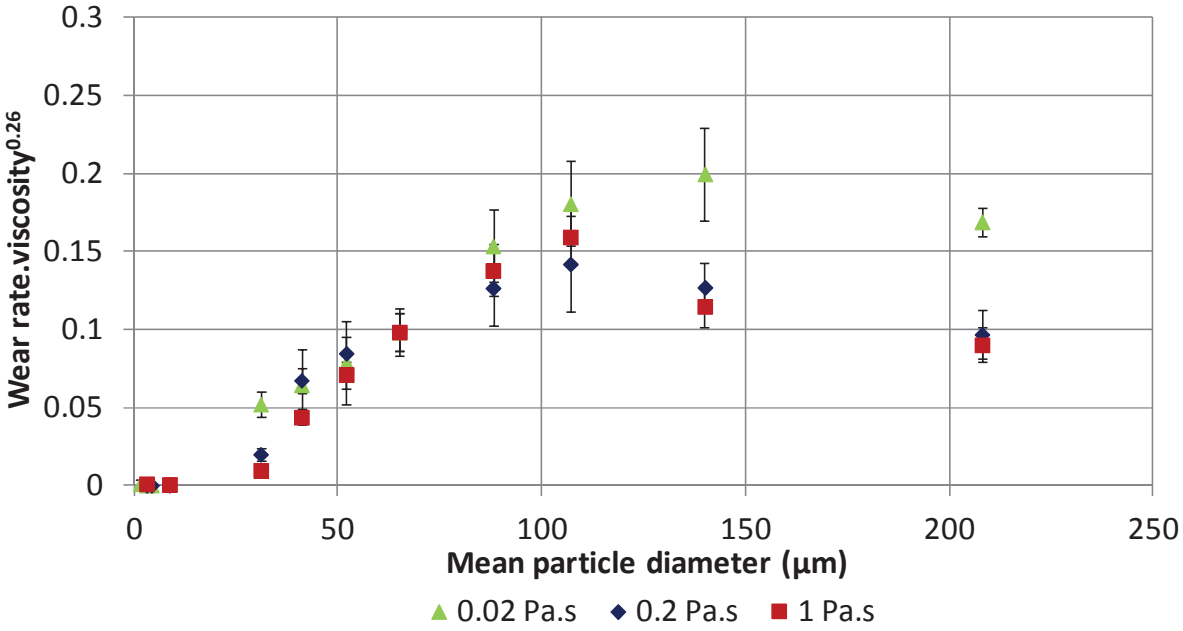

Figure 6.22: The wear rate as a function of particle size at multiple viscosities, from figure 6.18, divided by viscosity to the power -0.26. u= 7.6 Pa.s, W = 0.196 N and C = 8.4%vol.

The 31 µm data are more difficult to interpret as the lower particle size does not show significant wear. Given the peak in the friction data seen in figure 6.23 it may be that this is a system on the cusp of jamming due to low film height at low particle sizes, of 8.6 µm or less. This is supported by the fact that the minimum film height is predicted to be just 2 µm compared to 9 and 26 µm for the 0.2 Pa.s and 1 Pa.s solutions respectively. In fact the 31µm wear data may well be reduced because many particles can pass through the contact and not jam when the continuous phase has a higher viscosity.

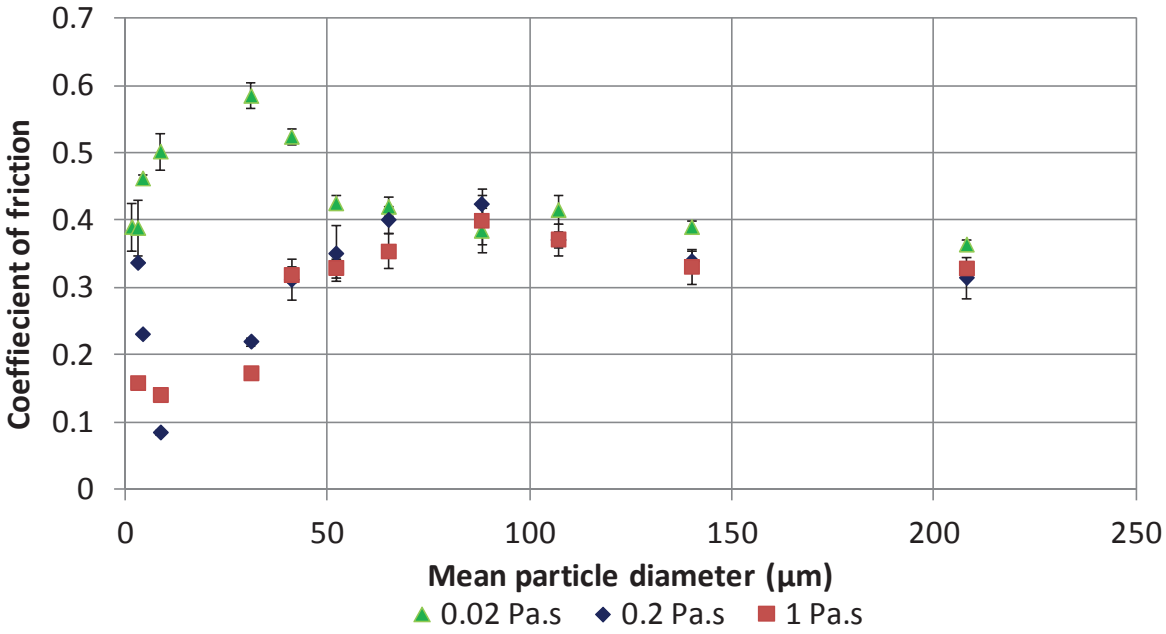

Figure 6.23: Coefficient of friction as a function of particle size at three viscosities. u = 7.6 mm.s^{-1}, W = 0.196 N and C = 8.4%vol. The data corresponds to the data in figure 6.21. The corresponding coefficient of friction based on the continuous phase is 0.7, 0.3 and 0.13 at 0.02 Pa.s, 0.2 Pa.s and 1 Pa.s respectively.

As before the friction data, in figure 6.23, above 52 µm shows little difference between samples. However, there is a decrease from a peak of ~0.4 to ~0.3. An explanation for this

effect has been outlined previously. A small difference between the two higher viscosity's coefficient of frictions and the lower viscosity data is also observed. This seems to support the notion presented previously that at larger particle sizes, the particles begin to drop out.

At low sizes the 0.02 Pa.s solution friction behaviour is again different to the other fluids. The higher viscosity fluids appear to show a similar trend to the effect of increased speed data shown in figure 6.20. This trend can again be interpreted as a transition where particles begin to flow through the contact region. The 1 Pa.s solution does not show a significant increase at very low particle sizes compared to the 0.2 Pa.s solution. This can be explained as being due to the fact the expected non-particle system being mixed to hydrodynamic lubrication and having a low friction coefficient of 0.13 (compared to a 0.3 mixed lubrication coefficient of friction for the 0.2 Pa.s system).

It was suggested previously that in order to best investigate the peak in size trend seen in figure 6.14 narrow particle sizes could be used. This was not possible however it is possible to use broader particle distribution. In particular there are commercially available, relevant ground FGNC samples. The wear rate of these samples are shown in figure 6.24 together with the data presented previously in figure 6.21. As the peak at 140 μm at 0.02 Pa.s is suspect (see previous comments) a 0.2 Pa.s solution was used. As there were only two commercial samples, a third was made by combining two in a 50:50 mixture. The corresponding coefficients of friction to this wear data are shown in figure 6.25.

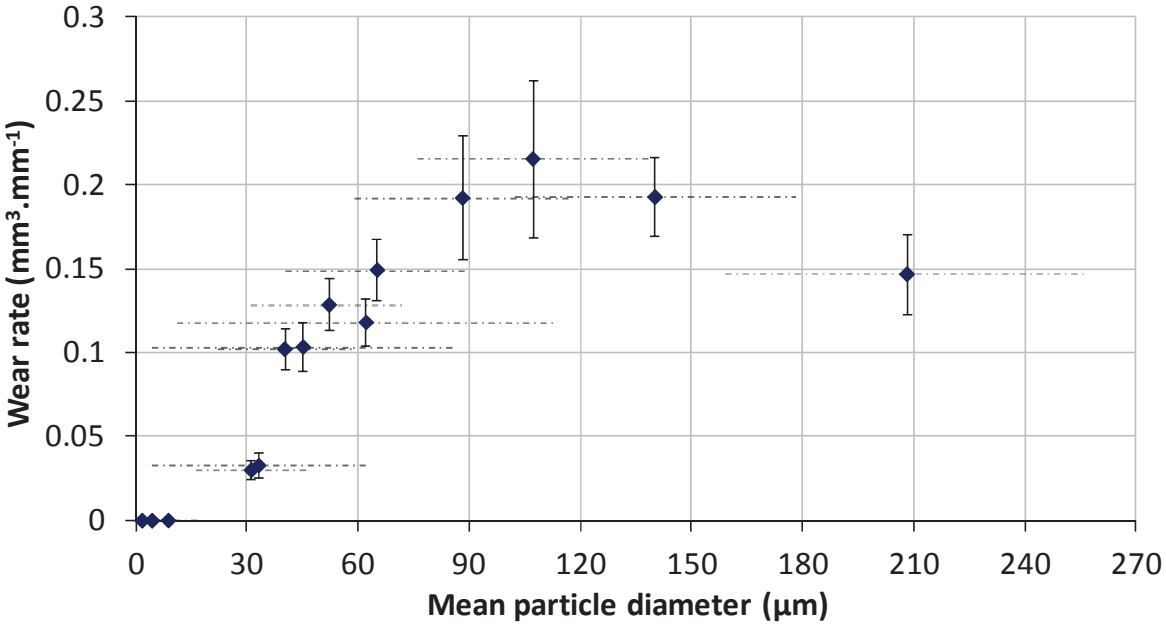

Figure 6.24: Wear rate as a function of particle size. η_0 = 0.2 Pa.s, u = 7.6 mm.s^{-1}, W = 0.196 N and C = 8.4%vol. The calculated minimum lubrication film thickness is 9 µm. Dash-dot horizontal "error bars" indicate the standard deviation of the particle size distribution

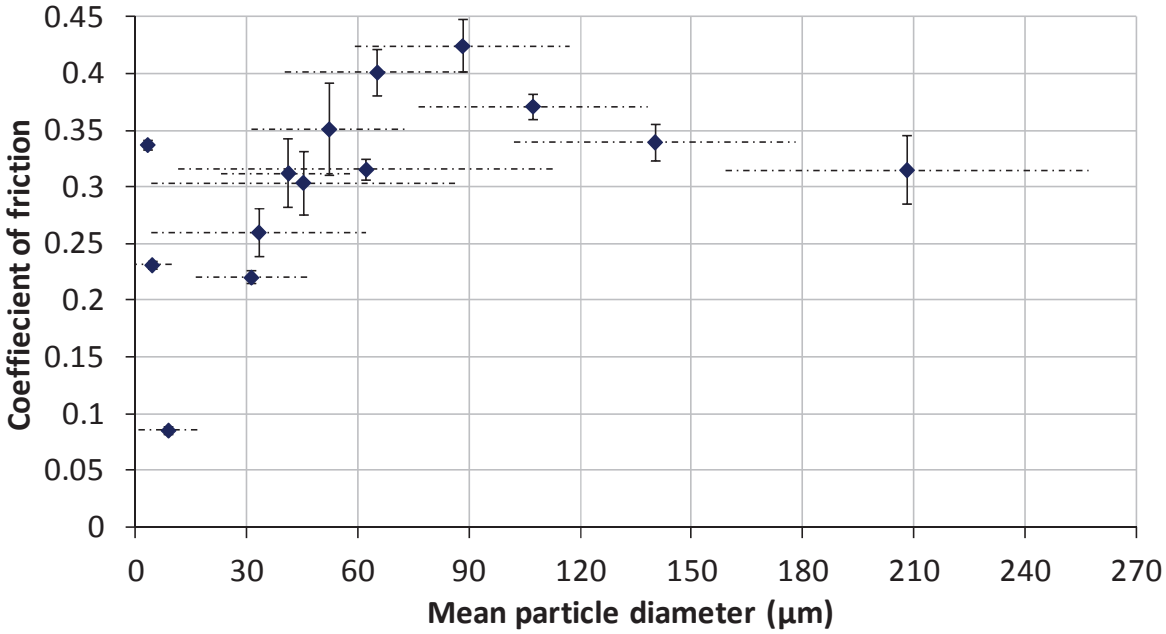

Figure 6.25: Coefficient of friction as a function of particle size. η_0 = 0.2 Pa.s, u = 7.6 mm.s^{-1}, W = 0.196 N and C = 8.4%vol. The corresponding coefficient of friction based on the continuous phase is 0.3. Dash-dot horizontal "error bars" indicate the spread of the particle size.

Figure 6.24 shows a reduction in the wear rate using the broadly distributed particles, compared to the trend of narrow distribution particles. This may be what would be expected as a broader distribution is likely to contain a lower number of larger particles per unit volume compared to at lower sizes. Hence broadening the distribution reduces the number mean diameter. This reduction appears to reduce the wear. The corresponding coefficients of friction similarly seem to be off the trend seen previously in the data. The data suggest that with a broader distribution there will be a higher coefficient of friction for 8.6 µm minimum in the data and a low coefficient of friction for the 88 µm maximum. This seems to suggest that the broadening of the distribution produces an "average" of the existing data. Put simply, broadening the size distribution seems to reduce the impact of size effects. At the lower mean particle size this means the restriction on the particles to cause wear is negated by a few larger particles. At the higher particle sizes this means there is insufficient particles to cause the more significant damage.

6.3 Summary

This final chapter aimed to analyze impact of the particle in terms of the concentration, size and distribution of size of particles on the wear. The wear rate as a function of concentration data could be separated into three regions: a stochastic regime, at ~8.2 %vol or less, where wear increases linearly with concentration; a jammed regime at ~35.6 %vol of higher, where flow is limited and wear is minimal; and a saturated regime at intermediate concentrations where the wear rate is independent of particle concentration. Further study is required to understand this trend further.

Particle size parameters did not show a simple relationship to wear rate and cannot easily incorporated into the Archard equation.

When the mean particle size diameter is less than 52 µm a significant number of particles can pass through the contact. This means that fluid and lubrication effects dominate the friction and fewer particles are held in contact and wear the surface. Above at a mean diameter of 107 µm the wear begins to limit and subsequent decrease. It is expected this limit due to a drop in particle number. Overall to avoid this drop the best cleaning was produced by the 107 µm sample

When wider particle distributions were studied it was shown that the wear drops. It is expected that the reduction in wear is due spreading of the particle sizes and lower particle sizes (which will have a higher particle number density) dominating.

7. CONCLUSIONS

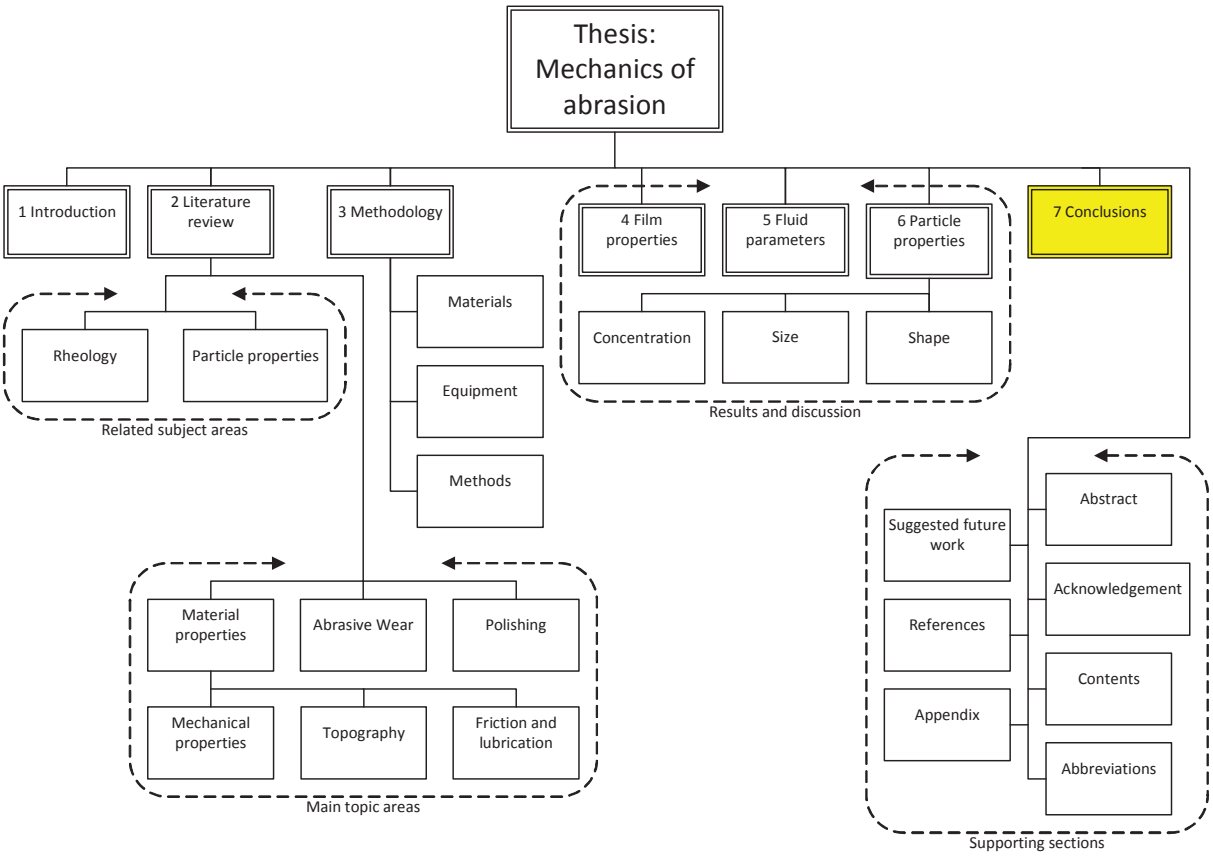

Figure 7.1: Thesis structure overview with the conclusion chapter highlighted

The primary objective of this project is to understand the relationship(s) between cleaning of a stained surface and the system parameters. Form this research it is possible to define a maximum cleaning system. Investigations have been carried out primarily under tribological wearing conditions of an oil stain in order to try and answer this challenging problem. This chapter will draw together the points from the discussion, reviewing them in terms of the original project aims.

There were many interlinked factors which combined to form an abrasive cleaning problem. This work studied the fluid, particle, and stain properties. The investigation measured the impact of these properties on stain removal by observing, characterising and quantifying the wear of the surface.

It was found during literature review that there is a lack of mechanistic studies in the area of household cleaning and so the study area is, of itself, novel. There were many lessons learned in the process of the thesis. The following chapter particularly outline those lessons and how they might be applied to research or industry.

Castor oil may not be the most widely used or obvious choice oil or fatty material for use as a “standardised” stain but it was able produce a repeatable surface for the wear study. Classification of the oil surfaces was problematic. It was possible to use standard nanoindentation techniques to classify the harder elastoplastic samples. Soft elastomer and transition films showed deviations from what might be considered a normal indentation. However there is no established method for characterising soft films such as these. As such, taking the measured values obtained as absolute values for the mechanical properties has not been proven to be without issue. However there was repeatability in the results for repeated experiments and between data gathered by different methods. This suggested that these values may, at the least, be related to the true mechanical properties.

The primary method used in this investigation to measure the physical surface topography and wear was relocation laser profilometry. Although before testing on a DCO system it is

important to understand the wear process in terms of its basic variables. Sliding distance was found, for the most part, to follow the established Archard wear equation. There was a significant deviation from this equation once a significant amount of material was removed. The limitation is thought to be due to the random wear of material when there is little material left to wear. Load was also found to obey the Archard equation. This was found to be due to both an increased severity of the wear process and longer entrainment. Overall the wear volume could always be found to be linearly proportional to load and sliding meaning the wear could be based on the Archard equation, within certain limits.

Next, the influence of the DCO mechanical properties on wear rate were outlined. Although wear of a surface has been varied as function of mechanical properties for two body abrasion [182-184] this systematic study of three body wear is not comparable to anything found in the literature. As oil soils and similar films are unlikely to be mechanically similar across homes and industries, the scientific study of oil soil wear over a range of properties is likely to be of relevance and interest in other applications, not just household care.

It was found that unlike the work in the literature [21, 147], the wear of the baked oil film was not inversely proportional to the hardness nor was a simple trend observed. In fact there was a significant deviation from the predictions of the Archard equation and the wear rate formed three regimes: a soft surface, hard surface and transition wear regime. This 3 regime trend seems to show that there is a fundamental change in the film properties between soft elastomer films and elastoplastic polymers. This transition in material type has

a significant impact on the mechanics of the wear which results in the transition in the wear coefficient.

From a scientific perspective this may not be unexpected as the wear coefficient is system specific and the system has fundamental changed in its deformation behaviour. However, in the context of home cleaning the resulting point may be easy to overlook: soils with different mechanical properties do not respond to abrasion in the same way. As a result, to accelerate the cleaning, harder particles or chemical additives may be considered. Although further research on other stains is recommended, LAC compositions are expected to only likely to be optimised for a limited range of soils (in terms of mechanical properties).

In chapter 5 the effect of speed was studied. The Archard wear equation does not predict that speed will impact the wear. However the equation is designed to explain 2 body wear and its derivation did not consider a fluid regime. Only at very low speed is it suggested that wear is not dependent upon speed indicating the possibility of a “boundary region” for three body wear. However, at less than 3 $mm.s^{-1}$ this “boundary region” is only of scientific interest as it is unlikely that a user would wipe or scrub a surface at this speed. It was found that wear at a speed of 3.2 $mm.s^{-1}$ of higher, drops with a power index of -0.33 in relation to speed. As a result it is hypothesised that as speed increases, a lubrication film builds up in proportion to the speed. This not only allows particles to escape the contact uncaptured, but also allows the contact point to rise such that particles may be deflected away from the centre of contact.

Similarly it was found that increasing viscosity results in the wear dropping as an inverse power of viscosity, -0.26. This time it is hypothesised that as viscosity increases a lubrication film builds. The fact that manufacturers can vary the viscosity makes it a more useful variable. However the viscosity of interest in a commercial LAC is not clear, as commercial liquids are more complicated than the simple systems in this study and introduce many variables from the complex rheology and chemistry: commercial LACs are structured, surfactant and solvent containing systems. An additional consideration is that, in a commercial LAC, the lowering of the continuous phase viscosity has a significant impact. Not only do ingredient costs change, and usually increase, but handling becomes more difficult both for manufacturing and user application. Lower viscosity fluids cannot suspend as well as higher viscosity fluids, meaning there is a potential for particles to fall out of suspension. Also the suspension is often made up of active ingredients and any change in their concentration will impact the rheology, which may subsequently impact the efficacy of the chemical cleaning. Changes to both the physical feel of the liquid (due to rheological differences) and /or chemical cleaning of the liquid may also create secondary costs as the user experience is altered, requiring sensory research and possibly changing the end users. Overall the inverse power is so low at -0.26 that deliberately designing a fluid by changing the viscosity of the system as a whole is not likely to provide an economic benefit.

It is unknown how the wear rate relationship of speed and viscosity might be modified by the presence of a less rigid or a porous applicator. Such considerations are likely to complicate the relationships and were not studied here. However factors such as the size, shape, porosity and water content, amongst others, remain areas for future study.

Particle properties are investigated in the final set of results. This is perhaps the most readily variable parameter from a manufacturer's point of view. Firstly, the particle concentration was varied and overall it is theorised that the results show there are effectively 3 regimes created by a change to the particle concentration: the stochastic, saturated and jammed regions. At low concentrations the wear increases as a function of concentration. As concentration increases the wear rate will become limited as the contact is saturated. Finally at high concentration the contact is packed or jammed, so the probe struggles to reach the surface, particles are not moved over the surface and wear decreases.

From this we can also conclude that designing a solution to abrade a surface would mean avoiding the jammed regime. A solution that is in the high end of the stochastic or in the low-mid saturated regime is preferred. The exact concentration chosen will also depend on other factors such as the cost of materials (both raw abrasive and the fluid suspension) and transport and the performance in other cleaning tests. The original 8.4 %vol concentration, used for experiments in the previous chapters was originally selected due to a common commercial sample having this concentration.

The wear rate is 30% lower than the maximum observed here. Concentration is expected to behave below the saturated regime but high in the stochastic regime. It is thought that increasing the particle concentration in this commercial solution should increase cleaning rate. However, the increase in particle concentration may come at a cost in terms of structuring ability, chemical cleaning, storage or consumer perception. As a result the

increase in purely particle concentration would need future investigation with a coomercial to negate any potentially negative impact(s).

Particles can be varied in terms of their size, distribution, shape and material: giving a large range of potential variables to investigate. For this investigation calcite particles were used due to their long history of use in LACs. Primarily size was varied. It was found that at low sizes (less than 52 µm) the wear is limited by the lubrication regime. As size increased the wear increased to a peak before dropping at high sizes (greater than 107 µm). This shows that the size increase should escalate the severity of wear however eventually there is a point at which the number of particles is too low leading to particle starvation in the contact.

The implication is that for designing a cleaning fluid the particle size must be sufficiently large to avoid lubrication effects and cause damage to the soil but not too large to avoid starvation. In the laboratory the optimal size can be relatively easy to find. Here it was at 107 µm. However, this number does not take into account the costs of the particles, in terms of their wear to other household surface, causing damage.

An additional consideration is that consumers will often dilute cleaning solutions, use a non-comparable cloth / applicator or apply the solution to a different soil / film type. As only one volume of oil was used in all the investigations herein, the study of thinner or thicker films would be required to conclusively prove the relations found in this investigation. Overall this data only indicates the features of the trend expected in size behaviour and further investigations using different methods are required. When wider particle distributions were

studied it was shown that the wear drops. It is expected that the reduction in wear is due spreading of the particle sizes and lower particle sizes (which will have a higher particle number density) dominating.

It was originally stated that the primary aim of this project is to understand the relationship(s) between cleaning of a stained surface and the system parameters. This chapter has outlines the results of varying many system parameters relate to cleaning. From a simplistic point of view the Archard wear equation for this test has been found to follow the equation:

$$Q = \frac{k_{H^* u \eta} WL}{H^*} \eta^{-0.26} u^{-0.33} \qquad (7.1)$$

Particle concentration and size cannot readily be incorporated into this simple equation and instead can be considered separately. Hardness has remained this equation although care must be taken to ensure the mechanism of wear does not change in addition to the hardness.

Future work

The work in this thesis shows that it is possible to setup a repeatable and representative systematic study of wear for household abrasives. The profilometer used in the investigation provided key data. Towards the end of this project a new interferometer instrument was acquired. Initial data gathered on this equipment showed potential as a future basis for a new method. Due to the time taken in setting up, transferring and focussing samples, as well as the limited number of profiles taken in the original investigation there would be little difference in terms of time taken for data collection and interpretation between the methods. However, the opinion of this researcher is that a properly developed relocation interferometer based method should provide more accurate and cost effective data. This work is particularly recommended as the laser profilometer stopped working.

From the work in this thesis it is possible to define the beat cleaning system only for a single soil film. An optimum cleaning system may have to be applied to a range of soils and the associated impact of cost and side effects such as damage would need to be considered.

In chapter 4 it was shown that the mechanical properties of a surface can heavy impact upon the wear of that surface. This work was only conducted on the DHO soils. A logical next step would be to further test the influence of surface properties by introducing other soils. These could be variable surfaces or soils similar to the DCO film or, alternatively, a collection of readily available polymer materials could be selected for a new series of experiments. This later could be directly comparable to the work conducted by Lancaster [182-184] but for

three body abrasion rather than two body abrasion. Additionally materials should be included that represent wear /damage susceptible surfaces in the home.

Additionally the amount of oil applied to the surface was fixed by the coating procedure and not varied. The study of thinner or thicker films would be required to conclusively prove the mathematical relations found in this investigation. Particularly the relationship between wear and the baked oil film's properties or mean particle size, which are expected to be influenced by film height.

Prior to starting this investigation, it was outlined that the inclusion of the experimental variables of the substrate properties and applicator parameters were considered outside the main scope of this investigation. However in the home these properties are often readily variable and both are of industrial and academic interest.

Variation in the substrate will alter the contact zone and surface pressure distribution changing the nature of the three body wear. To the industrial market, not only would understanding how the oil soil forms on the substrate make the design of cleaners more specific and relevant, but also knowing how the substrates soils readily form would aid the design of "smarter homes and workplaces". These smarter homes and workplaces would utilise surfaces that are designed to actively repel or inhibit soils formation, and /or they would make removal of fouling deposits easy.

Applicators are made from many materials with different forms, geometries, giving a wide range of physical and chemical properties. This means it would be difficult to study all possible applications. However through careful selection of a range of probes the influence particular phenomena such as material strength, porosity and chemical composition could be studied and quantified.

Following on from this study, the influence of fluid properties both physical and chemical could be varied. The chemical properties of the commercial fluids have not so far been studied in a mechanistic way and may significantly alter the method of wear. In particular, solvents and surfactants may cause other effects such as roll up, pitting and softening, amongst others. At this stage it is hard to deduce exactly how these additional components will influence wear and hence further work is required. Also the chemistry of commercial cleaning products will involve surfactants, solvents and other ingredients. However the addition of surfactants are likely to alter the lubrication of any probe or particle and confuse the effect of the bulk properties, such as viscosity, on wear.

Chapter 5 showed that influence of viscosity on wear, however commercial LAC systems are shear thinning and there may be significant differences between the model systems and commercial systems, particularly if the continuous phase is not truly continuous i.e. if discrete fluid properties exist such as soft particles, polymer chains and physical micro or nano structures. To a certain extent some of this work has already started, and although the methodology was less structured the work did form part of a patent for the author (appendix C).

Finally, the work in chapter 6 takes a selection of particle sizes and concentrations in order to study wear. A wider variety materials shapes and materials and distributions and mixtures thereof could be studied. This has already been starts (see appendix A). The aim would also to investigate the wear produced by these particles to evaluate their real world application potential.

All of the possible future activities have been summarised in table 7-1 for clarity.

Table 7-1: Summary of possible future activities, the benefits of conducting the work and possible negative factors to consider

Possible future activity	Benefits	Negatives
Develop a relocation interferometer based method for analysing tribological cleaning.	More data giving increased accuracy in the results. The profilometer was not working at end of testing so this is the only equipment option currently on site.	None
Study different soil systems or wear on different polymer surface to further understanding of material properties on cleaning	Would allow for some assessment of tribological behaviour over a wider range of materials. Giving greater confidence in how the specific household cleaning problems could be targeted. Allows the assessment of the possible negative impact, surface	Developing model soils suitable for abrasion and similar to real applications may be time consuming.

	damage, of an abrasive system	
Further investigation of DCO oil cleaning properties (such as oil thickness) and their cleaning	Would help to confirm the results presented here or show where limitations in the results arise.	None
Investigate the influence of substrate and applicator parameters on material properties and cleaning.	Better understanding of soil formation and cleaning outside of the laboratory environment.	Castor oil may not adhere to all substrates making aspects of the test definition difficult at the start. May also require a replacement for the Iron substrate to catalyse and harden the stain.
Study the influence of chemical properties of the continuous phase on cleaning.	Better understanding of real cleaning fluids.	May not be possible to distinguish chemical and physical affects if a chemical is also a structurant.
Study the influence of physical properties of the continuous phase on cleaning.	Better understanding of real cleaning fluids.	May not be possible to distinguish chemical and physical affects if a structurants is chemically active.
Study the cleaning of multiple particle mechanical properties and geometries	May allow for the production of better performing or more unique solutions to cleaning problems	None

References

1. K.Asteriadou, P.J.Fryer, *A prototype cleaning map- Classification of industrial cleaning processes.* Trends in food Science & Technology, 2009. **20**: p. 255-262.
2. D.Guoa Y.Huang, X.Lu, J.Luo, *Modeling of particle removal processes in brush scrubber cleaning.* Wear, 2011. 273 p.105-110
3. K.Wisniewski, G.Szewczyk, *Dish and Household Cleaning*, in *Handbook for Cleaning/Decontamination of Surfaces*, P.S. I.Johansson, Editor. 2007, Elsevier. p. 125-195.
4. W.von-Rybinski, *Physical Aspects of Cleaning Processes*, in *Handbook for Cleaning/Decontamination of Surfaces*, P.S. I.Johansson, Editor. 2007. p. 1-56.
5. C.Smith, *Toothpaste technology: even the pharoahs brushed their teeth.* Dental technology, 2000. 17: p. 26-27.
6. *Unilever brands in action Cif overview*. 2015 26/03/2015]; Available from: http://www.unilever.co.uk/brands-in-action/detail/Cif/298129/.
7. P.Ashley, *Toothbrushing: Why, when and how?* Dental Update, 2001. **28**: p. 36-40.
8. S.M.Higham, B.T.Amaechi, *Dental erosion: possible approaches to prevention and control.* Dentistry, 2005. **33**: p. 243-252.
9. *Brand shares (by global brand name) for abrasive scourers, metal polishes and furniture polishes*. Euromonitor International Passport Website [restricted accessed] 03/06/2014.
10. Amanda Cable. *How do dirt-cheap cleaning products scrub up against the big brands? AMANDA CABLE pulled on her rubber gloves to find out...* 2014 06/03/2014 [cited 2015; Available from: http://www.dailymail.co.uk/femail/article-2574201/How-dirt-cheap-cleaning-products-scrub-against-big-brands-AMANDA-CABLE-pulled-rubber-gloves-out.html.
11. S.Al-Malaika, K.Doudin, H.Dole, T.Stirling, M.Sharples, *Effect of contact surfaces on the thermal and photooxidation of dehydrated castor oil.* Polymer Degradation and Stability, 2011. **96**: p. 438-454.
12. D.S.Ogunniyi, *Castor oil: A vital industrial raw material.* Bioresource technology, 2006. **97**: p. 1086-1091.
13. G.W.Stachowiak, N.J.Fox, *Vegetable oil-based lubricants—A review of oxidation.* Tribology International, 2007. **40**: p. 1035-1046.
14. J.N.daSilva, V.Scholz, *Prospects and risks of the use of castor oil as a fuel.* Biomass and Bioenergy, 2008. **32**: p. 95-100.
15. S.Musso, R.Ploeger, O.Chiantore, *Contact angle measurements to determine the rate of surface oxidation of artist's alkyd paints during accelerated photo aging.* Progress in Organic Coatings, 2009. **65**: p. 77-83.
16. F.Gunstone, *The Chemistry of Oils and Fats: Sources, Composition, Properties, and Uses*. 2004: CRC Press.
17. A.Guerci, A.Scarpa, *Various uses of the castor oil plant (Ricinus Communis L.): A review.* Ethnopharmacology, 1982. **5**: p. 117-137.
18. M.Kutz, *Handbook of Materials Selection*. 2002 John Wiley & Sons.
19. A.A.H. Barnes, et al., *Composition for cleaning of hard surfaces*. 2014, Patent.
20. M.J.Leach, Y. Niwata, *Cleaning composition comprising monoalkyl cationic surfactants*. 1998, Patent.
21. W.Hirst, J.F. Archard, *The Wear of Metals under Unlubricated Conditions.* Proc. R. Soc. A, 1956. **236**. p. 397-410
22. R. Weatherhead, *Fillers and Pigments*, in *FRP Technology: Fibre Reinforced Resin Systems*. 2012, Springer Science & Business Media. p. p377.
23. A.Theodorou, *Mixed Surfactant Lamellar Phases: Studies under Shear*, in *Chemical Engineering and Analytical Science*. 2010, University of Manchester.

24. G.J.T.Tiddy, C.Richards, S.Casey, *Lateral Phase Separation Gives Multiple Lamellar Phases in a "Binary" Surfactant/Water System: The Phase Behavior of Sodium Alkyl Benzene Sulfonate/Water Mixtures.* Langmuir, 2007. **23**: p. 467-474.
25. G.J.T.Tiddy, C.Richards, S.Casey, *Liquid crystal and solution phases of sodium dodecyl-p-benzene sulphonate (NaLAS) and octa-oxyethylene glycol hexadecyl ether (C16E8): 1:1 mixtures in water.* Colloid Polymer Science, 2008. **286**: p. 31-46.
26. M.S.Mohammadi, C.Richards, G.J.T.Tiddy, *Formulating liquid detergents with naturally derived surfactants-Phase behaviour, crystallisation and rheo-stability of primary alkyl sulphates based on coconut oil.* Colloids and Surfaces A: Physicochemical and Engineering Aspects, 2009. **338**: p. 119-128.
27. A.Saiani, J.A.Stewart, A.Bayly, G.J.T.Tiddy, *The phase behaviour of lyotropic liquid crystals in linear alkylbenzene sulphonate (LAS) systems.* Colloids and Surfaces A: Physicochemical and Engineering Aspects, 2009. **338**: p. 115-161.
28. N.J.Wagner, J.Mewisa, *Current trends in suspension rheology.* Non-Newtonian Fluid Mechanics, 2009. **157**: p. 147-150.
29. J.Mewis, N.J.Wagner, *Thixotropy.* Advances in Colloid and Interface Science, 2009. **147**: p. 214-227.
30. P.R. deSouza Mendes, *Modeling the thixotropic behavior of structured fluids.* Journal of Non-Newtonian Fluid Mechanics, 2009. **164**: p. 66-75.
31. J.Llorens, J.Labanda, *A structural model for thixotropy of colloidal dispersions* Rheo Acta 2006. **45**: p. 305-314.
32. J.Mewis, K.Dullaert, *A structural kinetics model for thixotropy.* Non-Newtonian Fluid Mechanics, 2006. **139**: p. 21-30.
33. R.De Rooij, A.A. Potanin, D. van den Ende, J. Mellema, *Microrheological modeling of weakly aggregated dispersions.* Chemical Physics 1995. **102**: p. 5845-5853.
34. J.M.deSantos, F.Bautista, J.E.Puig, O.Manero, *Understanding thixotropic and antithixotropic behavior of viscoelastic micellar solutions and liquid crystalline dispersions.* Non-Newtonian Fluid Mechanics, 1999. **80**: p. 93-113.
35. S.M.Fielding, M.E.Cates, *Rheology of giant micelles.* Advance in Physics, 2006. **55**(7-8).
36. G.Subramanian, D.L.Koch, *The stress in a dilute suspension of spheres suspended in a second-order fluid subject to a linear velocity field.* Non-Newtonian Fluid Mechanics, 2006. **138**: p. 87-97.
37. B.J.P.Kaus, Y.Deubelbeiss, J.A.D.Connolly, *Direct numerical simulation of two-phase flow: Effective rheology and flow patterns of particle suspensions.* Earth and Planetary Science Letters, 2010. **290**: p. 1-12.
38. G.D'Avino, F.Greco, P.L.Maffettone, *Rheology of a dilute suspension of rigid spheres in a second order fluid.* Non-Newtonian Fluid Mechanics, 2007. **147**: p. 1-10.
39. R.I.Tanner, K.D.Housiadas, *On the rheology of a dilute suspension of rigid spheres in a weakly viscoelastic matrix fluid.* Non-Newtonian Fluid Mechanics, 2009. **162**: p. 88-92.
40. H.H.Hu, N.A.Patankar, *Rheology of a suspension of particles in viscoelastic fluids.* Non-Newtonian Fluid Mechanics, 2001. **96**: p. 427-443.
41. E.W.Llewellin, S. Mueller, H. M. Mader, *The rheology of suspensions of solid particles.* Proc. R. Soc. A, 2010. **466**: p. 1201-1228.
42. A.Einstein, *Eine neue Bestimmung der Moleküldimensionen.* Ann. Phys, 1906. **19**: p. 289-306.
43. D.G.Thomas, *Transport characteristics of suspension: 8. A note on the viscosity of Newtonian suspensions of uniform spherical particles. .* J. Colloid Sci. , 1965. **20**: p. 267-277.
44. Ir.R.Rutgers, *Relative viscosity of suspensions of rigid spheres in Newtonian liquids.* Rheol. Acta 1962. **2**: p. 202-210.
45. D.G.Thomas, *Transport characteristics of suspension: 8. A note on the viscosity of Newtonian suspensions of uniform spherical particles.* J. Colloid Sci., 1965. **20**: p. 267–277.

46. T. J. Dougherty, I. M. Krieger, *A mechanism for non-Newtonian flow in suspensions of rigid spheres.* T. Soc. Rheol., 1959. **3**: p. 137–152.
47. H.Brenner, *Rheology of a dilute suspension of axisymmetric Brownian particles.* Multiphase Flow, 1974. **1**: p. 195-341.
48. A.Acrivos, D.J.Jeffrey, *The rheological properties of suspensions of rigid particles, AIChE J. 22 (1976) 417.* AlChE, 1976. **22**: p. 417-432.
49. W.B. Russel, *Review of the role of colloidal forces in the rheology of suspensions.* Rheology, 1980. **24**: p. 287-318.
50. M. Anandha Rao, *Flow and Functional Models for Rheological Properties of Fluid Foods*, in *Rheology of Fluid and Semisolid Foods: Principles and Applications*. 2007, Springer US: Boston, MA. p. 27-58.
51. M.Paszkowski, *Some Aspects of Grease Flow in Lubrication Systems and Friction Nodes*, in *Tribology - Fundamentals and Advancements*, D.J. Gegner, Editor. 2013.
52. R.Bulkley, W.H.Herschel, *Konsistenzmessungen von Gummi-Benzollösungen. .* Kolloid Z. , 1926. **39**: p. 291–300.
53. D.M.Kalyon, H.S.Tang, *Estimation of the parameters of Herschel–Bulkley fluid under wall slip using a combination of capillary and squeeze flow viscometers.* Rheologica Acta, 2004. **43**: p. 80-88.
54. T.Cousseau, *Film Thickness and Friction in Grease Lubricated Contacts: Application to Rolling Bearing Torque Loss*, in *Engenharia Mecanica E Gestao Industrial*. 2013, Universidade Do Porto.
55. R.L.Powell, J.J. Stickel, *Fluid mechanics and rheology of dense suspensions.* Annu. Rev. Fluid Mech. , 2005. **37**: p. 129–149.
56. J.A.Williams, *Engineering Tribology*. 1995: Oxford University Press. 512.
57. I.M.Hutchings, *Tribology*. 1 ed. Metallurgy and Materials Science Series. 1992: Edward Arnold. 273.
58. D.Dowson, *History of Tribology*. 1979: Longman.
59. D.Tabor, F.P.Bowden, *The friction and lubrication of solids*. 1950: Clarendon Press.
60. M.J.Adams, S.A.Johnson, A.Arvanitaki, B.J.Briscoe, *Film thickness measurements in elastohydrodynamically-lubricated elastomeric contacts.* Elastohydrodynamics, 1997. **96**: p. 199-207.
61. J.Heymer R.S.Dyer-Joyce, *The Entrainment of Solid Particles into Rolling Elastohydrodynamic Contacts*, in *The Third Body Concept*, D.D.e. al, Editor. 1996. p. 135-140.
62. W.Yong, J.O.Marston, S.T.Thoroddsen, *Direct verification of the lubrication force on a sphere travelling through a viscous film upon approach to a solid wall.* Fluid Mechanics, 2010. **655**: p. 515-526.
63. C.F.Higgs,E.J.Terrell, *A Particle-Augmented Mixed Lubrication Modeling Approach to Predicting Chemical Mechanical Polishing.* Tribology, 2009. **131**: p. 1-10.
64. J.A.Wharton, D.Sun, R.J.K.Wood, *A Particle-Augmented Mixed Lubrication ModelingApproach to Predicting Chemical Mechanical Polishing.* Tribology International, 2009. **42**: p. 1596-1604.
65. S.Wirojanupatump, P.H.Shipway, *The role of lubrication and corrosion in abrasion of materials in aqueous environments.* Tribology International, 2002. **35**: p. 661-667.
66. P.Grodzinski, *The effect of lubrication on friction, wear and abrasion.* British Journal of Applied Physics, 1951. **2**: p. 86-90.
67. B.J.Roylance, S.Odi-Owei, *Lubricated three-body abrasive wear--contaminant condition versus bounding surface material hardness.* Tribology International, 1987. **20**: p. 32-40.
68. J.R.Stokes, J.deVicentea, H.A.Spikes, *Viscosity Ratio Effect in the Emulsion Lubrication of Soft EHL Contact.* Tribology, 2006. **128**: p. 795-800.
69. M.J.Furey, M.E.Freeman, B.J. Love, J.M.Hampton, *Friction, wear, and lubrication of hydrogels as synthetic articular cartilage.* Wear, 2000. **241**: p. 129-135.

70. A.Cameron, *Basic Lubrication Theory*. 1981: Ellis Horwood.
71. P.B.Davies, R.D.Arnell, J.Halling, T.L.Whomes, *Tribology: Principles and Design Applications*. 1991: Macmillan.
72. R.Underwood, *The tribological effects of contamination in rolling element bearings*. 2008, London University Press: London.
73. H.A.Spikes, *Boundary Lubrication and Boundary Films*, in *Thin Films in Tribology*, D.Dowson, Editor. 1993. p. 331-346.
74. C.Myant, K.Timm, H.A.Spikes, M.Grunze, *Particulate lubricants in cosmetic applications.* Tribology International, 2011.
75. C.A.C.Zavaglia, V.P.Bavaresco, M.C.Reis, J.R.Gomes, *Study on the tribological properties of pHEMA hydrogels for use in artificial articular cartilage.* Wear, 2008. **265**: p. 269-277.
76. J.R.Stokes, G.A.Davies, *Thin film and high shear rheology of multiphase complex fluids.* Non-Newtonian Fluid Mechanics, 2008. **148**: p. 73-87.
77. B.Edmondson, M.J.Adams, D.G.Caughey, R.Yahya, *An experimental and theoretical study of the squeeze-film deformation and flow of elastoplastic fluids.* Non-Newtonian Fluid Mechanics, 1994. **51**: p. 61-78.
78. P.L.Maffettone, G.D'Avino, F.Greco, M.A.Hulsen, *Viscoelasticity-induced migration of a rigid sphere in confined shear flow.* Non-Newtonian Fluid Mechanics, 2010. **165**: p. 466-474.
79. Z.Zhang, Y.Yan, D.Cheneler, J.R.Stokes, M.J.Adams, *The influence of flow confinement on the rheological properties of complex fluids.* Rheo Acta, 2010. **49**: p. 255-266.
80. G.Cicale, G.D'Avino, M.A.Hulsen, F. Greco, P.L. Maffettone, *Effects of confinement on the motion of a single sphere in a sheared viscoelastic liquid.* Non-Newtonian Fluid Mechanics, 2009. **157**: p. 101-107.
81. J.R.Stokes, G.R.Davies, *Thin film shear rheology of multiphase complex fluids.* Non-Newtonian Fluid Mechanics, 2008. **148**: p. 73-87.
82. I.Aydin, M.J.Adams, B.J.Briscoe, S.K.Sinha, *A finite element analysis of the squeeze flow of an elasto-viscoplastic paste material.* Non-Newtonian Fluid Mechanics, 1997. **71**: p. 41-57.
83. A.M. Jones, M.J. Edmonds, P.W. O'Callaghan, S.D. Probert, *A three-dimensional relocation profilometer stage.* Wear, 1977. **43**(3): p. 329-340.
84. T.R.Thomas, *Rough Surfaces*. 1982: Longman.
85. *4. - Real-Space Surface Profiling Techniques*, in *Experimental Methods in the Physical Sciences*, G.-C.W. Yiping Zhao and L. Toh-Ming, Editors. 2001, Academic Press. p. 63-82.
86. Sensofar, *S Neox: Non contact 3D optical profiler*. 2013.
87. M.B.Bauza, et al., *Surface profilometry of high aspect ratio features.* Wear, 2011. **271**(3–4): p. 519-522.
88. T.G.Mathia, P.Pawlus, M.Wieczorowski, *Recent trends in surface metrology.* Wear, 2011. **271**(3–4): p. 494-508.
89. P.W.Hawkes, J.C.H.Spence, *Science of Microscopy*. 2006: Springer Verlag.
90. P.A.Tucker, T.G.Rochow, *Introduction to microscopy by means of light, electrons, X rays, or acoustics*. 2 ed. 1994: Plenum.
91. D.J.Whitehouse, *Surfaces and their Measurement*. 2004, Elsevier.
92. Z.L.Wang, W.Zhou, *Scanning Microscopy for Nanotechnology: Techniques and Applications*. 2007: Springer.
93. P.Maloney, E.E.Hunter, M.Bendayan, *Practical Electron Microscopy: A Beginner's Illustrated Guide*. 1993: Cambridge University Press.
94. J.Humphreys, P.J.Goodhew, R.Beanland, *Electron Microscopy and Analysis*. 2000: CRC Press.
95. ASTM International, *E1508- 12a, Standard Guide for Quantitative Analysis by Energy-Dispersive Spectroscopy*. 2012.
96. C.F.Quate G.Binnig, Ch.Gerber, *Atomic Force Microscope.* Physical Review Letters, 1985. **56**(9): p. 930-933.

97. K.L.Johnson, *Contact Mechanics*. 1985: Cambridge University Press.
98. G.Haugstad, *Atomic force microscopy*. 2012:Wiley.
99. P.West P.Eaton, *Atomic Force Microscopy*. 2010: Oxford.
100. N.Hilal W.R.Bowen, *Atomic force microscopy in process engineering*. 2009: IChemE.
101. K.L.Mittal J.Drelich, *Atomic Force Microscopy in Adhesion Studies*. 2005: Koninklijke Brill.
102. C.A. Schuh, *Nanoindentation studies of materials.* Materials Today, 2006. **9**(5): p. 32-40.
103. ISO 6507-1, *Metallic materials -- Vickers hardness test -- Part 1: Test method*. 2005.
104. ASTM E384-16, *Standard Test Method for Microindentation Hardness of Materials*. 2016.
105. Mark R. VanLandingham, *Review of Instrumented Indentation.* Journal of Research of the National Institute of Standards and Technology, 2003. **108**: p. 249-265.
106. J.V. Fernandes N.A. Sakharova, J.M. Antunes, M.C. Oliveira, *Comparison between Berkovich, Vickers and conical indentation tests: A three-dimensional numerical simulation study.* International Journal of Solids and Structures, 2009. **46**(5): p. 1095-1104.
107. M.M. Khrushchov & E.S. Berkovich, *Methods of Determining the Hardness of Very Hard Materials: The Hardness of Diamond.* Industrial Diamond Review,, 1951. **11**: p. 42-49.
108. A.C. Fischer-Cripps, *A review of analysis methods for sub-micron indentation testing.* Vacuum, 2000. **58**: p. 569-585.
109. A. C. Fischer-Cripps, *Introduction to Contact Mechanics*. . 2007: Springer Science.
110. S.R.Cohen, E.Kalfon-Cohen, *Dynamic nanoindentation by instrumented nanoindentation and force microscopy: a comparative review.* Beilstein J Nanotechnology, 2013. **4**: p. 815-833.
111. W.D.Nix, *Elastic and plastic properties of thin films on substrates: nanoindentation techniques.* Materials Science and Engineering :A, 1997. **234-236**: p. 37-44.
112. G.M. Pharr W.C. Oliver, *An improved technique for determining hardness and elastic modulus using load and displacement sensing indentation experiments.* J. Mater. Res, 1992. **7**: p. 1564-1583.
113. G.M.Pharr, W.C.Oliver, *Measurement of hardness and elastic modulus by instrumented indentation: Advances in understanding and refinements to methodology.* J. Mater. Res, 2004. **19**: p. 3-20.
114. J.M.Wheeler, *Nanoindentation under Dynamic Conditions*, in *Materials Science & Metallurgy*. 2009, University of Cambridge.
115. B.B.X. Li, *A review of nanoindentation continuous stiffness measurement technique and its applications.* Materials Characterization, 2002. **48**(1): p. 11-36.
116. S.K.Biswas, M.S.Bobji, *Estimation of hardness by nanoindentation of rough surfaces.* Materials research, 1998. **13**: p. 3227-3233.
117. Hysitron inc. *Quasistatic Nanoindentation: An Overview*. 2016 [cited 2016 25/01/2016]; Available from: https://www.hysitron.com/resources-support/education-training/nanoindentation.
118. M.S.Bobji, S.K.Biswas, *Estimation of hardness by nanoindentation of rough surfaces.* Journal of Materials Research, 1998. **13**: p. 3227-3233.
119. M.S.Bobji, S.K.Biswas, *Deconvolution of hardness from data obtained from nanoindentation of rough surfaces.* Journal of Materials Research, 1999. **14**(6): p. 2259-2268.
120. L.Fiori, B.J.Briscoe, E.Pelillo, *Nano-indentation of polymeric surfaces.* Phys. D: Appl. Phys., 1998. **31**: p. 2395-2405.
121. S.K.Sitaraman, Z.Shan, *Elastic–plastic characterization of thin films using nanoindentation technique.* Thin solid films, 2003. **437**: p. 176-181.
122. R.Saha, W. D. Nix, *Effects of the substrate on the determination of thin film mechanical properties by nanoindentation.* Acta Materialia, 2002. **50**(1).

123. Y.Xiang, M.Zhao, J.Xu, N.Ogasawara, N.Chiba, X.Chen, *Determining mechanical properties of thin films from the loading curve of nanoindentation testing.* Thin Solid Films, 2008. **516**(21): p. 7571-7580.
124. H.Koh, A.Gouldstone, K.Y.Zeng, A.E.Giannakopoulos, S. Suresh, *Discrete and continuous deformation during nanoindentation of thin films.* Acta Materialia, 2000. **48**(9): p. 2277-2295.
125. A.M.Waas, C.Heinrich, A.S.Wineman, *Determination of material properties using nanoindentation and multiple indenter tips.* International Journal of Solids and Structures, 2009. **46**(2): p. 364-376.
126. D.Rittel, B.Poon, G.Ravichandran, *An analysis of nanoindentation in elasto-plastic solids.* International Journal of Solids and Structures, 2008. **45**(25-26): p. 6399-6415.
127. K.J.Lynne, Z.Hu, S.P.Markondapatnaikuni, F.Delfanian, *Material elastic-plastic property characterization by nanoindentation testing coupled with computer modeling.* Materials Science and Engineering: A, 2013. **587**: p. 268-282.
128. F.Carrillo, S.Gupta, C.Li, L.Pruitt, C.Puttlitz, *Adhesive forces significantly affect elastic modulus determination of soft polymeric materials in nanoindentation.* Materials Letters, 2007. **61**(2): p. 448-451.
129. J.C.Kohn , D.M.Ebenstein, *Eliminating adhesion errors in nanoindentation of compliant polymers and hydrogels.* Journal of the Mechanical Behavior of Biomedical Materials, 2013. **20**: p. 316-326.
130. Hysitron Inc. *NanoDMA III*. Hysitron Triboindenter User Manual 2010.
131. J.S.Villarrubia, M.R.VanLandingham, W.F.Guthrie, G.F.Meyers, *Nanoindentation of Polymers: An Overview.* Macromolecular Symposia, 2001. **167**: p. 15-43.
132. S.Diebels, Z.Chen, *Nanoindentation of Soft Polymers: Modeling, Experiments and Parameter Identification.* Technische Mechanik, 2014. **34**(3-4): p. 166-189.
133. W.C.Oliver, B.N.Lucas J.L.Loubet, *Measurement of the loss tangent of low-density polyethylene with a nanoindentation technique.* Journal of Materials Research, 2000. **15**(5): p. 1195-1198.
134. T.S.Gates, G.M.Odegard, H.M.Herring, *Characterization of viscoelastic properties of polymeric materials through nanoindentation.* Experimental Mechanics, 2005. **45**(2):p. 130-136.
135. S.Mishra, K.Park, G.Lewis, J.Losby, Z.Fan, J.B.Park, *Quasi-static and dynamic nanoindentation studies on highly crosslinked ultra-high-molecular-weight polyethylene.* Biomaterials, 2004. **25**(12): p. 2427-2436.
136. Hysitron inc, *Probe Calibration*, in *Hysitron Instruction Manual*. 2009.
137. M.L.Boas, *Mathematical Methods for Physical Sciences*. 3 ed. 2006: Wiley.
138. T.Y.Zhanga and W.H.Xu, *Surface Effects on Nanoindentation.* Journal of Materials Research, 2002. **17**(7): p. 17-15-1720.
139. J.J.Liu, Y.Zhang, L.Zhang, J.Calderon De Anda, X.Z.Wang, *Particle shape characterisation and classification using automated microscopy and shape descriptors in batch manufacture of particulate solids.* Particuology, 2015.
140. Renliang Xu, *Light scattering: A review of particle characterization applications.* Particuology, 2015. **18**: p. 11-21.
141. Sympatec GmbH. *QICPIC: particle size and shape analysis with image processing of highest order 1 µm - 30 mm*. 2016; Available from: https://www.sympatec.com/EN/ImageAnalysis/QICPIC.html.
142. K.Saga, E.T. Bowman, T.W.Drummond, *Particle Shape Characterisation using Fourier Analysis.* Géotechnique 2000. **51**: p. 542-554.
143. Malvern Instruments Ltd. *Laser Diffraction*. 2015; Available from: http://www.malvern.com/en/products/technology/laser-diffraction/.

144. T.Wriedt, *Mie Theory: A Review*, in *The Mie Theory: Basics and Applications*. 2012, Springer Series in Optical Sciences.
145. K.J.Hemker Jr., W.N.Sharpe, *Microscale Characterization of Mechanical Properties.* Annual Review of Materials Research. **37**: p. 93-126.
146. J.F.Archard, *Contact and Rubbing of Flat Surfaces* J. Appl. Phys., 1953. **24**. p. 981-988
147. H. C.Meng and K.C. Ludema, *Wear models and predictive equations: their form and content* Wear, 1995. **181-183**: p. 443-457.
148. A.W.Batcherlor G.W.Stachowiak, *Abrasive, erosive and cavitation wear*, in *Engineering Tribology*. 2006, Elsevier. p. 557-612.
149. R.S.Dwyer-Joyce R.Lewis, *Wear of human teeth: A tribological perspective.* Proc.IMechE Part J: J. Engineering Tribology, 2005. **219**: p. 1-18.
150. P.J.Bleu, *Fifty years of research on the wear of metals.* Tribology International, 1997. **30**: p. 321-331.
151. I.Finnie, A.Misra, *Correlations between two-body and three-body abrasion and erosion of metals.* Wear, 1981. **68**: p. 33-39.
152. I.Finnie, A.Misra, *An experimental study of three-body abrasive wear.* Wear, 1983. **85**: p. 57- 68.
153. A.Naik, N.Chand, S.Neogi, *Three-body abrasive wear of short glass fibre polyester composite.* Wear, 2000. **242**: p. 38-46.
154. G.W.Stachowiak, G.B.Stachowiak, *The effects of particle characteristics on three-body abrasive wear.* Wear, 2001. **249**: p. 201-207.
155. I.M.Hutchings, R.I.Trezona, *Three-body abrasive wear testing of soft materials.* Wear, 1999. **233**: p. 209-221.
156. M.A.Moore, *Abrasive Wear.* Materials in Engineering applications, 1978. **1**: p. 97-111.
157. K.-H.Zum Gahr, *Wear by hard particles.* Tribology International, 1998. **31**(10): p. 587-596.
158. R.Cook, D.Whitney, M.Broz, *Microhardness, toughness, and modulus of Mohs scale minerals.* American Mineralogist, 2015. **91**: p. 135-142.
159. L. Qian et al., *Comparison of nano-indentation hardness to microhardness.* Surface and Coatings Technology, 2005. **195**(2–3): p. 264-271.
160. T.Tanaka, T.Hisakado, H.Suda, *Effect of abrasive particle size on fraction of debris removed from plowing volume in abrasive wear.* Wear, 1999. **236**: p. 24-33.
161. M.V.Swain, B.R.Lawn, Materials science, 1975. **10**: p. 113-122.
162. K-H.Zum-Gahr, *Microstructure and wear of Materials*. 1987: Elsevier.
163. N.Saka, H.Sin, N.P.Suh, *Abrasive wear mechanisms and the grit size effect.* Wear, 1979. **55**: p. 163-190.
164. M.A.Shahid, K.E.Puttick, M.M.Hosseini, *Size effects in abrasion of brittle materials.* Phys. D: Appl. Phys., 1979. **12**: p. 1979.
165. T.Sun, T.Zeng, *Size Effect of Nanoparticles in Chemical Mechanical Polishing—A Transient Model.* Transactions on Semiconductor Manufacturing, 2005. **18**(4): p. 655-663.
166. Y.Zhao, Y.Wang, X.Li, *Modeling the effects of abrasive size, surface oxidizer concentration and binding energy on chemical mechanical polishing at molecular scale.* Tribology International, 2008. **41**: p. 202-210.
167. R.Lewis, A.Zorcolo, R.S.Dwyer-Joyce, *Particle/applicator interactions in household surface cleaning.* Wear, 2011. **271**: p. 2576-2587.
168. J.M.Challen, D.Dowson, K.Holmes, J.R.Atkinson. *The Wear of Non-metallic Materials*. in *3rd Leeds-Lyon Symposium on Tribology*. 1976: Mechanical Engineering Publications.
169. I.Finnie, A.Misra, *On the size effect in abrasive and erosive wear.* Wear, 1981(359-373).
170. A.T. Ashcroft et al., *Liquid composition for cleaning of head surfaces*. 2013, Patent.
171. M.R.Askari, H.A.H.Al-Khazali, *Geometrical and Graphical Representations Analysis of Lissajous Figures in Rotor Dynamic System.* IOSR Journal of Engineering, 2012. **2**: p. 971-978.

172. A.Shiratake, N.Ohnoa, N.Kuwanoa, F.Hirano, *Behavior of some vegetable oils in EHL contacts.* Elastohydrodynamics, 1997. **96**: p. 243-251.
173. T.Dutta, S.Nag, S.Tarafdar, *Spreading of fluids on solids under pressure: Slip and stick effects.* Colloid and interface science, 2011. **356**: p. 293-297.
174. Y.Yagcı, F.S.Gunera, A.T.Erciyes, *Polymers from triglyceride oils.* Progress in Polymer Science, 2006. **31**: p. 633-670.
175. B.Briscoe, *Wear of polymers: an essay on fundamental aspects.* Tribology International, 1981. **13**: p. 231-243.
176. D.Tabor, B.J.Briscoe, *Friction and Wear of Polymers*, in *Polymer Surfaces*, W.J.F. D.T.Clark, Editor. 1978, John Wiley. p. 1-23.
177. A.Schallamach, *How does rubber slide?* Wear, 1971. **17**: p. 301-312.
178. A. Schallamach, *Friction and abrasion of rubber.* Wear, 1958. **1**(5): p. 384-417.
179. P.Gabriel, Y.Fukahori, J.J.C.Busfield, *How does rubber truly slide between Schallamach waves and stick–slip motion?* Wear, 2010. **269**: p. 854-866.
180. P.Meijers B.Best, A.R.Savkoor, *The Formation of Schallamach waves.* Wear, 1981. **65**: p. 385-396.
181. S.Betz, H.Bohm, A.Ball, *The wear resistance of polymers.* Tribology International, 1990. **23**(6): p.399-406
182. J.K.Lancaster. *Relationship Between The Wear of Polymers and Their Mechanical Properties*. 1969. Tribology Conv. Institute of Mechanical Engineers, London.
183. J.K.Lancaster, *Friction and Wear*, in *Polymer Science*, A.D.Jenkins, Editor. 1972, North-Holland.
184. J.K.Lancaster, *Basic Mechanisms of Friction and Wear of Polymers.* Plastics and Polymers, 1973. **41**: p. 297-306.
185. O.K.DeFoe, A.H. Compton, *The Density of Rock Salt and Calcite.* Physical Review, 1925. **25**(5): p. 618-620.
186. All.Stainless.ltd. *TYPE 304 STAINLESS STEEL*. 10/01/2012]; Available from: http://www.allstainlessltd.co.uk/info_sheet_304_2.html.
187. A.C.Weber, *Precision Passive Alignment of Wafers*, in *Department of Mechanical Engineering*. 2002, Massachusetts Institute of Technology.
188. P.Willoughby, *Elastically Averaged Precision Alignment*, in *Department of Mechanical Engineering*. 2005, Massachusetts Institute of Technology.
189. R.T.Hunt, J.B.P.Williamson, *Relocation profilometry.* Journal of Physics E: Scientific Instruments, 1968. **1**: p. 749-752.
190. ASTM International, *ASTM E2546-15 Standard Practice for Instrumented Indentation Testing*. 2015.
191. ISO, *BS ISO 14577-4: Metallic materials — Instrumented indentation test for hardness and materials parameters*, in *Part 4: Test method for metallic and non-metallic coatings*. 2007.
192. W.J.Chang, T.H.Fang, S.L.Tsai, *Nanomechanical characterization of polymer using atomic force microscopy and nanoindentation.* Microelectronics Journal, 2005. **36**(1): p. 55-59.
193. G.Oncins J.J.Roa, J.Díaz, X.G.Capdevila, F.Sanz, M.Segarra, *Study of the friction, adhesion and mechanical properties of single crystals, ceramics and ceramic coatings by AFM.* European Ceramic Society, 2011. **31**: p. 429-449.
194. Hysitron Inc. *TI 950 Triboindenter*. 2016; Available from: https://www.hysitron.com/products-services/standalone-instruments/ti-950-triboindenter.
195. A.T. Ashcroft et al., *Liquid hard surface cleaning composition*. 2014, Patent.
196. H.Wensink, M.C.Elwenspoek, *A Closer Look at the Ductile–Brittle Transition in Solid Particle Erosion.* Wear 2002. **253**: p. 1035-1043.
197. I.M.Hutchings, *Ductile-brittle transitions and wear maps for the erosion and abrasion of brittle materials.* Phys. D: Appl. Phys., 1992. **25**: p. A212-221.

198. R.E.Winter, I.M.Hutchings, *Particle erosion of ductile metals: A mechanism of material removal.* Wear, 1974. **27**: p. 121-128.
199. G.A.Davies, J.R.Stokes, *On the gap error in parallel plate rheometry that arises from the presence of air when zeroing the gap.* Journal of Rheology, 2005. **49**(4): p. 919-922.
200. G.A.Davies, J.R.Stokes, *Thin film and high shear rheology of multiphase complex fluids.* Journal of Non-Newtonian Fluid Mechanics, 2008. **148**(1–3): p. 73-87.
201. Prasannarao Dontula, Christopher W. Macosko, and L. E. Scriven, *Does the Viscosity of Glycerin Fall at High Shear Rates?* Industrial & Engineering Chemistry Research, 1999. **38**(4): p. 1729-1735.

202. S.R.Schmid, B.J.Hamrock, B. O. Jacobson, *Fundamentals of Fluid Film Lubrication*. 2004: CRC Press.
203. A.Z.Szeri, *Fluid Film Lubrication*. 2010: Cambridge University Press.
204. B.J.Hamrock, D.Dowson, *Minimum film thickness in elliptical contacts for different regimes of fluid-film lubrication.* 1978.
205. I.B.Eryurek, I.Sevim, *Effect of abrasive particle size on wear resistance in steels.* Materials and Design, 2006. **27**: p. 173-181.
206. U.Mahajan, M.Bielmann, R.K.Singh, *Effect of Particle Size during Tungsten Chemical Mechanical Polishing.* Electrochemical and Solid-State Letters, 1999. **2**: p. 401-403.
207. B.Bhushan, Y.Xie, *Effects of particle size, polishing pad and contact pressure in free abrasive polishing.* Wear, 1996. **200**: p. 281-295.
208. R.Badruddin S.Bahadur, *Erodent particle characterization and the effect of particle size and shape on erosion.* Wear, 1990. **138**: p. 189-208.
209. S.Jacobson, R.Gahlin, *The particle size effect in abrasion studied by controlled abrasive surfaces.* Wear, 1999. **224**: p. 118-125.
210. W.Zhou, X.Wang, J Cao, W Liu, S Zhu, *Preparation of core-shell CaCO3 capsules via picking emulsion templates.* J Colloid Interface Sci, 2012. **372** p. 24-31.

Appendix A

This appendix details focussed study on rod-shaped precipitated calcium carbonate (PCC) rods. This additional section of work employs different methods to the tribological experiments seen so far, as these experiments were conducted in direct collaboration with URDPS and focussed on polishing rather than wear and the original tribological method was unsuccessful at finding wear using the rod particles. Hence this work is separate from the bulk of the thesis.

Abrasives for use in LACs, are primarily required to be effective in removing stains similar to those the work so far has focused on. However there is also the consideration of minimising damage to the underlying surface and, if possible, enhancing it. Many home surfaces are made of soft, easy-to-scratch polymer materials. These surfaces are easy to damage but it also possible to revive the appearance of these surfaces. The focus of this section is the use of high aspect ratio particles to polish /revive surfaces. Here we focus on the fundamental mechanics of the particles but it is worth noting that work related to this subject did inspire an investigation featured in a published patent (WO 2013/078949 A1) which, in turn, led to a patent published with this author's work (the work in the WO 2014/190865 A1 patent is included in this thesis as appendix B). Certain precipitated calcium carbonate (PCC) particles, with a rod-like morphology, were identified as 'smart abrasive' ingredients in LACs in proprietary work prior to the start of this activity.

A.1 Additional materials

Precipitated calcium carbonate (PCC) rods used in the later polishing experiments were sourced by Unilever China. Further study of the nature of these particles is conducted in chapter 6.

Additional work used optically flat PMMA samples to investigate polishing effects. PMMA sheets were also donated by URDPS and acquired as one batch from the supplier. The sheets were cut into 100 mm by 100 mm tiles on site for more convenient handling in the experiments.

The commercial sample of a cleaning fluid continuous phase, used in the polishing investigations, was from a single batch provided by Unilever Casali. The fluid could have been prepared "as required", however some preliminary work revealed sensitivity in the structure to small deviations in the proportion of ingredients, speed of mixing and the timing in adding and mixing ingredients. Hence to keep a repeatable rheology and structure of the surfactant system a single, sample batch was used throughout the project.

A.2 Additional methods

An optical rheometer experiment was conducted at Unilever R&D Colworth to examine the alignment of PCC rods under flow conditions between flat plates. The rheometer was a Haake Mars rheometer with Thermo Scientific RheoScope module and contains an inverted microscope. 0.5%wt rods were mixed into glycerol. A sample of this solution was placed

onto the lower plate of the instrument. The upper plate was then brought down to give a gap of 100 µm. The slurry was then subjected to the following shear rate profile:

1. Accelerate from 1–9800 s^{-1} in 8 s (images were captured once each second).
2. Maintain shear rate at 9800 s^{-1} for 20 mins (images captured every minute).
3. Decelerate from 9800–1 s^{-1} in 8 s (images were captured once each second).

The viscosity, shearing force and images were recorded and compared. It is stressed that this work was conducted off site by a separate researcher.

Cryo-SEM images were acquired by associated researchers and the equipment setup can be found in the literature [210]. Although the experiments were not carried out by this researcher the details of the experiment are detailed herein. PCC rods were incorporated into a standard continuous phase LAC formulation (containing no FGNC). A droplet of this formulation was put onto an SEM stage and immersed in liquid nitrogen. After a few minutes, it was transferred into the SEM cavity under vacuum. The surface of the sample was cut by sharp knife. The specimen was left to sublimate for a few minutes and then observed under SEM.

A.3 Results and discussion

Results are included that are primarily in terms of polishing and cleaning experiments that are different from the work in the bulk of the thesis. These methods highlight the mechanisms and benefits of using the higher aspect ratio particles.

A.2.1 Rod particle size and shape

Laser diffraction was used previously to classify the size of the particles. The algorithms that convert the raw diffraction data to a size distribution are assuming the particles to be approximately spherical. Therefore automated measurement of the particle sizes using this method is not possible as the data would not be reliable. Instead images are inspected in order to gain a typical size for the particles. Figure 7.1 shows SEM images of the rods. Inspection of images similar to figure 7.1 (b) suggests that the typical particles size in 20 µm by 1 µm.

Characterising the morphology is important when we are aiming to understand the behaviour of rods when moving over the substrate. Figure 7.1 (b) and (c) show the rods to have a spindle shape end. By breaking the particle ends, as shown in figure 7.1 (d), the cross section can be found. The cross section tends to be rounded irregular hexagonal indicating that the particles have practically flat faces. Flat faces are unlikely to cause damage as the contact pressure is spread over the area of the surface rather than being focused on a point /asperity. These PCC rods are much smoother /blunter than an equivalent 20 µm FGNC particle. The sharp ends seem to be the only place where cleaning /damage can occur as there are no asperities on the surface. The hexagonal cross-sectional shape and flat faces would also suggest that the particles should tend to slide rather than roll over a surface.

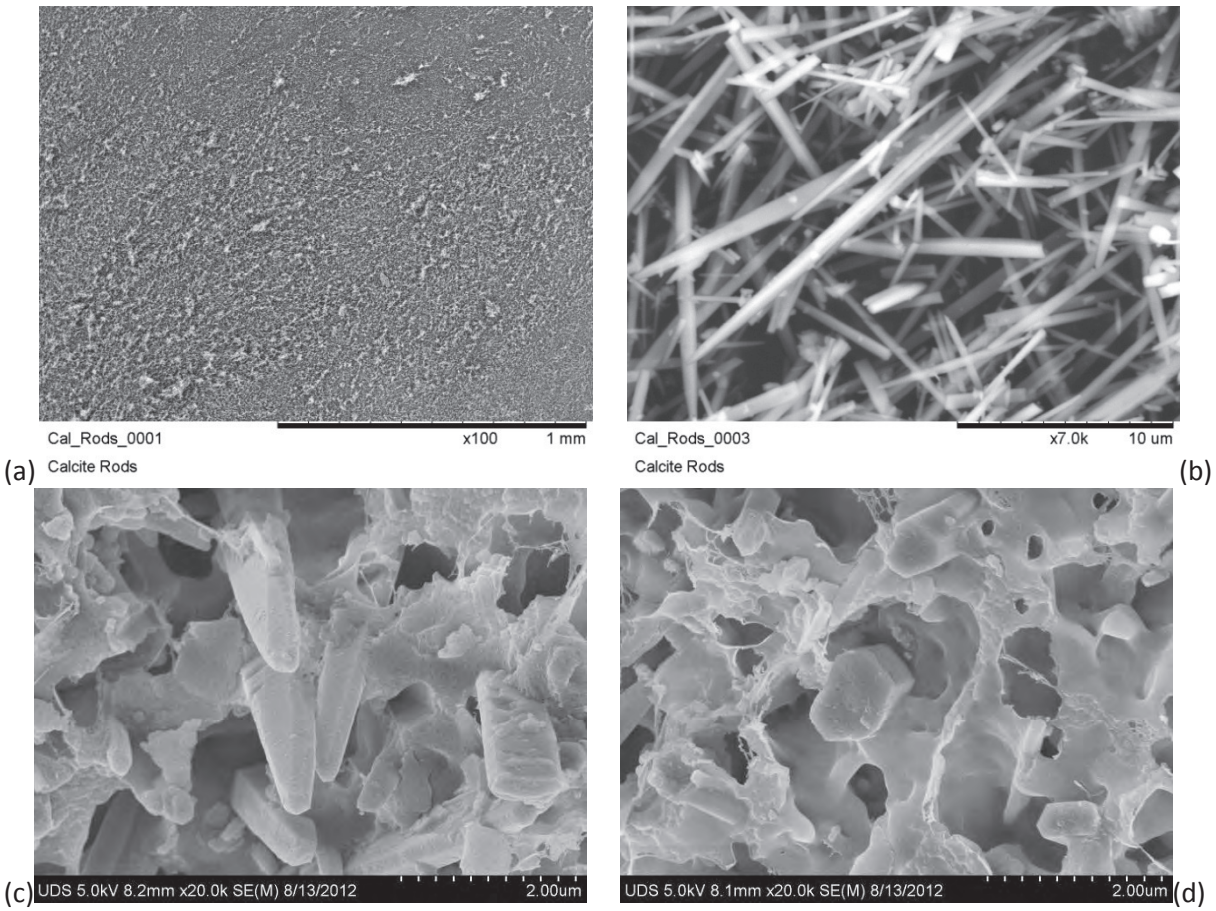

Figure 7.1: SEM images of the PCC rods (a) and (b) show SEM images of the dry PCC rod particles at different magnifications. (c) and (d) show the cross section of PCC rods as obtained using cryo-SEM. The rods are typically 20 µm in length and 1 µm in "diameter". The shape of the cross section is a rounded irregular hexagonal i.e. for a 1 µm diameter particle width may vary, typically 0.8 µm to 1.2 µm

A.2.2 Baked oil film removal using the Eldredge Tribometer

The abrasion of a baked DCO film has so far been conducted using a Newtonian continuous phase formulation. Figure 7.2 (a) shows an image of the overall damage resulting from a commercial formulation using the Eldredge tribological setup featured in the previous investigations. This represents the normal wear expected from angular FGNC abrasives. The particles used here are a 50:50 mixture of 33 µm and 62 µm particles shown in figure 6.8 and

used in a wear experiment whose results are presented in figure 6.24 and figure 6.25. When the PCC rods were placed in the Eldredge tribological setup used here it was found that the rods tend to move over a surface smoothly with little damage to the surface, as shown in figure 7.2 (b). Wear of this sample so low that it could not be measured and almost no wear features could be seen under any tribological conditions. Friction was marginally less than just using just the continuous phase with very little noise. Hence the rods fail to damage the surface because the particles were not interacting with the baked oil film.

This next stage of the investigation was to run the probe over an edge of the DCO film. Something not done in the previous tests however the result of the normal tests showed that the PCC rods have very little potential to wear in a direction normal to the surface, so this experiment is to test if the rods can laterally abrade. Figure 7.2 (c), (d) and (e) show that the rods can remove /clean an oil stain by wearing a path from the edge of the sample. Therefore, these results indicate that rods can cause damage parallel to the surface and in these tests damage the film because they have “edges to act on”. Attack angle is defined as angle from the horizontal plane of the surface. Damage of a flat surface (such as figure 7.2 (b)) can be described as a high attack angle process. Hence we can state that rods can cause a low damage due to a low attack angle. It would be expected that deliberately matted soft surfaces may see more damage from rods (see later notes on polishing) than smooth surfaces.

(a) (b) (c) (d) (e)

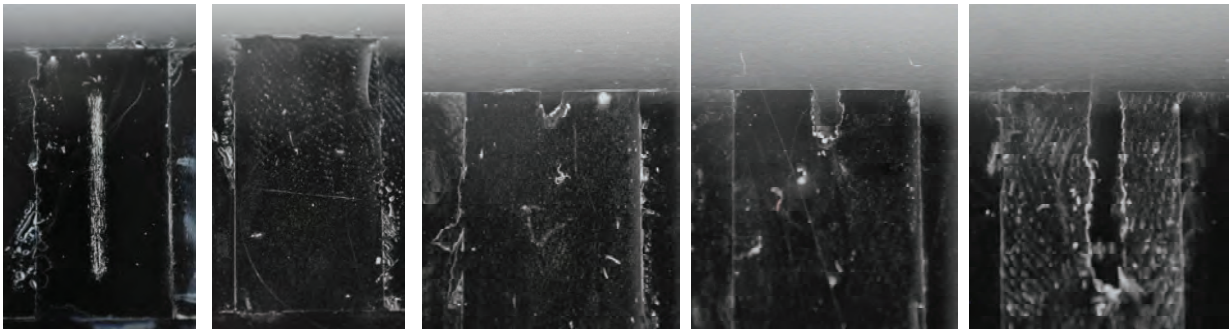

Figure 7.2: Damage caused to DCO films on polished SS plates using the Eldredge tribometer. W = 0.196N and u = 15.2 mm/s). (a) Normal damage seen using a commercial formulation after 20 passes. (b) Insignificant damage done by 20 %wt rods in a commercial continuous phase after 320 passes. The remaining images show damage caused by the 20 %wt rods in a commercial continuous phase after (c) 10, (d) 20 and (e) 40 passes over the film edge.

A.2.3 Rod particle movement and orientation under shear

Figure 7.3 shows the rheology data obtained on the optical rheometer as described in earlier. The data concerns the shearing of sample of rods suspended in glycerol. Glycerol is a Newtonian fluid, so its viscosity should not be affected by shear rate. From the data shown in figure 7.3 (a), it can be observed that the viscosity of suspension decreased when the shear rate was held at 9800 s^{-1}. This suggests shear thinning through orientation of rods as described in the literature [41]. This can be observed directly. Figure 7.3 (b) shows, firstly, that before the high shear rate is applied particles are dispersed in the suspension at random. After shearing for 20 minutes the rods tend to be aligned in the direction of shear flow as shown in figure 7.2 (b). These results demonstrate that orientation of rods can occur at high prolonged shear. Although the set-up of this experiment (concentration of particles, compositions of working fluid) is quite different from a tribological contact, it's clear that rods tend to align with the direction of shear force. Observation of the particles under

shearing also suggested rods are were sliding, spinning or rolling over the substrate and not tumbling, which is consistent with the literature [41].

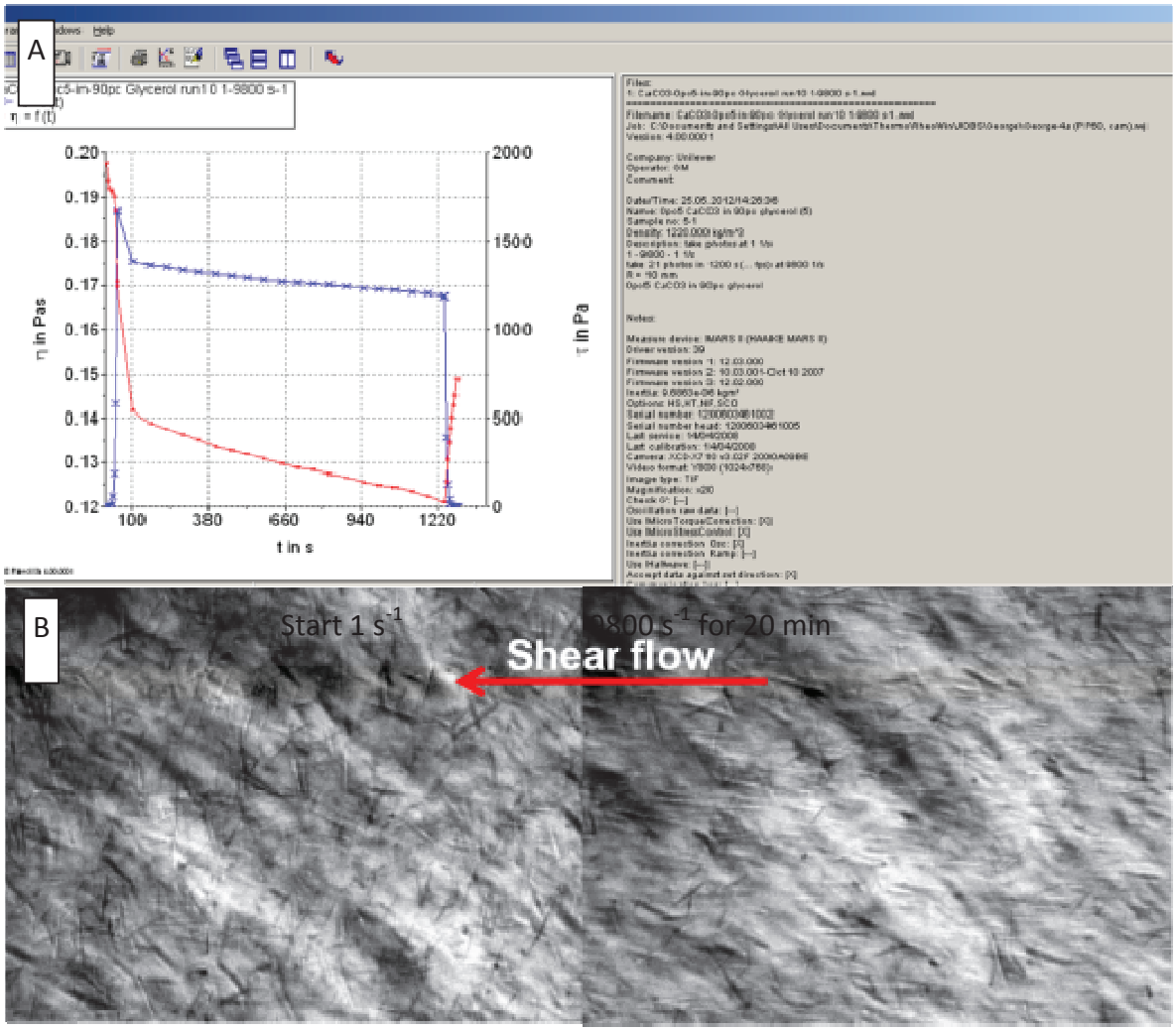

Figure 7.3: Orientation of rods by shearing. A: program set-up and rheology data; B: images captured in the beginning and after shearing for 20 min at 9800s^{-1}. These images, collected by Unilever Colworth and used with permission from URDPS, the associated comments are based only on the author's interpretation.

A.2.4 Laser profilometry of PMMA

The fact that particles align under shearing such that they may slide and cause damage at a low attack angle suggests they may be suitable for another low attack angle process: abrasive polishing. Abrasive polishing was first investigated scientifically using a FGNC formulation to randomly damage a PMMA surface for one minute by hand. Two pieces of tape were used to mask off all but a 2 mm strip of the sample. This unmasked section was then polished with rods. Visual inspection confirmed the area of the strip appeared to be polished. Laser profilometry was used to examine the mechanism by which PCC rods restored this scratched PMMA, this data is shown in figure 7.4.

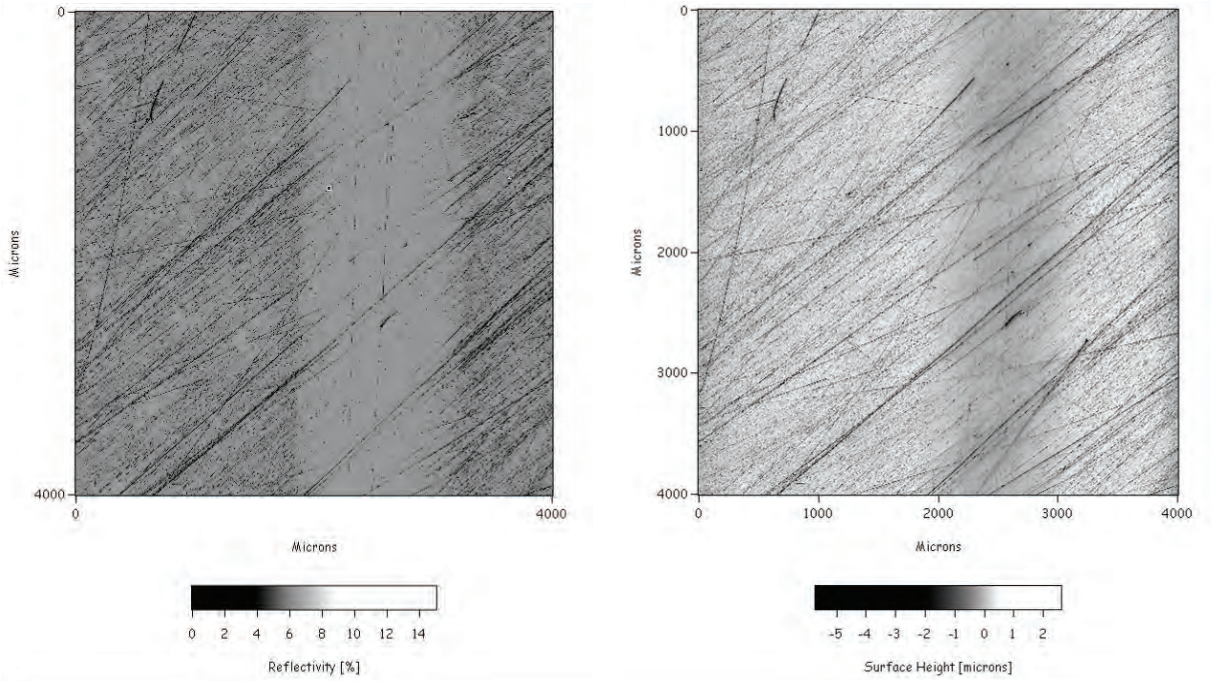

Figure 7.4: Laser profilometry data of randomly scratched PMMA. Left hand image is reflectivity. Right hand image is surface height. The whole sample was scratched with a FGNC formulation for two minutes. Circa X = 2000 µm to X = 3000 µm area was unmasked. The remaining surface was masked. The sample was subjected to polishing with a rods formulation for two minutes. The scan was taken by the laser profilometer over a 4000 by 4000 µm area; each line profile was taken 4 µm apart.

Figure 7.4 shows that there is a higher overall volume of wear along a strip polished by rods. The roughness in this region also appears to be lower. This can be investigated by examining a typical line profile, such as the one shown in figure 7.5. This effect can be explained by one of two mechanisms. Firstly the rods may remove material by vertically wearing material, whist creating a lower roughness. If this were the case than the wear rate would be independent of the initial surface roughness. Secondly, the cause could be from the rods smoothing the surface by removing asperities. In this case the rods would only attack sharp edges and raised ridges in the surface and the wear rate for a smooth surface would be much less than that of a rough surface.

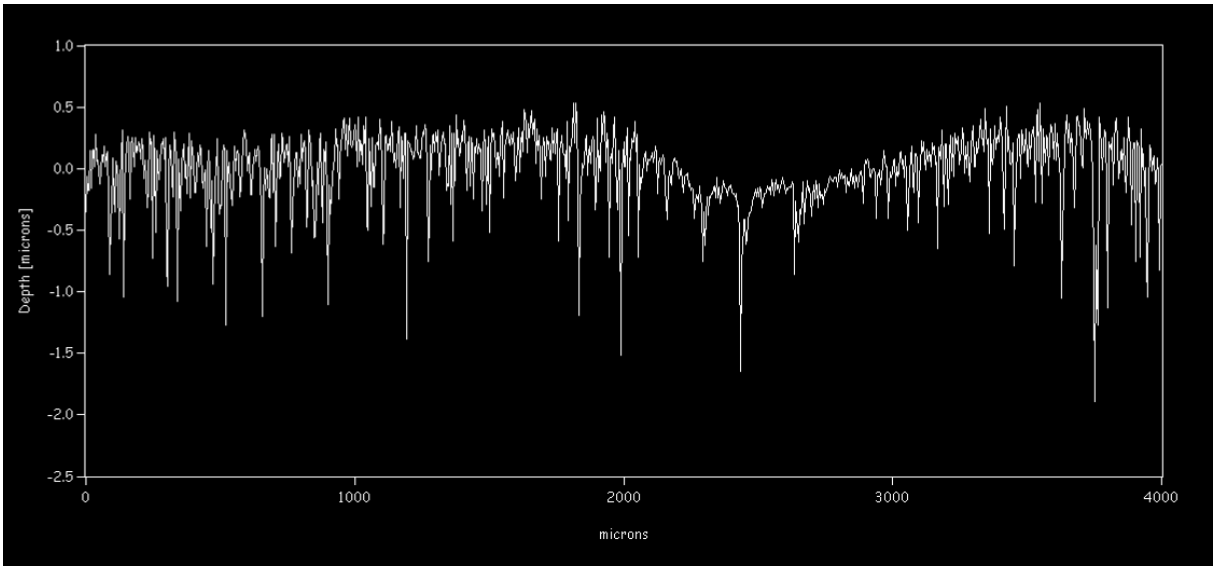

Figure 7.5: A single line profile taken from the data shown in figure 7.4.

In order to identify which of the two mechanisms is operating, a wear experiment on a smooth PMMA surface must be carried out. Firstly the height change of the average profile from figure 7.4 is taken, as shown in figure 7.6. It was calculated that 280 nm (difference between the background and rod worn areas of the graph) of wear had occurred. The

experiment was then repeated to determine the amount of wear produced by rods on smooth PMMA. Figure 7.7 shows that the amount of wear produced by rods on smooth PMMA is about 20 nm. This is an order of magnitude difference. As such, the polishing cannot primarily be due to vertical wear and these results support the hypothesis that rods preferentially polish, or smooth, sharp edges and asperities.

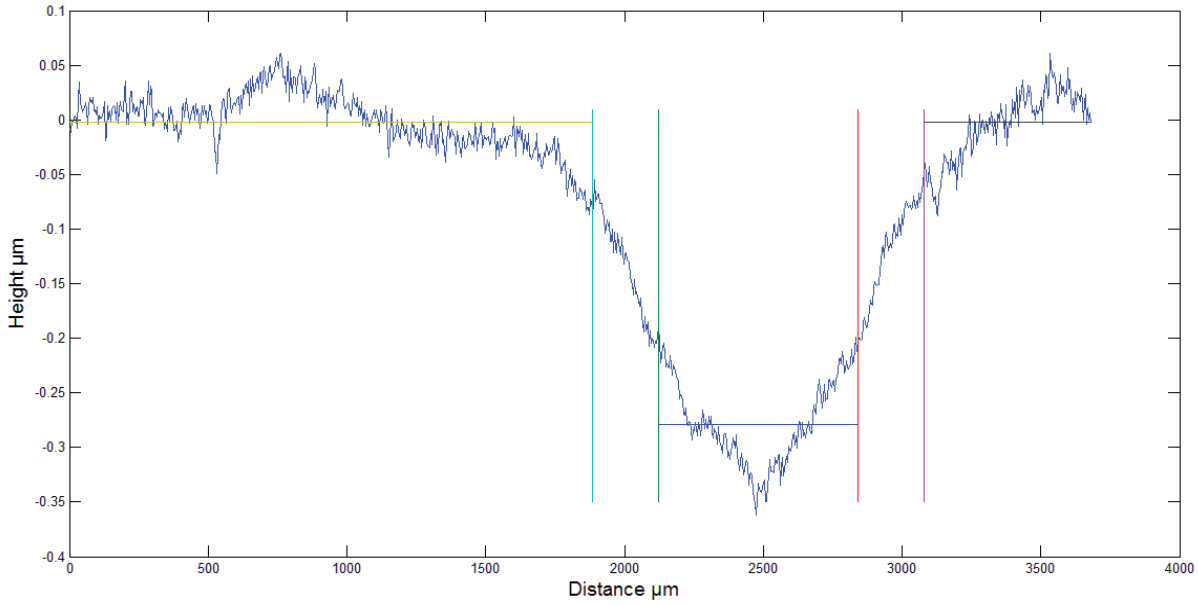

Figure 7.6: The average cross sectional height profile of 600 line scans taken from the data shown in figure 7.4. The graph indicates three regions of interest, 0–1900 µm and 3050–3700 µm are background regions, either side of the 2100–2850µm region worn by rods. Some of the data at the start or end of the line scan and area scan were removed due to the fact it appeared to be slightly erroneous.

For more detailed study of polishing mechanisms, a series of relatively large scratches were scored into a PMMA surface using a metal stylus. These scratches were then profiled. The whole sample was then rubbed using a rods formulation. The scratches were then re-

measured. In order to ensure the Perspex was repositioned properly, a Lego-based mounting system was adopted [187, 188]. Figure 7.8 shows the results and there do not appear to be any rods 'filling' the gaps in the scratches, which was another possible hypothesis that could explain the visual appearance of restoration. Instead, the rods appear to reduce the visible appearance of scratches by removing the ridges pushed up either side of the scratches. This removal of these features is expected to result in less light scattering; hence the polished surface would have a higher gloss value, making it appear smoother to the eye. This result is consistent with the rods' wear mechanism described previously: that rod abrasion is a low attack angle process that removes asperity material.

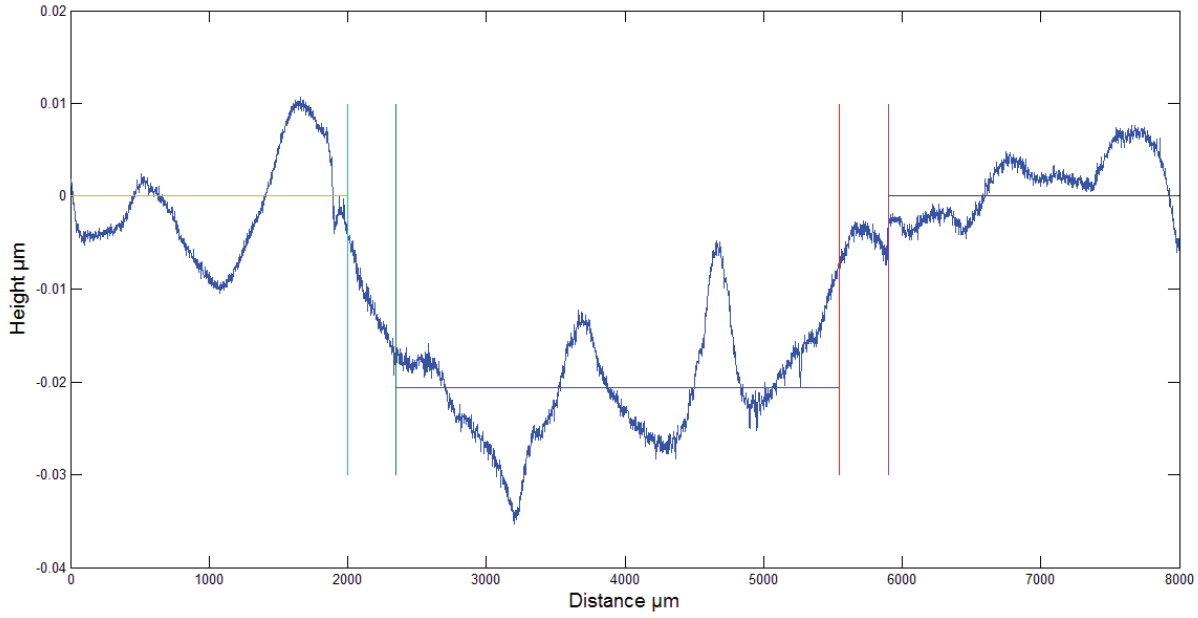

Figure 7.7: The average cross sectional height profile of 100 lines scans across a smooth PMMA surface featuring an unmasked region that has been worn by a rods formulation. The graph indicates three regions of interest, 0–2000 and 5950–8000 µm are background regions, either side of the 2300–5650µm worn region. The periodic oscillations shown may be a property of the surface but are most likely an artifact associated with the motion of the equipment used to scan the

sample. The scan was taken by the laser profilometer over an 8000 by 400 µm area; each line profile was taken 4 µm apart.

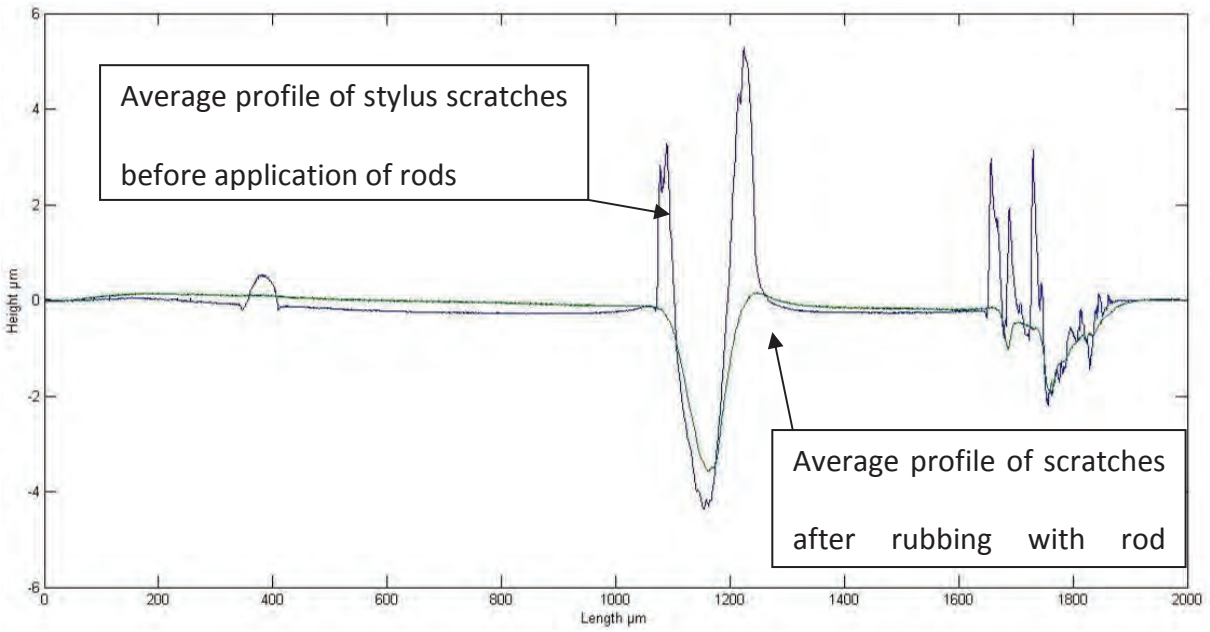

Figure 7.8: Average height profile of a series of scratches in Perspex made by a steel stylus. Two scratches are seen alongside what appears to be a piece of dirt on the left. The scan was taken by the laser profilometer over a 2000 by 250 µm area; each line profile was taken 0.5 µm apart.

A.4 Conclusion

High aspect ratio PCC rod particles are studied for their polishing properties. Rods alone do not give a significant benefit in the tribological experiment. The results presented are different from the standard calcite particle data in order to highlight the mechanisms and benefits of using the PCC rods. It is shown that the rods attack asperities and edges on the surface. This polishes rough surfaces and smoothes scratches. In terms of application there is potentially a large market for this type a polishing, particularly as polishing is higher value industry and polymer use is home increasing.